


12-2016

Unraveling the fingerprints of NO_x using stable isotopes: Implications for NO_x source partitioning and oxidation chemistry

Wendell William Walters
Purdue University

Follow this and additional works at: https://docs.lib.purdue.edu/open_access_dissertations

 Part of the [Atmospheric Sciences Commons](#), [Biogeochemistry Commons](#), and the [Environmental Sciences Commons](#)

Recommended Citation

Walters, Wendell William, "Unraveling the fingerprints of NO_x using stable isotopes: Implications for NO_x source partitioning and oxidation chemistry" (2016). *Open Access Dissertations*. 1025.
https://docs.lib.purdue.edu/open_access_dissertations/1025

This document has been made available through Purdue e-Pubs, a service of the Purdue University Libraries. Please contact epubs@purdue.edu for additional information.

UNRAVELING THE FINGERPRINTS OF NO_x USING STABLE ISOTOPES:
IMPLICATIONS FOR NO_x SOURCE PARTITIONING AND OXIDATION
CHEMISTRY

A Dissertation

Submitted to the Faculty

of

Purdue University

by

Wendell W. Walters

In Partial Fulfillment of the

Requirements for the Degree

of

Doctor of Philosophy

December 2016

Purdue University

West Lafayette, Indiana

**PURDUE UNIVERSITY
GRADUATE SCHOOL
Thesis/Dissertation Acceptance**

This is to certify that the thesis/dissertation prepared

By Wendell Walters

Entitled

UNRAVELING THE FINGERPRINTS OF NOX USING STABLE ISOTOPES: IMPLICATIONS FOR NOX SOURCE PARTITIONING AND OXIDATION CHEMISTRY

For the degree of Doctor of Philosophy

Is approved by the final examining committee:

Timothy R. Filley

Chair

Greg Michalski

Richard H. Grant

Timothy S. Zwier

To the best of my knowledge and as understood by the student in the Thesis/Dissertation Agreement, Publication Delay, and Certification Disclaimer (Graduate School Form 32), this thesis/dissertation adheres to the provisions of Purdue University's "Policy of Integrity in Research" and the use of copyright material.

Approved by Major Professor(s): Greg Michalski

Approved by: Indrajeet Chaubey

Head of the Departmental Graduate Program

11/2/2016

Date

I dedicate this work to my friends and family who have always been there for me and offered unconditional love and support. Thank you so much.

ACKNOWLEDGMENTS

I would like to express my deep appreciation and gratitude to my advisor Dr. Greg Michalski for the guidance and mentorship he provided me these past four years that has been completion of this dissertation possible. His patience, enthusiasm, encouragement, and immense knowledge has shaped my intellectual development and has made me into the researcher I am today.

I would also like to thank my committee members, Drs. Timothy Filley, Timothy Zwier, and Richard Grant for the friendly guidance and thought provoking-suggestions that each of them offered to me. I would like to recognize my lab mates and lab managers over the years for their helpful input, suggestions, and laboratory guidance. I thank the numerous undergraduate students that I have had the privilege to work with for their time, hard-work, and assistance in helping me complete numerous projects.

Special thanks are also due to the Purdue Climate Change Research Center (PC-CRC), the National Science Foundation Graduate Research Fellowship (NSF-GRFP; grant DGE-1333468), the Purdue Bilsland Fellowship, and the Department of Earth, Atmospheric, and Planetary Sciences at Purdue for their financial support that have allowed me to conduct independent research, and/or attend numerous academic conferences leading to my intellectual growth the past four years.

Lastly, I would like to express my thanks to Josh Martin for his love, encouragement, and sacrifices the past few years.

PREFACE

This dissertation is original, independent work by the author, Wendell Walters.

TABLE OF CONTENTS

	Page
LIST OF TABLES	x
LIST OF FIGURES	xiii
ABSTRACT	xix
1 INTRODUCTION	1
1.1 Nitrogen Oxides	1
1.2 Stable Isotopes	4
1.3 $\delta^{15}\text{N}$	6
1.3.1 $\delta^{15}\text{N}(\text{NO}_x)$	6
1.3.2 $\delta^{15}\text{N}(\text{NO}_3^-)$	9
1.4 $\delta^{18}\text{O}$	11
1.4.1 $\delta^{18}\text{O}(\text{NO}_x)$	12
1.4.2 $\delta^{18}\text{O}(\text{NO}_3^-)$	12
1.5 Research Objectives	14
1.6 Outline	15
2 NITROGEN STABLE ISOTOPE COMPOSITION ($\delta^{15}\text{N}$) OF VEHICLE- EMITTED NO_x	17
2.1 Introduction	17
2.2 Materials and Methods	19
2.2.1 NO_x Collection and Processing	19
2.2.2 Isotopic Analysis	21
2.3 Results and Discussion	22
2.3.1 NO_x Exhaust Concentration	22
2.3.2 $\delta^{15}\text{N}\text{-NO}_x$ Values	24
2.3.3 Thermal Production of NO	25

	Page
2.3.4 Catalytic Reduction of NO	29
2.3.5 $\delta^{15}\text{N-NO}_x$ Exhaust Fractionation Factor	30
2.3.6 Implications for $\delta^{15}\text{N-NO}_x$	31
2.4 Conclusion	34
3 NITROGEN STABLE ISOTOPE OF THERMALLY PRODUCED NO_x FROM VARIOUS FOSSIL-FUEL COMBUSTION SOURCES	35
3.1 Introduction	35
3.2 Materials and Methods	39
3.2.1 NO_x Collection and Processing	39
3.2.2 N Isotopic Analysis	40
3.3 Results and Discussion	41
3.3.1 Thermal NO_x $\delta^{15}\text{N}$ values:	41
3.3.2 Impact of catalytic reduction of NO_x on $\delta^{15}\text{N-NO}_x$	45
3.3.3 Regional and Seasonal $\delta^{15}\text{N-NO}_x$ Variations	49
3.4 Conclusion	52
4 THEORETICAL CALCULATION OF NITROGEN ISOTOPE EQUILIB- RIUM EXCHANGE FRACTIONATION FACTORS FOR VARIOUS NO_y MOLECULES	54
4.1 Introduction	54
4.2 Methods and Theory	57
4.2.1 Calculation of Equilibrium Isotope Exchange Fractionation Fac- tors	57
4.2.2 Computational Chemistry Methods	58
4.2.3 Determination of NO_y $^{15}\beta$ and $\alpha_{A/B}$ values	59
4.2.4 Solvent Effects	61
4.3 Results and Discussion	62
4.3.1 Experimental vs Calculated Harmonic Frequencies	62
4.3.2 Calculated NO_y harmonic frequencies	63
4.3.3 Calculated $^{15}\beta$	65

	Page
4.3.4	Calculated $\alpha_{A/B}$ 67
4.3.5	Calculated solvent effects 73
4.4	Conclusion 77
5	NITROGEN ISOTOPE EXCHANGE BETWEEN NO AND NO ₂ AND ITS IMPLICATIONS FOR $\delta^{15}\text{N}$ VARIATIONS IN TROPOSPHERIC NO _x AND ATMOSPHERIC NITRATE 80
5.1	Introduction 80
5.2	Methods 83
5.2.1	Experiment Design 83
5.2.2	N Isotopic Analysis 86
5.2.3	Experimental determination of $\alpha_{\text{NO}_2/\text{NO}}$ 86
5.3	Results and Discussion 87
5.3.1	$\alpha_{\text{NO}_2/\text{NO}}$ 87
5.3.2	Implications for $\delta^{15}\text{N}$ of atmospheric NO ₂ 90
5.4	Conclusions 94
6	THEORETICAL CALCULATION OF OXYGEN EQUILIBRIUM ISOTOPE FRACTIONATION FACTORS INVOLVING VARIOUS NO _y MOLECULES, •OH, AND H ₂ O AND ITS IMPLICATIONS FOR ISOTOPE VARIATIONS IN ATMOSPHERIC NITRATE 96
6.1	Introduction 96
6.2	Methods and Theory 99
6.2.1	Calculation of equilibrium isotope exchange fractionation factors 99
6.2.2	Computational chemistry methods 100
6.3	Results 101
6.3.1	Calculated $^x\beta$ values 101
6.3.2	Calculated $^{18}\alpha_{A/B}$ values 106
6.4	Discussion 108
6.4.1	Predicted daytime HNO ₃ $\delta^{18}\text{O}$ - $\delta^{15}\text{N}$ compositions 109
6.4.2	Predicted nighttime HNO ₃ $\delta^{18}\text{O}$ - $\delta^{15}\text{N}$ space 114
6.4.3	Implications of $\delta^{18}\text{O}$ - $\delta^{15}\text{N}$ compositions in HNO ₃ 116

	Page	
6.5	Conclusions	120
7	<i>AB INITIO</i> STUDY OF NITROGEN AND POSITION-SPECIFIC OXYGEN KINETIC ISOTOPE EFFECTS IN THE NO + O ₃ REACTION	121
7.1	Introduction	121
7.2	Methods	123
7.3	Results and Discussion	126
	7.3.1 Calculated geometries and vibrational frequencies	126
	7.3.2 Calculated kinetic isotope effects	130
	7.3.3 Comparison with experimental data	131
7.4	Conclusion	137
8	SUMMERTIME DIURNAL VARIATIONS IN THE ISOTOPIC COMPOSITION OF ATMOSPHERIC NITROGEN DIOXIDE AT A SMALL MIDWESTERN CITY	138
8.1	Introduction	138
8.2	Methods	141
	8.2.1 Sampling Location	141
	8.2.2 NO ₂ Collection	143
	8.2.3 Isotopic Characterization	144
	8.2.4 Control Tests	145
8.3	Results	146
	8.3.1 Measured [NO _x] and f(NO ₂)	146
	8.3.2 δ ¹⁵ N(NO ₂)	148
	8.3.3 δ ¹⁸ O(NO ₂)	149
8.4	Discussion	151
	8.4.1 δ ¹⁵ N(NO ₂)	151
	8.4.2 δ ¹⁸ O(NO ₂)	155
8.5	Conclusion	158
9	CONCLUSION	161
9.1	δ ¹⁵ N(NO _x) Characterization Studies	161

	Page
9.2 $\delta^{15}\text{N}$ and $\delta^{18}\text{O}$ Isotope Effects	162
9.3 <i>in situ</i> NO_x Isotopic Measurements	164
9.4 Future Outlook	166
LIST OF REFERENCES	168
A SUPPLEMENTARY DATA CHAPTER 6	189
B SUPPLEMENTARY DATA CHAPTER 7	190
VITA	193

LIST OF TABLES

Table	Page
2.1 Vehicle Details, NO _x Concentrations, and $\delta^{15}\text{N-NO}_x$ Values for Collected Exhaust Samples.	23
2.2 Data for the Reactions and the Rate Constants for the Thermal Production of NO ^a	28
3.1 Fossil-Fuel Combustion Source Details, NO _x Concentrations (ppm) and $\delta^{15}\text{N-NO}_x$ (‰) Values for Collected Exhaust or Flue Samples.	42
4.1 Calculated regression coefficients ^a for $^{15}\beta$ for gaseous NO _y molecules as a function of temperature (150 to 450 K) sorted in order of increasing β magnitude at 298 K.	66
4.2 Calculated regression ^a coefficients for $\alpha_{A/B}$ involving gaseous NO _y molecules as a function of temperature (150 to 450 K) sorted in increasing magnitude at 298 K.	69
4.3 Calculated regression coefficients ^a for $^{15}\beta$ for aqueous NO _y molecules as a function of temperature (150 to 450 K) in order of increasing magnitude at 298 K.	74
4.4 Comparison of the zero-point energy (ZPE, = $\frac{1}{2}\sum h\nu$ for harmonic oscillators) difference in the ^{14}N and ^{15}N isotopologues for several NO _y molecules in the gaseous and the aqueous phase, and the enrichment factor ($1000(\alpha_{\text{aq-gas}} - 1)$) between the gaseous and aqueous phases at 270 K.	75
5.1 Summary of NO pressure (p_{NO}), NO ₂ pressure (p_{NO_2}), measured $\delta^{15}\text{N-NO}_2$, and experimentally determined $\alpha_{\text{NO}_2/\text{NO}}$ for each trial conducted at 278 K, 297 K, and 310 K.	88
6.1 Comparison of calculated NO ₃ ν_i (cm ⁻¹) from different computational methods and experimental determined values. Values in parentheses represent the absolute difference between the calculated and experimental frequency for a particular vibrational mode.	103
6.2 Calculated $^{18}\beta$ regression coefficients ^a as a function of temperature (150 K to 450 K) and $^{18}\beta$ (298 K) values for NO _y molecules, •OH, and H ₂ O.	104

Table	Page	
6.3	Calculated $^{18}\alpha_{A/B}$ regression coefficients ^a as a function of temperature (150 to 450 K) and $^{18}\alpha_{A/B}$ (298 K) values for O isotopic equilibrium exchange reactions.	107
6.4	Shift in $\delta^{15}\text{N}$ and $\delta^{18}\text{O}$ of NO, NO ₂ , and HNO ₃ (1) relative to NO _x as a function of f_{NO_2}	113
7.1	Calculated and experimental geometries and harmonic frequencies (cm ⁻¹) of reactants and products calculated at CCSD(T)/6-31G(d) and CCSD(T)/6-311G(d). Bonds and angles are given in degrees and angstroms, respectively.	127
7.2	Comparison of calculated ZPE (cm ⁻¹) using fundamental frequencies derived from experimental data, and calculated using scaled CCSD(T)/6-31G(d), and CCSD(T)/6-311G(d) frequencies. The relative difference in the ZPE (ZPE) for the minor isotopologues relative to the most abundant is shown in parentheses (cm ⁻¹).	128
7.3	Calculated isotopic enrichment factors (ϵ) at CCSD(T)/6-31G(d) and CCSD(T)/6-311G(d) expressed in units of per mil (‰) at 298 K.	130
7.4	Calculated oxygen mass-dependence relationships ($\ln(^{17}\alpha)/\ln(^{18}\alpha)$) and mass-independence values ($\Delta^{17}\text{O}$) at 298 K.	131
7.5	Adapted rate constants (k) at 298 K (10^{-14} cm ³ molecules ⁻¹ s ⁻¹) of NO reactions with various O ₃ isotopologues using KIEs calculated at CCSD(T)/6-31G(d) and CCSD(T)/6-311G(d).	133
A.1	Adapted $^{15}\beta$ regression coefficients as a function of temperature (150 to 450 K) for NO, NO ₂ , NO ₃ , and N ₂ O ₅ that include corrections for zero point energy anharmonicity.	189
A.2	Adapted $^{15}\alpha_{A/B}$ regression coefficients as a function of temperature (150 to 450 K) for N isotopic exchange reactions between NO, NO ₂ , NO ₃ , and N ₂ O ₅ that include corrections for zero point energy anharmonicity.	189
B.1	Cartesian coordinates of the optimized geometries of reactants and products calculated at CCSD(T)/6-31G(d) and CCSD(T)/6-311G(d).	190
B.2	Scaled harmonic frequencies for the major ^{15}N , ^{17}O , and ^{18}O isotopologues of the reactants and products calculated using the ISOEFF program from force constants computed at CCSD(T)/6-31G(d) and CCSD(T)/6-311G(d).	191
B.3	Cartesian coordinates of the optimized geometries of TS1 calculated at CCSD(T)/6-31G(d) and CCSD(T)/6-311G(d).	192

Table	Page
B.4 Calculated isotope enrichment factors ($\epsilon(\text{‰})$) for the major heavy NO and O ₃ isotopologues as a function of temperature using CCSD(T)/6-31G(d) frequencies.	192
B.5 Calculated isotope enrichment factors ($\epsilon(\text{‰})$) for the major heavy NO and O ₃ isotopologues as a function of temperature using CCSD(T)/6-31G(d) frequencies.	192

LIST OF FIGURES

Figure	Page
1.1 NO _x chemistry results in numerous health and environmental impacts that include acid rain, eutrophication, particulate matter formation, smog production, and ozone production.	3
1.2 (a) Estimated NO _x emission budget in the United States and (b) NO _x mobile sector emission break-down.	4
1.3 The carbon isotopic composition relative to Pee Dee Belemnite of CO ₂ in ice core trapped air has decreased in the past two centuries. This provides significant support that the source of the atmospheric increase in CO ₂ derives from fossil-fuel combustion emissions that have characteristically low $\delta^{13}\text{C}$ values of approximately -25‰. Figure recreated from ref. [26].	5
1.4 Range of previously reported $\delta^{15}\text{N}$ values for various NO _x sources. Natural sources are indicated in white, anthropogenic sources are indicated in black, and a mixture of natural and anthropogenic sources are indicated in gray.	7
1.5 Measured $\delta^{15}\text{N}(\text{‰})$ of <i>in situ</i> NO _x (circle) and NO ₂ (square). Active sampling techniques are indicated by open points and passive sampling techniques are indicated by closed points. Average $\delta^{15}\text{N}$ is indicated by the red “X”. References: a [45], b [47], c [47], d [36], e [37], f [39], and g [46].	8
1.6 Measured $\delta^{15}\text{N}(\text{‰})$ of atmospheric nitrate (circles). Average $\delta^{15}\text{N}$ is indicated by the red “X”. References: a [28], b [51], c [52], d [49], and e [50].	9
1.7 Seasonal profile of $\delta^{15}\text{N}(\text{‰})$ of atmospheric nitrate (circles). References: a [28], b [28], c [50], and d [50].	10
1.8 $\delta^{18}\text{O}(\text{‰})$ ranges of various atmospheric O molecules that includes O ₃ , ROO•, H ₂ O, and •OH.	11
1.9 Seasonal cycle in $\delta^{18}\text{O}(\text{‰})$ of atmospheric nitrate. Highest $\delta^{18}\text{O}$ values are observed during the winter due to a higher contribution from the N ₂ O ₅ hydrolysis nitrate formation pathway, while lowest values are observed during the summer due to the higher contribution from the NO ₂ + •OH nitrate formation pathway.	14

Figure	Page
2.1 Emitted $[\text{NO}_x]$ as a function of vehicle run-time prior to sampling, represented as blue circles, that is fit with an exponential decay represented by a red solid line.	24
2.2 $\delta^{15}\text{N-NO}_x$ (‰) as a function of collected $\ln(\text{NO}_x)$ (ppm), where solid data points represent samples collected from vehicles while in neutral and open data points represent exhaust samples collected from vehicles while driven. Square points represent gasoline-powered engines, and circle points represent diesel-powered engines.	25
2.3 Regional variation in commute time and the resulting predicted $\delta^{15}\text{N-NO}_x$ from vehicle exhaust.	33
3.1 Box and whisker plot summarizing the distribution (lower extreme, lower quartile, median, upper quartile, and upper extreme) of $\delta^{15}\text{N-NO}_x$ previously measured and reported in this study for various NO_x emission sources and fuel types. Presence of catalytic NO_x reduction technology is indicated by SCR (selective catalytic reducer) and TWC (three-way catalytic converter).	38
3.2 $\delta^{15}\text{N-NO}_x$ (‰) as a function of collected $\ln[\text{NO}_x]$ (ppm) for gasoline-powered vehicle without (A) and with (B) a 3-way catalytic converter. (B) adapted from ref [100]. Copyright American Chemical Society. Linear fit is indicated by the red line, and 95% confidence interval is shown in light red.	46
3.3 Impact of SCR technology on $\delta^{15}\text{N-NO}_x$ (‰) as a function of $\ln[f_{\text{NO}_x}]$ where f_{NO_x} is the fraction of NO_x normalized to the highest $[\text{NO}_x]$ emission for heavy-duty diesel-powered buses and trucks (A) and coal-fired power plants (B) adapted from [40] Linear fit is indicated by the red line, and 95% confidence interval is shown in light red. Copyright American Chemical Society	48
3.4 Bimonthly $\delta^{15}\text{N-NO}_x$ isoscape across the contiguous U.S. Copyright American Chemical Society	50
4.1 Various transformation pathways for NO_x to HNO_3	56
4.2 The least-squares fitting of experimental harmonic frequencies (ω) calculated harmonic frequencies and residuals for a) B3LYP/cc-pVTZ and b) EDF2/cc-pVTZ levels of theory. The circle points represent the frequencies calculated for NO_3 , and the square points represent all other frequencies calculated for every NO_y molecule included in this study.	64

Figure	Page
4.3 Comparison of calculated B3LYP/cc-pVTZ harmonic frequencies (ω) with the difference between B3LYP/cc-pVTZ and EDF2/cc-pVTZ calculated harmonic frequencies (Δ EDF2). The circle points represent the frequencies calculated for NO_3 , and the square points represent all other frequencies calculated for every NO_y molecule included in this study.	65
4.4 Comparison of calculated gaseous $^{15}\beta$ values using B3LYP/cc-pVTZ (solid line) and EDF2/cc-pVTZ (dash line) methods with those computed in a previous study (dash dot line) and/or those computed from experimental harmonic frequencies (dot line) for a) NO, b) NO_2 , c) $\text{N}_2\text{O}^\alpha$, and d) HNO_3 .	68
4.5 Comparison of calculated equilibrium isotope fractionation factors using B3LYP/cc-pVTZ (solid line) and EDF2/cc-pVTZ (dash line) methods with neglect of solvent effects with those computed from experimental harmonic frequencies (dot line), those computed in previous studies (dash dot line) and/or those experimental measured (single points) for a) $\alpha_{\text{NOCl}\leftrightarrow\text{NO}}$, b) $\alpha_{\text{NO}_2\leftrightarrow\text{NO}}$, c) $\alpha_{\text{HNO}_3\leftrightarrow\text{NO}}$, and d) $\alpha_{\text{N}_2\text{O}_4\leftrightarrow\text{NO}_2}$	71
4.6 Enrichment factor ($1000(\alpha_{\text{aq-gas}} - 1)$) between aqueous and gaseous phase for various NO_y molecules (HNO_2 , N_2O_3 , HNO_3 , N_2O_5 , NO_3^-). Aqueous phase molecules were calculated using the IEP-PCM model with a dielectric (ϵ) constant of 78.39.	76
4.7 Comparison of calculated equilibrium isotope fractionation factors using B3LYP/cc-pVTZ (solid line) and EDF2/cc-pVTZ (dash line) methods with inclusion of solvent effects using the IEF-PCM model with those computed in previous studies (dash dot line) and/or those experimental measured (individual points) for a) $\alpha_{\text{HNO}_3\leftrightarrow\text{NO}}$ and b) $\alpha_{\text{N}_2\text{O}_4\leftrightarrow\text{NO}_2}$	76
5.1 Comparison between previous theoretical calculations of $\alpha_{\text{NO}_2/\text{NO}}$ using harmonic frequencies (solid lines), observable vibrational frequencies (dotted line), harmonic frequencies corrected for anharmonic zero-point energies (dashed line), and experimental measurements (square, circle, and triangle points).	82
5.2 Experimental set-up for the N isotopic exchange between NO and NO_2 . The symbols are: A = rotary pump, B = diffusion pump, C = vacuum gauge, D = NO bulb ($\delta^{15}\text{N} = -42.5\%$), E = NO_2 bulb ($\delta^{15}\text{N} = -32.0\%$), F = Argon tank ($> 99.5\%$), G = 1 L reaction vessel, H = flow meter, I = NO_2 binding denuder tube, and J = NO_2 breakthrough denuder tube.	84

Figure	Page
5.3 Hourly changes in $\delta^{15}\text{N-NO}_2(\text{‰})$ (assuming equilibrium between NO and NO_2 is achieved), temperature (K), and f_{NO_2} over a week at Indianapolis, IN, USA (September 13 - September 20, 2015) (a) and over a year (2007) at Chula Vista, CA, USA (b). (a) highlights the conditions that N isotope exchange has a strong influence on $\delta^{15}\text{N-NO}_2$ relative to $\delta^{15}\text{N-NO}_x$ (dotted line) and conditions that have little influence on $\delta^{15}\text{N-NO}_2$ relative to $\delta^{15}\text{N-NO}_x$ (dashed line). Heavy curves in (b) are 100 point (100 hour) moving averages.	91
6.1 Comparison of calculated $^{18}\beta$ values using B3LYP/cc-pVTZ with those computed in previous studies for (a) NO [71, 133], (b) NO_2 [29, 133, 202], (c) H_2O [71, 144], and (d) HNO_3^c [133]	105
6.2 Comparison of calculated $^{18}\beta$ for NO_3 using various computational methods that include B3LYP/cc-pVTZ, EDF2/cc-pVTZ, and QCISD/cc-pVDZ.	106
6.3 (a) Calculated O isotopic exchange enrichment factors ($1000(^{18}\alpha_{\text{(A/B)}} - 1)$) and (b) calculated O isotopic exchange induced mass-independence ($\Delta^{17}\text{O}(\text{‰}) = 1000\ln(^{17}\alpha_{\text{(A/B)}} - 1) - 0.52 \times 1000\ln(^{18}\alpha_{\text{(A/B)}} - 1)$) for the following exchange reactions: NO/ NO_2 , NO_2/NO_3 , $\text{N}_2\text{O}_5^{\text{geo}}/\text{NO}_2$, $\text{ClONO}_2/\text{NO}_2$, and $\text{ClONO}_2^{\text{t}}/\text{NO}_2$	108
6.4 Estimated $\delta^{18}\text{O-}\delta^{15}\text{N}$ compositions of several NO_y molecules assuming (a) daytime isotopic equilibrium between NO/ NO_2 with $f_{\text{NO}_2} = 0.7$ and (b) nighttime isotopic equilibrium between NO_2 , NO_3 , and N_2O_5 . Where $\text{HNO}_3(1)$, $\text{HNO}_3(2)$, and $\text{HNO}_3(3)$ represent various HNO_3 production pathways that include $\text{NO}_2 + \bullet\text{OH} \rightarrow \text{HNO}_3(1)$, $\text{N}_2\text{O}_5 + \text{H}_2\text{O} + \text{surface} \rightarrow 2\text{HNO}_3(2)$, and $\text{NO}_3 + \text{R} \rightarrow \text{HNO}_3(3) + \text{R}\bullet$	112
6.5 Predicted $\delta^{18}\text{O-}\delta^{15}\text{N}$ compositions for three major HNO_3 production pathways that is compared with previous atmospheric nitrate measurements [28, 49, 51, 52]. Where $\text{HNO}_3(1)$, $\text{HNO}_3(2)$, and $\text{HNO}_3(3)$ represent various HNO_3 production pathways that include $\text{NO}_2 + \bullet\text{OH} \rightarrow \text{HNO}_3(1)$, $\text{N}_2\text{O}_5 + \text{H}_2\text{O} + \text{surface} \rightarrow 2\text{HNO}_3(2)$, and $\text{NO}_3 + \text{R} \rightarrow \text{HNO}_3(3) + \text{R}\bullet$. The data points within the red circles are outside of the predicted equilibrium $\delta^{18}\text{O-}\delta^{15}\text{N}$ space, which may indicate a NO_x source with an extremely low $\delta^{15}\text{N}$ value such as soil denitrification.	117
7.1 Schematic diagram of the assumed potential energy curve for the reaction $\text{NO} + \text{O}_3 \rightarrow \text{NO}_2 + \text{O}_2$ based on prior calculations using QCISD(T)/6-311G(2d)//UMP2(full)/6-31G(d) [240] where R , TS1 , A , TS2 , and P refer to the reactants, transition state 1, intermediate, transition state 2, and products, respectively. Relative energies with respect to the reactants $\text{NO} + \text{O}_3$ are given in kJ/mol and includes ZPE and thermal corrections (298 K).	125

Figure	Page
7.2 Optimized geometry of TS1 at CCSD(T)/6-31G(d) and CCSD(T)/6-311G(d) (given in parentheses). Bond lengths are in Angstroms and angles are in degrees. The dihedral angles of TS1 $\angle(\text{O}_1\text{-N}_1\text{-O}_2\text{-O}_3)$ and $\angle(\text{N}_1\text{-O}_2\text{-O}_3\text{-O}_4)$ are $-169.6^\circ(-171.3^\circ)$ and $77.8^\circ(78.6^\circ)$, respectively.	129
7.3 Rayleigh distillation model of unreacted O_3 in the $\text{NO} + \text{O}_3$ reaction calculated using KIEs at CCSD(T)/6-31G(d) and CCSD(T)/6-311G(d) within <i>Kintecus</i> . The slopes of the linear regression model indicate an overall $\epsilon(\text{‰})$ of -18.6‰ and -19.6‰ for unreacted O_3 at CCSD(T)/6-31G(d) and CCSD(T)/6-311G(d), respectively.	135
7.4 Rayleigh distillation model of unreacted O_3 in the $\text{NO} + \text{O}_3$ reaction calculated using prior experimental data [249]. Inclusion of all experimental data indicate a slope of -0.0305 ± 0.003 that corresponds to an $\epsilon(\text{‰})$ of $-30.5 \pm 0.003\text{‰}$ (solid line, $R^2 = 0.966$). Omission of the data point at $\ln(f) = -3.04$ indicates a slope of -0.0209 ± 0.003 that corresponds to an $\epsilon(\text{‰})$ of $-20.9 \pm 0.003\text{‰}$ (dashed line, $R^2 = 0.969$).	136
8.1 Location of sampling site (star) for <i>in situ</i> NO_2 collection. Image from Google Earth [256]	142
8.2 Sampling apparatus schematic for collection of atmospheric NO_2 , where A is the flow meter (2 L/min), B is aerosol filter, C is the NO_2 binding denuder tube, D is the NO_2 breakthrough denuder tube, and E is the peristaltic pump.	144
8.3 Impacts of $\delta^{18}\text{O}$ exchange between NO_2^- and water ($\delta^{18}\text{O} = -8\text{‰}$) contained within the KOH/guacoil elutant as a function of time contained within solution before isotopic analysis, where the black circles represent the measured $\delta^{18}\text{O}(\text{NO}_2^-)$ and the blue squares represent the estimated fraction of O exchange between NO_2^- and water. The NO_2^- standard (RISL-N10219) has a $\delta^{18}\text{O}$ of 88.5‰ . Solutions immediately analyzed show no impacts of isotopic exchange with water. However, after about 3 days, a constant isotopic exchange is observed of about 2 to 5% with an average exchange of $2.7 \pm 2\%$, lowering the measured $\delta^{18}\text{O}$ of RISL-N10219 by about 2 to 4%.	147
8.4 Averaged diurnal variations in $[\text{NO}_x]$ (a) and $f(\text{NO}_2)$ (b) at our sampling location during the collection period of July 7 to August 4, 2016. Diamonds represent averages for each hour taken from measurements at 30 second intervals each day and the gray lines represent $\pm 1\sigma$ for each hour.	149
8.5 Measured (a) $\delta^{15}\text{N}(\text{NO}_2)$ and (b) $\delta^{18}\text{O}(\text{NO}_2)$ of <i>in situ</i> NO_x collected from July 7, 2016 to August 5, 2016 during the daytime (yellow) and nighttime (dark blue).	150

Figure	Page
8.6 Measured $[\text{NO}_x]$ (red line) and $[\text{NO}_2]$ (shaded) concentrations for the July 18 to July 19 nighttime sampling periods that had a high $\delta^{15}\text{N}(\text{NO}_2)$. Fog formation was indicated to occur between July 19 3:30 am and July 19 5:30 am that coincides with an increase in $[\text{NO}_x]$	154
8.7 (a) Daytime $\delta^{18}\text{O}(\text{NO}_2)(\text{‰})$ shown between previous $\delta^{18}\text{O}(\text{NO}_x)$ estimation of 117‰ resulting from $\text{NO}-\text{O}_3-\text{NO}_2-\text{O}_2$ photochemical cycling [55] and the estimated $\delta^{18}\text{O}(\text{ROO}\bullet)$ of 23‰ [30] and (b) estimated NO oxidation branching ratio between O_3 (red) and $\text{ROO}\bullet$ (black).	156
8.8 Linear least squares regression model between $\delta^{18}\text{O}(\text{NO}_2)$ (blue) and $\delta^{15}\text{N}(\text{NO}_2)$ during the nighttime indicates a correlation ($R^2 = 0.617$) which indicates that nighttime $\delta^{18}\text{O}(\text{NO}_2)$ is influenced by $\delta^{18}\text{O}(\text{NO})$ emission signatures. Applying a mass-balance model, the $\delta^{18}\text{O}(\text{NO})$ source has been estimated (green).	159

ABSTRACT

Walters, Wendell W. Ph.D., Purdue University, December 2016. Unraveling the Fingerprints of NO_x using Stable Isotopes: Implications for NO_x Source Partitioning and Oxidation Chemistry. Major Professor: Greg Michalski.

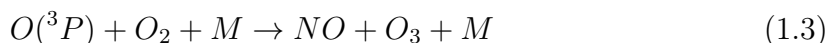
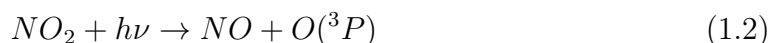
The nitrogen (N) and oxygen (O) stable isotope composition ($\delta^{15}\text{N}$ & $\delta^{18}\text{O}$) of nitrogen oxides (NO_x) maybe a useful tool for constraining NO_x emission sources as well as for understanding the atmospheric oxidation pathways responsible for its removal if various NO_x sources and sink processes exhibit characteristic isotopic compositions (“fingerprints”). However, this requires (1) an accurate and complete inventory of $\delta^{15}\text{N}(\text{NO}_x)$ values from major emission sources, (2) an assessment of the kinetic and equilibrium isotope effects that can impact $\delta^{15}\text{N}$ and $\delta^{18}\text{O}$ values of NO_x, (3) and test these assumptions by conducting accurate *in situ* $\delta^{15}\text{N}$ and $\delta^{18}\text{O}$ measurements of atmospheric NO_x. To this end, I have characterized the $\delta^{15}\text{N}(\text{NO}_x)$ signatures from various fossil-fuel NO_x sources, including buses, trucks, lawn equipment, natural gas-fired boilers, and airplanes. These $\delta^{15}\text{N}(\text{NO}_x)$ source characterization studies along with prior studies indicate that soil emission (nitrification/denitrification), “thermal” NO_x produced from fossil-fuel combustion, and “source” NO_x produced from coal-fired power plants have relative distinctive values. In addition, both my experimental and theoretical investigations on the isotope effects associated with NO_x oxidation indicate that isotopes effects via equilibrium isotope exchange and kinetic isotope effects occurring during NO_x oxidation reactions may influence the $\delta^{15}\text{N}$ and $\delta^{18}\text{O}$ values of atmospheric nitrate. Using these calculated isotope effects, I developed a simple model for the production of atmospheric nitrate through its three major pathways that include (1) $\text{NO}_2 + \bullet\text{OH} \rightarrow \text{HNO}_3$, (2) $\text{N}_2\text{O}_5 + \text{surface} \rightarrow 2\text{HNO}_3$, and (3) $\text{NO}_3 + \text{R} \rightarrow \bullet\text{R}$. This model indicated that these pathways result in distinctive $\delta^{18}\text{O}$ - $\delta^{15}\text{N}$ re-

relationships that tend to match reported literature values. Finally, in order to evaluate the influences of NO_x emission sources and isotope effects on the isotope composition of NO_2 , which serves as precursor molecule to atmospheric nitrate, ambient NO_2 was collected and analyzed for ^{15}N and ^{18}O . These results suggest that $\delta^{18}\text{O}$ of NO_2 has a distinctive diurnal profile reflecting the photochemical cycling of NO_x while $\delta^{15}\text{N}$ of NO_2 tends to track with NO_x sources with small but significant isotope effects altering daytime $\delta^{15}\text{N}(\text{NO}_2)$ by approximately 2-4‰. Overall, this research has refined the “fingerprints” of atmospheric NO_x and will be useful for future studies aimed at understanding regional and spatial distributions in NO_x emission budgets and tracing NO_x oxidation chemistry.

1. INTRODUCTION

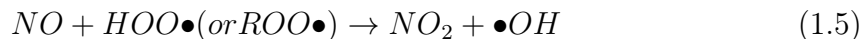
1.1 Nitrogen Oxides

Nitrogen oxides ($\text{NO}_x = \text{nitric oxide (NO)} + \text{nitrogen dioxide (NO}_2)$) are important trace gases and a form of reactive nitrogen (Nr) that influences biogeochemical processes in the atmosphere, terrestrial ecosystems, and freshwater and marine aquatic ecosystems [1–4]. In the atmosphere, NO_x is a key driver of tropospheric chemistry through its influence on the concentrations of the oxidants in the atmosphere, including ozone (O_3) and the hydroxyl radical ($\bullet\text{OH}$) [5]. Both O_3 and $\bullet\text{OH}$ are referred as the “detergents” of the atmosphere due to the role they play in removing many atmospheric pollutants. NO_x influences the concentrations of O_3 and $\bullet\text{OH}$ through its photochemically cycling during the daytime, known as the Leighton Cycle [6, 7]:

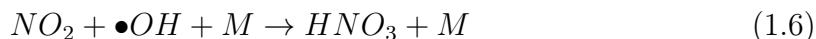


In this reaction sequence, emitted NO is oxidized by O_3 forming NO_2 , which may photolyze back to NO and $\text{O}({}^3\text{P})$. The liberated $\text{O}({}^3\text{P})$ atom regenerates O_3 through its reaction with molecular O_2 . In this reaction sequence, O_3 is conserved; for every O_3 molecule used in the oxidation of NO (R1) another is regenerated during the photolyze of NO_2 and subsequent reaction between $\text{O}({}^3\text{P})$ and O_2 . Thus at photochemical steady state $[\text{O}_3] = [\text{NO}]$ and ozone concentrations are less than total NO_x . Oxidation of NO by peroxy radicals [8], however, provides a pathway for the build-up of tropospheric O_3 :





In 1.4-1.5 the oxidation of NO proceeds without the consumption of an O₃ molecule, but O₃ may be generated from the subsequent photolysis of NO₂ formed from 1.5. This is important because tropospheric O₃ is a greenhouse gas, an oxidizing pollutant, and influences the lifetimes of other greenhouse gases [9]. Termination of this photochemical cycle occurs when NO₂ is oxidized by •OH to form nitric acid (HNO₃) [10]:



This HNO₃ can react with gaseous ammonia to form particulate ammonium nitrate or it can react on existing particles increasing their size (aerosol condensation).

Understanding emission sources and transformation process of NO_x is important due to its important implications for human health and the environment. For example, higher concentrations of Nr (in the form of NO_x or HNO₃) in the atmosphere can lead to an increase in air-pollution based respiratory illnesses due to increases in O₃ and particulate matter [4, 11]. Additionally, HNO₃ may be deposited to the ecosystem via wet and/or dry deposition, leading to the input of a form of Nr in ecosystems [4]. This has numerous consequences including the degradation of drinking water, soil acidification, lacustrine and estuarine eutrophication, and biodiversity changes in terrestrial ecosystems [4] (Fig. 1.1). Thus, due to the numerous human-health and environmental consequences of NO_x emission, it is important to understand the N cycling related to NO_x including its emission sources and the removal processes responsible for its eventual deposition to the biosphere.

Emission sources of NO_x are of both natural and anthropogenic origins [4, 12, 13]. Natural sources of NO_x include lightning, soil nitrification/denitrification, and wildfires [4, 13]. Anthropogenic sources of NO_x include fossil-fuel combustion related to transportation and energy generation, industrial processes, fertilization induced soil nitrification/denitrification, fires, and waste [4, 13]. Since the industrial revolution, the anthropogenic emission budget of NO_x has surpassed the natural emission budget [4, 13]. The increase in the anthropogenic NO_x emission budget is expected to continue

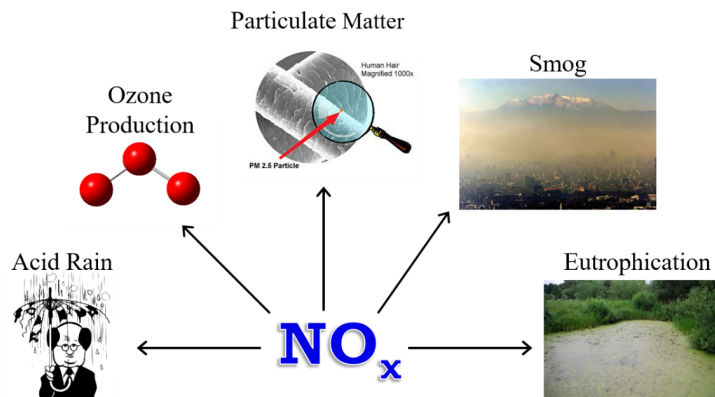


Fig. 1.1.: NO_x chemistry results in numerous health and environmental impacts that include acid rain, eutrophication, particulate matter formation, smog production, and ozone production.

to increase in the future reaching an estimated 71.8 Tg Nyr^{-1} compared to 36.2 TgNyr^{-1} in 1993 [4]. While there have been significant improvements made to reduce NO_x emissions from stationary and mobile sources, further progress is needed to reduce the health and ecosystem impacts related to NO_x emissions [11]. However, there are still large uncertainties in the emission inventories of NO_x that are estimated to be as high as 30% in industrialized regions of North America, Europe, and Japan [4]. In other regions, this uncertainty is as high as 50% [4].

The NO_x emission budget in the United States, indicates that mobile sources are the largest emission source of NO_x [14] (Fig. 1.2). However, within this sector there are large uncertainties in the relative contributions of gasoline and diesel vehicles [14]. Additionally, there are large uncertainties and overlapping NO_x emission budget estimates for energy generation, industrial processes, and soil emissions [14]. In order to estimate the relative importance of various NO_x sources in local/regional nitrogen studies, source identification and apportionment of NO_x and their oxidized products are required. This would help evaluate NO_x emission reduction technologies and help guide future NO_x reduction regulations to mitigate the impacts of Nr inputs in ecosys-

tems. In addition to NO_x source uncertainties, there are large uncertainties of the chemistry of NO_x oxidation related to the distribution between the oxidized forms of NO_x that includes atmospheric nitrate and organic N forms [4]. Thus, uncertainties in the emission budget and the oxidation branching ratios of NO_x remain. Concentration measurements alone, however, cannot partition or quantify the influence of NO_x emission sources and oxidation reactions, indicating a need for a new tool to help achieve these goals.

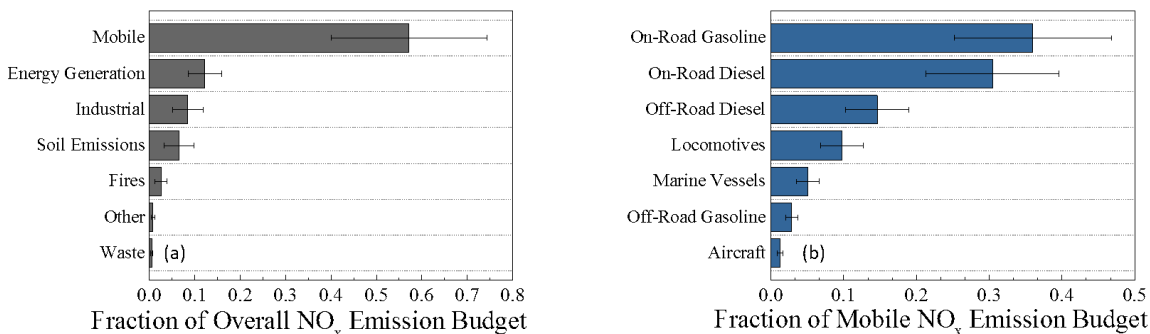


Fig. 1.2.: (a) Estimated NO_x emission budget in the United States and (b) NO_x mobile sector emission break-down.

1.2 Stable Isotopes

Analysis of the stable isotope composition of trace gases has become an established, useful tool for quantifying emission sources, [15], because various trace gas sources and sink processes often exhibit characteristic isotopic compositions (“fingerprints”) [16]. Variations in stable isotope compositions are typically reported in delta (δ) notation:

$$\delta(\text{‰}) = 1000 \left(\frac{R_{\text{sample}}}{R_{\text{standard}}} - 1 \right) \quad (1.7)$$

Where R refers to the ratio of the rare (heavy) isotope to the common (light) isotope in a sample relative to an international isotopic standard. Since these variations are

typically small, they are reported in units of parts per thousand or per mil (‰). Previous research in this field have used this technique to evaluate contributions of various sources and sink processes to numerous trace gases including methane (CH_4) [17, 18], carbon dioxide (CO_2) [19, 20] carbon monoxide (CO) [21, 22], and nitrous oxide (N_2O) [23, 24]. These studies have resulted in significant findings such as observable changes in the carbon isotopic composition of atmospheric CO_2 (Fig. 1.3) is caused by anthropogenic activities [25, 26], providing significant evidence that the excess CO_2 in the modern atmosphere is derived from fossil-fuel combustion. Implementing this stable isotope technique to NO_x and its oxidation products may provide to be a useful tool for partitioning NO_x emission sources and for evaluating the oxidation pathways responsible for the removal of NO_x from the atmosphere [27–30].

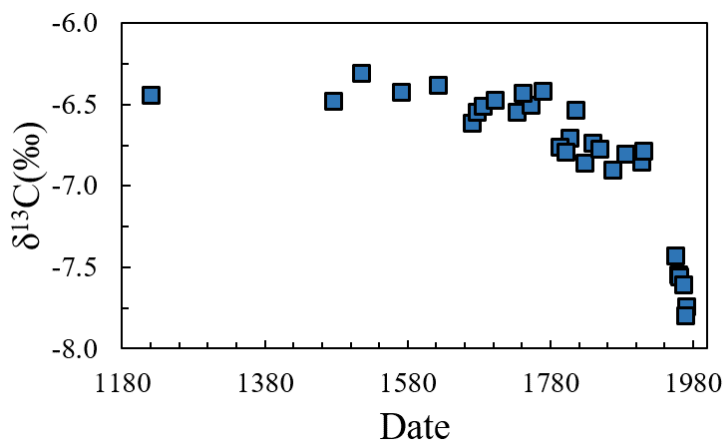


Fig. 1.3.: The carbon isotopic composition relative to Pee Dee Belemnite of CO_2 in ice core trapped air has decreased in the past two centuries. This provides significant support that the source of the atmospheric increase in CO_2 derives from fossil-fuel combustion emissions that have characteristically low $\delta^{13}\text{C}$ values of approximately -25‰ . Figure recreated from ref. [26].

1.3 $\delta^{15}\text{N}$

Once emitted into the atmosphere, NO_x may be oxidized to atmospheric nitrate (HNO_3 + particulate nitrate (p-NO_3^-)) and subsequently removed via wet or dry deposition [4]. Since the N atom in atmospheric nitrate derives from NO_x , the analysis of $\delta^{15}\text{N}$ of atmospheric nitrate has been suggested a useful tracer for NO_x emission sources [27, 28, 31–34]. This would be useful since generally it is much easier to collect atmospheric nitrate dissolved in precipitation or on aerosol filters than it is to collect *in situ* NO_x since it is a reactive gas that exists at low concentrations in the atmosphere (5–25 ppb_v). The drawback of using $\delta^{15}\text{N}$ of atmospheric nitrate for NO_x source partitioning, however, is $\delta^{15}\text{N}$ of NO_x must be conserved as NO_x is oxidized to atmospheric nitrate. Thus, in order to implement $\delta^{15}\text{N}$ for NO_x source partitioning requires (1) a complete and accurate NO_x emission $\delta^{15}\text{N}$ inventory and (2) an understanding of the isotope effects (kinetic, equilibrium, photolytic) that might alter $\delta^{15}\text{N}$ as NO_x is oxidized to atmospheric nitrate.

1.3.1 $\delta^{15}\text{N}(\text{NO}_x)$

Prior $\delta^{15}\text{N}$ measurements of NO_x emission sources are limited, but do indicate that NO_x sources may have a wide range of $\delta^{15}\text{N}$ values that overlaps with major NO_x emission sources (Fig. 1.4). Previous measurements of NO_x from vehicles estimate a wide range of $\delta^{15}\text{N}$ values that range from -13 to 3‰ [31, 33, 35]. Recent $\delta^{15}\text{N}(\text{NO}_x)$ studies from vehicles have based on $\delta^{15}\text{N}$ in roadside plant material [36, 37], tree rings [38], and roadside NO_2 [37, 39] have indicated that vehicle $\delta^{15}\text{N}(\text{NO}_x)$ may be as high as 17‰. However, conclusions reached by these studies should be treated cautiously since they did not measure the $\delta^{15}\text{N}$ of NO_x directly, rather secondary products formed from that NO_x , which may be subject to kinetic and/or equilibrium isotope effects that alter $\delta^{15}\text{N}$ values. Power plant $\delta^{15}\text{N}(\text{NO}_x)$ emissions studies have focused entirely on coal-fired boilers and indicate a $\delta^{15}\text{N}$ range of 6 to 25.6‰ [35, 40]. The relatively large range in $\delta^{15}\text{N}$ from coal-fired power plants has been suggested

to be the result of selective catalytic reduction of NO_x that alters $\delta^{15}\text{N}$ as NO_x is reduced [40]. Soil NO_x ^{15}N values have been measured to range from -48.6 to -19.9‰ [39, 41, 42], which are the lowest $\delta^{15}\text{N}$ of the major NO_x emission sources and are the result of denitrification/nitrification kinetically favoring the light (^{14}N) N isotope resulting in NO_x depleted in ^{15}N . NO_x produced by lightning ^{15}N has been estimated to range between 0 to 2‰ based on laboratory generated sparks [43]. Wildfire's $\delta^{15}\text{N}(\text{NO}_x)$ has been estimated to be 13‰ based on a Greenland ice core study [44], although this value is highly uncertain. In total these measurements of $\delta^{15}\text{N}-\text{NO}_x$ cover the main NO_x emission sources, but there are numerous approximations and uncertainties in the $\delta^{15}\text{N}(\text{NO}_x)$ emission inventory. Thus, further characterization of $\delta^{15}\text{N}(\text{NO}_x)$ is required to minimize the uncertainty in partitioning NO_x source contributions.

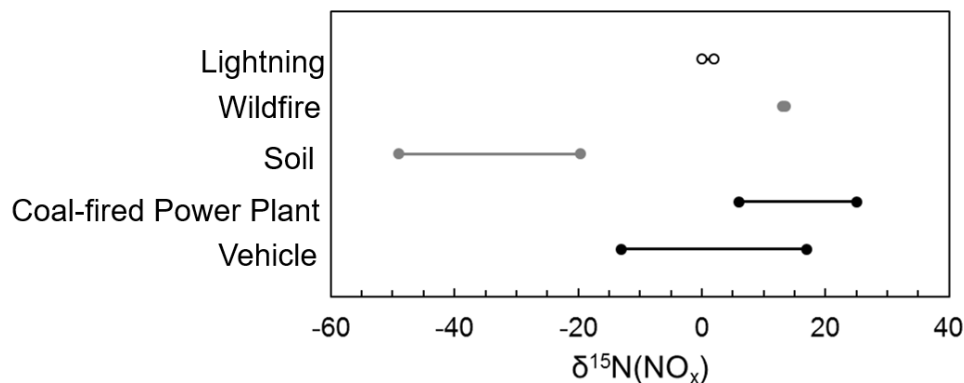


Fig. 1.4.: Range of previously reported $\delta^{15}\text{N}$ values for various NO_x sources. Natural sources are indicated in white, anthropogenic sources are indicated in black, and a mixture of natural and anthropogenic sources are indicated in gray.

Due to the difficulty in collecting *in situ* NO_x , only a few $\delta^{15}\text{N}$ measurements of *in situ* NO_x are available. Collection of total NO_x has been accomplished using an active sampling technique that either scrubs *in situ* NO_x and converts it into NO_3^- [45] or preferentially binds NO_2 [36, 46] as NO_2^- using denuder tubes. Alternatively, NO_2 can be collected using passive diffusion samplers [37, 39, 47] that binds NO_2 and total

NO_x as NO_2^- . The reported $\delta^{15}\text{N}$ values from these *in situ* NO_x or NO_2 studies are shown in Fig. 1.5. A wide $\delta^{15}\text{N}$ range of NO_x (-13.2 to -0.6‰) and NO_2 (-24.3 to 17.0‰) has been reported that spans the same range as the $\delta^{15}\text{N}$ measured in NO_x emission sources. It is unclear whether the large variations in $\delta^{15}\text{N}$ of *in situ* NO_x is driven by the large range of $\delta^{15}\text{N}$ from NO_x emission sources, influences from *in situ* NO_x or NO_2 collection devices, or influences from isotope effects occurring during NO_x cycling. Except for ref. [39] and ref. [36], most of the $\delta^{15}\text{N}$ values of NO_x and NO_2 tend to be negative (Fig. 1.5). Additionally, $\delta^{15}\text{N}(\text{NO}_2)$ tends to be larger than $\delta^{15}\text{N}(\text{NO}_x)$. The data may suggest that $\delta^{15}\text{N}$ of NO_2 may be impacted by $\delta^{15}\text{N}$ of NO_x emission sources as well as isotope effects that may preferentially partition ^{15}N between NO and NO_2 [46]. The influences on $\delta^{15}\text{N}$ of NO_2 needs to be addressed since it serves as precursor to atmospheric nitrate.

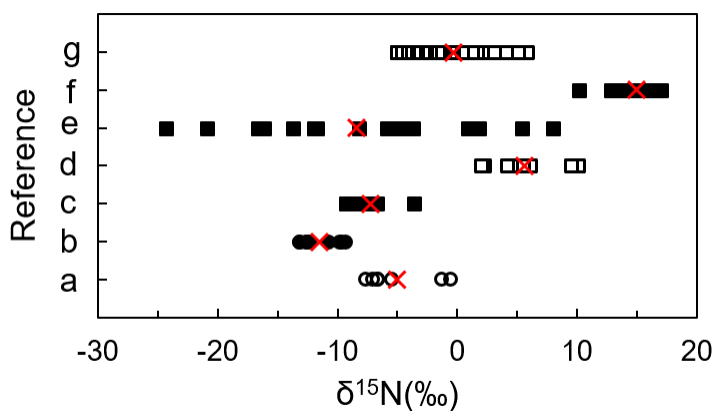


Fig. 1.5.: Measured $\delta^{15}\text{N}$ (‰) of *in situ* NO_x (circle) and NO_2 (square). Active sampling techniques are indicated by open points and passive sampling techniques are indicated by closed points. Average $\delta^{15}\text{N}$ is indicated by the red “X”. References: a [45], b [47], c [47], d [36], e [37], f [39], and g [46].

1.3.2 $\delta^{15}\text{N}(\text{NO}_3^-)$

Numerous studies have characterized the $\delta^{15}\text{N}$ of atmospheric nitrate [27, 28, 31, 48–50]. Fig. 1.6 displays the measured $\delta^{15}\text{N}(\text{NO}_3^-)$ for several studies [28, 49–52]. In general, it is observed that $\delta^{15}\text{N}(\text{NO}_3^-)$ has large variations that range from -19.9 to 11.4‰. Are these large variations related to changing importance of various NO_x sources with varying $\delta^{15}\text{N}$ values or are it due to possible isotope effects as NO_x is oxidized into atmospheric nitrate? On average, $\delta^{15}\text{N}(\text{NO}_3^-)$ tends to be positive (Fig. 1.6), which may provide support that $\delta^{15}\text{N}$ might increase as NO_x oxidizes to NO_3^- since on average *in situ* NO_x $\delta^{15}\text{N}$ values tend to be negative. However, due to the large reported variations in $\delta^{15}\text{N}$ of both *in situ* NO_x and atmospheric nitrate, the controls on $\delta^{15}\text{N}$ (i.e. source, chemistry, or both) cannot be explicitly determined. Thus, both *in situ* NO_x measurements and an isotopic mechanism that may explain how $\delta^{15}\text{N}$ is altered during the oxidation of NO_x to atmospheric nitrate are needed.

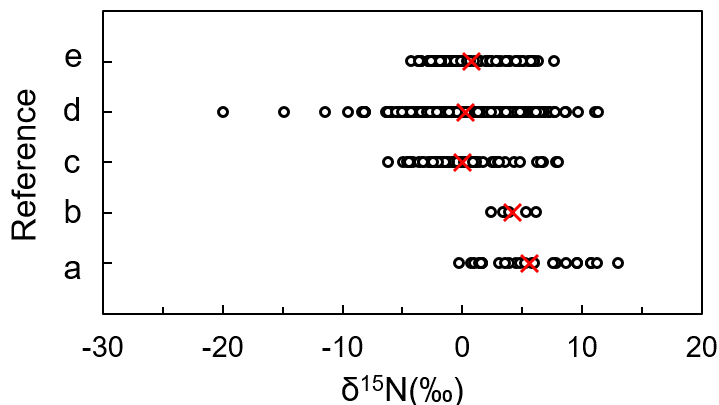


Fig. 1.6.: Measured $\delta^{15}\text{N}(\text{‰})$ of atmospheric nitrate (circles). Average $\delta^{15}\text{N}$ is indicated by the red “X”. References: a [28], b [51], c [52], d [49], and e [50].

In mid-latitude studies, generally a seasonal cycle is observed in $\delta^{15}\text{N}(\text{NO}_3^-)$ (Fig. 1.7) [28, 31, 50]. In each dataset, the similar seasonal $\delta^{15}\text{N}(\text{NO}_3^-)$ trends are observed

in which $\delta^{15}\text{N}$ is highest during the winter and lowest during the summer. This trend has been suggested to be the result of changing importance of various NO_x emission sources [27,28,50]. During the summer, higher NO_x contributions from soil emissions may drive $\delta^{15}\text{N}$ values down, while higher contributions from energy generating units such as coal-fired power plants during the winter may drive $\delta^{15}\text{N}$ values up. However, NO_x emission is regionally dependent, and not every location will likely have influences from soil emission or coal-fired power plants. Another factor that may influence $\delta^{15}\text{N}(\text{NO}_3^-)$ that needs to be considered is a seasonal shift in NO_x oxidation chemistry. During the summer, atmospheric NO_3^- is mostly produced through the reaction of NO_2 with photochemically produced $\bullet\text{OH}$. However, during the winter, atmospheric NO_3^- is mostly produced through the thermal equilibrium between NO_2 , nitrate radical (NO_3), and dinitrogen pentoxide (N_2O_5), and subsequent N_2O_5 hydrolysis of a wetted aerosol. The shift in NO_x oxidation may play a role in the observed $\delta^{15}\text{N}$ of atmospheric nitrate; however, the impact these two distinctive oxidation pathways on $\delta^{15}\text{N}$ needs to be determined in order to understand how oxidation chemistry may influence $\delta^{15}\text{N}$ values.

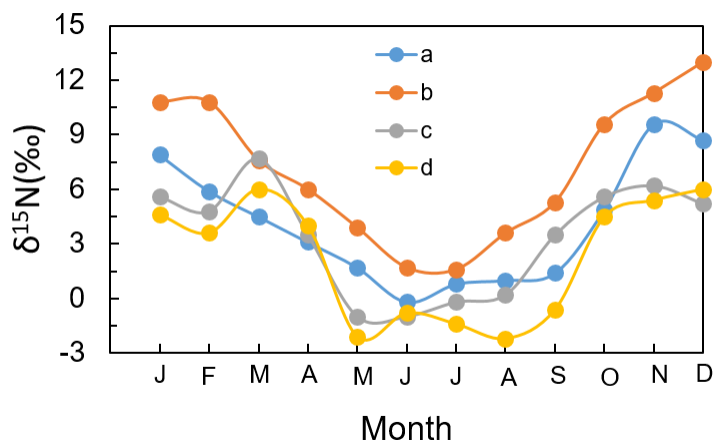


Fig. 1.7.: Seasonal profile of $\delta^{15}\text{N}$ (‰) of atmospheric nitrate (circles). References: a [28], b [28], c [50], and d [50].

1.4 $\delta^{18}\text{O}$

The oxygen (O) stable isotope composition of NO_x ($\delta^{18}\text{O}$) and atmospheric nitrate may provide information about NO_x photochemical cycling and an evaluation of oxidation pathways responsible for the conversion of NO_x to atmospheric nitrate [30, 53–56]. This is because once NO_x is emitted, it cycles its O atoms with atmospheric oxidants. These atmospheric oxidants, including O_3 , $\bullet\text{OH}$, and RO_2 , have distinctive $\delta^{18}\text{O}$ values that can help elucidate which atmospheric oxidants reacted with NO_x (Fig. 1.8). Atmospheric O_3 has characteristic elevated $\delta^{18}\text{O}$ values that have been measured to range 95 to 130‰ [48, 57, 58]. Photochemically produced $\bullet\text{OH}$ is suspected to achieve O isotopic equilibrium with H_2O [59]. For mid-latitudes, $\delta^{18}\text{O}$ of tropospheric water vapor is estimated to range between -25 to 0‰ [30]. Isotopic equilibrium exchange would result in the lowering of $\bullet\text{OH}$ relative to H_2O by 44‰. RO_2 (or HO_2) molecules are formed when radical species combine with atmospheric O_2 . Since O is derived from molecular O_2 , $\text{ROO}\bullet$ is hypothesized to have a $\delta^{18}\text{O}$ reflected air O_2 [30] of approximately 23‰ [60]

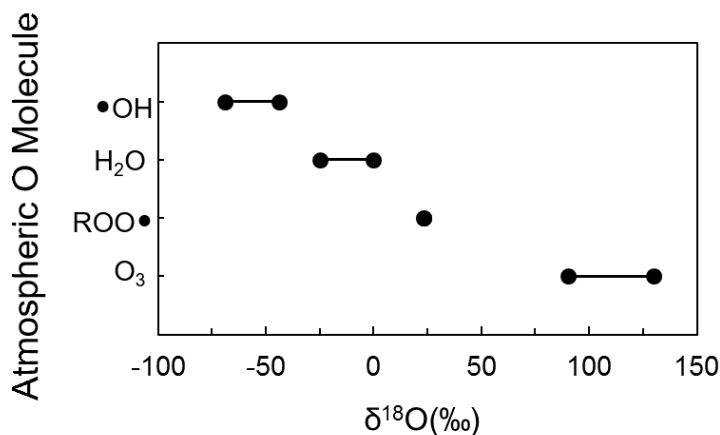


Fig. 1.8.: $\delta^{18}\text{O}$ (‰) ranges of various atmospheric O molecules that includes O_3 , $\text{ROO}\bullet$, H_2O , and $\bullet\text{OH}$.

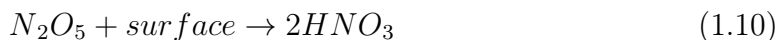
1.4.1 $\delta^{18}\text{O}(\text{NO}_x)$

The photochemical cycling of NO_x is rapid, and is predicted to erase any original $\delta^{18}\text{O}(\text{NO}_x)$ signatures from NO_x emission sources [30, 53, 55, 56]. A recent $\text{NO}-\text{O}_2-\text{O}_3-\text{NO}_2$ photochemical cycle experimental found that O isotopic equilibrium is achieved between NO_x and O_3 resulting in NO_x with a high $\delta^{18}\text{O}$ of $117 \pm 5\%$ relative to VSMOW, reflecting the influence from O_3 oxidation [55]. Previous O isotopic measurements have been performed using Ogawa passive diffusion collectors and indicate lower than expected $\delta^{18}\text{O}$ values for atmospheric NO_x [39, 47]. At an urban location, $\delta^{18}\text{O}$ of NO_2 was found to be $50.5 \pm 3.2\%$ and $47.4 \pm 1.2\%$ during the summer and winter, respectively, which is significantly lower than the model predictions considering that in an urban environment NO is suspected to be primarily oxidized by O_3 [47]. NO_2 collected inside and outside of a tunnel indicate $\delta^{18}\text{O}$ of $-12.6 \pm 3.1\%$ and $-2.0 \pm 5.0\%$ and again reflect lower than expected $\delta^{18}\text{O}$ values. The apparent disagreement between $\delta^{18}\text{O}$ of *in situ* NO_x and model predictions may be due to influences from the capture and conversion of NO_x to nitrite (NO_2^-) that may alter $\delta^{18}\text{O}$. In addition to collection influences, $\delta^{18}\text{O}$ may be influenced by NO oxidation by $\text{ROO}\bullet$ with a significantly lower $\delta^{18}\text{O}$ than O_3 . Also, while the photochemical cycling of NO_x during the daytime may erase any original $\delta^{18}\text{O}(\text{NO}_x)$ signature, the $\delta^{18}\text{O}$ of nighttime NO_x may have a source component as NO_x photochemical cycling ceases. Thus, there are still numerous uncertainties in the $\delta^{18}\text{O}$ of *in situ* NO_x that currently limits our $\delta^{18}\text{O}$ models of NO_x chemistry.

1.4.2 $\delta^{18}\text{O}(\text{NO}_3^-)$

Atmospheric nitrate $\delta^{18}\text{O}$ measurements indicate elevated values with a strong seasonal cycle [27, 28, 49, 52, 61–63] (Fig. 1.9). The $\delta^{18}\text{O}$ values of atmospheric nitrate are suspected to reflect the $\delta^{18}\text{O}$ of the oxidants responsible for the oxidation of NO_x . Thus, the observed seasonal change in $\delta^{18}\text{O}$ reflects the change NO_x oxidation pathways that favors atmospheric nitrate production by the reaction of NO_2 with

$\bullet\text{OH}$ during the summer and formation of N_2O_5 and its subsequent hydrolysis on a wetted aerosol surface during the winter:



Applying O isotopic mass-balance indicates that the $\text{NO}_2 + \bullet\text{OH}$ (1.4) nitrate pathway has a lower contribution from O_3 than the N_2O_5 hydrolysis nitrate formation pathway (1.10) (2/3 vs 5/6). Additionally, $\text{NO}_2 + \bullet\text{OH}$ (1.4) nitrate formation pathway has a relatively high O atom contribution from $\bullet\text{OH}$ (1/3) that is suspected to have an extremely low $\delta^{18}\text{O}$ (Fig. 1.8). These differences result in atmospheric nitrate with lower $\delta^{18}\text{O}$ values during the summertime due to higher relative contribution from the (1.4) pathway and higher $\delta^{18}\text{O}$ values during the wintertime due to higher relative contributions from the (1.10) pathway. In addition to O mass balance considerations, isotopic fractionation processes such as kinetic, equilibrium, or photolytic isotope effects may induce significant $\delta^{18}\text{O}$ variations in atmospheric nitrate. These are important to understand in order to refine the model predictions of $\delta^{18}\text{O}$ of atmospheric nitrate, which could be used to more accurately predict the branching path ratio of NO_x oxidation [53]. Additionally, these fractionation processes may also influence the $\delta^{15}\text{N}$ of atmospheric nitrate and may explain the seasonal cycle also observed in $\delta^{15}\text{N}$ of atmospheric nitrate (Fig. 1.7). Thus, $\delta^{18}\text{O}$ and $\delta^{15}\text{N}$ of atmospheric nitrate may be related, reflecting to some degree the fractionation processes responsible for the formation of atmospheric nitrate in addition to isotopic mass-balance considerations. However, few studies have evaluated the impacts of NO_x oxidation fractionation processes on $\delta^{18}\text{O}$ and their implications for possible $\delta^{18}\text{O}$ - $\delta^{15}\text{N}$ relationships of the atmospheric nitrate end product.

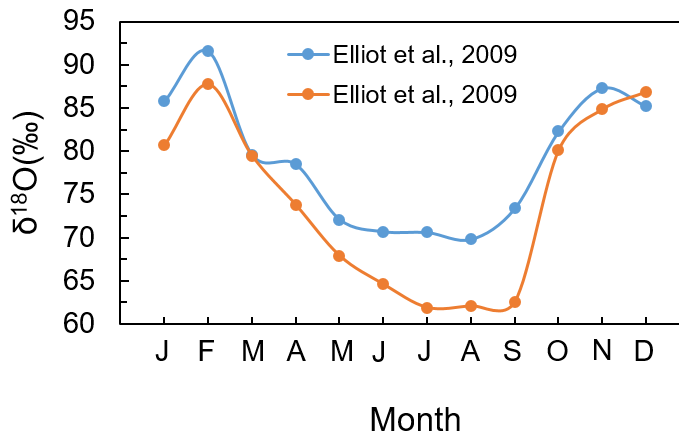


Fig. 1.9.: Seasonal cycle in $\delta^{18}\text{O}$ (‰) of atmospheric nitrate. Highest $\delta^{18}\text{O}$ values are observed during the winter due to a higher contribution from the N_2O_5 hydrolysis nitrate formation pathway, while lowest values are observed during the summer due to the higher contribution from the $\text{NO}_2 + \bullet\text{OH}$ nitrate formation pathway.

1.5 Research Objectives

In order to address the numerous raised uncertainties in the $\delta^{15}\text{N}$ and $\delta^{18}\text{O}$ of NO_x and atmospheric nitrate, this dissertation has the following research objectives:

1. Further characterize and improve upon previous measurement of the $\delta^{15}\text{N}$ signatures from various NO_x emission sources. Particularly, the large range in previous vehicle $\delta^{15}\text{N}$ needs to be addressed since vehicles represent the largest source of NO_x emission in the United States. Additionally, the $\delta^{15}\text{N}$ signatures from many important sources such as diesel trucks and buses, natural gas fired-boilers, and airplanes have yet to be characterized and will be the subject of the reported research.

2. Evaluate possible equilibrium isotope effects associated with NO_x oxidation chemistry. This may have important implications for the $\delta^{15}\text{N}$ and $\delta^{18}\text{O}$ of NO_x and its oxidation products. If significant, these effects may indicate that $\delta^{18}\text{O}$ - $\delta^{15}\text{N}$ relationships in atmospheric nitrate.

3. Evaluate the isotope effects associated with the partitioning of ^{15}N and ^{18}O between NO and NO_2 . This includes the equilibrium isotope exchange reaction and the oxidation of NO by O_3 .

4. Develop a method that can be used to collect *in situ* NO_2 for $\delta^{15}\text{N}$ and $\delta^{18}\text{O}$ analysis. Using this method, $\delta^{15}\text{N}$ and $\delta^{18}\text{O}$ of *in situ* NO_2 will be measured to understand the source and chemistry influences on the isotope composition of atmospheric NO_x .

1.6 Outline

This dissertation is composed of 9 chapters, including this introduction and is organized as the following:

- Chapter 2: Nitrogen stable isotope composition $\delta^{15}\text{N}$ of vehicle-emitted NO_x . (Published by Walters, W. W.; Goodwin, S. R. and Michalski, G. in *Environ. Sci. Technol.* **2015**, 49(4), 2278-2285.)
- Chapter 3: Nitrogen isotope composition of thermally produced NO_x from various fossil-fuel combustion sources. (Published by Walters, W. W.; Tharp, B. H.; Fang, H. and Michalski, G. in *Environ. Sci. Technol.* **2015**, 49(19), 11363-11371.)
- Chapter 4: Theoretical calculation of nitrogen isotope equilibrium exchange fractionation factors for various NO_y molecules. (Published by Walters, W.W. and Michalski, G. in *Geochim. Cosmochim. Acta* **2015**, 164, 284-297.)
- Chapter 5: Nitrogen isotope exchange between NO and NO_2 and its implications for $\delta^{15}\text{N}$ variations in tropospheric NO_x and atmospheric nitrate. (Published by Walters, W. W.; Simonini, D.S. and Michalski, G. in *Geophys. Res. Lett.* **2016**, 43(1), 440-448.)
- Chapter 6: Theoretical calculation of oxygen isotope fractionation factors involving NO_y molecules, OH , and H_2O and its implications for isotope variations

in atmospheric nitrate. (Published by Walters, W. W. and Michalski, G. in *Geochim. Cosmochim. Acta* **2016**, 191, 89-101.)

- Chapter 7: *Ab initio* study of nitrogen and position-specific oxygen kinetic isotope effects in the $\text{NO} + \text{O}_3$ reaction. (Published by Walters, W. W. and Michalski, G. in *J. Chem. Phys.* (accepted with revisions))
- Chapter 8: Summertime diurnal variations in the isotopic composition of atmospheric nitrogen dioxide at a small Midwestern city.
- Chapter 9: Conclusions.

2. NITROGEN STABLE ISOTOPE COMPOSITION ($\delta^{15}\text{N}$) OF VEHICLE-EMITTED NO_x

The following chapter is a reprint from a published article (Walters, W. W.; Goodwin, S. R.; Michalski, G. Nitrogen stable isotope composition ($\delta^{15}\text{N}$) of vehicle-emitted NO_x . *Environ. Sci. Technol.* **2015** 49(4) 2278-2285).

2.1 Introduction

Nitrogen oxides ($\text{NO}_x = \text{NO} + \text{NO}_2$) are important trace gases that affect atmospheric chemistry, air quality, and climate [9]. NO_x plays a key role in the troposphere by acting to control the concentrations of ozone (O_3) and the hydroxyl radical ($\bullet\text{OH}$) as well as forming nitrate (NO_3^-) aerosols [5]. The reactions between NO_x and hydrocarbons (HC) are major sources of tropospheric O_3 , which is a greenhouse gas, an oxidizing pollutant, and influences lifetimes of other greenhouse gases [2, 64]. Ultimately, NO_x is oxidized to nitric acid (HNO_3) and deposited as acid rain leading to degradation of drinking water, soil acidification, lacustrine and estuarine eutrophication, and biodiversity changes in terrestrial ecosystems [4].

Sources of NO_x are both natural and anthropogenic, but there are uncertainties in the relative importance of these sources [4, 12, 13]. Natural sources of NO_x include lightning, soil nitrification/denitrification, and wildfires [4, 13]. Anthropogenic sources of NO_x include fossil fuel and biofuel combustion, mainly emitted from power plants, transport (vehicles, ships, and aircrafts) and industry [12, 13]. Since the industrial revolution, anthropogenic emissions of NO_x have surpassed natural NO_x emissions [4, 12]. While significant improvements have been made to reduce NO_x emissions from stationary and mobile sources, further progress is needed to reduce the health and ecosystems impacts associated with NO_x emissions; however, the uncertainty of

total NO_x emissions is relatively high, with an estimated uncertainty on the order of 30% to 50% [4]. In order to estimate the relative importance of various NO_x sources, and to assess the effectiveness of NO_x reduction technologies, a way of partitioning NO_x sources based on nitrogen (N) deposition studies is required.

Once emitted in the atmosphere, NO_x is primarily oxidized to HNO_3 and subsequently removed from the atmosphere via wet or dry deposition. Therefore, analysis of the N stable isotopes of atmospheric derived nitrate ($\delta^{15}\text{N-NO}_3^-$) could be used as a regional indicator for partitioning NO_x sources, which would help identify the contribution of various NO_x sources to local/regional N deposition, as well as help evaluate the effectiveness of NO_x emission reductions. Previous works have observed spatial variations in $\delta^{15}\text{N-NO}_3^-$ in wet and dry deposition that correlated with the $\delta^{15}\text{N-NO}_x$ of the surrounding areas stationary NO_x emission sources, suggesting $\delta^{15}\text{N-NO}_3^-$ are linked to NO_x sources [27, 28]. However, the impact of kinetic and equilibrium isotopic fractionation of NO_x sink processes (chemical reactions and photolysis) on $\delta^{15}\text{N}$ during the conversion of NO_x to NO_3^- must also be considered but few fractionation factors for these sinks processes have been determined. Previous measurements of $\delta^{15}\text{N-NO}_x$ of various NO_x sources are limited, but indicate that NO_x sources may have a wide $\delta^{15}\text{N}$ range [31, 33, 35–37, 39–41, 44, 65]. Although these prior measurements of $\delta^{15}\text{N-NO}_x$ allow for an approximation of relative source contributions, further characterization of $\delta^{15}\text{N-NO}_x$ is required to minimize uncertainty in partitioning NO_x source contributions, and to understand the impacts of NO_x oxidation to HNO_3 on $\delta^{15}\text{N}$ values. Further, it is possible that technology developments could influence the $\delta^{15}\text{N-NO}_x$ values of various NO_x sources; thus, preventing the application of previous $\delta^{15}\text{N-NO}_x$ measurements to all regions.

In this study, the $\delta^{15}\text{N-NO}_x$ values of vehicle exhaust, the main source of anthropogenic emitted NO_x , were measured. The source of N in vehicle exhaust is air with $\delta^{15}\text{N} = 0\text{‰}$; thus, it was previously assumed that NO_x formed by the oxidation of air would also have $\delta^{15}\text{N}$ near 0‰ [32, 46]. However, previous measurements of $\delta^{15}\text{N-NO}_x$ emitted directly from vehicle exhaust, indicate a rather large range of $\delta^{15}\text{N-NO}_x$

from -13 to 3‰ [31, 33, 35]. Initial studies reported $\delta^{15}\text{N-NO}_x$ values of 3.7‰ and -1.8‰, supporting the assumption that $\delta^{15}\text{N-NO}_x$ emitted from vehicle exhaust is close to 0‰ [31, 33]. However, a subsequent study reported a much wider range of $\delta^{15}\text{N-NO}_x$ values from -13 to -2‰, suggesting that $\delta^{15}\text{N-NO}_x$ from vehicle exhaust may not be as close to the previously assumed value of 0‰ [35]. Recent studies of $\delta^{15}\text{N-NO}_x$ from vehicle exhaust have measured the $\delta^{15}\text{N}$ in plant material [36, 37, 65], tree rings [38], and/or the $\delta^{15}\text{N}$ from roadside NO_2 [36, 37, 39], and indicate that vehicle-derived $\delta^{15}\text{N-NO}_x$ may have positive values as high as 17‰. Such inferences should be treated cautiously because they measure the $\delta^{15}\text{N}$ of a secondary product formed from vehicle emitted NO_x that may be subject to kinetic and equilibrium isotope fractionation factors that can alter the initial $\delta^{15}\text{N-NO}_x$ value [31, 46], and in plant material $\delta^{15}\text{N}$ studies, plant N requirements are likely not entirely derived from NO_x precursors. In order to characterize the $\delta^{15}\text{N-NO}_x$ emitted from modern vehicles, we measured the $\delta^{15}\text{N-NO}_x$ directly emitted from vehicle exhaust for model years 1995 to 2015 in this study.

2.2 Materials and Methods

2.2.1 NO_x Collection and Processing

NO_x was collected from the tailpipes of 26 different vehicles that included 15 passenger cars, 7 sports utility vehicles (SUV) and 4 trucks using a modification of the US-EPA Method 7 at West Lafayette, Indiana, U.S.A. (40.45°N, 86.91°W) between June 20, 2014 and September 26, 2014. The majority of exhaust samples were collected while vehicles were in neutral ($n = 22$), and a smaller set of exhaust samples were collected while vehicles were driven ($n = 4$); under both modes, the engine speed was kept between 2000 to 2500 rpm during sampling. Nineteen of the vehicles sampled had a “cold-engine” (running less than 2 minutes prior to sampling) and seven had a “warm-engine” (running longer than 2 minutes prior to sampling). The vehicles sampled model year ranged from 1995 to 2015, and all vehicles had

gasoline-powered engines except for one which had a diesel-powered engine. Every vehicle sampled was equipped with a 3-way catalytic converter.

The sampling method used in this study was modified from U.S. EPA, "Determination of Nitrogen Oxide Emissions from Stationary Sources." Briefly, exhaust samples were collected into evacuated 2 L borosilicate bottles. The 2 L bottles were connected to a Teflon tube with a length of 35 cm and an inlet diameter of 1 cm attached to a borosilicate probe with a length of 20 cm and an inlet diameter of 0.5 cm. The probe was placed into the tailpipes of each vehicle and the stopcock to the borosilicate bottle was opened allowing the exhaust to be collected. After a sampling period of approximately 10 seconds, the stopcock was closed. Since in the limiting case the diameter of the sampling apparatus (0.5 cm) is approximately 73,500 times larger than the mean-free path at ambient pressures (68 nm) [66], and the sampling time is approximately 1,520 times quicker than the lifetime of NO diffusion through air ($\tau_{\text{diff}} = L^2/D \hat{=} 15216.3$ s, L = length of diffusion, D is diffusion constant = 0.1988 cm²/s) [67] for the total sampling apparatus length of 55 cm, diffusion isotope effects are negligible in this set-up. Additionally, the estimated volume of the Teflon tube and the borosilicate probe was 30 mL making the volume of air in the probe sampled negligible compared to that of the collected exhaust. The sampling bottles contained 10 mL of a NO_x absorbing solution, which was synthesized by mixing 2.8 mL of concentrated sulfuric acid (H₂SO₄) with 0.6 mL of 30% hydrogen peroxide (H₂O₂) and diluted to 1 L using high-purity Millipore water. The absorbing solution quantitatively oxidizes NO_x into NO₃⁻. Triplicate samples were collected for each vehicle approximately 30 seconds apart.

After NO_x exhaust collection, the containers were allowed to stand for at least 72 hours with occasional shaking every 10 to 12 hours to facilitate the conversion of NO_x to NO₃⁻. The residual NO_x headspace concentration was then measured using a Thermo Environmental Instrument Chemiluminescence NO-NO₂-NO_x Analyzer. The absorbing solution was collected and neutralized using 1 mL of 1 M sodium bicarbonate, and the NO₃⁻ concentration was measured using a Cary 5000 UV-Vis

spectrometer. Using the residual NO_x and NO_3^- concentrations, the percent of NO_x conversion to NO_3^- was calculated. Every sample had over 97.5% of the NO_x collected converted to NO_3^- ; therefore, the N isotopic fractionation resulting from this conversion should be minimized. A potential interference that could impact the collected $\delta^{15}\text{N}-\text{NO}_3^-$ is the oxidation of ammonium (NH_4^+) to NO_3^- . Ammonia (NH_3) is known to be a major component of vehicle emitted exhaust [68], and once dissolved in the absorbing solution would presumably form NH_4^+ . Since H_2O_2 , a strong oxidizer, was a component of the absorbing solution, control tests were conducted to determine the possible conversion of NH_4^+ to NO_3^- . The results of the control tests indicated that no detectable NO_3^- formed from relatively high NH_4^+ concentrations (100 ppm) in the absorbing solution used in this study. Therefore, NH_3 should have a minimal if any at all influence on the measured $\delta^{15}\text{N}-\text{NO}_3^-$. Overall, our control studies indicate that our absorbing solution and successive neutralization induces no N isotope fractionation.

2.2.2 Isotopic Analysis

For N isotopic analysis, approximately 250 nmoles of NO_3^- was injected into a 12 mL vial containing 1 mL of a denitrifying strain of bacteria (*P. aureofaciens*) that converts NO_3^- to nitrous oxide (N_2O) [69]. The N_2O was extracted and purified using an automated head space gas chromatography system and analyzed for $\delta^{15}\text{N}$ values by a Thermo Delta V Continuous Flow Isotope Ratio Mass Spectrometer (CF-IRMS) at the Purdue Stable Isotopes lab. Values of $\delta^{15}\text{N}$ are reported in parts per thousand relative to atmospheric N_2 as follows (Eq. 2.1):

$$\delta^{15}\text{N}_{\text{sample}} = 1000\left(\frac{{}^{15}\text{R}_{\text{sample}}}{{}^{15}\text{R}_{\text{standard}}} - 1\right) \quad (2.1)$$

where ${}^{15}\text{R}$ is the ratio of the abundance of ${}^{15}\text{N}$ to ${}^{14}\text{N}$ in a sample and standard, respectively. The isotopic standard for N is atmospheric air. Working lab standards calibrated to NIST isotope reference nitrates USGS34 and USGS35 were used to correct for isotopic fractionation resulting from the denitrification of NO_3^- and the

subsequent N₂O purification process. The working standards had an average standard deviation of 0.3‰ for $\delta^{15}\text{N}$.

2.3 Results and Discussion

Table 2.1 details the vehicle information and the data measured from the vehicles sampled in this study. The text below summarizes the NO_x concentrations (ppm) and $\delta^{15}\text{N}\text{-NO}_x$ (‰) values of the collected samples and discusses our interpretation of these results.

2.3.1 NO_x Exhaust Concentration

The average concentration of NO_x for individual vehicles ranged from 8.5 to 286 ppm with standard deviations ranging from 0.2 to 250 ppm for triplicate samples. The large range and variance of emitted NO_x can be explained by the run time of the engine prior to sampling that were divided into either “cold-engines” (running less than 2 minutes prior to sampling) or “warm-engines” (running longer than 2 minutes prior to sampling). Vehicles with cold-engines emitted significantly more NO_x (95 ± 70 ppm, $n = 19$) compared to warm-engines (17 ± 8.6 ppm, $n = 7$); statistically significant at a confidence level of 0.01 ($p < 0.01$). In the case of vehicles with cold-engines, the highest NO_x concentrations were always collected from the first sample, and NO_x concentrations drastically decreased for subsequent samples; alternatively, warm-engine vehicles generally, emitted NO_x at a consistent concentration for all samples collected. Overall, emitted NO_x concentrations exhibited an exponential decay that moderately correlated with the vehicle run time prior to sampling for all samples (Fig. 2.1).

Table 2.1: Vehicle Details, NO_x Concentrations, and δ¹⁵N-NO_x Values for Collected Exhaust Samples.

year	make	\bar{x} -NO _x ^a	σ -NO _x ^b	\bar{x} -δ ¹⁵ N ^a	σ -δ ¹⁵ N ^b	mode	engine temp
1995	Ford	72.3	15	-8.1	1.7	driven	cold
1996	Chevy	101.1	35	-9.5	1.8	neutral	cold
2000	Chevy	285.6	55	-10.3	1.9	neutral	cold
2000	Ford	31.2	13	-0.8	3.1	neutral	cold
2003	Chevy	55.2	80	0.3	5.4	neutral	cold
2003	Ford	56.1	80	2	8.7	neutral	cold
2003	Honda	31.2	22	-0.4	1.5	neutral	warm
2003	Toyota	23.1	4.5	-2.9	1.6	neutral	warm
2004	Ford	121.2	150	-5.3	6.5	neutral	cold
2005	Dodge	36.5	40	-3.6	7.9	neutral	cold
2005	Ford	138.9	10	-8.3	1.1	neutral	cold
2005	Pontiac	15.7	4	-0.4	1.8	driven	warm
2006	Kia	22.7	13	0.6	3	neutral	cold
2006	Toyota	9.9	0.2	8.6	1.6	driven	warm
2006	Volkswagen	30.1	6	-4.6	3.5	neutral	cold
2008	Ford	21.3	10	1.6	4	neutral	warm
2008	Pontiac	81.4	120	3.4	4.1	neutral	cold
2009	Mazda	106.6	70	-9.6	4.3	neutral	cold
2009	Pontiac	206.2	250	-9	5.3	neutral	cold
2010 ^c	GMC	48.3	30	-19.1	3.8	neutral	cold
2011	Hyundai	138.7	160	-4.4	6.2	driven	cold
2013	Kia	20.9	10	2.4	6.7	neutral	cold
2014	Dodge	197.9	45	-12.2	0.4	neutral	cold
2014	Hyundai	8.8	0.9	9.8	1.1	neutral	warm
2014	Jeep	44.5	4	-5.5	0.8	neutral	cold
2015	Chevy	8.5	0.5	1.6	1.1	neutral	warm

^a \bar{x} = mean. ^b σ = standard deviation. ^c indicates diesel-powered engine

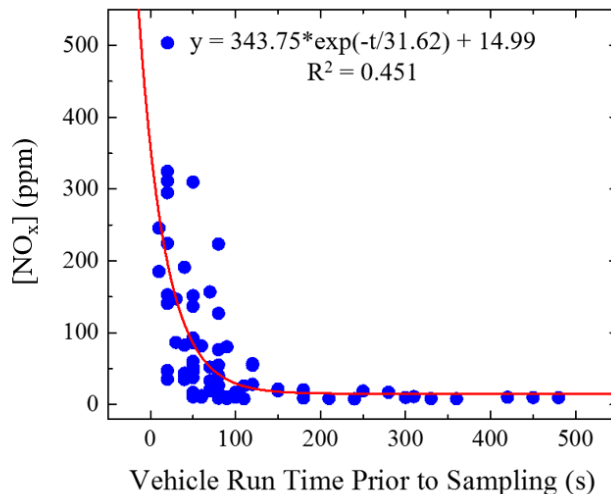


Fig. 2.1.: Emitted $[\text{NO}_x]$ as a function of vehicle run-time prior to sampling, represented as blue circles, that is fit with an exponential decay represented by a red solid line.

2.3.2 $\delta^{15}\text{N-NO}_x$ Values

The average $\delta^{15}\text{N-NO}_x$ measured for each vehicle ranged from -19.1 to 9.8% and the standard deviation ranged from 0.4 to 8.7% for triplicate samples. For most cases, the reported standard deviation was much greater than the analytical uncertainty of $\pm 0.3\%$. This large $\delta^{15}\text{N-NO}_x$ variance can be explained in terms of the emitted NO_x concentration. A strong, negative logarithmic correlation is observed between $\delta^{15}\text{N-NO}_x$ values and NO_x concentrations for gasoline-powered engines ($R^2 = 0.84$) and for diesel-powered-engines ($R^2 = 0.98$) (Fig. 2.2). There was no significant difference between vehicles sampled while in neutral or while driven, as both modes resulted in $\delta^{15}\text{N-NO}_x$ that similarly correlated with emitted NO_x concentration (Fig. 2.2). The measured $\delta^{15}\text{N-NO}_x$ values are hypothesized to have arisen from the thermal production of NO_x in the combustion chamber that would result in NO_x depleted in ^{15}N and from the subsequent equilibrium isotope effects and the catalytic

reduction of NO_x to N_2 which would enrich ^{15}N relative to the thermally produced NO_x . This hypothesis was tested using theoretical isotope fractionation factors in kinetic and Rayleigh distillation models.

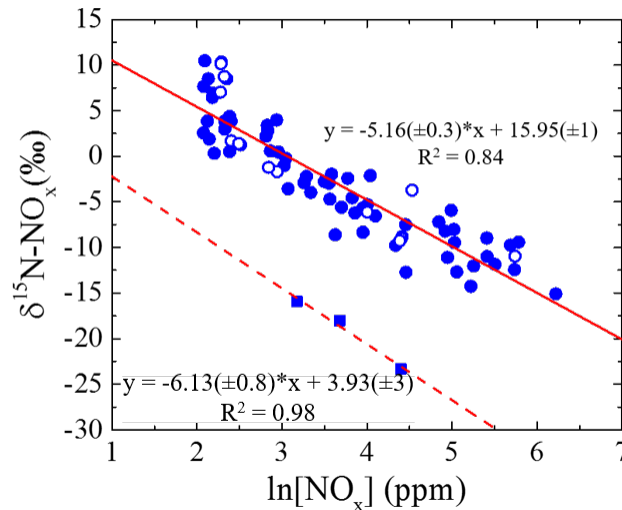
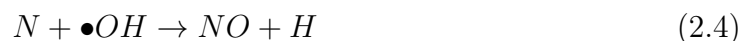


Fig. 2.2.: $\delta^{15}\text{N}-\text{NO}_x$ (‰) as a function of collected $\ln(\text{NO}_x)$ (ppm), where solid data points represent samples collected from vehicles while in neutral and open data points represent exhaust samples collected from vehicles while driven. Square points represent gasoline-powered engines, and circle points represent diesel-powered engines.

2.3.3 Thermal Production of NO

The most well-known chemical pathway for the formation of NO in internal combustion engines is the Zeldovich mechanism [70], in which NO is formed by the reaction between nitrogen and oxygen in the intake air:



Under temperatures of the thermal production of NO ($T > 2000$ K), it has been previously assumed that N_2 , O_2 , and NO exist at isotopic equilibrium [31,32]:



The calculated equilibrium exchange fractionation factor for this reaction is extremely small ($< 1.69\text{‰}$) [71]; therefore, the thermally produced NO should have a $\delta^{15}\text{N}$ value close to air (0‰). However, the majority of our measured NO_x was depleted in ^{15}N , especially for cold-engine vehicles. This suggests that the thermal production of NO in a combustion chamber in a vehicle engine is not always achieving equilibrium, and its formation is kinetically limited by the large amount of energy required to break the triple bond of N_2 (2.2).

A previous study that measured depleted ^{15}N abundances in vehicle exhaust NO_x accredited the ^{15}N depletion to the kinetic isotope effect associated with the breaking the triple bond of N_x [32]. Due to the difference in zero-point energies (ZPE), this bond breaking is faster for the lighter isotopologues ($^{14}\text{N}^{14}\text{N}$, $\text{ZPE} = 1175.7 \text{ cm}^{-1}$; [72]) relative to the heavier isotopologue ($^{15}\text{N}^{14}\text{N}$, $\text{ZPE} = 1156.0 \text{ cm}^{-1}$; [72]). If the difference between N_2 bond dissociation for $^{14}\text{N}^{14}\text{N}$ molecule and $^{15}\text{N}^{14}\text{N}$ molecule is significant at combustion temperatures, then the thermally produced NO will tend to have $\delta^{15}\text{N}$ values lower than atmospheric N_2 . In order to quantify this kinetic isotope effect to understand its impact on $\delta^{15}\text{N}\text{-NO}_x$, the kinetics of the thermal production of NO_x was simulated using *Kintecus*, a kinetics compiler that can be used to model chemical kinetic processes [73]. Table 2.2 summarizes the reactions included in this model and the corresponding Arrhenius rate parameters [74–77]. Rate constants for the molecules involving ^{14}N were taken from NIST chemical kinetics database [78]. These rate constants were adjusted for ^{15}N by calculating the relative reaction rates and therefore fractionation factors (α) of the heavy isotope to the light isotope from the inverse of the reduced masses (μ) of the activated complex at the transition state

(Eq. 2.6) and subsequently scaling the reaction rate of the light isotope for the heavier isotope (Eq. 2.7).

$$\alpha_{H/L} = \sqrt{\frac{\mu_L^\ddagger}{\mu_H^\ddagger}} \quad (2.6)$$

$$k(T)_{\text{heavy}} = \alpha_{H/L} A \left(\frac{T}{298}\right)^n e^{(-E_a/RT)} \quad (2.7)$$

In Eq. 2.6, k is the reaction rate, μ^\ddagger is the reduced mass of the activated complex, H represents the heavier N isotopologue (^{15}N), and L represents the lighter N isotopologue (^{14}N). In Eq. 2.7, A is the Arrhenius pre-exponential factor, T is temperature (Kelvin), n is the temperature dependence, E_a is the activation energy, and R is the gas constant. Kinetic isotope effects are caused by differences in the activation energy for reactions involving different isotopes due to the transition state having different zero-point vibrational energies. Vibrational frequencies (ω_e) and thus vibrational zero-point energies, depend on the reduced mass (μ) of the vibrating system (Eq. 2.8):

$$\omega_e = \frac{1}{2\pi} \sqrt{\frac{k}{\mu}} \quad (2.8)$$

where k is the bond force constant. The ground vibrational mode ($\frac{1}{2}\omega_e$), where h is planck's constant, is inversely proportional to the square root of the reduced mass ($\mu^{1/2}$). Therefore, the inverse of the reduced mass of the activated complex is an adequate approximation for the kinetic isotope effect associated with chemical reactions. For this approximation to be valid at high temperatures, the population of the ground vibrational modes needs to be considered. Both N_2 and NO have relatively high-energy vibrational modes of 2359 and 1904 cm^{-1} associated with vibrational stretching modes [79]. The population of molecules in the ground vibrational state can be calculated based on Boltzmann distribution and the harmonic oscillator approximation (Eq. 2.9):

$$f_i = \left(1 - e^{-\frac{h\nu}{kT}}\right) \quad (2.9)$$

where h is plank's constant, ν is the vibrational frequency, k is Boltzmann constant, and T is temperature. At typical combustion temperatures (2000 K), the majority of

Table 2.2: Data for the Reactions and the Rate Constants for the Thermal Production of NO^a

	reaction	α	A	n	E _a (kJ/mol)
1	$^{14}\text{N}_2 \rightarrow 2^{14}\text{N}$	1	9.86×10^{-5}	-3.33	940
	$^{15}\text{N}^{14}\text{N} \rightarrow ^{14}\text{N} + ^{15}\text{N}$	0.983	9.86×10^{-5}	-3.3	940
2	$\text{O}_2 \rightarrow 2\text{O}$		1.01×10^{-8}	-1	494
3	$^{14}\text{N}_2 + \text{O} \rightarrow ^{14}\text{NO} + ^{14}\text{N}$	1	3.01×10^{-10}	0	318
	$^{15}\text{N}^{14}\text{N} + \text{O} \rightarrow ^{14}\text{NO} + ^{15}\text{N}$	0.997	1.51×10^{-10}	0	318
	$^{15}\text{N}^{14}\text{N} + \text{O} \rightarrow ^{15}\text{NO} + ^{14}\text{N}$	0.995	1.51×10^{-10}	0	318
4	$^{14}\text{N} + \text{O}_2 \rightarrow ^{14}\text{NO} + \text{O}$	1	4.47×10^{-12}	1	27.19
	$^{15}\text{N} + \text{O}_2 \rightarrow ^{15}\text{NO} + \text{O}$	0.994	4.47×10^{-12}	1	27.19
5	$^{14}\text{N} + \bullet\text{OH} \rightarrow ^{14}\text{NO} + \text{H}$	1	4.70×10^{-8}	0	-0.71
	$^{15}\text{N} + \bullet\text{OH} \rightarrow ^{15}\text{NO} + \text{H}$	0.999	4.70×10^{-8}	0	-0.71

N₂ (81.7%) and NO (73.3%) are populated in the ground vibrational state. Therefore, this harmonic oscillator approximation of the activated complexes will be an adequate approximation for this system.

Our $\delta^{15}\text{N}$ thermal NO production model is an approximation; however, the model suggests that the thermal production of NO will result in a $\delta^{15}\text{N}$ value of -9.5‰ assuming that the source of N is air which has a $\delta^{15}\text{N} = 0\text{‰}$. This value is in excellent agreement with the $\delta^{15}\text{N}\text{-NO}_x$ values previously measured (-11 to -7‰) for gasoline-powered vehicle exhaust associated with the kinetically limited thermal production of NO [35]. Presumably, this is the lowest $\delta^{15}\text{N}\text{-NO}_x$ value emitted from vehicles as subsequent equilibrium isotope effect between N₂ and NO (R4) [35], and the catalytic reduction of NO_x would increase the $\delta^{15}\text{N}\text{-NO}_x$ value. However, diesel-powered vehicles seem to have slightly lower $\delta^{15}\text{N}\text{-NO}_x$ values than what our thermal production of NO_x model predicts. The NO_x samples from diesel-powered vehicles analyzed in this study had $\delta^{15}\text{N}\text{-NO}_x$ values that ranged from -23.3 to -15.9‰, and in a previous study $\delta^{15}\text{N}\text{-NO}_x$ values were measured to range from -13 to -12‰ for the kinetically limited thermal production of NO_x [35]. These lower $\delta^{15}\text{N}\text{-NO}_x$ values

likely occur due to the different combustion conditions in diesel vehicles compared to gasoline-powered vehicles [80]. While the exact $\delta^{15}\text{N-NO}_x$ produced from combustion is difficult to predict due to the variability in combustion conditions, the kinetically limited thermal NO_x production should result in negative $\delta^{15}\text{N}$ values.

2.3.4 Catalytic Reduction of NO

Another kinetic isotope effect to consider is from the reaction of NO_x with a 3-way catalytic converter. A 3-way catalytic converter uses a metal catalyst, typically platinum and rhodium, to reduce NO_x emissions upwards of 90% [81]. The catalytic reduction of NO_x to N_2 can be described as NO decomposition on the catalyst surface followed by the removal of the oxygen on the catalyst surface through a reaction with a reducing agent, such as carbon monoxide (CO) [81]. Infrared studies of NO adsorption on alumina and silica supported rhodium have provided evidence for stable molecular adsorption of NO on rhodium [82–84], and temperature-programmed desorption studies have provided evidence for the dissociation of NO on rhodium to form N and O [85–88]. For NO to be reduced to N_2 it has to first undergo adsorption onto the metal catalyst surface. For this process to occur, NO_x has to diffuse through a washcoat layer approximately 10-50 μm thick and then bind onto the catalyst surface [89, 90], likely leading to isotopic fractionation. The lighter molecules (^{14}NO) will diffuse through the washcoat diffusion layer of the catalyst and undergo adsorption more quickly onto the catalyst surface than the heavier molecules (^{15}NO) due to differences in mass and zero-point energies, respectively. This will cause the lighter NO molecules to preferentially decompose to their elemental components with the heavier NO molecules to be emitted when the catalytic converter is effectively operating thus causing the emitted NO_x to be enriched in ^{15}N relative to the thermally produced NO. The number of potentially fractionating reactions and difficulties in assessing catalytic isotope effects for each step is beyond the scope of this work. Rather, the observed $\delta^{15}\text{N-NO}_x$ and NO_x concentration were used in a Rayleigh dis-

tillation model to determine the catalytic converters net isotope effect, which includes diffusion, equilibrium and kinetic effects.

2.3.5 $\delta^{15}\text{N-NO}_x$ Exhaust Fractionation Factor

The results of this study indicate a strong relationship between the emitted NO_x concentration and $\delta^{15}\text{N-NO}_x$ (Fig. 2.2). In general, the more concentrated the NO_x emission was, the lower the $\delta^{15}\text{N-NO}_x$ value. Our kinetics model indicate that thermally produced NO is depleted in ^{15}N , In the absence of a 3-way catalytic converters or under conditions of inefficient NO_x reduction (cold-engine and catalytic converter), the kinetically-limited NO_x production is likely to result in a negative $\delta^{15}\text{N-NO}_x$ value. As the vehicle engine becomes more efficient and the catalytic converter warms up, NO_x emissions are reduced, and the NO_x becomes enriched in ^{15}N relative to the thermally produced NO likely due to the equilibrium isotope effect between N_2 and NO (2.5), as well as the kinetic isotope effect associated with the diffusion and adsorption of NO_x onto the catalytic converter surface as previously discussed. In order to quantitatively determine the $\delta^{15}\text{N}$ isotope fractionation associated with the reduction of NO_x due to warming of a vehicle engine and catalytic converter, this process was modeled according to a Rayleigh type fractionation (Eq. 2.10).

$$\delta^{15}N_f = \delta^{15}N_0 - \epsilon \ln[\text{NO}_x] \quad (2.10)$$

where $\delta^{15}N_f$ is the measured $\delta^{15}\text{N-NO}_x$, $\delta^{15}N_0$ is $\delta^{15}\text{N-NO}_x$ value that vehicle emitted NO_x reaches as NO_x emissions approach zero, and ϵ is the enrichment factor for $\delta^{15}\text{N}$ as the concentration of NO_x decreases. Enrichment factor (ϵ) is related to the fractionation factor (α) of the reduction of NO_x by the following relationship (Eq. 2.11).

$$\epsilon(\text{‰}) = 1000(\alpha - 1) \quad (2.11)$$

From Fig. 2.2 the enrichment factor (ϵ) for the production of vehicle emitted NO_x was calculated for gasoline and diesel-powered engines to be $5.2(\pm 0.3)\text{‰}$ and $6.13(\pm 0.8)\text{‰}$, respectively. This indicates that as the engine and catalytic converter warms up, the

lighter molecules of NO_x are preferentially decomposed, leaving the emitted NO_x enriched in ^{15}N compared to atmospheric air. This suggests that vehicle emitted NO_x has likely become enriched in the ^{15}N isotope relative to the vehicle NO_x emitted prior to 1975 due to the advent of the 3-way catalytic converter.

2.3.6 Implications for $\delta^{15}\text{N}\text{-NO}_x$

The data obtained from this study are limited and do not represent the $\delta^{15}\text{N}\text{-NO}_x$ emitted from all types of vehicles, but they are useful for $\delta^{15}\text{N}\text{-NO}_x$ source characterization of vehicle exhaust. In this study, we measured a rather large range of $\delta^{15}\text{N}\text{-NO}_x$ for individual samples ranging from -15.1 to 10.5‰ for gasoline-powered vehicles and -23.3 to -15.9‰ for diesel-powered vehicles. In general, the lowest $\delta^{15}\text{N}\text{-NO}_x$ values came from cold-start vehicles that were emitting high concentrations of NO_x . As previously mentioned, approximately 60-80% of the total emissions for a typical vehicle occur during the first 200 seconds of cold-start operation [91]. Therefore, in order to estimate the mass-weighted $\delta^{15}\text{N}\text{-NO}_x$ emitted from vehicles, the mass balance of the emitted NO_x concentration needs to be accounted for. To this end, a model was constructed based on numerical integration methods to relate the concentration of emitted NO_x (Fig. 2.1) as a function of vehicle run time with the instantaneous vehicle emitted $\delta^{15}\text{N}\text{-NO}_x$ for gasoline-powered vehicles. This model predicts the mass-weighted $\delta^{15}\text{N}\text{-NO}_x$ emitted from vehicles to have the following relationship with vehicle run time (Eq. 2.12):

$$y = -12.35 + 3.02\ln(t + 0.455) \quad (2.12)$$

where y is the mass-weighted $\delta^{15}\text{N}\text{-NO}_x$ (‰) emitted from vehicles and t is vehicle run time (min). This model shows the importance of NO_x mass-balance to the overall $\delta^{15}\text{N}\text{-NO}_x$. Since NO_x emissions are highest and are most depleted in ^{15}N during the cold-start period, this will lower the overall emitted $\delta^{15}\text{N}\text{-NO}_x$ from vehicles. A similar type of analysis was not performed for diesel-powered engines due to the small sample size measured in this study ($n = 3$).

The average commute time varies regionally in the United States [92], and this likely leads to slight differences in the emitted $\delta^{15}\text{N-NO}_x$ from vehicle exhaust. The U.S. Census Bureau American Community Survey's zip code one-way commute time inventory [92] was used with the $\delta^{15}\text{N-NO}_x$ cumulative release time function (2.12), to estimate the $\delta^{15}\text{N-NO}_x$ of vehicle exhaust emissions in each zip code in the continental U.S. (Fig. 2.3). Overall, the average one-way commute time in the United States is approximately 25.4 minutes, corresponding with a $\delta^{15}\text{N-NO}_x$ value of $-2.5 \pm 1.5\%$. While this average commute time represents all modes of transportation, the majority of transportation is from vehicles (86.1%) so this should be an adequate estimate for the regional $\delta^{15}\text{N-NO}_x$ emitted from vehicle exhaust. This $\delta^{15}\text{N-NO}_x$ approximation only accounts for gasoline-powered engines. Our few measurements of diesel-powered engines had lower $\delta^{15}\text{N-NO}_x$ values than gasoline-powered engines. Therefore, if these measurements are representative of all diesel-powered engines, inclusion of diesel-powered engines to the overall mass-weighted $\delta^{15}\text{N-NO}_x$ would lead to a lower $\delta^{15}\text{N-NO}_x$ value.

Several studies have measured the $\delta^{15}\text{N-NO}_3^-$ in wet [27,31,93] and dry deposition [28], and these values range from -9.5 to 14.1‰, outside of the mass-weighted $\delta^{15}\text{N-NO}_x$ value of vehicle emitted NO_x . Additionally, a recent highway tunnel $\delta^{15}\text{N-NO}_2$ study measured $\delta^{15}\text{N}$ values that ranged from 10.2 to 17‰ [39], which is higher than the majority of the $\delta^{15}\text{N-NO}_x$ measurements made in this study. This discrepancy in $\delta^{15}\text{N-NO}_x$ of vehicle emitted NO_x and of $\delta^{15}\text{N-NO}_3^-$ deposition and $\delta^{15}\text{N-NO}_2$ roadside studies are likely explained by either equilibrium [46] and/or kinetic isotope effects [31] that slightly alter the $\delta^{15}\text{N}$ of the original NO_x source or due to the contribution of other NO_x sources with different $\delta^{15}\text{N-NO}_x$ values. The exact causation of the alteration of $\delta^{15}\text{N}$ is beyond the scope of this work; however, if the $\delta^{15}\text{N}$ of atmospheric NO_3^- is controlled by the source $\delta^{15}\text{N-NO}_x$ then Fig. 2.3 suggests that 1) there will be spatial variations in the $\delta^{15}\text{N}$ of NO_3^- tied to commute time and vehicle NO_x mitigation efficiency, 2) there would be temporal variations in $\delta^{15}\text{N}$ of NO_3^- related to the transition from non-vehicle to vehicle NO_x production during the day and week,

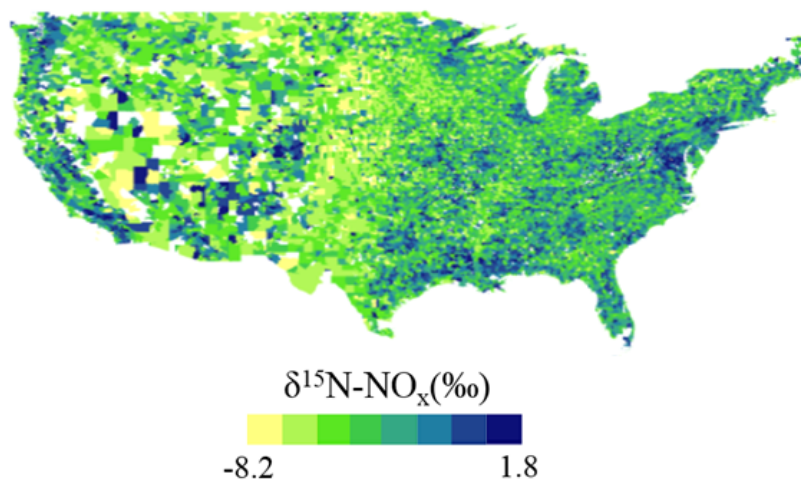


Fig. 2.3.: Regional variation in commute time and the resulting predicted $\delta^{15}\text{N-NO}_x$ from vehicle exhaust.

and 3) the $\delta^{15}\text{N}$ of atmospheric NO_3^- produced between 1950 and 1975 should be significantly lower relative to NO_3^- produced post-1980 and this should be detectable in the northern hemisphere ice core record [44, 94].

The continual improvements of the 3-way catalytic converter will likely have a future impact on the $\delta^{15}\text{N-NO}_x$ values. Once catalytic converters are warmed up, they are up to 97% effective at reducing toxic gas emissions [81, 95]. However, these high conversion rates are only achieved when the converter is typically 300°C or greater which can take several minutes to achieve [95]. This results in more than 60-80% of total emissions occurring during cold-start emissions [96]. Decreasing these cold-start emission is the objective of future catalytic converter improvements [97]. As these technological advancements become commonplace for catalytic converter equipped vehicles, it will likely lead to an increase of the $\delta^{15}\text{N-NO}_x$ value relative to the current value due to the fractionation factor associated with the catalytic reduction of NO_x .

2.4 Conclusion

NO_x concentrations and $\delta^{15}\text{N-NO}_x$ from exhaust was measured from 26 vehicles under various engine run times. NO_x concentration ranged from 8.5 to 503 ppm and $\delta^{15}\text{N-NO}_x$ values ranged from -23.3 to 10.8‰. There was a strong correlation between the emitted NO_x concentration and the associated $\delta^{15}\text{N-NO}_x$ value suggesting that the operating condition of the vehicle contributes to the $\delta^{15}\text{N-NO}_x$ value. In general, when a vehicle has a cold engine, it emitted higher NO_x concentration and was depleted in $\delta^{15}\text{N-NO}_x$. The high concentration of emitted NO_x is accredited to a rich air-fuel ratio and an inefficient 3-way catalytic converter and depleted $\delta^{15}\text{N-NO}_x$ values were caused by the kinetic fractionation of the production of thermal NO. The kinetic isotope effect of the thermal production of NO was modeled to have a $\delta^{15}\text{N}$ value of approximately -9.5‰. Much lower concentrations of NO_x and enriched $\delta^{15}\text{N-NO}_x$ values were observed from vehicles with a warm engine. This is accredited to air-fuel ratio reach the stoichiometric point and an efficient 3-way catalytic converter, and this resulted in enriched $\delta^{15}\text{N-NO}_x$ values associated with the fractionation factor induced from the catalytic reduction of NO_x . Only one vehicle had a diesel-powered engine, but had the most depleted $\delta^{15}\text{N-NO}_x$ out of all the samples suggesting that different fossil-fuel combustion transportation sectors may have distinctive $\delta^{15}\text{N}$ values. Implications for this data are regional variations of $\delta^{15}\text{N-NO}_x$ emitted from vehicle exhaust that depend on average vehicle travel time. Catalytic converter advancements in the near future that will reduce cold start emissions will likely lead an enrichment in $\delta^{15}\text{N-NO}_x$. Future studies should measure $\delta^{15}\text{N-NO}_x$ from other transportation sectors and fuel types in order to evaluate NO_x source partitioning and reduction technologies from atmospheric derived $\delta^{15}\text{N-NO}_3^-$ measurements.

3. NITROGEN STABLE ISOTOPE OF THERMALLY PRODUCED NO_x FROM VARIOUS FOSSIL-FUEL COMBUSTION SOURCES

The following chapter is a reprint from a published article (Walters, W. W.; Tharp, B. D.; Fang, H.; Kozak, B. J.; Michalski, G. Nitrogen isotope composition of thermally produced NO_x from various fossil-fuel combustion sources. *Environ. Sci. Technol.* **2015**, *49*(19), 11363-11371).

3.1 Introduction

Nitrogen oxides (NO_x = NO + NO₂) are trace gases that play several important roles in tropospheric chemistry [3,9]. NO_x controls the photochemical production of ozone, a tropospheric oxidant and greenhouse gas, and influences the concentration of the hydroxyl radical, which acts as the detergent of the atmosphere, removing carbon monoxide, methane, and volatile organic compounds [98]. Oxidation of NO_x leads to the formation of nitric acid (HNO₃), which is subsequently deposited via wet and/or dry deposition leading to the acidification of the environment [4]. The major sources of NO_x are soil emissions, biomass burning, lightning, and fossil-fuel combustion [4,12], and since the industrial revolution, anthropogenic NO_x emissions have surpassed natural NO_x emissions [4,12]. However, the NO_x emission budget is regionally and seasonally variable and differs significantly between remote and urban areas [13,99]. In order to estimate the relative importance of various NO_x sources in local/regional nitrogen (N) deposition, source identification and apportionment of NO_x and their oxidized products is required.

Once emitted into the atmosphere, NO_x primarily oxidizes to particulate nitrate (p-NO₃⁻) and HNO₃; therefore, analysis of their N stable isotope ratio (¹⁵N/¹⁴N)

might be a useful tool for partitioning NO_x sources or reactivity [27, 28, 31]. Previous measurements of the nitrogen stable isotope composition of NO_x ($\delta^{15}\text{N}\text{-NO}_x$; $\delta^{15}\text{N}(\text{‰}) = [(1000(^{15}\text{N}/^{14}\text{N})_{\text{sample}} / (^{15}\text{N}/^{14}\text{N})_{\text{air}} - 1)]$, where air N_2 is the N isotopic reference) have indicated a rather large range for various NO_x sources (Fig 3.1) [31–33, 35–37, 39–43, 45, 100]. Whether these large ranges of $\delta^{15}\text{N}\text{-NO}_x$ are due to actual variations within a source or from differences in measurement methodology is not entirely clear [45]. For example, vehicle $\delta^{15}\text{N}\text{-NO}_x$ has been characterized to range from -13 to 17‰ [31, 33, 35, 38, 39, 65, 100]. We recently performed an extensive study on NO_x emitted directly from vehicle tailpipes and found $\delta^{15}\text{N}\text{-NO}_x$ to range from -15.1 to 10.5‰ that negatively correlated with the emitted NO_x concentration and vehicle run time [100]. This trend was hypothesized to be the result of thermal NO_x production that is depleted in $^{15}\text{NO}_x$ abundance and subsequent NO_x reduction by three-way catalytic converters that increases $\delta^{15}\text{NO}_x$ abundance as a function of reduction efficiency [100]. Vehicle $\delta^{15}\text{N}\text{-NO}_x$ higher than 10.5‰ were not determined from NO_x emitted directly from vehicle tailpipes. Instead, they were inferred from $\delta^{15}\text{N}$ in roadside plant material [36, 37, 65], tree rings [38], and roadside NO_2 [36, 37, 39]. Since these measurements are the $\delta^{15}\text{N}$ of a secondary product formed from vehicle-emitted NO_x , the measured $\delta^{15}\text{N}$ may be subject to kinetic and equilibrium isotope effects that can alter the original $\delta^{15}\text{N}\text{-NO}_x$ emitted from vehicles [31, 46, 101]. Therefore, further characterization of $\delta^{15}\text{N}\text{-NO}_x$ emitted directly from NO_x sources is required to minimize uncertainty in current published values to help assess the utility of $\delta^{15}\text{N}\text{-NO}_3^-$ as a NO_x source or chemistry tracer.

The variation of $\delta^{15}\text{N}\text{-NO}_x$ for different combustion sources may be related to the mechanism in which NO_x is produced [102, 103]. The production of NO_x from combustion processes can be classified into two general categories either “thermal NO_x ” or “fuel NO_x ” [102–104]. Thermal NO_x forms due to the thermal fixation of atmospheric N_2 , while fuel NO_x forms due to the oxidation of chemically bound nitrogen within the fuel [102–104]. The majority of NO_x production in transportation related combustion sources originates from the thermal production, as the N content

in gasoline, diesel, aviation fuel and natural gas is negligible [102,103,105–108]. Thermal NO_x production occurs through four main mechanisms: the extended Zeldovich mechanism, the “prompt” mechanism, the nitrous oxide (N_2O) mechanism, and the NNH intermediate mechanism [106,109,110]. The prevalence of these mechanisms depends on the combustion conditions such as temperature, pressure, and amount of oxygen present in the combustion chamber [106]. Regardless of the mechanism, the N source for the thermally produced NO_x is air ($\delta^{15}\text{N}_{\text{air}} = 0\text{‰}$); consequently, it was first thought that combustion NO_x would be close to $\delta^{15}\text{N} = 0\text{‰}$ [31,35]. However, direct $\delta^{15}\text{N}$ - NO_x measurements of thermally produced NO_x tend to be negative (Fig. 3.1) [35,45,100]. The depletion in $^{15}\text{NO}_x$ abundance is likely due to the kinetic isotope effect associated with the breaking of the triple bond of N_2 that favors the dissociation of $^{14}\text{N}^{14}\text{N}$ over $^{15}\text{N}^{14}\text{N}$, due to $^{14}\text{N}^{14}\text{N}$ having a higher zero point energy (1175.7 cm^{-1}) than $^{15}\text{N}^{14}\text{N}$ (1156.0 cm^{-1}) [72]. Previously, we have estimated the $\delta^{15}\text{N}$ - NO_x associated with the extended Zeldovich mechanism (the dominant mechanism for NO_x production in vehicles) [81]) using a harmonic oscillator approximation for relative reaction rates for the formation of ^{14}NO and ^{15}NO to be approximately -9.5‰ [100]. Presumably, other mechanisms for the thermal NO_x production will also emit NO_x depleted in ^{15}N , because in each case a N bond must break, which will favor the dissociation of ^{14}N over ^{15}N . Though, the exact N fractionation for the various thermal NO_x production pathways may be slightly different due to the pathway's reaction energetics and temperature since the magnitude of an isotopic fractionation is temperature dependent [111].

The characterization of $\delta^{15}\text{N}$ - NO_x emitted directly from fossil-fuel combustion sources has improved in recent years, but uncertainties remain [31,33,35,40,45,100]. It has been suggested that anthropogenic NO_x emission sources have $\delta^{15}\text{N}$ - NO_x values close to zero or positive [31,112], but this may not be true for all anthropogenic NO_x sources, since production of thermal NO_x results in negative $\delta^{15}\text{N}$ - NO_x values [100]. The presence of NO_x reduction technology (i.e. three-way catalytic converters), though, appears to increase $\delta^{15}\text{N}$ - NO_x values relative to the produced NO_x as observed

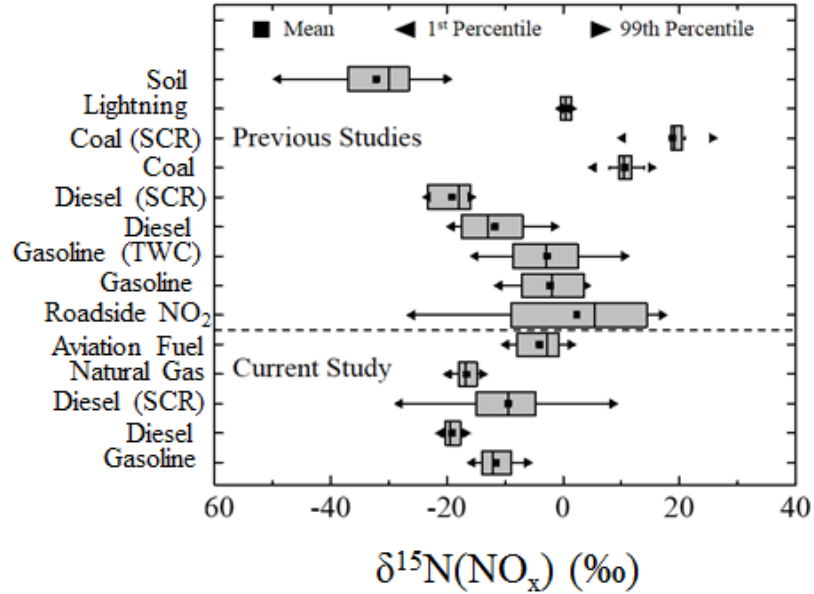


Fig. 3.1.: Box and whisker plot summarizing the distribution (lower extreme, lower quartile, median, upper quartile, and upper extreme) of $\delta^{15}\text{N}\text{-NO}_x$ previously measured and reported in this study for various NO_x emission sources and fuel types. Presence of catalytic NO_x reduction technology is indicated by SCR (selective catalytic reducer) and TWC (three-way catalytic converter).

in vehicles [100] and in coal-fired power plants [40]. The magnitude of this $\delta^{15}\text{N}\text{-NO}_x$ increase, however, is not clear for all NO_x sources, and in many cases, combustion engines are not equipped with catalytic NO_x reduction technology. To the best of our knowledge, there is no $\delta^{15}\text{N}\text{-NO}_x$ data for fossil-fuel combustion sources that make up a significant percentage of the NO_x emission budget of the U.S. and can have limited NO_x reduction capabilities. These include: aircraft (0.7%), off-road diesel-powered engines and equipment (8%), off-road gasoline-powered engines and equipment (2%), natural gas-burning EGU's (8%), and on-road heavy duty diesel-powered engines (17%) [113]. In this study we measured the N isotopic composition in these fossil-fuel combustion sources.

3.2 Materials and Methods

3.2.1 NO_x Collection and Processing

Exhaust grab samples were collected from nineteen different fossil-fuel combustion sources that included: three airplanes, two gasoline-powered vehicles not equipped with a three-way catalytic converter, five gasoline-powered lawn tools, one 4 × 4 utility vehicle, three diesel-electric urban buses, three diesel semi-trucks, one residential gas furnace, and one natural gas-fired power plant using a modification of the U.S. Environmental Protection Agency Method 7 [14]. Briefly, exhaust or flue samples were collected into a 2 L borosilicate bottle evacuated to 75 Torr. The sampling bottles contained 10 mL of a NO_x absorbing solution that was prepared by diluting 2.8 mL of concentrated sulfuric acid (H₂SO₄) and 0.6 mL of 30% hydrogen peroxide (H₂O₂) to 1 L using Millipore water. The absorbing solution quantitatively oxidizes NO_x into NO₃⁻. Isotope effects associated with diffusion fractionation or collection of NO_x in ambient air are negligible in our NO_x grab sample setup [100]. Between three and twelve replicate samples were collected for each combustion source usually as a function of engine run time. Seven fossil-fuel combustion sources were equipped with either pre- or post-combustion NO_x reduction technology. Both the natural gas residential furnace and power plant were equipped with low-NO_x burners, a type of pre-combustion NO_x reduction technology that limits the formation of NO_x [114], and three urban buses and two semi-trucks sampled had selective catalytic reducers (SCR), a type of post-combustion catalytic NO_x reduction technology. Prior to collection, the various combustion sources were typically warmed up between 1 and 5 minutes. Details for each combustion source (i.e. fuel type, NO_x reduction technology, and warm-up time) can be found in Table 1.

After sampling, the exhaust/flue gases collected within the bottles were equilibrated with the NO_x absorbing solution for at least 72 hours with occasional shaking every 10 to 12 hours to facilitate the conversion of NO_x to NO₃⁻. Residual NO_x headspace concentrations were measured using a chemiluminescence NO-NO₂-NO_x

analyzer (Thermo-Environmental Instrument), and the NO_x absorbing solution was collected and neutralized using 1 mL of 1 M sodium bicarbonate buffer. The converted NO_3^- concentrations were measured using a UV-Vis spectrometer (Cary 5000), and the percent of NO_x conversion to NO_3^- was calculated based on the residual NO_x and converted NO_3^- concentrations. In each case, at least 99.3% of all collected NO_x was converted to NO_3^- , suggesting that N isotopic fractionation during this conversion should be minimized. Control tests indicate that the NO_3^- blank in the NO_x absorbing solution was below the detection limit. Recently, the presence of ammonia (NH_3) has been suggested as a possible interference in NO_x absorbing solutions specifically those that use potassium permanganate (KMnO_4) which will slowly oxidize NH_3 to NO_3^- under basic conditions [45]. This was tested as a possible interference by adding NH_3 into the employed NO_x absorbing solution. No detectable NO_3^- formed even at relatively high ammonium (NH_4^+) concentrations (100 ppm) and a wait time of one month, which is the longest time the solutions sat before being analyzed for $\delta^{15}\text{N}$. Therefore, we believe that NH_3 has a minimal to no impact on neither the measured NO_3^- concentrations nor the $\delta^{15}\text{N}$ - NO_x values. Control tests using NO and NO_2 of a known isotopic composition that went through the entire NO_x collection procedure indicate that the reproducibility in our measured $\delta^{15}\text{N}$ - NO_x values to be $\pm 1.3\%$.

3.2.2 N Isotopic Analysis

N isotopic analysis was carried out on the product NO_3^- in the absorption solution. Approximately 250 nmoles of NO_3^- was injected into a 12 mL vial containing 1 mL of a denitrifying strain of bacteria (*P. aureofaciens*) that lacks the nitrous oxide (N_2O) reductase enzyme, converting NO_3^- into nitrous oxide (N_2O) [69]. The N_2O was extracted and purified using an automated head space gas chromatography system and analyzed by a Thermo Delta V Continuous Flow Isotope Ratio Mass Spectrometer (CF-IRMS) for m/z 44, 45, and 46 at the Purdue Stable Isotopes Lab. Working lab standards, calibrated to NIST isotope reference nitrates USGS34 and USGS35, were

used to correct for isotopic fractionation resulting from the denitrification of NO_3^- and the subsequent N_2O purification process. The working standards had an average standard deviation of 0.3‰ for $\delta^{15}\text{N}$.

3.3 Results and Discussion

Table 3.1 details the data measured from the various fossil-fuel combustion sources. The text below summarizes the measured $\delta^{15}\text{N}\text{-NO}_x$ values of the collected samples and discusses our interpretation of these results and possible implications. The $\delta^{15}\text{N}\text{-NO}_x$ values measured for the various fossil-fuel combustion sources are summarized in Fig. 3.1 sorted by fuel type.

3.3.1 Thermal NO_x $\delta^{15}\text{N}$ values:

The $\delta^{15}\text{N}\text{-NO}_x$ values for most of the combustion sources appear to be associated with the production of thermal NO_x . Excluding the NO_x sources equipped with an SCR (Table 3.1), the average $\delta^{15}\text{N}\text{-NO}_x$ for each source tended to be negative, ranging from -19.1 to 0.6‰ , indicating that these samples generally had less $^{15}\text{NO}_x$ abundance than the N isotopic reference N (air). Within any given source, the standard deviations ranged from 0.3 to 3‰ . This $\delta^{15}\text{N}\text{-NO}_x$ range is consistent with previous isotopic measurements of NO_x collected from the tailpipes of vehicles without catalytic converters (-13 to -2‰) [35] and exhaust samples collected from a diesel engine in a smog chamber ($-18.0 \pm 1\text{‰}$) [45]. Negative $\delta^{15}\text{N}$ values in NO_x produced by vehicles with cold-engines, when NO_x catalytic reduction is inefficient, has also been observed [100]. All together, this suggests that thermally produced NO_x tends to be depleted in ^{15}N abundance.

The fuel type and engine-design may have played a role in the $\delta^{15}\text{N}\text{-NO}_x$ emitted by different combustion sources (Fig. 3.1). The gasoline-powered combustion engines that included light duty vehicles, lawn equipment/tools, and a utility vehicle had an average $\delta^{15}\text{N}\text{-NO}_x$ of $-11.5 \pm 2.7\text{‰}$ ($n = 46$). This average $\delta^{15}\text{N}\text{-NO}_x$ is within one

Table 3.1: Fossil-Fuel Combustion Source Details, NO_x Concentrations (ppm) and $\delta^{15}\text{N-NO}_x(\text{‰})$ Values for Collected Exhaust or Flue Samples.

Source	Fuel	$\bar{x}\text{-NO}_x$ ^a	$\sigma\text{-NO}_x$ ^b	$\bar{x}\text{-}\delta^{15}\text{N}$ ^a	$\sigma\text{-}\delta^{15}\text{N}$ ^b	n
Airplane 1 (Idle)	Aviation Fuel	39	10	-7.5	3	4
Airplane 1 (Throttle)	Aviation Fuel	185	50	-7.7	3	4
Airplane 2	Aviation Fuel	456	60	0.6	1	4
Airplane 3	Aviation Fuel	462	95	-1.5	0.7	4
Car 1	Gasoline	63	7	-13.6	1	11
Car 2	Gasoline	71	13	-9.5	1	5
4 × 4	Gasoline	30	5	-7.6	1	5
Bus 1 ^c	Diesel-Electric	160	40	-20.9	7	4
Bus 2 ^c	Diesel	146	20	-15.7	2	4
Bus 3 ^c	Diesel-Electric	32	4	-1.7	3	4
Semi-Truck 1	Diesel	160	20	-19.1	2	5
Semi-Truck 2 ^c	Diesel	24	10	-2.0	8	6
Semi-Truck 3 ^c	Diesel	45	23	-10.9	3	4
Leaf Blower	Gasoline	132	40	-14.3	1	8
Yard Trimmer	Gasoline	80	30	-9.6	1	7
Tractor 1	Gasoline	141	15	-14.6	1	4
Tractor 2	Gasoline	47	10	-10.7	1	3
Tractor 3	Gasoline	31	1	-8.5	0.3	3
Residential Furnace ^d	Natural Gas	34	10	-15.5	1	12
Power Plant ^d	Natural Gas	70	10	-17.9	1	11

^a \bar{x} = mean. ^b σ = standard deviation. Only ^c(SCR) and ^d(Pre:Low-NO_x Burner) had equipped NO_x reduction technology.

standard deviation of our predicted value for the extended Zeldovich mechanism of -9.5‰ [100]. In contrast, the average $\delta^{15}\text{N-NO}_x$ for diesel sources without SCR was $-19.1 \pm 1.8\text{‰}$ ($n = 5$) and $-16.5 \pm 1.7\text{‰}$ ($n = 33$) for a natural gas combustion sources (power plant and residential furnace), which were significantly lower than gasoline-powered sources ($p < 0.01$). Both gasoline and diesel combustion engines generally produce NO_x through the extended Zeldovich mechanism during the peak-temperature phase when temperatures exceed 2000 K [115, 116]; therefore, N fractionation associated with the temperature that NO forms likely cannot explain the observed difference in $\delta^{15}\text{N-NO}_x$. We hypothesize that the observed difference may be related to the significance of NO decomposition in the combustion chamber. During the peak-temperature phase, NO concentrations reach a maximum, but NO subsequently decomposes post-combustion due to high temperature reactions with N, O, and H radicals [115, 117]. In diesel engines, combustion gases cool more quickly post-combustion than in gasoline engines due to mixing of high temperature gas with air or cooler burned gases, which does not occur in gasoline engines [115]. Consequently, less NO decomposition occurs in diesel engines compared to gasoline engines [115]. If NO decomposition reactions are kinetically controlled then they will occur faster for ^{14}NO than for ^{15}NO , and this would lead to the enrichment of ^{15}NO . Thus, if NO decomposition were more significant in gasoline engines than for diesel engines, this would enrich ^{15}NO abundance in gasoline engines compared to diesel engines and may explain higher $\delta^{15}\text{N-NO}_x$ values in gasoline engines. Though other differences between gasoline and diesel engines such as air-to-fuel ratios, cylinder pressures, ignition timing, and exhaust gas recirculation rates may also play a role in the observed difference in $\delta^{15}\text{N-NO}_x$ [116].

Unlike gasoline and diesel engines, low- NO_x burner natural-gas combustion does not predominately produce NO_x through the extended Zeldovich mechanism [118]. The flames in low- NO_x burners natural-gas combustion have temperatures that have been measured to range from 800 to 1600 K [119], but the extended Zeldovich mechanism is significant only at temperatures more than 1800 K because of its high activation

energy (≈ 76 kcal/mol) [106]. Natural gas combustion models indicate that below 1400 K, NO_x production occurs mainly through the N_2O and the NNH mechanism [118]. While difficult to estimate the N fractionation associated with the N_2O and NNH mechanism due to the complicated nature of these mechanisms, we expect the observed $\delta^{15}\text{N-NO}_x$ from natural-gas combustion to reflect the average contribution of the thermal NO_x production mechanism and their associated temperature dependent N fractionation. Thus, the difference between the $\delta^{15}\text{N-NO}_x$ values for gasoline and natural gas combustion sources is likely due to both the N_2O and NNH mechanism possibly having a different NO_x isotopic fractionation signature than the extended Zeldovich mechanism, as well as natural gas combusting at lower temperatures.

The other type of fuel used by combustion sources in this study was aviation fuel, which is a highly refined form of gasoline [107, 108]. These samples (3 airplane piston engines) had an average $\delta^{15}\text{N-NO}_x$ of $-4.0 \pm 4.0\%$ (n = 16). Interestingly, airplane 1, had an average $\delta^{15}\text{N-NO}_x$ of $-7.6 \pm 1.8\%$ (n = 8), which is nearly within one standard deviation of our estimated value for the extended Zeldovich mechanism. Airplane 1 was sampled both with at idle and while under load, but no significant difference in $\delta^{15}\text{N-NO}_x$ was observed ($p > 0.1$; Table 3.1). However, both airplanes 2 and 3, which were both sampled while under load, had an average $\delta^{15}\text{N-NO}_x$ value of $-0.45 \pm 1.4\%$ (n = 8). The $\delta^{15}\text{N-NO}_x$ values for airplanes 2 and 3 were statistically significantly higher than any other of the combustion sources analyzed in this study ($p < 0.01$). These two airplanes' $\delta^{15}\text{N-NO}_x$ values suggest isotope equilibrium, rather than kinetic isotope effects might have been important [35]. Theory predicts that the N isotopic exchange between N_2 , O_2 , and NO (3.1) would result in $\delta^{15}\text{N-NO}_x$ of -0.9% at combustion temperatures of 2200 K [71].



This predicted value is within one standard deviation of the average $\delta^{15}\text{N-NO}_x$ emitted from airplanes 2 and 3, indicating that under their combustion conditions, N isotopic equilibrium might have been reached [35]. Previously, ref [35] used isotopic equilibrium to explain high NO_x concentrations and $\delta^{15}\text{N-NO}_x$ values that were close

to 0‰ for gasoline and diesel vehicles operating under heavy-load conditions when combustion temperatures are higher and reaction times longer. Engine load may explain why airplanes 2 and 3 reached equilibrium, but airplane 1 while under load, did not seem to reach isotopic equilibrium based on its average $\delta^{15}\text{N-NO}_x$. While not entirely clear why two of the airplanes reached isotopic equilibrium unlike all other combustion engines in this study, in general, the thermal NO_x tends to be depleted in ^{15}N abundance with the magnitude of depletion dependent on combustion engine design and temperature. Further identification of the importance of N equilibrium isotope effects in combustion sources will need to be addressed in future $\delta^{15}\text{N-NO}_x$ characterization studies.

3.3.2 Impact of catalytic reduction of NO_x on $\delta^{15}\text{N-NO}_x$

Our previous suggestion that catalytic reduction of NO_x enriches $^{15}\text{NO}_x$ abundance relative to the combustion produced NO_x is supported by the data in this study [100]. In our previous study, there were no measurements of $\delta^{15}\text{N-NO}_x$ produced by gasoline-powered vehicles not equipped with a three-way catalytic converter. In this study, we measured the $\delta^{15}\text{N-NO}_x$ emitted from two vehicles without three-way catalytic converters. The $\delta^{15}\text{N-NO}_x$ and NO_x concentration emitted by these two vehicles were compared to vehicles equipped with three-way catalytic converters (Fig. 3.2). Overall, the vehicles without catalytic converters emitted NO_x with negative $\delta^{15}\text{N-NO}_x$ values with low variation ($-13.6 \pm 1\%$ and $-9.5 \pm 1\%$) that did not correlate with the emitted NO_x concentrations ($R^2 = 0.01$). This is in contrast to gasoline-powered vehicles equipped with three-way catalytic converters that exhibited a strong correlation between NO_x concentrations and $\delta^{15}\text{N-NO}_x$ ($R^2 = 0.84$). This supports our previous hypothesis that catalytic reduction of NO_x increases $\delta^{15}\text{N-NO}_x$ values relative to the thermally produced NO_x during diffusion and absorption in the catalytic converter that favors $^{14}\text{NO}_x$ reduction over $^{15}\text{NO}_x$ [100].

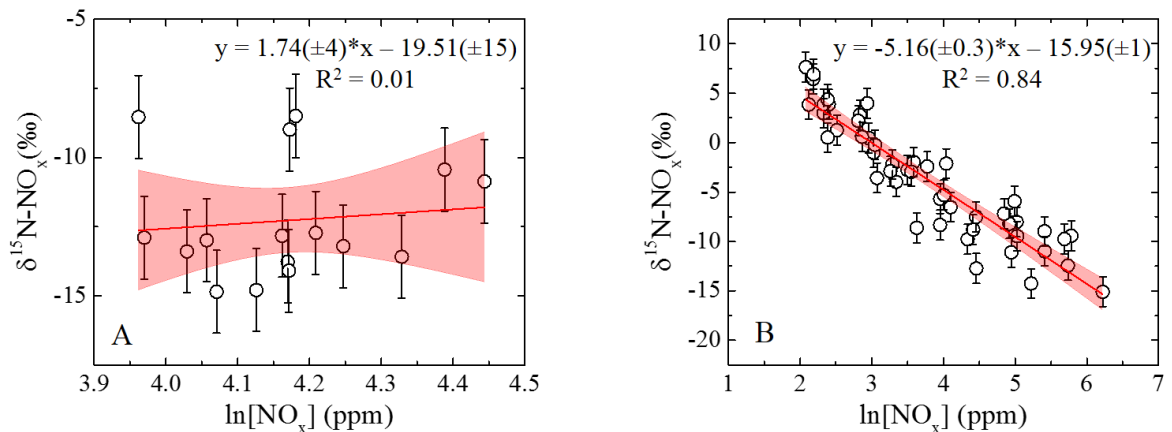


Fig. 3.2.: $\delta^{15}\text{N-NO}_x$ (‰) as a function of collected $\ln[\text{NO}_x]$ (ppm) for gasoline-powered vehicle without (A) and with (B) a 3-way catalytic converter. (B) adapted from ref [100]. Copyright American Chemical Society. Linear fit is indicated by the red line, and 95% confidence interval is shown in light red.

A similar trend of increasing $\delta^{15}\text{N-NO}_x$ with decreasing NO_x concentrations was observed for heavy-duty diesel-powered engines equipped with SCR technology. Both heavy-duty diesel and diesel-electric powered engines emitted $\delta^{15}\text{N-NO}_x$ that strongly correlated with the emitted NO_x concentrations ($R^2 = 0.74$; 3.2). Generally, under cold-engine conditions, the emitted NO_x concentrations were higher because of the inefficiency of SCRs at low temperatures [120, 121] and low $\delta^{15}\text{N-NO}_x$ values were reflecting the predominance of thermal NO_x (Fig. 3.3). As the converter warms up, the efficiency of the catalytic reduction of NO_x increases, NO_x emissions diminish [120, 121], and the catalytic reduction of NO_x enriches $^{15}\text{NO}_x$. In order to determine the $\delta^{15}\text{N}$ isotope enrichment factor associated with the catalytic reduction of NO_x by diesel-powered engines equipped with SCRs, the process was modeled as a Rayleigh distillation process (Eq. 3.2):

$$\delta^{15}\text{N}_{\text{Reduced}} = \delta^{15}\text{N}_{\text{Thermal}} + \epsilon_{\text{R/T}} \ln[f_{\text{NO}_x}] \quad (3.2)$$

where $\delta^{15}\text{N}_{\text{Reduced}}$ is the measured $\delta^{15}\text{N}$ - NO_x exiting the catalytic converter, $^{15}\text{N}_{\text{Thermal}}$ is the ^{15}N value of thermal NO_x exiting the combustion chamber, f_{NO_x} is the fraction of the thermal NO_x remaining after catalytic reduction, and $\epsilon_{\text{R/T}}$ (‰) is the enrichment factor associated with catalytic NO_x reduction (R) relative to the initial thermal NO_x (T). From Fig. 3.3, $\epsilon_{\text{R/T}}$ for the reduction of heavy-duty diesel-powered engines was calculated to be $-8.7(\pm 1)\%$, which is close to the $\epsilon_{\text{R/T}}$ previously calculated for light-duty diesel-powered engines of $-6.1(\pm 0.8)\%$ [100]. Both the heavy and light-duty diesel-powered engines were equipped with SCR technology. In this catalytic system, liquid urea is injected into the exhaust pipeline leading to its vaporization and subsequent decomposition to NH_3 . NH_3 is then absorbed on the surface of the catalytic converter and reacts with NO_x to form water and nitrogen [116,122]. Therefore, we hypothesize that the observed $\epsilon_{\text{R/T}}$ could be due to the following isotopic fractionation processes: (1) NO diffusion through N_2 to the catalyst surface, (2) kinetic isotope effect associated with NO binding onto the surface of the metal catalyst, and/or (3) kinetic isotope effect of NO dissociating on the metal catalyst. To this end, we have calculated the following ϵ for these processes: (1) -7.8% , (2) -16.3% , and (3) -17.9% . Based on these calculations, it appears that the observed fractionation is most likely due to rate limitation caused by NO diffusion through N_2 .

Recently, the impact of SCR in coal-fired power plants on $\delta^{15}\text{N}$ - NO_x has been studied [40], and also indicates that SCR technology increases $\delta^{15}\text{N}$ - NO_x values. In order to determine the $\epsilon_{\text{R/T}}$ associated with SCR technology in coal-fired power plants, we modeled the measured $\delta^{15}\text{N}$ - NO_x values for power-plant “D” [40] under conditions with SCR technology on and off also as a Raleigh distillation process (Eq. 3.2; Fig. 3.3). This gives an $\epsilon_{\text{R/T}}$ of $-9.2 \pm 0.6\%$, which is within one standard deviation of the calculated value for SCR in heavy-duty diesel vehicles. This result suggests that similar NO_x reduction technologies involving catalysts are fractionating NO_x because of a diffusion layer near the catalytic surface resulting in comparable enrichment factors. While the $\epsilon_{\text{R/T}}$ associated with SCR technology for both diesel-engines and coal-fired power plants seem to be similar, the absolute $\delta^{15}\text{N}$ - NO_x value associated

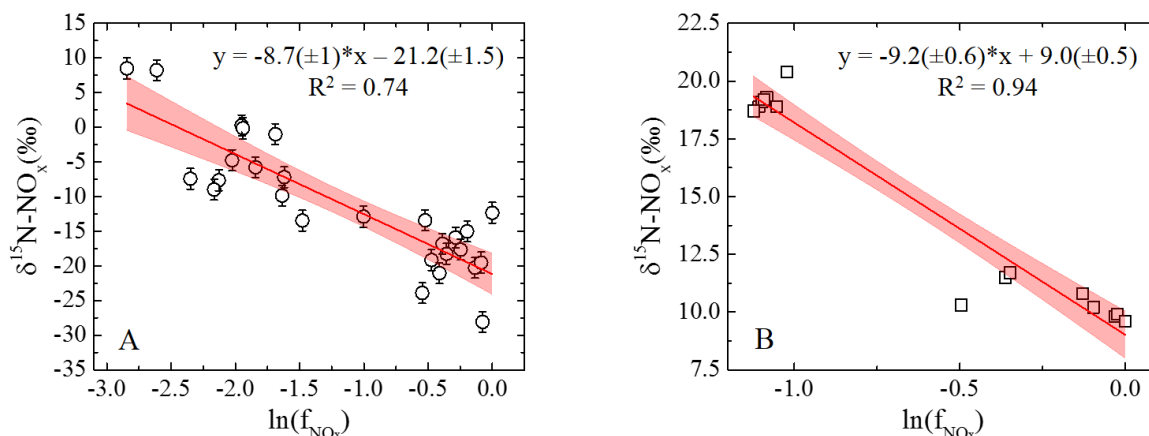


Fig. 3.3.: Impact of SCR technology on $\delta^{15}\text{N-NO}_x$ (‰) as a function of $\ln[f_{\text{NO}_x}]$ where f_{NO_x} is the fraction of NO_x normalized to the highest $[\text{NO}_x]$ emission for heavy-duty diesel-powered buses and trucks (A) and coal-fired power plants (B) adapted from [40]. Linear fit is indicated by the red line, and 95% confidence interval is shown in light red. Copyright American Chemical Society

with these two sources is quite different. In absence of SCR technology, our model indicates that diesel engines would emit $\delta^{15}\text{N-NO}_x$ of $-21.5 \pm 1.5\text{‰}$, while coal-fired power plants would emit $\delta^{15}\text{N-NO}_x$ of $9.0 \pm 0.5\text{‰}$ (Fig. 3.3). The difference in these values can be explained by the NO_x production mechanism. In diesel engines, NO_x is produced thermally, and as previously discussed, favors the formation of $^{14}\text{NO}_x$ compared to $^{15}\text{NO}_x$, resulting in negative $\delta^{15}\text{N-NO}_x$ values. However, coal-fired power plants combustion temperature (1550 to 1675 K) are too low for significant formation of thermally produced NO_x [123]. Instead, most of the NO_x is formed from the N derived from the coal as “fuel NO_x ” [124]. Coal has been measured to have a $\delta^{15}\text{N}$ value of 1 to 1.2‰ [35] and 2.0 to 2.2‰ [40]. Our modeled value for the coal-fired power plant emitted $\delta^{15}\text{N-NO}_x$ is significantly higher than the $\delta^{15}\text{N}$ of the coal. This likely occurs due to the influence of by post-combustion reactions involving the decomposition of NO that significantly lowers NO concentrations [35]. Based on the

kinetic isotope effect, NO decomposition will occur faster for ^{14}NO than for ^{15}NO , resulting in $\delta^{15}\text{N-NO}_x$ larger than the $\delta^{15}\text{N}$ of the coal.

Overall, the observed trend in the catalytic reduction of NO_x and $\delta^{15}\text{N-NO}_x$ is significant and suggests that regulated NO_x emissions (i.e. equipped catalytic NO_x reduction technology) from combustion sources has resulted in the gradual elevation of $\delta^{15}\text{N-NO}_x$ in the U.S. since the implementation of the Clean Air Acts [125]. This is suspected to occur since our data and previous studies [40, 100] indicate that the catalytic reduction of NO_x increases $\delta^{15}\text{N-NO}_x$ values relative to the produced NO_x from fossil-fuel combustion sources. The magnitude of this elevation will depend on both the catalytic reduction technologies NO_x fractionation signature and the efficiency of the NO_x reduction. Thermally produced NO_x without catalytic NO_x reduction technology will tend to have negative $\delta^{15}\text{N-NO}_x$ values with the magnitude depending on engine design and combustion temperature conditions. This may allow for the prediction of $\delta^{15}\text{N-NO}_x$ from other NO_x sources, assuming that the majority of the NO_x originates from the thermal production and that the combustion temperature is known. To this end, we estimate that marine vessels and locomotives (both sources yet to be characterized for $\delta^{15}\text{N-NO}_x$) that operate using diesel fuel will emit $\delta^{15}\text{N-NO}_x$ values close to -19‰ and those vessels equipped with SCR will emit $\delta^{15}\text{N-NO}_x$ values close to 0‰ .

3.3.3 Regional and Seasonal $\delta^{15}\text{N-NO}_x$ Variations

The $\delta^{15}\text{N-NO}_x$ inventory was used to predict the spatial and temporal variation of $\delta^{15}\text{N-NO}_x$ values across the contiguous U.S. The data obtained in this study, combined with other $\delta^{15}\text{N-NO}_x$ source characterization studies [31–33, 35–37, 39–43, 45, 100] accounts for roughly 80% of all emitted NO_x in the contiguous U.S. based on 2011 U.S. EPA NO_x emission inventory [113]. The fraction of NO_x (f_{source_i}) from each EPA source category was estimated at the county level using the 2011 EPA NO_x emission

inventory [113]. The $\delta^{15}\text{N-NO}_x$ mean value for each source ($\delta^{15}\text{N}_{\text{source}_i}$) and f_{source_i} was then used to solve the isotope mass balance equation for each county (Eq. 3.3).

$$(\delta^{15}\text{N} - \text{NO}_x)_{\text{total}} = \sum_i (f_{\text{source}_i}) \times (\delta^{15}\text{N} - \text{NO}_x(\text{source}_i)) \quad (3.3)$$

The total NO_x emission for each source by county from the 2011 U.S. EPA NO_x emission inventory was scaled for bi-monthly NO_x emissions. The annual county NO_x totals for soil [126], coal [127], and natural gas [127], were apportioned on a monthly basis according to seasonal usage and soil emission estimates. All other NO_x sources were assumed to emit at a constant rate throughout the year. Bi-monthly $\delta^{15}\text{N-NO}_x$ isoscapes for the contiguous U.S. were produced using ArcMap, and the inverse distance weighted (IDW) interpolation technique was applied between counties. The $\delta^{15}\text{N-NO}_x$ values used in the constructed isoscape (Fig. 3.4).

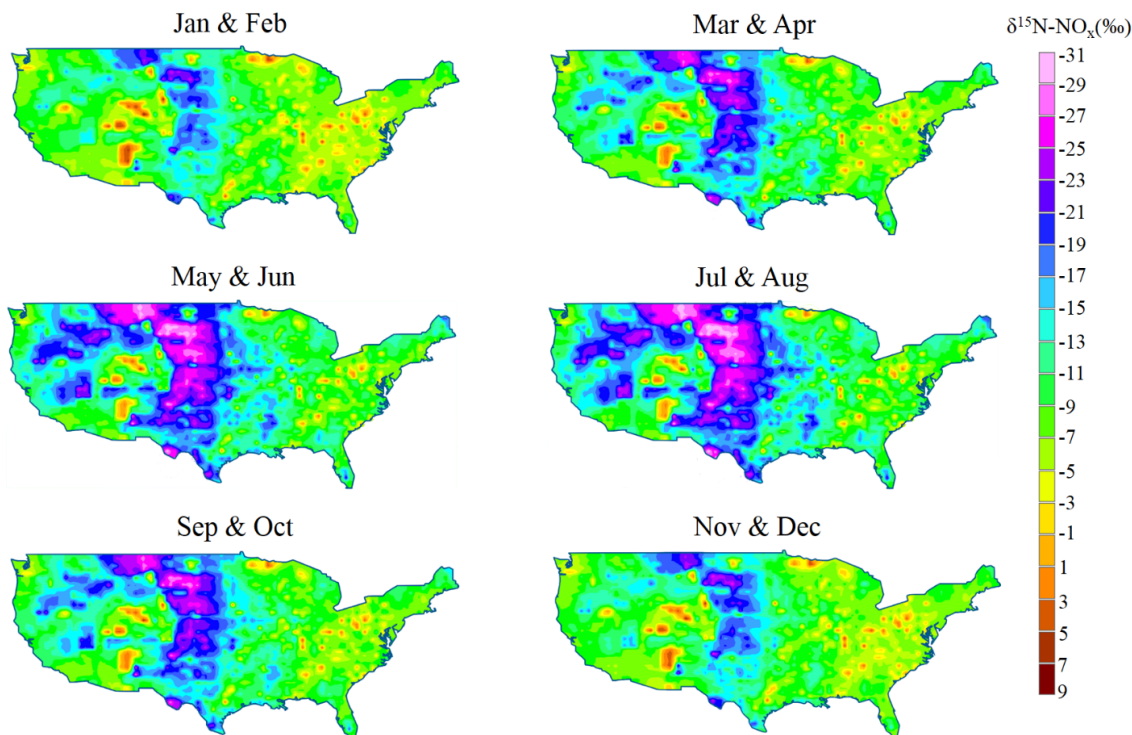


Fig. 3.4.: Bimonthly $\delta^{15}\text{N-NO}_x$ isoscape across the contiguous U.S. Copyright American Chemical Society

Fig. 3.4 stresses the regional dependency of $\delta^{15}\text{N-NO}_x$ based on the dominant NO_x emission source of the region. The high percentage of soil emissions over the Great Plains region and the low $\delta^{15}\text{N-NO}_x$ values of soil emissions resulted in this region typically having the lowest $\delta^{15}\text{N-NO}_x$ in the U.S. On the other hand, locations near coal-fired power plants have the highest $\delta^{15}\text{N-NO}_x$ as this source tends to have the highest $\delta^{15}\text{N-NO}_x$ [35,40]. Generally, the more polluted a region is, the higher the $\delta^{15}\text{N-NO}_x$ since the largest natural emissions (soil) has the lowest $\delta^{15}\text{N-NO}_x$ [39,41,42]. Additionally, Fig 3.4 shows the importance of seasons on the regional $\delta^{15}\text{N-NO}_x$ that are generally driven by soil emissions. During the summer, when soil emissions are largest [126], lower $\delta^{15}\text{N-NO}_x$ values are predicted relative to the other months. Conversely, during the winter, $\delta^{15}\text{N-NO}_x$ values are highest because soil emissions are lowest since denitrification is limited at cold temperatures [126]. Seasonal variations in $\delta^{15}\text{N-NO}_x$ are not predicted in regions in which the major NO_x source contributor remains relatively unchanged throughout the year, such as regions dominated by vehicle NO_x emissions and power plants.

The predicted $\delta^{15}\text{N-NO}_x$ values for the contiguous U.S. were compared to observed $\delta^{15}\text{N}$ values in NO_x and NO_3^- in precipitation. Studies of $\delta^{15}\text{N-NO}_x$ from ambient air in the U.S. report values ranging from -24.6 to 7.3‰ [37,45], which is an excellent agreement with our $\delta^{15}\text{N-NO}_x$ isoscape model that has values ranging from -31 to 9.7‰. Measurements the $\delta^{15}\text{N-NO}_3^-$ in wet and dry deposition, in the U.S., however, range from -9.5 to 14.1‰ [27,28,37], typically on the higher end of our predicted $\delta^{15}\text{N-NO}_x$ isoscape model. Though, it is important to point out that the availability of both $\delta^{15}\text{N-NO}_x$ and $\delta^{15}\text{N-NO}_3^-$ data is exceedingly limited and mainly exists for the northeastern region of the U.S. [27,28,37,45]. The discrepancy in the predicted $\delta^{15}\text{N-NO}_x$ and the measured $\delta^{15}\text{N-NO}_3^-$ in wet and/or dry deposition could be related to limited $\delta^{15}\text{N-NO}_3^-$ data or due to several other reasons. First, equilibrium isotope effects likely increase the $\delta^{15}\text{N}$ as NO_x is converted to NO_3^- prior to deposition [46,101]. The observed difference may then be associated with regional differences in NO_x oxidation pathways. Additionally, $\delta^{15}\text{N}$ may increase as NO is oxidized to NO_3^- due

to dry deposition of NO and NO₂ which kinetically would favor the loss of ¹⁴N. Alternatively, the discrepancy may be due to an incomplete assessment of δ¹⁵N values from all NO_x sources. We note that the data obtained from this study have limited sample size and may not accurately represent the δ¹⁵N-NO_x emitted from all types of gasoline, diesel, and natural gas fossil-fuel combustion sources. Similar types of studies in the future are necessary to reduce uncertainty in δ¹⁵N-NO_x values. While the exact causation of the alteration of δ¹⁵N is beyond the scope of this work, if δ¹⁵N-NO₃⁻ is linked to δ¹⁵N-NO_x, Fig.3.4 suggests that: (1) there are regional variations in δ¹⁵N-NO₃⁻ based on the region's dominant NO_x source, (2) δ¹⁵N-NO_x values may not be as high as previously thought [112], and positive values generally only exist in regions with a significant amount of coal-fired NO_x emissions, and (3) δ¹⁵N-NO₃⁻ should reflect seasonal changes in areas where seasons affect the relative importance of NO_x sources, however, meteorological conditions may transport NO_x and NO₃⁻, and this would alter measured δ¹⁵N-NO₃⁻ compared to a regions emitted δ¹⁵N-NO_x. Future studies should be directed towards further characterizing δ¹⁵N-NO_x sources that include industrial processes, marine vessels, oil, and biomass-burning fossil fuel combustion, which represent approximately 8.5%, 2.9%, 1.9%, 0.8% of all NO_x emission in the U.S. respectively [113] . Additionally, the impact of N fractionation processes due to chemical reactions and photolysis during the conversion of NO_x to NO₃⁻ needs to be better assessed and will be the subject for a future study.

3.4 Conclusion

Here we have measured δ¹⁵N-NO_x from several fossil-fuel combustion sources that includes: airplanes, gasoline-powered vehicles not equipped with a three-way catalytic converter, lawn equipment, utility vehicles, urban buses, semi-trucks, residential gas furnaces, and natural-gas-fired power plants. A relatively large range of δ¹⁵N-NO_x was found from -28.1 to 8.5‰ for individual exhaust/flue samples that generally tended to be negative due to the kinetic isotope effect associated with thermal NO_x

production. A negative correlation between NO_x concentrations and $\delta^{15}\text{N-NO}_x$ for fossil-fuel combustion sources equipped with selective catalytic reducers was observed, suggesting that the catalytic reduction of NO_x increases $\delta^{15}\text{N-NO}_x$ values relative to the NO_x produced through fossil-fuel combustion processes. Combining the $\delta^{15}\text{N-NO}_x$ measured in this study with previous published values, a $\delta^{15}\text{N-NO}_x$ regional and seasonal isoscape was constructed for the contiguous U.S., which demonstrates seasonal and regional importance of various NO_x sources. Our predicted $\delta^{15}\text{N-NO}_x$ model tends to predict negative values, which is in general agreement with prior $\delta^{15}\text{N-NO}_x$ studies. However, $\delta^{15}\text{N-NO}_3^-$ studies generally find positive values, indicating that isotope effects might play a major role on $\delta^{15}\text{N}$ as NO_x is oxidized into atmospheric nitrate. This will be the subject for future research.

4. THEORETICAL CALCULATION OF NITROGEN ISOTOPE EQUILIBRIUM EXCHANGE FRACTIONATION FACTORS FOR VARIOUS NO_Y MOLECULES

The following chapter is a reprint from a published article (Walters, W. W.; Michalski, G. Theoretical calculation of nitrogen equilibrium isotope exchange fractionation factors for various NO_y molecules. *Geochim. Cosmochim. Acta.* **2015**, *164*, 284-297).

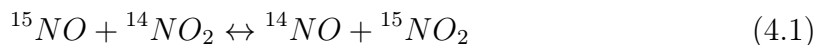
4.1 Introduction

The family of oxidized nitrogen molecules in the atmosphere, denoted as NO_y , which includes the sum of nitrogen oxides ($\text{NO}_x = \text{NO} + \text{NO}_2$) and its oxidation products ($\text{NO}_y = \text{NO}_x + \text{PAN}$ (peroxyacetyl nitrate = $\text{C}_2\text{H}_3\text{NO}_5$) + HNO_3 + NO_3 + HONO + N_2O_5 + particulate nitrates + etc) [3], are environmentally-relevant molecules that play a crucial role in many atmospheric processes [9]. In the troposphere, NO_x controls the concentrations of ozone (O_3) and the hydroxyl radical ($\bullet\text{OH}$), and is primarily oxidized to form nitrate aerosols ($\text{NO}_3^-_{(s)}$) and nitric acid (HNO_3) [2, 5, 64]. Subsequent wet and/or dry deposition of HNO_3 leads to numerous deleterious environmental impacts, including degradation of drinking water, soil acidification, eutrophication, and biodiversity changes in terrestrial ecosystems [4]. During the nighttime, the nitrate radical (NO_3) is a major atmospheric oxidant, influencing the lifetime of various other trace gases [128]. Reactions involving volatile organic compounds (VOCs) and NO_2 can lead to the formation of PAN, which can be transported over relatively large distances and introduce NO_x to pristine environments [129]. In the stratosphere, HNO_3 is the primary component of polar stratospheric clouds (PSCs) that form by the reactions of dinitrogen pentoxide (N_2O_5) and chlorine nitrate (ClONO_2) on the surface of stratospheric cloud particles in Polar

Regions [130]. PSCs provide a surface for heterogeneous chemical reactions to occur which leads to ozone destruction in the stratosphere.

In general, the precursor to the formation of NO_y is the emission of NO_x that is subsequently oxidized by various atmospheric oxidants such as O_3 , $\bullet\text{OH}$, NO_3^- , HO_2 , and the organoperoxy radicals (RO_2). Due to the important impacts NO_y molecules have on the environment, it is important to understand the sources of NO_x and the processes that transform it into NO_y . While significant efforts have been made to reduce the NO_x emission from stationary and mobile sources [11], there are still relatively large uncertainties in the total NO_x emission budget, both natural and anthropogenic, estimated between 30-50% [4]. In order to better estimate the relative importance of various NO_x sources to the overall NO_x emission budget, the analysis of the nitrogen (N) stable isotope ratio ($^{15}\text{N}/^{14}\text{N}$) of atmospherically derived HNO_3 and NO_3^- from wet and/or dry deposition has been suggested as a possible tool for partitioning NO_x sources [27], because various NO_x sources have relatively distinct $^{15}\text{N}/^{14}\text{N}$ ratios [33, 35–37, 39–41, 45, 65, 100]. Therefore, if the $^{15}\text{N}/^{14}\text{N}$ ratios of NO_x are preserved when oxidized to NO_3^- and HNO_3 , they can be used as a proxy for NO_x source partitioning. However, implementation of this method requires knowledge of how kinetic and equilibrium isotopic fractionations impacts $^{15}\text{N}/^{14}\text{N}$ ratios during the conversion of NO_x to NO_y [31, 46]. If these factors are considerable, then they may limit the utility of using $^{15}\text{N}/^{14}\text{N}$ ratios of NO_x for source partitioning. Yet, few fractionation factors for this conversion have been determined.

The transformation of NO_x to HNO_3 is a complicated process that involves several different reaction pathways (Fig 4.1) [131]. During this transformation, various NO_y molecules exist in equilibrium and are likely to undergo isotope exchange reactions involving the N isotopologues such as the exchange of NO and NO_2 (Eq. 4.1):



A field study has indicated that this equilibrium isotope exchange may have a strong influence on the observed $^{15}\text{N}/^{14}\text{N}$ ratios in atmospheric NO and NO_2 [46],

suggesting that isotope exchange equilibrium may play a significant role in influencing the $^{15}\text{N}/^{14}\text{N}$ ratios of various NO_y molecules. In order to fully understand studies of the N isotopic composition of atmospherically derived NO_y compounds [27,28,31,44,94,112], the effects of isotope exchange on $^{15}\text{N}/^{14}\text{N}$ ratios involving NO_y molecules needs to be addressed.

Previous studies have calculated equilibrium isotope exchange fractionation factors involving several NO_y molecules based on experimental measurements of harmonic frequencies [71,132] and on empirical force field methods [133]. However, equilibrium isotope exchange fractionation factors have not been determined for all atmospherically relevant NO_y molecules including but not limited to: NO_3 , N_2O_5 , halogen nitrates (XONO_2), and PAN due primarily to the absence of spectroscopic data for ^{15}N isotopologues of these NO_y molecules. Recently, computational quantum chemistry methods have been used to calculate equilibrium isotope exchange fractionation factors for H & O [134], Li [135], B [136], Cr [137], Fe [138], Cu [139], Mo [140], and S [141]. Here we use computational quantum chemistry methods to calculate equilibrium isotope exchange fractionation factors for the major NO_y molecules that are suspected to exist in equilibrium and compare them to experimental and prior theoretical determinations.

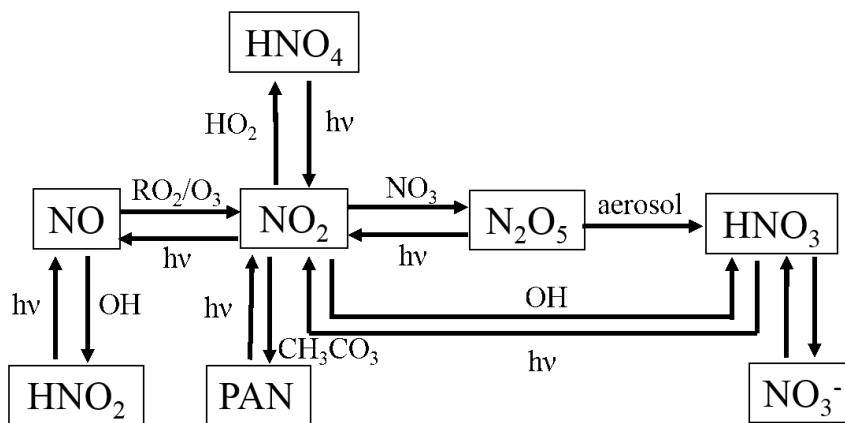


Fig. 4.1.: Various transformation pathways for NO_x to HNO_3 .

4.2 Methods and Theory

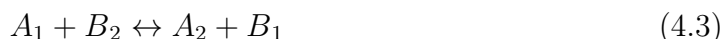
4.2.1 Calculation of Equilibrium Isotope Exchange Fractionation Factors

Early treatment of equilibrium isotope exchange factors were reported in 1947 by Urey in terms of isotopic partition function ratios, and by Bigeleisen and Mayer who introduced the isotopic reduced partition function ratio (RPFR) now in general use [111,142]. Assuming the Born-Oppenheimer and harmonic oscillator approximations, the RPFR (denoted as β is written as (Eq. 4.2):

$$\beta = \left(\frac{s_2}{s_1}\right)_f = \prod_i^N \frac{u_{2i}}{u_{1i}} \times \exp\left(\sum_i^N \frac{u_{1i} - u_{2i}}{2}\right) \times \prod_i^N \frac{1 - \exp(-u_{1i})}{1 - \exp(-u_{2i})} \quad (4.2)$$

$$= (CF)(ZPE)(EXC)$$

In Eq. 4.2, subscripts 1 and 2 refer to the light and heavy isotopologue respectively, $u_i = hc\nu_i/kT$, h is planck's constant, c is speed of light, ν_i is vibrational frequency, k is Boltzmann constant, T is temperature, N refers to the normal mode frequencies ($3N-6$ or $3N-5$ if linear), and s_1 and s_2 are symmetry numbers that do not lead to any isotope effect but must be considered from a statistical perspective. Eq. 4.2 points out that β can be considered the product of a classical factor (CF) that accounts for translational and rotational energy, the zero point energy contribution (ZPE), and an excitation factor (EXC). For an equilibrium isotope exchange reaction (Eq. 4.3):



where A and B are different chemical species, and subscripts 1 and 2 again refer to the light and heavy isotopologue respectively, the reduced equilibrium constant, written as $K_{A/B}$, and also defined as the equilibrium isotope fractionation factor ($\alpha_{A/B}$), can be obtained from the β of A and B (Eq. 4.4):

$$K_{A/B} = \alpha_{A/B} = \beta_A/\beta_B \quad (4.4)$$

By this notation, the equilibrium constant for $\text{NO}_2 \leftrightarrow \text{NO}$ isotope exchange between ^{14}N and ^{15}N isotopologue pairs (Eq. 4.1) is written as (Eq. 4.5):

$$K_{\text{NO}_2/\text{NO}} = {}^{15}\alpha_{\text{NO}_2/\text{NO}} = RPFRR = \frac{{}^{15}\beta_{\text{NO}_2}}{{}^{15}\beta_{\text{NO}}} \quad (4.5)$$

Neglecting the symmetry-number factor, since the purely classical symmetry numbers cannot lead to isotope fractionation [143], $\alpha_{\text{A/B}}$ only depends on the isotopic dependent vibrational frequencies. Therefore, if the N isotopologue vibrational frequencies are known for various NO_y molecules, theoretical equilibrium isotope exchanges involving NO_y molecules can be calculated in the rigid rotor and harmonic oscillator approximations. Theoretically, for proper use of the Bigeleisen-Mayer equation (Eq. 4.2) for β calculations, pure harmonic vibrational frequencies must be used to satisfy the approximations used within the Teller-Redlich product rule [144]. Isotopologue harmonic frequencies have been obtained from experimental spectroscopic data for many di- and some tri- atomic molecules, but few have been experimentally determined for larger molecules or radicals because of challenges in isotopologue synthesis. However, they can be calculated using computational quantum chemistry methods.

4.2.2 Computational Chemistry Methods

The optimized geometries (bond angles and bond lengths) and harmonic frequencies were calculated for the following nineteen NO_y molecules: NO , NO_2^- , NO_3 , NO_3^- , HNO_3 , PAN, N_2O_5 , ClONO_2 , nitrite anion (NO_2^-), nitrous acid (HONO), peroxyntitric acid (HNO_4), dinitrogen trioxide (N_2O_3) dinitrogen tetroxide (N_2O_4), nitrous oxide (N_2O), nitryl bromide (BrNO_2), nitryl chloride (ClNO_2), bromine nitrate (BrONO_2), nitrosyl chloride (NOCl), and nitrosyl bromide (NOBr) using computational quantum chemistry methods. The masses that correspond to the most abundant naturally occurring isotopes of elements (^1H , ^{12}C , ^{14}N , ^{16}O , ^{35}Cl , and ^{79}Br) and the mono-substitution of ^{15}N for ^{14}N were used in the harmonic frequency calculations. All calculations were performed with the Q-Chem 4.2 program suite [145] using both the

B3LYP [146,147] and EDF2 [148] hybrid density functional theory (DFT) methods, with the latter method specifically optimized for harmonic frequency calculations. DFT calculations are not strictly first-principle methods, but include some of the electron correlation accounting for the instantaneous interactions of pairs of electrons at a favorable computational cost [149]. For each method, the Dunning correlation-consistent polarized valence triple ζ (cc-pVTZ) basis set was used [150].

Computational methods for calculating harmonic frequencies are obtained from the force constant matrix (second derivative of the energy) evaluated at the equilibrium geometry [149], and are generally larger than the experimentally observed harmonic frequencies, due to incomplete incorporation of electron correlation and the use of finite basis sets [151]. To check the accuracy of our chosen levels of theory, harmonic frequencies were calculated for both B3LYP/cc-pVTZ and EDF2/cc-pVTZ and compared with experimental harmonic frequencies for a variety of di- and tri- atomic molecules that included: NO, NO₂, N₂, N₂O, carbon dioxide (CO₂), water (H₂O), carbonyl sulfide (OCS), sulfur dioxide (SO₂), disodium (Na₂), hydrogen cyanide (HCN), nitrogen monohydride (NH), dilithium (Li₂), hydroxyl radical (\bullet OH), carbon disulfide (CS₂), and hydrogen sulfide (H₂S) for a total of 37 vibrational modes covering a harmonic frequency range of 159.08 to 3938.74 cm⁻¹. A least squares linear regression fitting was applied to relate calculated harmonic frequencies to experimental values for each DFT method in order to assess their accuracy and to determine a scale factor which was subsequently used to scale all calculated vibrational frequencies to more closely match experimental values.

4.2.3 Determination of NO_y ¹⁵ β and $\alpha_{A/B}$ values

The scaled harmonic frequencies for both DFT methods were used to calculate ¹⁵ β values for each NO_y isotopologue. In the case of N₂O and N₂O₃, positionally dependent ¹⁵N substitution was taken into account in the calculations of ¹⁵ β . For all other NO_y molecules in which there are multiple N atoms, the N atoms were

ruled equivalent due to molecular symmetry. To the best of our knowledge, $^{15}\beta$ values have not previously been calculated for NO^3 , HNO_4 , N_2O_5 , PAN, ClONO_2 , and BrONO_2 . To assess the accuracy of our calculated $^{15}\beta$ values, they were compared to $^{15}\beta$ values calculated from experimental harmonic frequencies and/or calculated using empirical force field methods for NO [71, 133], NO_2 [71, 133], N_2O [152, 153], and HNO_3 [133]. Using our calculated $^{15}\beta$ values, $\alpha_{\text{A/B}}$ were calculated for the following gaseous exchange processes ($\text{A} \leftrightarrow \text{B}$): $\text{NOCl} \leftrightarrow \text{NO}$, $\text{HNO}_2 \leftrightarrow \text{NO}$, $\text{N}_2\text{O}_5 \leftrightarrow \text{NO}_2$, $\text{N}_2\text{O}_4 \leftrightarrow \text{NO}_2$, $\text{ClONO}_2 \leftrightarrow \text{NO}_2$, $\text{PAN} \leftrightarrow \text{NO}_2$, and $\text{HNO}_3 \leftrightarrow \text{NO}$ in the temperature range from 150 to 450 K. The thermodynamic energy that governs the equilibrium isotope exchange for a particular isotopologue arises due to small differences in the vibrational energies of isotopically substituted molecules (Urey, 1947). NO_y molecules that have been substituted with a heavier N isotope (^{15}N) will vibrate at lower frequencies than NO_y molecules containing the more common light N isotope (^{14}N). The relative lower vibrational frequency for ^{15}N containing molecules will reduce the vibrational zero-point energy (ZPE, $= \frac{1}{2}h\nu$ for harmonic oscillators) compared to ^{14}N containing molecules. The reduction of vibrational ZPE for a ^{15}N containing molecule will be greater for a particular N-bearing molecule that depends on the strength of bonds that N is involved in, and this will drive the direction of an N isotope equilibrium exchange. For example, in the N isotopologue equilibrium exchange between NO and NO_2 (Eq. 4.1), the vibrational ZPEs are 11.35, 11.15, 22.41, and 21.04 kJ/mol for ^{14}NO , ^{15}NO , $^{14}\text{NO}_2$, and $^{15}\text{NO}_2$ respectively (Begun and Fletcher, 1960). Because the difference in the vibrational ZPE is greater for NO_2 with the substitution of ^{15}N ($\Delta\text{ZPE} = 0.37$ kJ/mol) than it is for NO ($\Delta\text{ZPE} = 0.20$ kJ/mol), this will drive the equilibrium isotope exchange between NO and NO_2 (Eq. 4.1) to the right, because the total vibrational ZPE for the right-hand side is lower by approximately 0.16 kJ/mol than the vibrational ZPE on the left-hand side. Consequently, at equilibrium between NO and NO_2 , there will be a greater abundance of ^{14}NO and $^{15}\text{NO}_2$ than would be expected if N isotopes were randomly distributed. Several of our calculated $\alpha_{\text{A/B}}$ were compared to those calculated in previous studies using empirical force

field methods [133], experimental harmonic frequencies [71] and/or experimentally measured [154] [155] [156] [157] [158]. Here we consider a handful of NO_y exchange process, but many other $\alpha_{A/B}$ may be determined using our calculated $^{15}\beta$ values.

4.2.4 Solvent Effects

A solvent can have a major impact on equilibrium constants, reaction rates, and molecular properties [159, 160], and several NO_y compounds are important in gas-aqueous exchange chemistry. Computational quantum chemistry methods treat solvent effects by inclusion of a continuum solvent model, referred as Self-Consistent Reaction Field (SCRF) [149]. In these type of models, a potential energy term, V_{solv} , is added to the molecular electronic Hamiltonian, and the solvent is treated as a continuous dielectric surrounding a cavity that contains the solute molecule ignoring the detailed molecular structure of the solvent [161]. To obtain V_{solv} , charges are placed on various parts of the cavity surface and the effect of the electrostatic field on both the polarization of the dielectric continuum, and the electric moments of the molecule are calculated, with the charges themselves depending on the solute electrons and nuclei in a self-consistent manner. The key quantities that define this solvent continuum are the dielectric constant, ϵ [162], and cavity shape [161].

Various methods exist for the quantum mechanical calculation of solvent effects that depend on the model's description of the cavity [149]. In the widely used Polarizable Continuum Solvation Model (PCM), a sphere shaped cavity of radius 1.2 times the Van der Waal's radius around each atom of the molecule is used [161]. Charges are placed on the surface of the cavity resulting from intersecting spheres to simulate the external field of the solvent [161]. PCM improves upon early solvent models by providing a more realistic description of molecular shape and using the exact electron density of the solute to polarize the continuum. Various PCM models exist such as the conductor-like models known as COSMO [163], GCOSMO [164] or C-PCM [165, 166] as well as more sophisticated models such as the surface and simula-

tion of volume polarization for electrostatics known as the SS(V)PE approach [167] or equivalently known as the integral equation formalism (IEF-PCM) [168], which provides an exact treatment of the surface polarization. Previous studies have successfully applied PCM models to predict fractionation factors for boron [169], iron [138], and sulfur [141].

In this study we used the IEF-PCM to investigate the solvent effect on $^{15}\beta$ of eight soluble NO_y molecules that included: HNO_2 , HNO_3 , HNO_4 , N_2O_3 , N_2O_4 , N_2O_5 , NO_2^- , and NO_3^- . The IEF-PCM model was incorporated in the geometry optimization and harmonic frequency calculations of these molecules using both B3LYP/cc-pVTZ and EDF2/cc-pVTZ levels of theory, and $^{15}\beta$ values were calculated in the temperature range of 150 to 450 K. The key parameter that determines the solvent effect for the IEF-PCM is the dielectric constant, ϵ , and for our calculations was set to 78.39 which is the value for water at 298 K [170]. While ϵ of water might vary slightly over the temperature ranged considered in our $^{15}\beta$ calculations, previous studies have shown that this slight variation has minimal to no impact on the calculated β [141]. To assess the solvent effect, $\alpha_{\text{A/B}}$ between gaseous and aqueous phases was calculated for these eight NO_y molecules, and equilibrium N isotope exchange processes involving aqueous phase molecules were compared with experimentally determined values as well as those calculated from previous theoretical studies.

4.3 Results and Discussion

4.3.1 Experimental vs Calculated Harmonic Frequencies

Fig. 4.2 compares the calculated harmonic frequencies obtained from the B3LYP/cc-pVTZ and the EDF2/cc-pVTZ levels of theory with those experimentally determined for a variety of molecules [71, 153, 171]. The linear fittings of experimental vs. calculated harmonic frequencies (Fig. 4.2), have slopes of $0.995(\pm 0.003)$ and $0.990(\pm 0.003)$ and R^2 values of 0.9997 and 0.9996 for B3LYP/cc-pVTZ and EDF2/cc-pVTZ levels of theory, respectively. The slope for each respective level of theory was used to scale

all calculated harmonic frequencies with the aim of predicting more accurate values. In general, the scaled harmonic frequencies are in good agreement with observations; however, small differences between the scaled and the experimental harmonic frequencies still exist (Fig. 4.2). These discrepancies are caused by either the inadequacy of the level of theory used or by experimental error [144]. Measurement of a molecule's IR or Raman vibrational spectra can be difficult without using a condensed vapor or trapping the molecules in inert matrices, which may lead to interferences. These types of interferences do not apply to computational methods in which harmonic frequencies are calculated for a single molecule in vacuum. Only the most abundant isotopes for elements were used when calculating the harmonic frequency scale factors, but it is important to note that if the harmonic frequencies calculated for the most abundant isotopologue are accurate, then those for other isotopologues are guaranteed to be accurate as well, because any shift in frequencies due to mass occurs only from changes in the mass term in front of the potential matrix term [141]. Overall, we feel that the scaled harmonic frequencies are quite accurate and should allow for the determination of the harmonic frequencies for the various N isotopologue NO_y molecules of interest in this study.

4.3.2 Calculated NO_y harmonic frequencies

The scaled harmonic frequencies calculated using B3LYP/cc-pVTZ and EDF2/cc-pVTZ levels of theory for gaseous N isotopologue molecules are displayed in Fig. 4.3. In general, there is excellent agreement between the two DFT methods used to calculate harmonic frequencies; they are within 0.3 and 21.5 cm^{-1} for each vibrational mode (Fig. 4.3), indicating that both DFT methods calculated similar potential matrix terms. The only exception to this general agreement was for NO_3 in which the two DFT methods computed harmonic frequencies that differed by up to 136.6 cm^{-1} (Fig 4.3), signifying a disagreement in the calculated potential matrix terms. Previous computational quantum chemistry studies on NO_3 have indicated the difficulty in

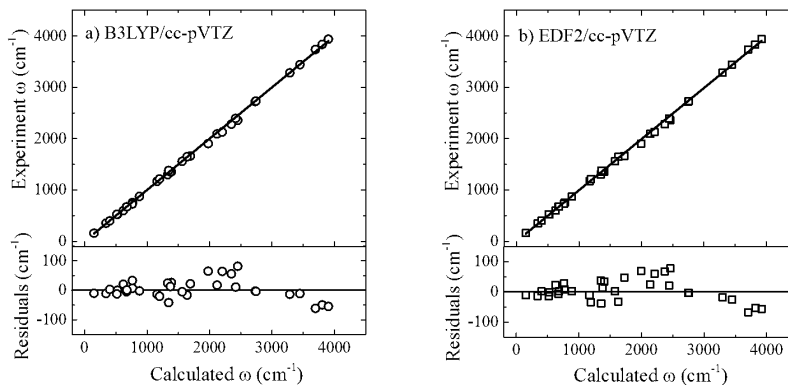


Fig. 4.2.: The least-squares fitting of experimental harmonic frequencies (ω) calculated harmonic frequencies and residuals for a) B3LYP/cc-pVTZ and b) EDF2/cc-pVTZ levels of theory. The circle points represent the frequencies calculated for NO_3 , and the square points represent all other frequencies calculated for every NO_y molecule included in this study.

calculating accurate geometries and therefore vibrational frequencies due to it being a polyatomic doublet radical [172,173]. Many methods including DFT, perform poorly in the case of polyatomic open-shell doublet radicals because of problems associated with the open-shell single reference wave function such as spin contamination [174, 175], symmetry breaking [176], near-singularities in the Hartree-Fock solution [177, 178], pseudo-Jahn-Teller effects [179], and the presence of multi-reference character. It has been suggested that the electron of motion-coupled cluster singlet and doublet (EOM-IP-CCSD) wave function method can more accurately predict the properties of doublet radical molecules due to its incorporation of a balanced description of the dynamic and non-dynamic correlation [180–183]. Therefore, we performed geometry and harmonic frequency calculations for NO_3 using the EOM-IP-CCSD method with the Dunning augmented correlation-consistent polarized valence double ζ (aug-cc-pVDZ) basis set (Dunning, 1989). These harmonic frequencies were used to calculate

the $^{15}\beta$ of NO_3 assuming no harmonic frequencies scale factor is needed for this highly electron- correlated and generally accurate method.

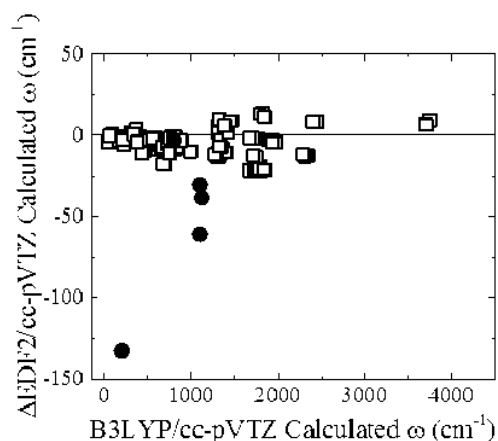


Fig. 4.3.: Comparison of calculated B3LYP/cc-pVTZ harmonic frequencies (ω) with the difference between B3LYP/cc-pVTZ and EDF2/cc-pVTZ calculated harmonic frequencies (ΔEDF2). The circle points represent the frequencies calculated for NO_3 , and the square points represent all other frequencies calculated for every NO_y molecule included in this study.

4.3.3 Calculated $^{15}\beta$

The $^{15}\beta$ of all gaseous NO_y compounds were calculated over the temperature range of 150 to 450 K for each computational method used in this study. Table 4.1 presents the average regression parameters calculated from B3LYP/cc-pVTZ and EDF2/cc-pVTZ for the temperature dependence of $^{15}\beta$ for the nineteen gaseous NO_y molecules in order of increasing magnitude for ^{15}N substitution at 150 K. In general, the magnitude of $^{15}\beta$ increases roughly with the number of atoms bonded to a particular N atom within a molecule. The smallest $^{15}\beta$ values are found for NO, NOBr, and NOCl since in the case of these molecules, N is only bonded to one other atom. The largest $^{15}\beta$ values are found in NO_3^- , HNO_3 , PAN, and HNO_4 , and in all of these molecules, N

Table 4.1: Calculated regression coefficients^a for $^{15}\beta$ for gaseous NO_y molecules as a function of temperature (150 to 450 K) sorted in order of increasing β magnitude at 298 K.

Molecule	A	B	C	D	$\beta(298 \text{ K})$
NO	5.528	-9.894	6.756	0.704	1.069
NOBr	5.682	-10.208	7.389	0.8	1.079
NOCl	5.617	-10.111	7.351	0.814	1.079
$\text{N}_2\text{O}_3^\alpha$	5.854	-11.061	8.878	0.613	1.086
$\text{N}_2\text{O}^\alpha$	6.217	-11.637	8.839	0.721	1.088
HNO_2	6.73	-13.02	10.419	0.433	1.091
NO_2^-	8.439	-16.065	12.271	0.195	1.095
NO_2	9.113	-16.976	12.909	0.56	1.112
NO_3^*	8.024	-15.955	13.722	0.077	1.107
$\text{N}_2\text{O}_3^\beta$	9.778	-18.339	15.139	0.574	1.133
N_2O^β	7.607	-14.414	12.74	1.295	1.142
BrNO_2	9.4	-17.882	15.318	0.631	1.138
ClNO_2	9.423	-18.092	15.621	0.567	1.139
N_2O_5	9.782	-18.547	15.637	0.687	1.141
N_2O_4	10.057	-18.952	16.049	0.699	1.145
ClONO_2	10.008	-19.194	16.626	0.606	1.148
BrONO_2	10.257	-19.629	16.988	0.618	1.151
HNO_4	10.452	-19.963	17.169	0.621	1.152
PAN	10.338	-19.584	16.998	0.667	1.153
HNO_3	11.169	-21.349	18.193	0.529	1.156
NO_3^-	12.533	-23.817	19.835	0.315	1.160

^a $1000(\beta - 1) = \frac{A}{T^4} \times 10^{10} + \frac{B}{T^3} \times 10^8 + \frac{C}{T^2} \times 10^6 + \frac{D}{T} \times 10^4$ (typical misfit of the regression is 0.1‰). $^\alpha$ signifies terminal substitution of ^{15}N . $^\beta$ signifies central substitution of ^{15}N . * EOM-IP-CCSD/aug-cc-pVTZ level of theory was used to calculate $^{15}\beta$ for NO_3

is bonded to three other atoms. The ordering of $^{15}\beta$ values for N containing molecules that have the same number of atoms bonded to N, depends on the bond strength and bond order between N and the atom or atoms to which it is bonded.

In Fig. 4.4, $^{15}\beta$ of NO, NO₂, N₂O^α, and HNO₃ are compared with those estimated by other empirical force field methods [133,152] and available experimental harmonic frequency data [71,153]. For N₂O the α signifies ¹⁵N substitution in the terminal N atom (¹⁵N-¹⁴N-O). Overall, our calculated $^{15}\beta$ values using computational quantum chemistry methods are in excellent agreement with $^{15}\beta$ values calculated using experimental harmonic frequencies, and harmonic frequencies calculated from molecular force fields and geometries. Therefore, we expect that our chosen levels of theory for the calculation of $^{15}\beta$ values are fairly accurate and will enable the calculation for various other NO_y molecules in which harmonic frequencies are challenging to measure experimentally.

4.3.4 Calculated $\alpha_{A/B}$

The calculated $\alpha_{A/B}$ regression coefficients as a function of temperature (Table 4.2) for the following exchange processes in the gas phase (A \leftrightarrow B): NOCl \leftrightarrow NO, HNO₂ \leftrightarrow NO, N₂O₅ \leftrightarrow NO₂, N₂O₄ \leftrightarrow NO₂, ClNO₂ \leftrightarrow NO₂, NO₂ \leftrightarrow NO, PAN \leftrightarrow NO₂, and HNO₃ \leftrightarrow NO in increasing order of magnitude over the temperature range of 150 to 450 K for the B3LYP and EDF2 methods. Since $^{15}\beta$ values for individual N-bearing molecules involved in the equilibrium isotope exchange process dictates the value of $\alpha_{A/B}$, the smallest values occur for equilibrium isotope exchange in which the number of atoms N is bonded to does not change. Thus, of the exchange processes assessed, NOCl \leftrightarrow NO had the lowest $\alpha_{A/B}$ value because in both cases, N is bonded to the same number of atoms in both molecules involved in the exchange (1 in NOCl \leftrightarrow NO). Conversely, the isotope exchange between HNO₃ \leftrightarrow NO had the highest $\alpha_{A/B}$ of those assessed, because the exchange involves N bonded to either one other atom (NO) or 3 other atoms (HNO₃). This general trend may allow for *a priori* way to predict the direction and magnitude of $\alpha_{A/B}$ based on molecular structure. This could be useful in predicting the direction of ¹⁵N enrichment in other equilibrium isotope exchange processes involving N, and could be useful in evaluating kinetic isotope effects (KIE)

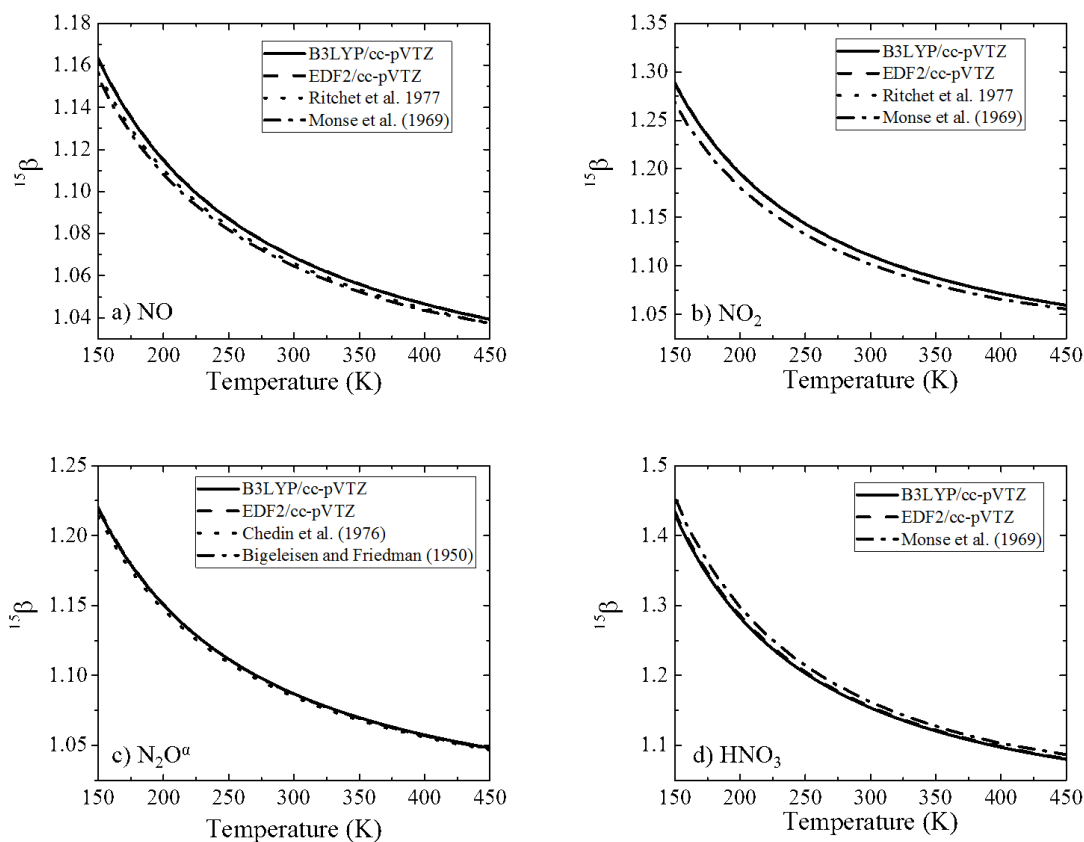


Fig. 4.4.: Comparison of calculated gaseous $^{15}\beta$ values using B3LYP/cc-pVTZ (solid line) and EDF2/cc-pVTZ (dash line) methods with those computed in a previous study (dash dot line) and/or those computed from experimental harmonic frequencies (dot line) for a) NO, b) NO₂, c) N₂O^α, and d) HNO₃.

involving N isotopologues assuming that the transition state and reactants exists in equilibrium (Van Hook, 2011). For example, a N-bearing molecule that reacts with another molecule causing the N atom to form an additional bond in the transition state would favor the formation of ^{15}N isotopologue in the transition state, which could lead to inverse kinetic isotope effects.

To assess the accuracy of our calculated values, $\alpha_{A/B}$ for $\text{NOCl}_{(l)} \leftrightarrow \text{NO}$, $\text{NO}_2 \leftrightarrow \text{NO}$, $\text{HNO}_{3(aq)} \leftrightarrow \text{NO}$, and $\text{N}_2\text{O}_{4(aq)} \leftrightarrow \text{NO}_2$ were compared with those estimated by other

Table 4.2: Calculated regression^a coefficients for $\alpha_{A/B}$ involving gaseous NO_y molecules as a function of temperature (150 to 450 K) sorted in increasing magnitude at 298 K.

alpha A-B	A	B	C	D	β (298 K)
$\alpha_{\text{NOCl} \leftrightarrow \text{NO}}$	0.12	-0.345	0.572	0.113	1.009
$\alpha_{\text{HNO}_2 \leftrightarrow \text{NO}}$	1.483	-3.721	3.687	-0.265	1.020
$\alpha_{\text{N}_2\text{O}_5 \leftrightarrow \text{NO}_2}$	1.004	-2.525	2.718	0.135	1.027
$\alpha_{\text{N}_2\text{O}_4(\text{aq}) \leftrightarrow \text{NO}_2}$	0.923	-2.426	2.772	0.063	1.025
$\alpha_{\text{N}_2\text{O}_4 \leftrightarrow \text{NO}_2}$	1.279	-3.003	3.11	0.15	1.030
$\alpha_{\text{ClONO}_2 \leftrightarrow \text{NO}_2}$	1.372	-3.509	3.748	0.054	1.032
$\alpha_{\text{PAN} \leftrightarrow \text{NO}_2}$	1.697	-4.031	4.065	0.142	1.037
$\alpha_{\text{NO}_2 \leftrightarrow \text{NO}}$	3.847	-7.68	6.003	-0.118	1.039
$\alpha_{\text{HNO}_3(\text{aq}) \leftrightarrow \text{NO}}$	6.099	-12.75	11.16	-0.179	1.079
$\alpha_{\text{HNO}_3 \leftrightarrow \text{NO}}$	6.166	-12.836	11.215	-0.133	1.081

^a $1000(\beta - 1) = \frac{A}{T^4} \times 10^{10} + \frac{B}{T^3} \times 10^8 + \frac{C}{T^2} \times 10^6 + \frac{D}{T} \times 10^4$ (typical misfit of the regression is 0.1‰).

theoretical studies [132, 133], measured values [154–156, 158, 184, 185], and/or available experimental harmonic frequency data [71] (Fig. 4.5). Due to the difficulty in measuring the $\alpha_{A/B}$ for exchange reactions involving NO_y molecules, few measurements have been made, and the majority of those that have been involve a molecule in a condensed phase (aqueous or liquid phase). Here, we neglect the condensed phase or solvent effect for a couple of reasons (1) to compare our computational determined values with those in previous theoretical studies that have also neglected solvent effects (2) to evaluate the inclusion of solvent effects on $^{15}\beta$ and on $\alpha_{A/B}$. Both DFT methods resulted in extremely similar $\alpha_{A/B}$ values for all exchanges considered (Fig. 4.5). In general, the DFT calculated $\alpha_{A/B}$ values were in good agreement with experimental measurements (Fig. 4.5) and better estimated the $\alpha_{A/B}$ values than previous theoretical studies [133]. A detailed discussion of the various exchange processes used to compare our calculated $\alpha_{A/B}$ with those previously calculated is presented below.

$\alpha_{\text{NOCl}_{(l)} \leftrightarrow \text{NO}}$: The N isotope exchange reaction between $\text{NOCl}_{(l)} \leftrightarrow \text{NO}$ has been previously measured to have an $\alpha_{\text{NOCl}_{(l)} \leftrightarrow \text{NO}}$ value of 1.013 ± 0.003 at 223 K [156]. This value is an excellent agreement with the $\alpha_{\text{NOCl}_{(l)} \leftrightarrow \text{NO}}$ calculated from the DFT methods which had an average value of 1.014 at 223 K (Fig. 4.5) even with the neglect of the condensed phase, suggesting that the condensed phase has little influence on $^{15}\beta$ for NOCl. Our calculated $\alpha_{\text{NOCl}_{(l)} \leftrightarrow \text{NO}}$ seems to significantly improve upon previous theoretical studies of this exchange reaction that calculated a value of 1.024 [133].

$\alpha_{\text{NO}_2 \leftrightarrow \text{NO}}$: There has been some uncertainty in the measurement of the $\alpha_{\text{NO}_2 \leftrightarrow \text{NO}}$ for the N isotope exchange between $\text{NO}_2 \leftrightarrow \text{NO}$, one of the few N isotope exchanges that has been measured in which both molecules are in the gas phase. The earliest study of this isotope equilibrium exchange measured an $\alpha_{\text{NO}_2 \leftrightarrow \text{NO}}$ of 1.040 at 298 K [154]. This value agrees well with the $\alpha_{\text{NO}_2 \leftrightarrow \text{NO}}$ calculated using DFT methods that had an average value of 1.0395 at 298K, which is also near the $\alpha_{\text{NO}_2 \leftrightarrow \text{NO}}$ calculated using experimental harmonic frequencies for the ^{14}N and ^{15}N isotopologues of NO and NO_2 of 1.0415 [71], and a previous study that corrected for accurate ZPEs and calculated 1.040 [132] (Fig. 4.5). However, a subsequent study found this exchange

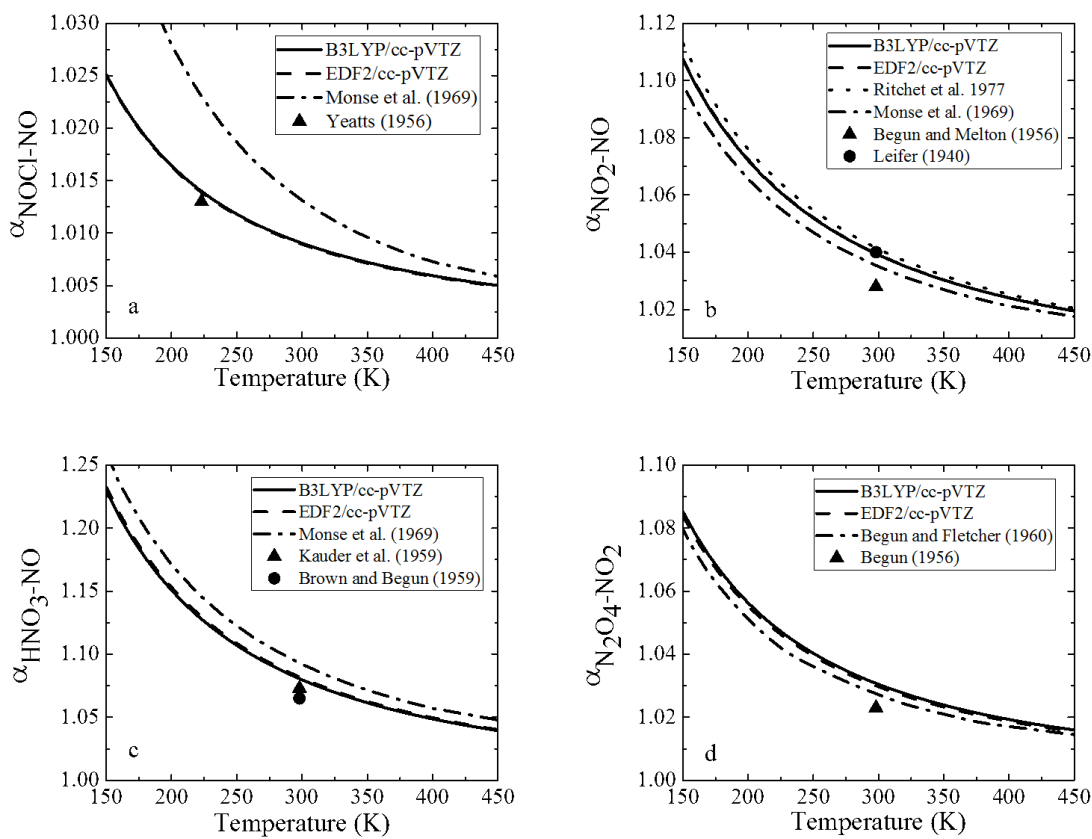


Fig. 4.5.: Comparison of calculated equilibrium isotope fractionation factors using B3LYP/cc-pVTZ (solid line) and EDF2/cc-pVTZ (dash line) methods with neglect of solvent effects with those computed from experimental harmonic frequencies (dot line), those computed in previous studies (dash dot line) and/or those experimental measured (single points) for a) $\alpha_{\text{NOCl}\leftrightarrow\text{NO}}$, b) $\alpha_{\text{NO}_2\leftrightarrow\text{NO}}$, c) $\alpha_{\text{HNO}_3\leftrightarrow\text{NO}}$, and d) $\alpha_{\text{N}_2\text{O}_4\leftrightarrow\text{NO}_2}$

to have a $\alpha_{\text{NO}_2\leftrightarrow\text{NO}}$ value of 1.028 ± 0.002 at 298 K [155]. A previous theoretical study based on empirical force field calculations estimated an $\alpha_{\text{NO}_2\leftrightarrow\text{NO}}$ value of 1.0353 [133], somewhere in between the two experimental measurements. Experimental measurements of the N isotope exchange between $\text{NO}_2\leftrightarrow\text{NO}$ are difficult due to a number of reasons. First, the pressure of NO and NO_2 must remain low (less than

0.5 Torr) to prevent the formation of N_2O_3 and N_2O_4 [186], which would complicate the $\text{NO}_2 \leftrightarrow \text{NO}$ exchange measurement. Additionally, previous studies have measured and NO_2^+ ions that originate from NO_2 . Due to the small number of measurements and disagreement in these values, it is difficult to justifiably determine the accuracy of our calculated $\alpha_{\text{NO}_2 \leftrightarrow \text{NO}}$ value; however, our value does agree quite well with the value determined from the experimental harmonic frequencies, which is the best that we could hope for considering that the accuracy of our calculated $\alpha_{\text{NO}_2 \leftrightarrow \text{NO}}$ is based essentially on calculating accurate harmonic frequencies. The determination of $\alpha_{\text{A/B}}$ for this exchange reaction at various temperatures that circumvents the problems associated with previous experiments will be the subject for a future study.

$\alpha_{\text{HNO}_3(\text{aq}) \leftrightarrow \text{NO}}$: The N isotope exchange between $\text{HNO}_3(\text{aq}) \leftrightarrow \text{NO}$ has been experimentally measured to have an $\alpha_{\text{HNO}_3(\text{aq}) \leftrightarrow \text{NO}}$ of 1.073 ± 0.006 [158] and 1.065 ± 0.001 [185] at 298 K. The DFT methods calculated an average $\alpha_{\text{HNO}_3(\text{aq}) \leftrightarrow \text{NO}}$ of 1.081 (Fig. 4.5). While our calculated $\alpha_{\text{HNO}_3(\text{aq}) \leftrightarrow \text{NO}}$ slightly overestimates the experimental value, it is closer than the previously calculated $\alpha_{\text{HNO}_3(\text{aq}) \leftrightarrow \text{NO}}$ value of 1.093 based on empirical force field methods [133]. It is important to point out that the $\text{HNO}_3(\text{aq}) \leftrightarrow \text{NO}$ exchange occurs with HNO_3 in the aqueous phase, and this could be the reason for the DFT methods overestimation of $\alpha_{\text{HNO}_3(\text{aq}) \leftrightarrow \text{NO}}$, which assumes both HNO_3 and NO are in the gaseous phase.

$\alpha_{\text{N}_2\text{O}_4(\text{aq}) \leftrightarrow \text{NO}_2}$: The N isotope exchange reaction between $\text{N}_2\text{O}_4(\text{aq}) \leftrightarrow \text{NO}_2$ has been experimentally measured to have an $\alpha_{\text{N}_2\text{O}_4(\text{aq}) \leftrightarrow \text{NO}_2}$ of 1.023 at 298 K [184]. This value is slightly lower than the average value calculated using DFT methods of 1.030. At 298 K, Begun and Fletcher (1960) calculated $\alpha_{\text{N}_2\text{O}_4 \leftrightarrow \text{NO}_2}$ to be 1.027 which is closer to the experimental value than the DFT methods (Fig. 4.5). However, ref [132] calculated $^{15}\beta$ for N_2O_4 using observed fundamental vibrational frequencies, which theoretically should not be used in the Bigeleisen-Mayer equation in the rigid rotor and harmonic oscillator approximations [144]. Additionally, the calculation of $^{15}\beta$ values from observed frequencies suffers the disadvantage that spectroscopic vibrational frequencies for isotopologues are not always that accurate, and the Teller-Redlich

product rule is not necessarily obeyed so that the important interplay of various factors such as mass-moment-of-inertia factor and excitation factor that contribute to $^{15}\beta$ does not necessarily occur to sufficient accuracy [187]. Therefore, ref [132] more accurate calculated $\alpha_{\text{N}_2\text{O}_4 \leftrightarrow \text{NO}_2}$ maybe fortuitous. Similarly to the $\text{HNO}_3(\text{aq}) \leftrightarrow \text{NO}$ exchange, the experimental measurement of $\text{N}_2\text{O}_4(\text{aq}) \leftrightarrow \text{NO}_2$ occurred with N_2O_4 in the aqueous phase, and our calculated $^{15}\beta$ N_2O_4 used in our $\alpha_{\text{N}_2\text{O}_4 \leftrightarrow \text{NO}_2}$ calculation was for N_2O_4 in the gas phase. The difference in the phase of N_2O_4 might be the reason for our calculated $\alpha_{\text{A/B}}$ discrepancy with the experimentally measured value.

Overall, we believe that our calculated $^{15}\beta$ values for gaseous NO_y molecules are fairly accurate in the rigid rotor and harmonic oscillator approximations and will allow for the determination of $\alpha_{\text{A/B}}$ for various isotope exchanges involving these gaseous molecules. These $\alpha_{\text{A/B}}$ values maybe useful to understand the trends observed in the N stable isotope ratio of NO_y species in the atmosphere.

4.3.5 Calculated solvent effects

Table 4.3 presents the regression parameters for the temperature dependence of $^{15}\beta$ for HNO_4 , N_2O_3 , N_2O_4 , N_2O_5 , NO_2^- , and NO_3^- in order of increasing magnitude for ^{15}N substitution. Like the gaseous NO_y molecules, $^{15}\beta$ values increase in magnitude with increasing number of atom attachment to the N atom. To assess the significance of solvent effects on $^{15}\beta$ values, Fig. 4.5 shows the calculated enrichment factors ($1000(\alpha_{\text{aq-gas}} - 1)$) between five gaseous NO_y molecules and their aqueous counterparts (i.e., the IEF-PCM modeled species, $\epsilon = 78.39$) as a function of temperature. Overall, both B3LYP/cc-pVTZ and EDF2/cc-pVTZ calculated similar enrichment factors that were slightly negative between the aqueous and gaseous phase for these molecules that asymptotically increase as temperature increases but with varying magnitude for different NO_y molecules. This indicates that the $^{15}\beta$ values for the gaseous phase is higher than for the aqueous phase, signifying that the ^{15}N isotope preferentially form in the gaseous phase. This occurs because the aqueous phase lowers the ZPEs

Table 4.3: Calculated regression coefficients^a for $^{15}\beta$ for aqueous NO_y molecules as a function of temperature (150 to 450 K) in order of increasing magnitude at 298 K.

	A	B	C	D	β (298K)
$\text{N}_2\text{O}_3^\alpha$	5.843	-11.006	8.805	0.636	1.086
HNO_2	6.69	-13.006	10.45	0.374	1.090
NO_2^-	8.208	-15.695	12.044	0.17	1.092
$\text{N}_2\text{O}_3^\beta$	9.612	-18.082	14.867	0.486	1.128
N_2O_5	9.42	-17.896	15.013	0.643	1.135
N_2O_4	9.7	-18.406	15.652	0.617	1.140
HNO_4	10.103	-19.42	16.768	0.544	1.147
HNO_3	11.011	-21.156	18.043	0.439	1.152
NO_3^-	12.007	-23.009	19.278	0.243	1.154

^a $1000(\beta - 1) = \frac{A}{T^4} \times 10^{10} + \frac{B}{T^3} \times 10^8 + \frac{C}{T^2} \times 10^6 + \frac{D}{T} \times 10^4$ (typical misfit of the regression is 0.1‰).

between the ^{14}N and ^{15}N isotopologues compared to the gaseous phase (Table 4.4) due to the stabilization resulting from dispersion interactions between water and the NO_y molecule. Subsequently, the $^{15}\beta$ value for the aqueous phase is lower than for the gaseous phase. The magnitude in the fractionation between the aqueous and gaseous phase in general depends on the ZPE difference between the ^{14}N and ^{15}N isotopologues of the aqueous and gaseous phase; the greater the ZPE is lowered in the aqueous phase, the larger the fractionation between the aqueous and gas phase (Table 4.4).

From the aqueous phase calculated $^{15}\beta$ for HNO_3 and N_2O_4 , the N equilibrium isotope exchange between $\text{HNO}_{3(\text{aq})} \leftrightarrow \text{NO}$ and $\text{N}_2\text{O}_{4(\text{aq})} \leftrightarrow \text{NO}_2$ were reevaluated and compared with previous theoretical studies as well as experimental measurements (Fig. 4.7). A detailed assessment of the inclusion of the solvent effect on equilibrium isotope exchange processes are discussed below.

$\alpha_{\text{HNO}_{3(\text{aq})} \leftrightarrow \text{NO}}$: As previously mentioned, the N isotope exchange between $\text{HNO}_{3(\text{aq})} \leftrightarrow \text{NO}$ has been experimentally measured to have an $\alpha_{\text{HNO}_{3(\text{aq})} \leftrightarrow \text{NO}}$ of 1.073 ± 0.006 [158] and

Table 4.4: Comparison of the zero-point energy (ZPE, $= \frac{1}{2}\Sigma h\nu$ for harmonic oscillators) difference in the ^{14}N and ^{15}N isotopologues for several NO_y molecules in the gaseous and the aqueous phase, and the enrichment factor ($1000(\alpha_{\text{aq-gas}} - 1)$) between the gaseous and aqueous phases at 270 K.

Molecule	$\Delta^{\text{a}}\text{ZPE Gas}$	$\Delta^{\text{a}}\text{ZPE Aqueous}$	$\Delta\text{ZPE Aqueous-Gas}$	$1000(\alpha_{\text{aq-gas}} - 1)$ at 270K
HNO_2	324.9	322.8	-2.1	-1.6
NO_2^-	329.9	327.5	-2.4	-2.3
N_2O_3	401.7	395.1	-6.6	-2.6
HNO_3	546.0	537.2	-8.8	-4
HNO_4	536.9	524.9	-12.0	-5.3
N_2O_4	516.9	504.0	-12.8	-5.4
NO_3^-	556.9	543.0	-13.9	-6.1
N_2O_5	532.1	513.1	-19.0	-6.5

^a Δ is the average difference between the ZPE in the harmonic oscillator approximation for the ^{14}N and ^{15}N isotopologues.

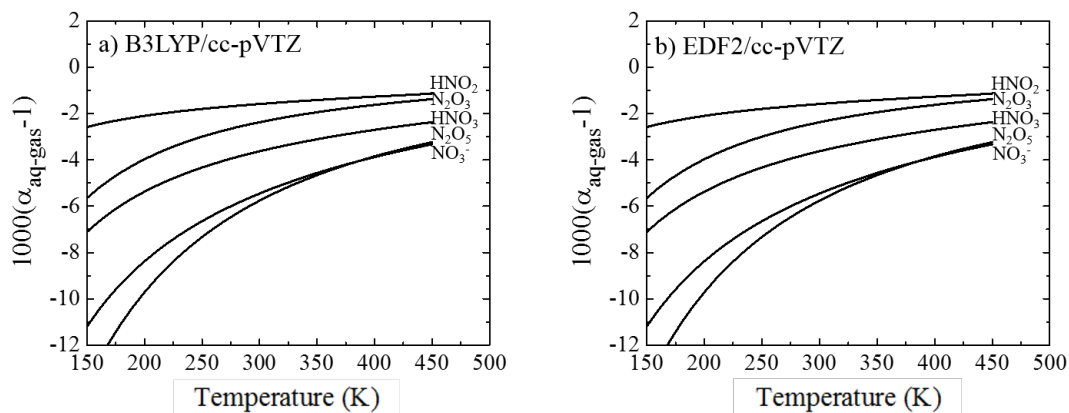


Fig. 4.6.: Enrichment factor ($1000(\alpha_{\text{aq-gas}} - 1)$) between aqueous and gaseous phase for various NO_y molecules (HNO_2 , N_2O_3 , HNO_3 , N_2O_5 , NO_3^-). Aqueous phase molecules were calculated using the IEP-PCM model with a dielectric (ϵ) constant of 78.39.

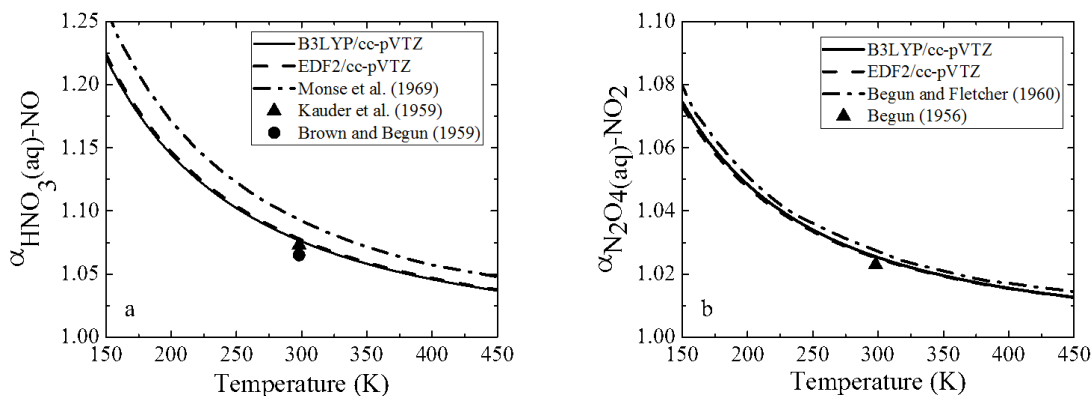


Fig. 4.7.: Comparison of calculated equilibrium isotope fractionation factors using B3LYP/cc-pVTZ (solid line) and EDF2/cc-pVTZ (dash line) methods with inclusion of solvent effects using the IEF-PCM model with those computed in previous studies (dash dot line) and/or those experimental measured (individual points) for a) $\alpha_{\text{HNO}_3 \leftrightarrow \text{NO}}$ and b) $\alpha_{\text{N}_2\text{O}_4 \leftrightarrow \text{NO}_2}$.

1.065 ± 0.001 [185] at 298 K. Inclusion of the solvent effect on $^{15}\beta$ for HNO_3 , the DFT methods calculated $\alpha_{\text{HNO}_3(\text{aq}) \leftrightarrow \text{NO}}$ to be 1.076 (Fig. 4.7), which is closer to the experimentally measured values than the DFT value calculated with neglect of the solvent effect of 1.081 ± 0.001 (Fig. 4.7). Our calculated $\alpha_{\text{HNO}_3(\text{aq}) \leftrightarrow \text{NO}}$ value is a significant improvement from previous theoretical studies that have calculated a value of 1.093 [133].

$\alpha_{\text{N}_2\text{O}_4(\text{aq}) \leftrightarrow \text{NO}_2}$: Inclusion of the solvent effect on the $^{15}\beta$ value of N_2O_4 , the DFT methods calculated $\alpha_{\text{N}_2\text{O}_4(\text{aq}) \leftrightarrow \text{NO}_2}$ to be 1.025 (Fig. 4.7). This value is in better agreement with the experimentally determined value of 1.023 [155] than either the DFT calculated value with neglect of the solvent effect of 1.034 ± 0.0005 or the value calculated using observed fundamental vibrational frequencies of 1.027 [132].

Overall, the solvent effect while not very strong, are still significant for calculating accurate fractionation factors. Inclusion of the solvent effect for the molecules analyzed in this study lowered $\alpha_{\text{A/B}}$ and resulted in values closer in agreement with experimentally determined values. Even with accounting for solvent effects, calculated $\alpha_{\text{A/B}}$ in the rigid rotor and harmonic oscillator approximations tend to be slightly overestimated compare to the experimentally measured value, and this is likely due to the neglect of anharmonicity in this approximation. Inclusion of anharmonic corrections will in general lower $\alpha_{\text{A/B}}$ values, which would help match calculated values with those determined experimentally; however, corrections for anharmonicity are computationally expensive, and even with the neglect of anharmonicity, our calculated $\alpha_{\text{A/B}}$ values are within or nearly within the experimental error for these measurements and are a significant improvement from previous theoretical $\alpha_{\text{A/B}}$ studies involving NO_y molecules.

4.4 Conclusion

Harmonic frequencies have been calculated for various NO_y molecules that are relevant to NO_x tropospheric and stratospheric chemistry using B3LYP/cc-pVTZ and

EDF2/cc-pVTZ levels of theory. Our calculated harmonic frequencies were in excellent agreement with those determined experimentally. Using our calculated harmonic frequencies, $^{15}\beta$ were calculated for mono-substitution of the ^{15}N isotope using the Bigeleisen-Mayer equation in the rigid rotor and harmonic oscillator approximations. Our $^{15}\beta$ values agreed well with those calculated using experimentally determined harmonic frequencies and with those calculated using empirical force field methods. In general, the magnitude of $^{15}\beta$ value increases with the number of atoms bound to the N atom in a particular molecule, allowing for *a priori* way to arrange $^{15}\beta$ values for NO_y molecules. Equilibrium isotope exchange fractionation factors ($\alpha_{\text{A/B}}$) were evaluated for various exchange processes involving NO_y molecules. Our calculated $\alpha_{\text{A/B}}$ values were generally in closer agreement with the experimentally measured $\alpha_{\text{A/B}}$ than previous theoretical assessments of $\alpha_{\text{A/B}}$ involving N isotope exchange. Since most of the $\alpha_{\text{A/B}}$ values involving N isotope exchange involved a species in the aqueous phase, the solvent effect on $^{15}\beta$ and $\alpha_{\text{A/B}}$ were assessed. Inclusion of the solvent effect improved the accuracy of our calculated $\alpha_{\text{A/B}}$ values so that they were just outside of or within the experimental variability reported for various N isotope exchange processes. Slight overestimations even after corrections for the solvent effect might be the result of neglect of anharmonicity which are believed to lower $\alpha_{\text{A/B}}$ values. In general, we believe our calculated $^{15}\beta$ and $\alpha_{\text{A/B}}$ values are accurate in the rigid rotor and harmonic oscillator approximations and will allow for the estimation of the isotope fractionation involved with NO_y molecules.

These $\alpha_{\text{A/B}}$ values predict trends that may be observed in the N stable isotope ratio of NO_y species in the atmosphere. Assuming that NO_y species exists in equilibrium, this would suggest (1) since the ^{15}N isotope prefers to enrich in the more oxidized form of NO_y , the transformation of NO_x to atmospheric nitrates (HNO_3 , $\text{NO}_3^-_{(\text{aq})}$, $\text{NO}_3^-_{(\text{g})}$) would increase the $^{15}\text{N}/^{14}\text{N}$ ratios from the initial $^{15}\text{N}/^{14}\text{N}$ ratio of the NO_x source, (2) the long range transport of NO_x via PAN would have higher $^{15}\text{N}/^{14}\text{N}$ ratios than the NO_x source, (3) based on $^{15}\beta$ values, atmospheric nitrates would have $^{15}\text{N}/^{14}\text{N}$ ratios in order of increasing magnitude of $\text{NO}_3^-_{(\text{aq})}$, HNO_3 , $\text{NO}_3^-_{(\text{s})}$. Simultaneous

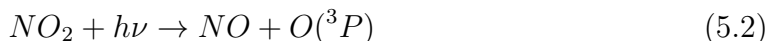
measurements of the $^{15}\text{N}/^{14}\text{N}$ ratios of different NO_y molecules is needed to determine the importance of various equilibrium isotope exchanges on $^{15}\text{N}/^{14}\text{N}$ ratios, and this will be the subject for future research.

5. NITROGEN ISOTOPE EXCHANGE BETWEEN NO AND NO₂ AND ITS IMPLICATIONS FOR δ¹⁵N VARIATIONS IN TROPOSPHERIC NO_x AND ATMOSPHERIC NITRATE

The following chapter is a reprint from a published article (Walters, W. W.; Simonini, D. S.; Michalski, G. Nitrogen isotope exchange between NO and NO₂ and its implications for δ¹⁵N variations in tropospheric NO_x and atmospheric nitrate. *Geophys. Res. Lett.* **2016**, *43*(1), 440-448).

5.1 Introduction

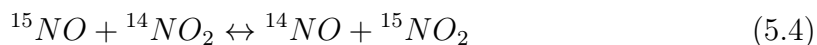
Nitrogen oxides [NO_x = nitric oxide (NO) + nitrogen dioxide (NO₂)] are important trace gases that influence the concentrations of the major tropospheric oxidants including ozone (O₃) and hydroxyl radical (•OH) that drive tropospheric chemistry [1–3,6]. During the daytime, NO and NO₂ exist in a photochemical steady state in which NO is oxidized by O₃ forming NO₂, which then may photolyze back to NO leading to the production of O₃ [6]. This cycling of NO and NO₂ is known as the Leighton Cycle and is described by the following reaction sequence [6]:



The cycling between NO and NO₂ is relatively rapid with photochemical equilibrium being achieved within a few minutes [46, 131]. Thus, during the daytime, the Leighton cycle controls the relative concentrations of NO and NO₂ depending on O₃ concentrations and NO₂ photolysis rate.

The nitrogen (N) isotope exchange equilibrium between NO and NO₂ has been suggested to play an important role in the ¹⁵N/¹⁴N ratios of NO and NO₂ [46] and atmospherically derived nitrate: nitric acid (HNO₃), nitrate (NO₃⁻), and particulate nitrate (p-NO₃⁻) [188]. The partitioning of ¹⁵N between NO and NO₂ depends on their relative concentration (NO/NO_x and NO₂/NO_x) and the temperature dependent isotope equilibrium fractionation factor [46]. During the daytime, when near equal concentrations of NO and NO₂ coexist due to the Leighton Cycle, the N isotope exchange between NO and NO₂ has been suggested to influence their individual ¹⁵N/¹⁴N ratios via the equilibrium isotope effect [46]. During the nighttime, however, NO concentrations may approach zero if O₃ concentrations are high, as NO is oxidized into NO₂ (5.1) without photolyzing back to NO (5.2) [46, 189]. Under these conditions, the NO₂ in the atmosphere likely reflects ¹⁵N/¹⁴N ratios of local NO_x sources [46]. Therefore, this isotope exchange reaction has important implications for using the N stable isotope composition of atmospheric nitrate to partition NO_x sources [27, 28, 32, 190], or as a chemical tracer of atmospheric processes [31, 101, 188, 190].

N isotope exchange between NO and NO₂ has equilibrium constant ($K = k_1/k_{-1}$):



that depends on the thermodynamic differences between the N isotopologues of NO and NO₂ [111]. In the Born-Oppenheimer approximation, differences in the thermodynamics of an isotopologue pair depend on the isotopologue dependent vibrational frequencies [111]. Substitution of a heavier isotope will lower the vibrational frequency and the vibrational zero-point energy (ZPE) of a molecule. Based on N isotopologue ZPEs, 5.4 is favored to the right as the ZPE is lower on the right side (ZPE = 32.39 kJ/mol) than for the left (ZPE = 33.56 kJ/mol) [132], indicating that ¹⁵N will preferentially form in NO₂ over NO.

While the NO and NO₂ exchange favoring the formation of ¹⁵NO₂ has been observed in experimental measurements [154, 155] and predicted by theoretical calculations [71, 101, 132, 133], there is disagreement between theoretical and experimental studies on the value of the equilibrium constant, also called the fractionation factor

(α) (Fig. 5.1). Using the Bigeleisen-Mayer equation in the harmonic oscillator approximation [111,142], theoretical studies have predicted fractionation factors for ^{15}N substitution between NO_2 and NO ($\alpha_{\text{NO}_2/\text{NO}}$) to range from 1.0354 to 1.042 at 298 K [71, 101, 132, 133]. However, these predicted values are substantially different than the experimental of 1.028 ± 0.002 at 298 K [155]. At 238 K, theory predicts $\alpha_{\text{NO}_2/\text{NO}}$ to range from 1.0552 to 1.0596 [71,101,132]. Experimental $\alpha_{\text{NO}_2/\text{NO}}$ at 238 K has been measured to be 1.040 ± 0.02 [Leifer, 1940], technically within experimental error of the theoretical value, but with a relative large uncertainty.

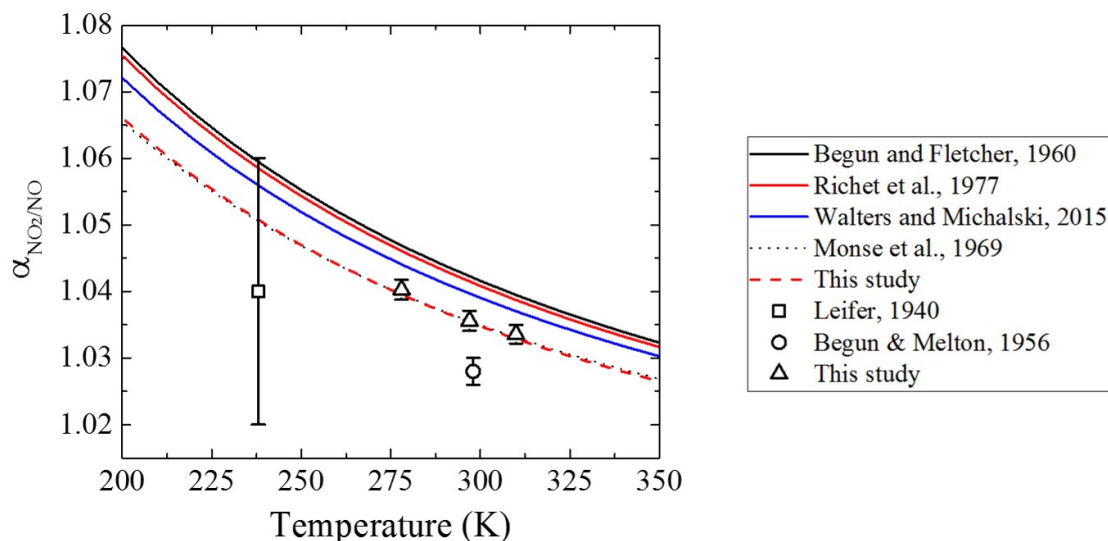


Fig. 5.1.: Comparison between previous theoretical calculations of $\alpha_{\text{NO}_2/\text{NO}}$ using harmonic frequencies (solid lines), observable vibrational frequencies (dotted line), harmonic frequencies corrected for anharmonic zero-point energies (dashed line), and experimental measurements (square, circle, and triangle points).

The disagreement between experiment and theory might be due to the analytical method used to measure the abundances of the N isotopologues of NO and NO_2 . The mass spectrometer technique used to measure NO_2 is subject to mass interference via the formation of NO^+ and NO_2^+ ions that originate from NO_2 [154, 155]. Dis-

agreements could also be related to the harmonic approximation used to calculate the theoretical $\alpha_{\text{NO}_2/\text{NO}}$ values as inclusion of anharmonicity will tend to lower α values [144]. In this study, we will revisit the N isotope exchange between NO and NO₂ using measurement techniques that will overcome previous experimental measurement limitations in an effort to reconcile previous experimental and theoretical differences for this isotope exchange reaction.

5.2 Methods

5.2.1 Experiment Design

The experiment utilized a reaction vessel, vacuum line and a series of denuder tubes (Fig. 5.2). A 1 L two-necked reaction vessel was attached to one end of the vacuum line and a series of denuder tubes were connected to the other end. A NO bulb ($\delta^{15}\text{N} = (-42.5 \pm 0.9)\text{‰}$), NO₂ bulb ($\delta^{15}\text{N} = (-32.0 \pm 0.9)\text{‰}$), and a high-purity argon (Ar) tank ($> 99.5\%$) were connected to the vacuum line inlet ports using ultratorr fittings. Here $\delta^{15}\text{N}(\text{‰}) = [({}^{15}\text{N}/{}^{14}\text{N})_{\text{sample}}/({}^{15}\text{N}/{}^{14}\text{N})_{\text{air}} - 1] \times 1000$. The reaction vessel and vacuum line was evacuated to 10^{-4} Pa and then a mixture of roughly 6.70 Pa of NO and 27.0 Pa of NO₂ was introduced into the system. The reaction vessel was sealed off from the vacuum line, and the vacuum line was then evacuated back down to 10^{-4} Pa. The vacuum line was isolated and high-purity Ar was introduced into the vacuum line and bled into the reaction vessel until a pressure of 101.3 kPa was achieved. The NO and NO₂ pressures were kept low in order to prevent appreciable formation of N₂O₃ or N₂O₄ molecules. With the pressures of NO and NO₂ used in this experiment, we calculated N₂O₃ pressures to be less than 2.05 mPa using the NO + NO₂ \leftrightarrow N₂O₃ equilibrium constant [191], and less than 16.6 mPa for N₂O₄ using 2NO₂ \leftrightarrow N₂O₄ equilibrium constant [186]. Therefore, N₂O₃ and N₂O₄ formation should be negligible in our experimental set-up.

The NO/NO₂ mixture was allowed to equilibrate for 5 minutes, and then NO₂ was collected using the denuder tubes. The N isotope exchange rate between NO and

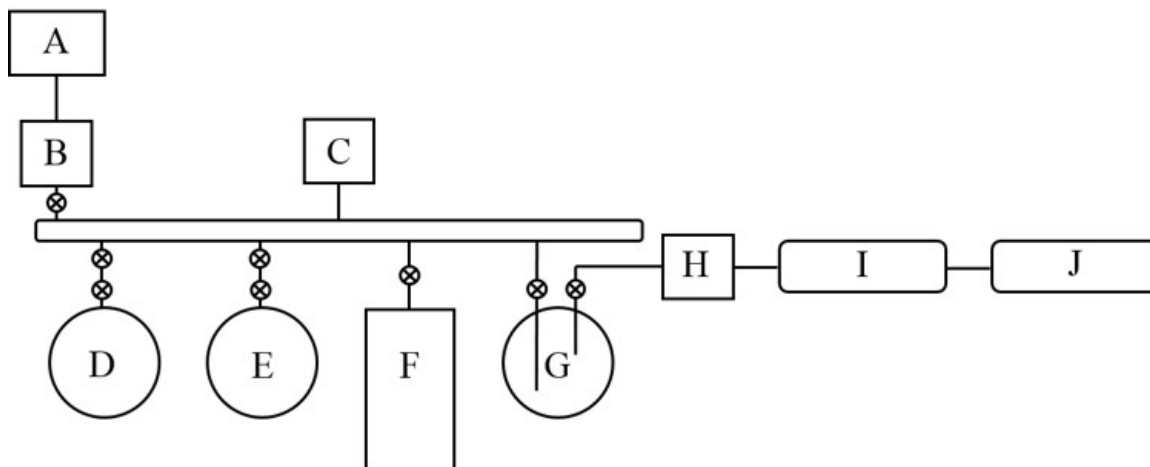


Fig. 5.2.: Experimental set-up for the N isotopic exchange between NO and NO₂. The symbols are: A = rotary pump, B = diffusion pump, C = vacuum gauge, D = NO bulb ($\delta^{15}\text{N} = -42.5\text{‰}$), E = NO₂ bulb ($\delta^{15}\text{N} = -32.0\text{‰}$), F = Argon tank ($> 99.5\%$), G = 1 L reaction vessel, H = flow meter, I = NO₂ binding denuder tube, and J = NO₂ breakthrough denuder tube.

NO₂ has been previously measured to be $8.14 \times 10^{-14} \text{ cm}^3 \text{ molecules}^{-1}\text{s}^{-1}$ [192]. Kinetic modeling of this reaction indicates that N isotopic equilibrium should be reached in less than 1 second at the NO and NO₂ pressures used in this experiment; therefore, N isotopic equilibrium between NO and NO₂ will easily be achieved in the experimental set-up. The NO and NO₂ was purged from the bulb by flowing Ar at a rate of 2 L/min for 10 minutes. The gases passed through a denuder tube (inner diameter = 3 mm, length = 1 m) coated with a 0.5 mL dried solution of 2.5 M potassium hydroxide and 25% by weight of guaiacol (C₇H₈O₂) using methanol as a solvent. This coated mixture selectively binds NO₂ as nitrite (NO₂⁻) [36,41,193]. The denuder tube binding efficiency is based on the time for NO₂ to diffuse to the surface of the coated denuder tube, which depends on the flow rate, time to achieve laminar flow, and time for NO₂ to diffuse to the surface of the coated denuder tube [194]. Mathematical modeling of these processes indicates that a tube length of 1 m will allow more than 99.9% of

all NO_2 to be absorbed by the employed denuder tube and experimental conditions (i.e. flow rate and denuder diameter) [194]. A second denuder tube was connected in series with the first tube to check for NO_2 breakthrough.

After sampling, the denuder tubes are separately rinsed with 3 mL of 18.2 M Ω Millipore water. Control tests using NO_2 pressures of 13.3 Pa (upper limit of actual NO_2 pressures used in exchange experiments) indicate that NO_2^- in the second denuder tube was below the detection limit (100 ppb) of an Ion Chromatography (Dionex IonPac AS19). Additionally, the out-flow from the second denuder tube was analyzed using a $\text{NO-NO}_2\text{-NO}_x$ analyzer (Thermo Scientific) and NO_x was never detected above the background level. These control tests suggest that NO_2 breakthrough did not occur, and there is a negligible NO_2^- blank in the guaiacol/KOH binding salt. Nitrate (NO_3^-)/ NO_2^- test strips (Aquacheck) indicated that NO_2^- in the second denuder tube was below the detection limit of 500 ppb in each of our exchange trials. Control tests using only the NO_2 bulb that went through the entire NO_2 binding procedure indicate that the reproducibility in our measured $\delta^{15}\text{N-NO}_2$ values to be $-32.5 \pm 0.7\text{‰}$ ($n = 5$), in excellent agreement with the N isotope composition of the NO_2 bulb (-32.0‰). Additionally, control tests using only the NO bulb indicate that NO does not bind onto the denuder tubes that are designed to specifically bind NO_2 .

Five trials at three different temperatures (278 K, 297 K, and 310 K) were performed. Since the exchange rate between NO and NO_2 is extremely fast (< 1 second under experimental conditions), it was necessary to temperature control both the reaction vessel and the denuder tubes. For the trials at 278 K and 310 K, temperatures were controlled by submerging the reaction vessel and denuder tubes into an ice water (278 K) or hot water (310 K) bath. The reaction vessel and denuder tubes were allowed 10 minutes to equilibrate with the temperature of the water bath before each trial was performed. Temperatures were monitored throughout the experiment for each trial and indicate that the cold and hot water bath did not vary by more than 0.5 K for each individual trial and by no more than 1 K for the five trials at the

same temperature. For the room temperature exchange (297 K), a water bath was not used but the laboratory room temperature was monitored and did not vary by more than 0.5 K for each individual exchange and by no more than 1 K between the different trials.

5.2.2 N Isotopic Analysis

N isotopic analysis was performed on the product NO_2^- in the elutant from the first denuder tube for each exchange trial. Approximately 250 nmol of NO_2^- was converted into nitrous oxide (N_2O) using sodium azide in an acetic acid buffer [195]. The N_2O was extracted and purified using an automated headspace gas chromatography system and analyzed by a Thermo Delta V Continuous Flow Isotope Ratio Mass Spectrometer (GC-CF-IRMS) for m/z 44, 45, and 46 at the Purdue Stable Isotopes Lab. Five working lab NO_3^- standards, calibrated to NIST isotope reference USGS34 and USGS35 were used to correct for isotopic fractionation associated with the N_2O purification process. Our working lab standards have the following $\delta^{15}\text{N}(\text{‰})$ relative to air: -20.0, -7.6, 0.5, 10.6, and 15.3. Before the working lab NO_3^- standards were converted to N_2O using the sodium azide and acetic acid buffer, they were first reduced to NO_2^- using an activated cadmium metal in a 5M NaCl solution [196]. Working lab standards had an average standard deviation of 0.5‰ for $\delta^{15}\text{N}$.

5.2.3 Experimental determination of $\alpha_{\text{NO}_2/\text{NO}}$

The α associated with N isotope exchange between NO and NO_2 (5.4) can be related by the abundances of ^{14}NO , ^{15}NO , $^{14}\text{NO}_2$, and $^{15}\text{NO}_2$ at equilibrium (Eq. 5.5):

$$K_{\text{NO}_2/\text{NO}} = \alpha_{\text{NO}_2/\text{NO}} = \frac{(^{15}\text{NO}_2)(^{14}\text{NO}_2)}{(^{14}\text{NO}_2)(^{15}\text{NO})} = \frac{(^{15}R_{\text{NO}_2})}{(^{15}R_{\text{NO}})} \quad (5.5)$$

where $^{15}\text{R} = ^{15}\text{N}/^{14}\text{N}$ ratios. Since initial ^{15}R and pressures are known for NO and NO_2 , mass-balance will enable us to calculate the total ^{15}R in our equilibrium system (Eq. 5.6:

$$^{15}R_{\text{Total}} = ^{15}R_{\text{NO}_{(i)}} \times p_{\text{NO}} + ^{15}R_{\text{NO}_{2(i)}} \times p_{\text{NO}_2} \quad (5.6)$$

where p is the partial pressure fraction (e.g. $p_{\text{NO}}/p_{\text{NO}_x}$) of either NO or NO_2 and (i) denotes the initial ^{15}R of either NO or NO_2 . At equilibrium, we only measured ^{15}R for NO_2 ; however, ^{15}R of NO at equilibrium can be calculated using our mass-balance relationship in Eq. 5.6 as the following (Eq. 5.7):

$$^{15}R_{\text{NO}_{(e)}} \times p_{\text{NO}} = ^{15}R_{\text{Total}} - ^{15}R_{\text{NO}_{2(e)}} \times p_{\text{NO}_2} \quad (5.7)$$

where (e) denotes the equilibrium ^{15}R of either NO or NO_2 . Using the equilibrium $^{15}\text{R}_{\text{NO}}$ and $^{15}\text{R}_{\text{NO}_2}$, $\alpha_{\text{NO}_2/\text{NO}}$ can be calculated from Eq. 5.5.

5.3 Results and Discussion

5.3.1 $\alpha_{\text{NO}_2/\text{NO}}$

The NO and NO_2 pressures, measured $\delta^{15}\text{N}$ of NO_2 at equilibrium, and experimental determined values for each trial is reported in Table 5.1. The experimental $\alpha_{\text{NO}_2/\text{NO}}$ values were determined to be 1.0403 ± 0.0015 , 1.0356 ± 0.0015 , and 1.0336 ± 0.0014 at 278 K, 297 K, and 310 K, respectively. These values are within experimental error of values calculated using GF matrix derived vibrational frequencies [133] in the Bigeleisen-Mayer equation (1.0396, 1.0355, and 1.0331 at 278 K, 297 K, and 310 K, respectively). In contrast, the experimental values tend to be slightly lower than the values theoretically calculated at these temperatures using experimental harmonic frequencies in the Bigeleisen-Mayer equation (1.0461, 1.0415, and 1.0387, respectively) [71] and slightly lower than the values predicted using harmonic frequencies calculated using quantum mechanical methods (1.0441, 1.0397, 1.03704, respectively) [101] (Fig 5.1).

Table 5.1: Summary of NO pressure (p_{NO}), NO_2 pressure (p_{NO_2}), measured $\delta^{15}\text{N}$ - NO_2 , and experimentally determined $\alpha_{\text{NO}_2/\text{NO}}$ for each trial conducted at 278 K, 297 K, and 310 K.

Temperature (K)	p_{NO} (Pa)	p_{NO_2} (Pa)	$\delta^{15}\text{N}\text{-NO}_2$ (‰)	$\alpha_{\text{NO}_2/\text{NO}}$
278	25.33	13.33	-10.2	1.0398
278	29.33	12	-10.5	1.0393
278	28	9.33	-10.2	1.0417
278	25.33	9.33	-10.5	1.042
278	25.33	6.67	-14.3	1.0403
			$^{\text{a}}\bar{x}$	1.0403
			σ^{b}	0.0015
297	29.33	9.33	-14.1	1.0359
297	29.33	9.33	-13.6	1.0366
297	30.66	9.33	-12.9	1.0373
297	22.66	6.67	-17.6	1.0349
297	29.33	9.33	-15.9	1.0334
			$^{\text{a}}\bar{x}$	1.0356
			σ^{b}	0.0015
310	25.33	6.67	-16.5	1.0355
310	20	5.33	-21.3	1.0317
310	26.66	10.67	-15	1.0344
310	25.33	5.33	-18.8	1.0331
310	25.33	8	-17.3	1.0332
			$^{\text{a}}\bar{x}$	1.0336
			σ^{b}	0.0014

$^{\text{a}}\bar{x}$ = mean. $^{\text{b}}\sigma$ = standard deviation.

While our experimental $\alpha_{\text{NO}_2/\text{NO}}$ agree well with the values calculated by ref [133], there are some concerns in the way those values were calculated. In ref [133], frequencies for the N isotopologues of NO and NO_2 were calculated using force fields observed from fundamental vibrational frequencies, and these computed frequencies were used to calculate using the Bigeleisen-Mayer equation. However, constructing

the force fields of polyatomic molecules is complex and often requires several simplifications and approximations [144,197]. Therefore, this method is not recommended to calculate isotope exchange α values as it tends to result in larger errors relative to α values calculated using harmonic frequencies [144]. Thus, the agreement between our calculated values and the values calculated by [133], might be fortuitous. Theoretical predictions of isotope exchange processes using the Bigeleisen-Mayer equation can be improved by accounting for corrections for anharmonicity on the ZPE which can have a significant impact on α values [144]. To this end, we have calculated theoretical values using a modified version of the Bigeleisen-Mayer equation with anharmonic corrections for accurate zero-point energies [144], using experimental harmonic frequencies for the N isotopologues of NO and NO₂ [198,199] and experimental zero-point energies [200–202] (Fig. 5.1). Using this approach, we calculated values of 1.0395, 1.0352, and 1.0329 at 278 K, 297 K and 310 K, respectively, which is within the experimental uncertainty of our measurements (Fig 5.1).

Overall, there is excellent agreement between our theoretical calculated $\alpha_{\text{NO}_2/\text{NO}}$ and our experimental measured values. Ref [154] measured $\alpha_{\text{NO}_2/\text{NO}}$ of 1.040 ± 0.020 at 238 K is also in agreement with our theoretical calculated value of 1.0508 at 238 K, though the experimental uncertainty is relatively high. However, both our experimental and theoretical $\alpha_{\text{NO}_2/\text{NO}}$ values disagree with the value reported by ref [155]. Ref [155] determined $\alpha_{\text{NO}_2/\text{NO}}$ to be 1.028 ± 0.002 at 298 K, which is slightly lower than our experimental value of 1.0356 ± 0.0015 at 297 K or our theoretical calculated value of 1.0352 at 298 K. The disagreement or relatively high uncertainty in these previous $\alpha_{\text{NO}_2/\text{NO}}$ measurements may be explained due to the experimental measurement techniques. In both of these previous studies, the abundances of the N isotopologues of NO and NO₂ were measured by flowing gaseous NO and NO₂ into a mass spectrometer, but the separate mass analysis for the NO₂ and NO peaks is complicated due to the formation of NO⁺ and NO₂⁺ ions that originate from NO₂ [154,155]. This may have artificially lowered the abundance of ¹⁵NO₂ and increased the abundance of ¹⁵NO. In our experimental measurement technique, our samples were converted into

a relatively inert gas (N_2O) and $^{15}N/^{14}N$ ratios were directly compared to N isotopic references, which should eliminate previous experimental measurement limitations. Therefore, we believe our data reconciles previous disagreements between experimental measurements and theoretical calculations for this N isotope exchange process and will be useful in interpreting $^{15}N/^{14}N$ ratios of atmospheric NO and NO_2 .

5.3.2 Implications for $\delta^{15}N$ of atmospheric NO_2

In order to understand the impact the N isotope exchange between NO and NO_2 has on $\delta^{15}N-NO_2$, we modeled the diurnal cycle and seasonal changes in $\delta^{15}N-NO_2$ (Fig. 5.3), using a NO_x mass-balance model assuming that NO and NO_2 achieve N isotopic equilibrium. The exchange $\alpha_{NO_2/NO}$ can be related to δ notation by the following (Eq. 5.8):

$$\alpha_{NO_2/NO} = 1000 \times \left(\frac{\delta^{15}N-NO_2 + 1000}{\delta^{15}N-NO_x + 1000} - 1 \right) \quad (5.8)$$

Here, we define $\delta^{15}N$ to be relative to the total NO_x , for example $\delta^{15}N-NO_2$ is expressed as (Eq. 5.9):

$$\delta^{15}N-NO_2(\text{‰}) = 1000 \times \left(\frac{^{15}R_{NO_2}}{^{15}R_{NO_x}} - 1 \right) \quad (5.9)$$

with $\delta^{15}N-NO_x$ set to 0‰ relative to atmospheric air. Mass and isotopic balance for NO and NO_2 results in the following relationship (Eq. 5.10) :

$$f_{NO_2} \times \delta^{15}N-NO_2 + f_{NO} \times \delta^{15}N-NO = 1 \times \delta^{15}N-NO_x = 0(\text{‰}) \quad (5.10)$$

where f is mole fraction of NO or NO_2 to the total NO_x . Combining Eq. 5.8-5.10 results in the following relationship between $\delta^{15}N-NO_2$, $\alpha_{NO_2/NO}$, and f_{NO_2} (Eq. 5.11):

$$\delta^{15}N-NO_2(\text{‰}) = 1000 \times \left(\frac{(\alpha_{NO_2/NO} - 1)(1 - f_{NO_2})}{(1 - f_{NO_2}) + (\alpha_{NO_2/NO} \times f_{NO_2})} \right) \quad (5.11)$$

The mass-balance model highlights that the $\delta^{15}N-NO_2$ value will change depending on f_{NO_2} and temperature dependent $\alpha_{NO_2/NO}$ relative to the $\delta^{15}N-NO_x$ (Fig. 5.3).

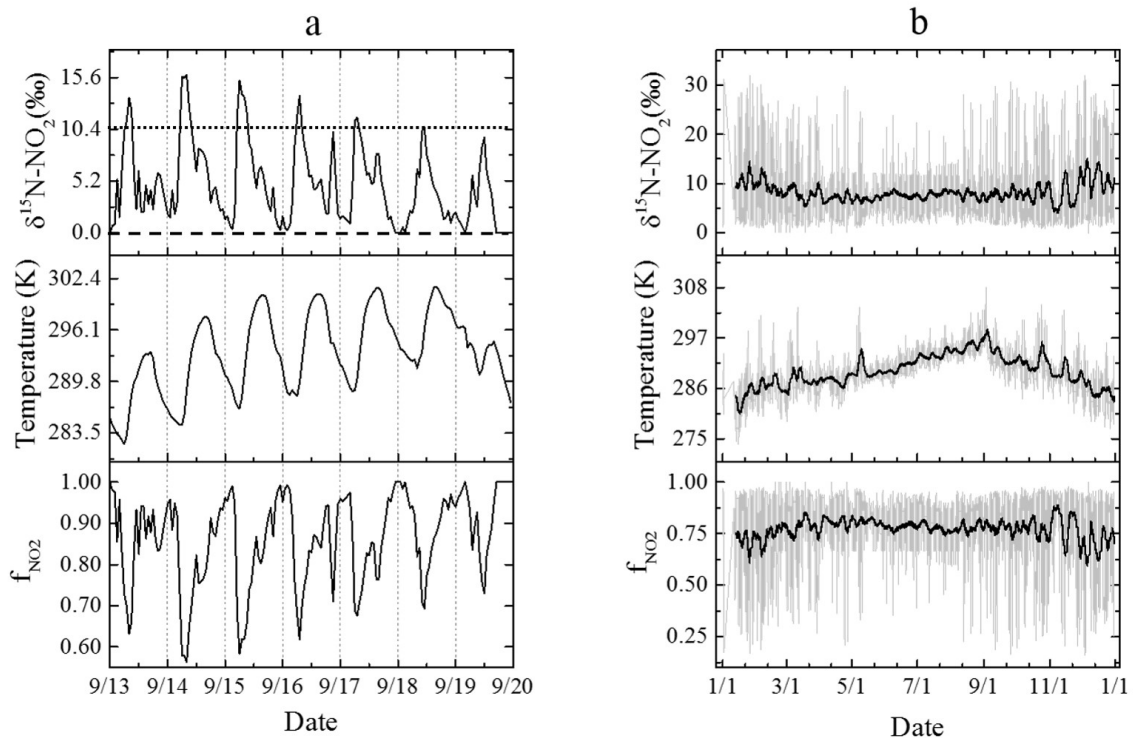


Fig. 5.3.: Hourly changes in $\delta^{15}\text{N-NO}_2$ (‰) (assuming equilibrium between NO and NO_2 is achieved), temperature (K), and f_{NO_2} over a week at Indianapolis, IN, USA (September 13 - September 20, 2015) (a) and over a year (2007) at Chula Vista, CA, USA (b). (a) highlights the conditions that N isotope exchange has a strong influence on $\delta^{15}\text{N-NO}_2$ relative to $\delta^{15}\text{N-NO}_x$ (dotted line) and conditions that have little influence on $\delta^{15}\text{N-NO}_2$ relative to $\delta^{15}\text{N-NO}_x$ (dashed line). Heavy curves in (b) are 100 point (100 hour) moving averages.

In Fig. 5.3, the $\delta^{15}\text{N-NO}_2$ diurnal profile is from hourly measurements of NO, NO_2 , and temperature at Indianapolis, IN, USA (39.8151°N , -86.1118°W) from September 13, 2015 to September 19, 2015, [203]. The $\delta^{15}\text{N-NO}_2$ has a diurnal cycle (Fig. 5.3) with a daily maximum of $12.9 \pm 2.4\text{‰}$, which typically occurs between 8:00 am and 1:00 pm when local f_{NO_2} values are the lowest. The f_{NO_2} is lowest during this period due to the emission of NO from transportation-related combustion sources,

typical of urban areas [204], as well as the photolysis of NO_2 during the daytime [6]. Under these conditions, the NO_x isotope exchange has a significant influence on the partitioning of $\delta^{15}\text{N}$ between NO and NO_2 , and this is shown in Fig. 5.3 with a dotted line. During the evening and nighttime, however, f_{NO_2} approaches 1 as all NO is oxidized by O_3 into NO_2 , but NO is not reformed due to the absence of NO_2 photolysis [6]. Under these conditions, $\delta^{15}\text{N-NO}_2$ approaches 0‰ indicating that $\delta^{15}\text{N-NO}_2$ is approximately equal to the $\delta^{15}\text{N-NO}_x$, and this is shown in Fig. 5.3.

Predicted seasonal changes in $\delta^{15}\text{N-NO}_2$ (Fig. 5.3) were derived from hourly measurements of NO , NO_2 , and temperature recorded at Chula Vista, CA, USA (32.6278°N, 117.0481°W) from January 1, 2007 to December 31, 2007 [205]. There is relatively large scatter in $\delta^{15}\text{N-NO}_2$ and f_{NO_2} throughout the year (Fig. 5.3), and this is related to the diurnal cycle that both $\delta^{15}\text{N-NO}_2$ and f_{NO_2} exhibit. The 100-hour moving average, however, shows that there may be slight seasonal variations in $\delta^{15}\text{N-NO}_2$ (Fig. 5.3). The model predicts that during the winter (December-February), $\delta^{15}\text{N-NO}_2$ would have the highest average 100-hour moving average of 10.3‰, compared to the other seasons that have similar average 100-hour moving averages of 7.36‰, 7.79‰, and 7.83‰ for spring (March-May), summer (June-August), and fall (September-November), respectively. The observed slightly higher $\delta^{15}\text{N-NO}_2$ 100-hour moving average for winter is related to both the seasonal changes in f_{NO_2} and in temperatures. Both of these parameters will result in higher $\delta^{15}\text{N-NO}_2$ values in winter relative to the other seasons, as N isotopic exchange is temperature dependent and is greater at lower temperatures and a lower f_{NO_2} will result in more ^{15}N enrichment in NO_2 . At Chula Vista, there is relatively small fluctuations in seasonal temperatures and f_{NO_2} (Fig. 5.3), however, at sites with larger variations in these parameters, it is expected that there will be a more pronounced seasonal cycling of $\delta^{15}\text{N-NO}_2$.

The simple case in which NO and NO₂ always exist in N isotopic equilibrium is competing with isotope fractionation factors and lifetimes associated with the Leighton cycle [46] (Eq. 5.12):

$$\tau_{\text{NO}+\text{O}_3} = \frac{1}{k_{\text{NO}+\text{O}_3}[\text{O}_3]} \quad (5.12)$$

$$\tau_{\text{NO-exchange}} = \frac{1}{k_{^{15}\text{NO}+^{14}\text{NO}_2}[\text{NO}_2]} \quad (5.13)$$

$$\tau_{\text{NO}_2\text{-exchange}} = \frac{1}{k_{^{15}\text{NO}+^{14}\text{NO}_2}[\text{NO}]} \quad (5.14)$$

$$\tau_{\text{NO}_2+h\nu} = \frac{1}{j_{\text{NO}_2}} \quad (5.15)$$

Here τ is lifetime (e-folding time) of each reaction, k are the rate constants ($\text{NO} + \text{O}_3 = 1.73 \times 10^{-14} \text{ cm}^3\text{molecules}^{-1}\text{s}^{-1}$ [206] and NO_x isotope exchange = $8.14 \times 10^{-14} \text{ cm}^3\text{molecules}^{-1}\text{s}^{-1}$ [192], and j is photolysis rate constant $5 \times 10^{-3} \text{ s}^{-1}$, which depends upon solar zenith angle [207]). Using these constants and concentrations of 5 ppb of NO, 5 ppb NO₂, and 20 ppb of O₃, $\tau_{\text{NO} + \text{O}_3}$, $\tau_{\text{NO}_{\text{exchange}}}$, $\tau_{\text{NO}_2\text{exchange}}$, and $\tau_{\text{NO}_2 + h\nu}$ are calculated to be 1.9, 1.6, 1.6, and 1.9 minutes respectively. Under these conditions, the lifetimes of the Leighton cycle reactions and NO_x exchange are comparable, therefore, the associated N fractionation factor between NO and NO₂ will be a mixture of these processes. If one of the lifetimes is an order of magnitude shorter relative to the others, the associated N fractionation factor between NO and NO₂ will be closer to the shorter lifetime's N fractionation factor. For example, when NO and NO₂ concentrations are increased to 80 ppb, $\tau_{\text{NO}_{\text{exchange}}}$ and $\tau_{\text{NO}_2\text{exchange}}$, decreases to 0.1 minutes and the NO and NO₂ $\delta^{15}\text{N}$ values will more closely match the NO_x exchange fractionation factor. Such conditions may exist down wind of smoke stack plumes during the daytime. Conversely, during high O₃ (20 ppb) and low NO_x (100 ppt), such as the open ocean, $\tau_{\text{NO}_{\text{exchange}}}$ and $\tau_{\text{NO}_2\text{exchange}}$ are 100 times slower than photolysis and O₃ oxidation and thus is unlikely to be relevant. The N fractionation factors associated with the NO + O₃ reaction and NO₂ photolysis has yet to be determined but will be the subject of ongoing research. During the night when photolysis ceases and nearly all NO_x exists as NO₂, the $\delta^{15}\text{N}$ of NO₂ will reflect the $\delta^{15}\text{N}$ of the emitted NO_x in that

region. Overall, the N fractionation between NO and NO₂ is complicated, but future research in the kinetic modeling of Leighton/NO_x exchange process will help elucidate the importance of the various N fractionation factors under varying conditions.

The $\delta^{15}\text{N}$ value of atmospheric nitrate formed from the NO_x will depend not only on the $\delta^{15}\text{N}$ value of the NO₂ but also kinetic and equilibrium isotope effects occurring during its oxidation into NO₃⁻. During the daytime, atmospheric nitrate is primarily formed through the reaction NO₂ + •OH + M → HNO₃. Therefore, $\delta^{15}\text{N}$ value of atmospheric nitrate formed during the day will be a complex function of the $\delta^{15}\text{N}$ of the emitted NO_x, the NO_x equilibrium/Leighton reaction fractionation factors, and the fractionation factor associated with the NO₂ + •OH + M → HNO₃ + M reaction, which is currently unknown.

During the nighttime, atmospheric nitrate is primarily formed through the formation of N₂O₅ and its subsequent hydrolysis. N₂O₅ exists in equilibrium with NO₂ and nitrate radical (NO₃):



Since nighttime $\delta^{15}\text{N}$ -NO₂ should be reflective of the $\delta^{15}\text{N}$ of the NO_x sources, the N₂O₅ $\delta^{15}\text{N}$ value will depend on the emitted NO_x sources and the isotope exchange associated with the N₂O₅ equilibrium (5.4). At N isotopic equilibrium, N₂O₅ is predicted to be 26.9‰ and 31.1‰ enriched in $\delta^{15}\text{N}$ relative to NO₂ and NO₃ at 298 K [101]. Therefore, $\delta^{15}\text{N}$ of atmospheric nitrate formed in the absence of sunlight should be ¹⁵N enriched relative to the NO_x, which is a possible explanation for the observed high $\delta^{15}\text{N}$ values of atmospheric nitrate during winter months when there is less sunlight [27, 28, 31, 190] in addition to predicted seasonal changes in $\delta^{15}\text{N}$ -NO_x [208].

5.4 Conclusions

Previously, there has been disagreement between experimental measurements and theoretical calculations of the N isotope exchange between NO and NO₂. In this

study, we measured this exchange process to have an $\alpha_{\text{NO}_2/\text{NO}}$ of 1.0403 (278 K), 1.0356 (297 K), and 1.0336 (310 K). These values are within experimental error of the values calculated using a modified version of the Bigeleisen-Mayer equation corrected for accurate ZPEs by including anharmonicity. Temperature dependent fractionation factors were calculated and used to model seasonal changes in $\delta^{15}\text{N-NO}_2$. The model predicts that $\delta^{15}\text{N-NO}_2$ values will exhibit a pronounced diurnal oscillation and have seasonal variations that depend upon f_{NO_2} and ambient temperature. If $\delta^{15}\text{N}$ of atmospheric nitrate is linked to the $\delta^{15}\text{N-NO}_2$, then our model predicts that: (1) $\delta^{15}\text{N}$ diurnal variations would be found in atmospheric nitrate, (2) elevated winter $\delta^{15}\text{N}$ should be observed in $\delta^{15}\text{N}$ of atmospheric nitrate due to N isotope exchange between NO and NO_2 , (3) relatively large seasonal variations in $\delta^{15}\text{N}$ of atmospheric nitrate will be observed in regions with relatively large seasonal changes in temperature and f_{NO_2} , and (4) there will be diurnal variation in $\delta^{15}\text{N-NO}_x$ values, with night-time values reflecting the local/regional NO_x sources. Future simultaneous $\delta^{15}\text{N}$ measurements of atmospheric nitrate and NO_2 will be useful in determining the correlation between the two. Additionally, other N isotope effects involving the oxidation of NO_x to atmospheric nitrate, the dry deposition of NO and NO_2 , and the photolysis of NO_2 still need to be considered and will be the subject for future research.

6. THEORETICAL CALCULATION OF OXYGEN EQUILIBRIUM ISOTOPE FRACTIONATION FACTORS INVOLVING VARIOUS NO_y MOLECULES, •OH, AND H₂O AND ITS IMPLICATIONS FOR ISOTOPE VARIATIONS IN ATMOSPHERIC NITRATE

The following chapter is a reprint from a published article (Walters, W. W.; Michalski, G. Theoretical calculation of oxygen equilibrium isotope fractionation factors involving various NO_y molecules, •OH, and H₂O and its implications for isotope variations in atmospheric nitrate. *Geochim. Cosmochim. Acta*, **2016**, *191*, 89-101).

6.1 Introduction

Stable isotopes are useful for understanding complex chemical systems such as the cycling and oxidation of NO_x [NO_x = nitric oxide (NO) + nitrogen dioxide (NO₂)]. For example, the oxygen (O) stable isotope composition of atmospheric nitrate, which includes nitric acid (HNO₃), nitrate (NO₃⁻), and particulate nitrate (p-NO₃⁻), indicates the proportion of NO_x that reacts with ozone (O₃) during its oxidation [53,54,209–211]. The O isotope composition of a sample is typically reported in delta notation (δ), which is expressed as the ratio (R) of the heavy (¹⁷O and ¹⁸O) to the light (¹⁶O) isotope in a sample relative to the same ratio of an international standard (Vienna Standard Mean Ocean Water (VSMOW) (Eq. 6.1):

$$\delta^x O(\text{‰}) = 1000 \left(\frac{{}^x R_{\text{sample}}}{{}^x R_{\text{VSMOW}}} - 1 \right) \quad (6.1)$$

where x represents the abundance of either ¹⁷O or ¹⁸O. Several studies have shown that atmospheric O₃ has elevated δ¹⁷O and δ¹⁸O values relative to VSMOW and a

strong mass-independent component [48, 57, 58, 212, 213], which is quantified by $\Delta^{17}\text{O}$ notation (Eq. 6.2) :

$$\Delta^{17}\text{O}(\text{‰}) = 1000 \ln \left(1 + \frac{\delta^{17}\text{O}}{1000} \right) - 0.52 \times 1000 \ln \left(1 + \frac{\delta^{18}\text{O}}{1000} \right) \quad (6.2)$$

These elevated $\delta^{18}\text{O}$ and $\delta^{17}\text{O}$ signatures are transferred to atmospheric nitrate proportionally when O_3 oxidizes NO_x [55, 56, 209, 214]. Thus, O isotopic analysis, particularly $\Delta^{17}\text{O}$, of atmospheric nitrate has been suggested as a useful proxy for assessing changes in NO_x oxidation and for evaluating long-term changes in the atmosphere's oxidation capacity [53, 211, 215].

There may be additional useful information in $\delta^{18}\text{O}$ variations, because mass-dependent fractionation processes (MDFP) such as equilibrium or kinetic isotope effects will have a minimal impact on $\Delta^{17}\text{O}$ but may induce significant $\delta^{18}\text{O}$ variations. These fractionation processes may also influence the nitrogen (N) isotopic composition ($\delta^{15}\text{N}(\text{‰}) = 1000[(^{15}\text{N}/^{14}\text{N})_{\text{sample}}/(^{15}\text{N}/^{14}\text{N})_{\text{air}} - 1]$, where air N_2 is the N isotopic reference) as NO_x is oxidized to atmospheric nitrate [46, 52, 216]. Thus, $\delta^{18}\text{O}$ and $\delta^{15}\text{N}$ of atmospheric nitrate may be related, reflecting to some degree the fractionation processes responsible for the formation of atmospheric nitrate. However, few studies have quantitatively evaluated the impacts of NO_x oxidation fractionation processes on $\delta^{18}\text{O}$ and their implications for possible $\delta^{18}\text{O}$ - $\delta^{15}\text{N}$ relationships of the atmospheric nitrate end product.

One such fractionation process that may play an important role on the $\delta^{18}\text{O}$ and $\delta^{15}\text{N}$ of atmospheric nitrate is isotopic equilibrium exchange or partial exchange. For example, it has been previously suggested that isotopic equilibrium between NO and NO_2 has a significant impact on the $\delta^{15}\text{N}$ of HNO_3 produced during the daytime [46, 52, 188, 217]. The same exchange processes may also generate useful $\delta^{18}\text{O}$ signatures in HNO_3 . Additionally, it has been suggested that NO_2 , the nitrate radical (NO_3), and dinitrogen pentoxide (N_2O_5) may reach isotopic equilibrium during the nighttime [190, 216, 218]. Isotopic equilibrium involving NO_2 , NO_3 , and N_2O_5 will affect partitioning of ^{18}O and ^{15}N between these molecules, which has implications for variations in $\delta^{18}\text{O}$ and $\delta^{15}\text{N}$ of HNO_3 produced at night. Thus, isotopic equilibrium

exchange in addition to mass-balance considerations may have important implications for diurnal and seasonal variations in $\delta^{18}\text{O}$ - $\delta^{15}\text{N}$ compositions of atmospheric nitrate. In this case, knowing the isotopic equilibrium fractionation factors involving a variety of oxidized N molecules (denoted as $\text{NO}_y = \text{NO}_x + \text{HNO}_3 + \text{p-NO}_3^- + \text{NO}_3 + \text{N}_2\text{O}_5 + \text{nitrous acid (HONO)} + \text{etc}$) would be useful.

Prior studies have calculated O isotopic equilibrium exchange fractionation factors involving some NO_y molecules using measured vibrational spectroscopic data [71] or empirically determined interatomic force constants [133, 219]. However, O isotopic equilibrium fractionation factors have not been determined for many atmospherically relevant NO_y molecules such as N_2O_5 , NO_3 , and halogen nitrates (XONO_2). This is primarily due to the absence of spectroscopic data for the isotopologues of these molecules. Previously, we have used computational quantum chemistry methods to calculate N isotopic equilibrium fractionation factors involving some NO_y molecules [101]. Here we will extend that study and calculate O isotopic equilibrium exchange fractionation factors for singly substituted O isotopologues of numerous NO_y molecules. We will also calculate the fractionation factor associated with equilibrium isotopic exchange between the hydroxyl radical ($\bullet\text{OH}$) and water (H_2O) due to the importance this reaction has on the $\delta^{18}\text{O}$ of atmospheric $\bullet\text{OH}$ [30, 59, 220]. Knowing $\delta^{18}\text{O}$ of $\bullet\text{OH}$ is important because it will be transferred proportionally to the atmospheric nitrate end product from $\bullet\text{OH}$ reaction with NO_2 [30]. Our calculated O isotopic equilibrium fractionation factors will allow for the evaluation of the impact various exchange reactions have on $\delta^{18}\text{O}$ values of these molecules and how it may be propagated into the atmospheric nitrate end product. Combining our O and N isotopic equilibrium fractionation factors will allow for the prediction of $\delta^{18}\text{O}$ - $\delta^{15}\text{N}$ arrays resulting from various atmospheric nitrate formation pathways.

6.2 Methods and Theory

6.2.1 Calculation of equilibrium isotope exchange fractionation factors

The theoretical calculation of isotopic fractionation associated with isotope exchange equilibrium reactions has long been carried out in the harmonic approximation using partition functions [111,142]. In the Born-Oppenheimer, harmonic oscillator, and rigid-rotor approximations, the reduced partition function ratio (RPFR, commonly denoted as ${}^x\beta$) for an oxygen isotopic pair is written as (Eq. 6.3):

$$RPFR = {}^x\beta_{\text{har}} = \left(\frac{s_2}{s_1}\right)_f = \prod_i^N \frac{u_{2i}}{u_{1i}} \times \exp\left(\sum_i^N \frac{u_{1i} - u_{2i}}{2}\right) \times \prod_i^N \frac{1 - \exp(-u_{1i})}{1 - \exp(-u_{2i})} \quad (6.3)$$

where x and subscript 2 refer to one of the heavy isotopes (^{17}O or ^{18}O) and subscript 1 refers to ^{16}O . The $u_i = hc\omega_i/kT$ where h is Planck's constant, c is the speed of light, ω_i is the harmonic frequency (cm^{-1}) for each vibrational mode (i), k is Boltzmann constant, T is temperature in Kelvin, and N refers to the number of normal mode vibrational frequencies. In Eq. 6.3, the Teller-Redlich rule was employed [221], which converts translational and rotational motion into vibrational frequencies. Symmetry numbers are not considered, because symmetry in itself does not lead to isotopic enrichment during equilibrium [142] but must be considered from a statistical perspective [222] [223].

The ${}^x\beta$ values calculated using Eq. 6.3 are accurate in the harmonic oscillator and rigid-rotor approximations. However, corrections for anharmonicity, vibration-rotation coupling, centrifugal distortion, hindered internal rotation, and quantum mechanical correction to rotation have been shown to be important for calculating accurate ${}^x\beta$ values for some molecules [71,144,224]. Generally, for atoms other than H most of the corrections can be ignored as ${}^x\beta$ is impacted by less than 0.01‰. The main exception is anharmonic correction to the zero point energy (ZPE), which can play a significant role in the calculation of accurate ${}^x\beta$ values [144]. If accurate ZPEs

are known or can be accounted for, ${}^x\beta$ values can more accurately be calculated by the following [144] (Eq. 6.4):

$${}^x\beta_{\text{anhar}} = \frac{\exp(-ZPE_{\text{anhar},2}/kT)}{\exp(-ZPE_{\text{anhar},1}/kT)} \prod_i^N \left(\frac{u_{2i}}{u_{1i}} \right) \times \left(\frac{1 - \exp(-u_{1i})}{1 - \exp(-u_{2i})} \right) \quad (6.4)$$

where ZPE_{anhar} is the anharmonic corrected ground ZPE.

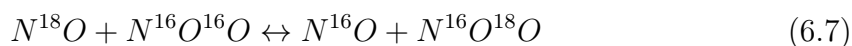
A general representation for an equilibrium isotope exchange reaction involving two different chemical compounds, A and B, is (Eq. 6.5):



where subscripts 1 and 2 again refer to the light and heavy isotopologue, respectively. The equilibrium constant, ${}^xK_{A/B}$, which is also called the equilibrium isotope fractionation factor (${}^x\alpha_{A/B}$), can be obtained from the ${}^x\beta$ values of A and B (Eq. 6.6: (Eq. 6.6):

$${}^xK_{A/B} = {}^x\alpha_{A/B} = \frac{{}^x\beta_A}{{}^x\beta_B} \quad (6.6)$$

For example, using this notation, the equilibrium isotope exchange reaction between NO and NO₂ involving the singly substituted ¹⁸O and ¹⁶O isotopologue pair is written as (Eq.6.7):



The equilibrium constant for this isotope exchange reaction is written as (Eq. 6.8):

$${}^{18}K_{\text{NO}_2/\text{NO}} = {}^{18}\alpha_{\text{NO}_2/\text{NO}} = \frac{{}^{18}\beta_{\text{NO}_2}}{{}^{18}\beta_{\text{NO}}} \quad (6.8)$$

6.2.2 Computational chemistry methods

Using *ab initio* methods to obtain β and $\alpha_{A/B}$ values for use in geochemical systems is a relatively recent advance [134, 135, 137, 138, 141, 144, 169, 225]. In this study, the Becke-3 parameter-Lee-Yang-Parr (B3LYP) hybrid density function theory (DFT) method [146, 147] and Dunning correlation-consistent polarized valence triple ζ (cc-pVTZ) basis set (Dunning, 1989) were used to calculate geometries (bond angles

and bond lengths) and harmonic frequencies for the following molecules: NO, NO₂, HONO, HNO₃, N₂O₅, nitrate (NO₃⁻), chlorine nitrate (ClONO₂), nitrite (NO₂⁻), dinitrogen tetroxide (N₂O₄), nitryl bromide (BrNO₂), nitryl chloride (ClNO₂), bromine nitrate (BrONO₂), •OH, and H₂O. We also calculated the geometry and vibrational frequencies of NO₃ using the EDF2 DFT method [148] with the cc-pVTZ basis set (EDF2/cc-pVTZ) and the QCISD method with the cc-pVDZ basis set (QCISD/cc-pVDZ). These additional methods were used to compare the calculated vibrational frequencies of NO₃ due to the difficulties this molecule presents for computational studies related to it being a polyatomic doublet radical with multireference character [172, 173]. Calculations involving the B3LYP/cc-pVTZ and QCISD/cc-pVDZ methods were performed using the Gaussian09 program package revision D.01 [226] on the Purdue Radon cluster. The EDF2/cc-pVTZ calculations were performed using the QChem 4.2 program package [145] on an IBM personal computer. The masses of the most abundant isotopes of each element (¹H, ¹²C, ¹⁴N, ¹⁶O, ³⁵Cl, ⁷⁹Br) were used to calculate harmonic frequencies, and isotope effects were subsequently determined via single-atom substitutions of either ¹⁷O or ¹⁸O for each ¹⁶O position. Systematic model errors and anharmonic corrections to the ZPE were accounted for by applying a constant scale factor to the calculated harmonic ZPE, as recommended by ref. [144]. We used a constant scale factor of 0.9787, recommended by ref. [227] to correct calculated harmonic ZPE using B3LYP/cc-pVTZ to match experimental ZPEs. This scale factor was also used to correct the ZPE of NO₃ calculated using EDF2/cc-pVTZ. The ZPE of NO₃ calculated from QCISD/cc-pVDZ was scaled by 0.9776, based on a recommended value for QCISD/6-31G(d) [228].

6.3 Results

6.3.1 Calculated $\alpha\beta$ values

The NO₃ vibrational frequencies calculated using B3LYP/cc-pVTZ, EDF2/cc-pVTZ, QCISD/cc-pVDZ, and EOM-CCSD/aug-cc-pVDZ [101] were compared (Ta-

ble 6.1) with experimental data [229–231]. Generally, it is found the most accurate NO_3 vibrational frequencies are from the EDF2/cc-pVTZ method (Table 6.1). Using calculated frequencies, ${}^x\beta$ values were calculated for each molecule over a temperature range from 150 to 450 K using Eq. 6.4. For the molecules that had non-equivalent O sites (i.e. HNO_3 , N_2O_5 , ClONO_2 , HONO , and BrONO_2), two ${}^x\beta$ values were calculated. These are designated as “c” to refer to the substitution of ${}^x\text{O}$ in the central bridging O atom position (e.g. $\text{HONO}^c = \text{H}^x\text{ONO}$) and “t” to refer to the substitution of ${}^x\text{O}$ in the terminal O atom position (e.g. $\text{HONO}^t = \text{HON}^x\text{O}$). For molecules with more than one terminal O atom, but with slight break in symmetry (e.g. HNO_3 , BrONO_2 , and ClONO_2), the geometric mean ${}^x\beta$ at all terminal sites is reported. These terminal sites are nearly equivalent as their O ${}^x\beta$ values were generally within 0.001.

Regression fit parameters calculated for ${}^{18}\beta$ as a function of temperature, and ${}^{18}\beta$ values at 298 K, are reported in Table 6.2. At 298 K, ${}^{18}\beta$ ranged from 1.0258 to 1.1110, increasing in the following order: $\bullet\text{OH} < \text{H}_2\text{O} < \text{BrONO}_2^c < \text{ClONO}_2^c < \text{N}_2\text{O}_5^c < \text{HONO}^c < \text{NO}_3 < \text{HNO}_3^c < \text{NO}_3^- < \text{NO}_2 < \text{NO}_2^- < \text{NO} < \text{N}_2\text{O}_4 < \text{BrNO}_2 < \text{ClNO}_2 < \text{HNO}_3^t < \text{HONO}^t < \text{BrONO}_2^t < \text{ClONO}_2^t < \text{N}_2\text{O}_5^t$ (Table 6.2). The magnitude of ${}^{18}\beta$ appears to be related to the number of bonds and the electronegativity of the oxygen bond-partner and increased in the following order: 1 hydrogen $<$ 2 hydrogen $<$ 1 halogen + 1 nitrogen $<$ 2 nitrogen $<$ 1 hydrogen + 1 nitrogen $<$ 1 nitrogen (Table 6.2). This ordering of atoms that O is directly bonded to may provide a rough *a priori* way to arrange ${}^{18}\beta$ values based solely on molecular structure.

Fig. 6.1 compares our calculated ${}^{18}\beta$ values for NO , NO_2 , H_2O , and HNO_3^c with those previously reported [71, 133, 144] as well as calculated using experimental data [29, 202]. Overall, our calculated ${}^{18}\beta$ values agree with those previously reported (Fig. 6.1). For example, at 300 K, we calculated ${}^{18}\beta(\text{NO})$ to be 1.0995, which is close to previously calculated values of 1.0973 [71] and 1.0963 [133]. Additionally, our calculated ${}^{18}\beta(\text{NO}_2)$ at 300 K is 1.0909, which is close to the value of 1.0899 previously calculated by ref. [133] and the value of 1.0867 calculated from empirically determined

Table 6.1: Comparison of calculated NO_3 ν_i (cm^{-1}) from different computational methods and experimental determined values. Values in parentheses represent the absolute difference between the calculated and experimental frequency for a particular vibrational mode.

	ν_1 (asym bend)	ν_2 (asym bend)	ν_3 (um- brella)	ν_4 (sym stretch)	ν_5 (asym stretch)	ν_6 (asym stretch)	Average Error*
B3LYP /cc-pVTZ ^a	204.93 (160.7)	206.64 (159.0)	809.25 (46.2)	1107.09 (54.1)	1108.04 (8.0)	1129.61 (29.6)	76.3
EDF2 /cc-pVTZ ^a	337.75 (27.9)	339.79 (25.8)	816.47 (53.4)	1142.11 (89.1)	1171.90 (71.9)	1174.35 (74.3)	57.1
QCISD /cc-pVDZ ^a	201.82 (163.8)	203.80 (161.8)	813.92 (50.8)	1144.00 (91.0)	1168.86 (68.9)	1169.08 (69.1)	100.9
EOM-CCSD /aug-cc-pVDZ ^b	310.80 (54.8)	312.94 (52.7)	743.37 (19.7)	1103.92 (50.9)	1263.96 (164.0)	1264.34 (164.3)	84.4
Experiment	365.6 ^c	365.6 ^c	763.1 ^d	1053.0 ^e	1100.0 ^c	1100.0 ^c	

^a calculated from this work. ^b calculated previously from ref. [101]. ^c from ref. [231]. ^d from ref. [23]. ^e from ref. [230]. * calculated as the average absolute deviation from experimental vibrational frequencies (i).

Table 6.2: Calculated $^{18}\beta$ regression coefficients^a as a function of temperature (150 K to 450 K) and $^{18}\beta$ (298 K) values for NO_y molecules, $\bullet\text{OH}$, and H_2O .

	A	B	C	D	$^{18}\beta(298\text{ K})$
$\bullet\text{OH}$	1.1036	-1.9577	1.2889	0.51636	1.0258
H_2O	3.2070	-5.7294	3.9525	1.1030	1.0639
BrONO_2^c	2.1489	-6.1744	8.3297	-0.22623	1.0656
ClONO_2^c	2.6464	-7.0231	8.6922	-0.22784	1.0671
N_2O_5^c	2.6369	-6.9058	8.6047	-0.20778	1.0672
HONO^c	3.3651	-7.2949	7.0520	0.51606	1.0734
NO_3^*	6.7853	-13.499	11.279	-0.08248	1.0818
HNO_3^c	3.9484	-8.8137	9.0903	0.38699	1.0871
NO_3^-	6.3617	-13.388	12.124	-0.10652	1.0904
NO_2	7.8475	-15.028	11.690	0.20838	1.0918
NO_2^-	7.8614	-15.049	11.700	0.20718	1.0918
NO	8.1294	-14.507	10.124	0.93160	1.1008
N_2O_4	7.7029	-14.916	12.695	0.21039	1.1034
BrNO_2	7.9945	-15.453	13.127	0.19084	1.1060
ClNO_2	8.0617	-15.674	13.396	0.19632	1.1084
HNO_3^t	7.9932	-15.922	13.776	0.10526	1.1086
HONO^t	8.5480	-16.103	12.686	0.50745	1.1099
BrONO_2^t	8.0302	-15.747	13.703	0.14583	1.1099
ClONO_2^t	8.0808	-15.824	13.748	0.16979	1.1110
N_2O_5^t	8.1801	-15.985	13.792	0.17181	1.1110

^a $1000(\beta - 1) = \frac{A}{T^4} \times 10^{10} + \frac{B}{T^3} \times 10^8 + \frac{C}{T^2} \times 10^6 + \frac{D}{T} \times 10^4$ (typical misfit of the regression is 0.1%). ^c and ^t corresponds to the substitution of ^{18}O at the bridging or terminal O atom position, respectively for a particular molecule (e.g. $\text{HONO}^c = \text{H}^{18}\text{ONO}$, $\text{HONO}^t = \text{HON}^{18}\text{O}$). ^{*} All $^{18}\beta$ values calculated using B3LYP/cc-pVTZ, except for NO_3 , which was calculated using EDF2/cc-pVTZ

interatomic force constants [29] and experimental ZPEs [202]. For H_2O , we calculated $^{18}\beta(\text{H}_2\text{O})$ at 300 K to be 1.0635, which is close to values previously calculated of 1.0632 [144] and 1.0630 [71]. Finally, for HNO_3^c , we calculated $^{18}\beta(\text{HNO}_3^c)$ to be 1.0862 at

300 K, which is close to the value of 1.0860 reported by ref. [133]. Fig. 6.2 compares the $^{18}\beta$ calculated for NO_3 using B3LYP/cc-pVTZ, EDF2/cc-pVTZ, and QCISD/cc-pVDZ methods and indicates general agreement. For example, at 300 K, $^{18}\beta$ for NO_3 is calculated to be 1.0775, 1.08135, and 1.0796 for B3LYP/cc-pVTZ, EDF2/cc-pVTZ, and QCISD/cc-pVDZ, respectively. However, since EDF2/cc-pVTZ calculated the most accurate NO_3 vibrational frequencies of the considered computational methods (Table 6.1), we used the EDF2/cc-pVTZ calculated $^{18}\beta$ values for $^{18}\alpha_{\text{A/B}}$ calculations involving NO_3 .

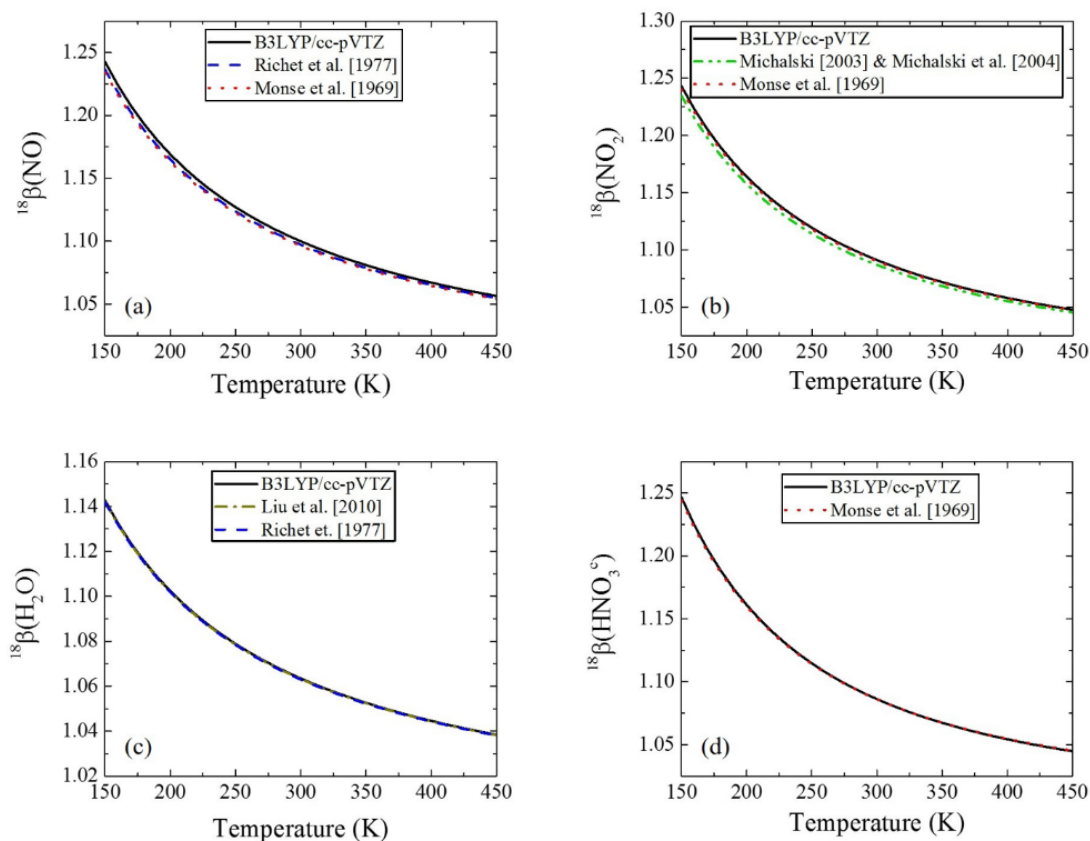


Fig. 6.1.: Comparison of calculated $^{18}\beta$ values using B3LYP/cc-pVTZ with those computed in previous studies for (a) NO [71, 133], (b) NO_2 [29, 133, 202], (c) H_2O [71, 144], and (d) HNO_3^c [133]

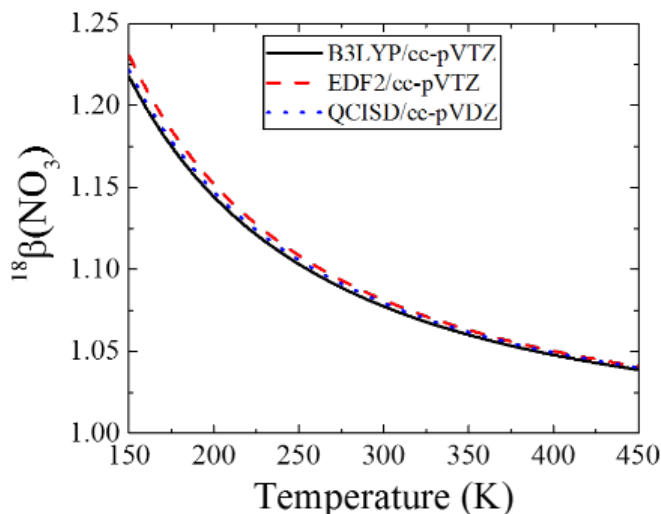


Fig. 6.2.: Comparison of calculated $^{18}\beta$ for NO_3 using various computational methods that include B3LYP/cc-pVTZ, EDF2/cc-pVTZ, and QCISD/cc-pVDZ.

6.3.2 Calculated $^{18}\alpha_{\text{A/B}}$ values

Using our calculated $^{18}\beta$ values, $^{18}\alpha_{\text{A/B}}$ were calculated for the following exchange reactions (A/B): NO/NO_2 , NO_2/NO_3 , $\text{N}_2\text{O}_5^{\text{geo}}/\text{NO}_2$, $\text{N}_2\text{O}_4/\text{NO}_2$, $\text{BrNO}_2/\text{NO}_2$, $\text{ClNO}_2/\text{NO}_2$, $\text{BrONO}_2^{\text{t}}/\text{NO}_2$, $\text{ClONO}_2^{\text{t}}/\text{NO}_2$, $\text{NO}_3^-/\text{H}_2\text{O}$, and $\text{H}_2\text{O}/\bullet\text{OH}$ over the temperature range of 150 to 450 K, where “geo” refers to the geometric mean $^{18}\beta$. These exchange reactions were chosen due to their common molecular structure (e.g. NO, NO_2 , or OH subunits), and therefore, possibility that O isotopic exchange might occur at a rate comparable to the atmospheric lifetime of these compounds (1 week). Few studies have experimentally determined $\alpha_{\text{A/B}}$ involving the considered molecules, limiting our ability to evaluate our calculated $\alpha_{\text{A/B}}$ values. One study that we are aware of involves the O isotopic exchange between NO_3^- and H_2O [232], in which $\alpha_{\text{NO}_3^-/\text{H}_2\text{O}}$ was determined to be 1.0215 and 1.0131 at 295 K and 373 K, respectively.

Table 6.3: Calculated $^{18}\alpha_{A/B}$ regression coefficients^a as a function of temperature (150 to 450 K) and $^{18}\alpha_{A/B}$ (298 K) values for O isotopic equilibrium exchange reactions.

A/B	A	B	C	D	$^{18}\alpha_{A/B}(298\text{K})$
NO/NO ₂	-0.04129	1.1605	-1.8829	0.74723	1.0082
NO ₂ /NO ₃	1.03163	-1.38703	0.24875	0.3082	1.0092
N ₂ O ₅ ^{geo} /NO ₂	-0.54136	0.13073	1.2477	-0.1272	1.0096
N ₂ O ₄ /NO ₂	-0.02333	-0.36888	1.0789	-0.00256	1.0106
BrNO ₂ /NO ₂	0.29493	-0.96875	1.5039	-0.02007	1.0130
ClNO ₂ /NO ₂	0.41012	-1.2744	1.7759	-0.01414	1.0152
BrONO ₂ ^t /NO ₂	0.43126	-1.4765	2.1167	-0.06681	1.0166
ClONO ₂ ^t /NO ₂	0.48353	-1.5568	2.1511	-0.04177	1.0176
NO ₃ ⁻ /H ₂ O	3.6280	-8.6540	8.2763	-1.1983	1.0249
H ₂ O/•OH	2.1137	-3.8026	2.5653	0.59410	1.0371

These experimentally determined values agree reasonably well with our calculated values of 1.0256 and 1.0126 at 295 K and 373 K, respectively.

Table 6.3 presents the calculated $^{18}\alpha_{A/B}$ regression fit coefficients for these exchange reactions sorted in order of increasing $^{18}\alpha_{A/B}$ at 298 K. Overall, the calculated $^{18}\alpha_{A/B}$ values ranged from 1.0082 to 1.0371 at 298 K (Table 6.3) and increased in the following order: NO/NO₂ < NO₂/NO₃ < N₂O₅^{geo}/NO₂ < N₂O₄/NO₂ < BrNO₂/NO₂ < ClNO₂/NO₂ < BrONO₂^t/NO₂ < ClONO₂^t/NO₂ < NO₃⁻/H₂O < H₂O/•OH (Table 6.3). This trend indicates that at the most exchangeable sites (i.e. terminal O atoms), ¹⁸O will generally partition into NO_y molecules other than NO and NO₂. This is true for all considered equilibrium exchange reactions except for NO₂/NO₃, in which ¹⁸O is found to prefer NO₂. Additionally, our calculations indicate that the exchange between H₂O/•OH will result in atmospheric •OH depleted in ¹⁸O relative to local H₂O vapor by approximately -35‰ at 298 K.

Fig. 6.3 displays the isotopic equilibrium exchange enrichment factors ($^{18}\epsilon_{A/B} = 1000(^{18}\alpha_{A/B}-1)$) for the following five isotopic equilibrium exchange reactions: NO/NO₂, NO₂/NO₃, N₂O₅^{geo}/NO₂, ClNO₂/NO₂, and ClONO₂^t/NO₂. Generally, as

temperature increases, it is observed that $^{18}\epsilon_{A/B}$ decreases towards zero as expected for equilibrium isotope effects in the high temperature limit. This was the observed trend for all of the considered isotopic exchange reactions except for NO/NO₂, in which $\alpha_{A/B}$ switches from less than 1 to greater than 1 at approximately 152.5 K. Fig. 6.3 also shows $\Delta^{17}\text{O}$ arising from the considered isotopic equilibrium exchange reactions where $\Delta^{17}\text{O}$ was calculated according to the following:

$$\Delta^{17}\text{O}(\text{‰}) = 1000\ln(1 + (^{17}\alpha_{A/B} - 1)) - 0.52 \times 1000\ln(1 + (^{18}\alpha_{A/B} - 1)) \quad (6.9)$$

For the considered exchange reactions, $\Delta^{17}\text{O}$ was found to minimally deviate from 0‰(Fig. 6.3), ranging from 0.02 to 0.18‰(Fig. 6.3) at 298 K.

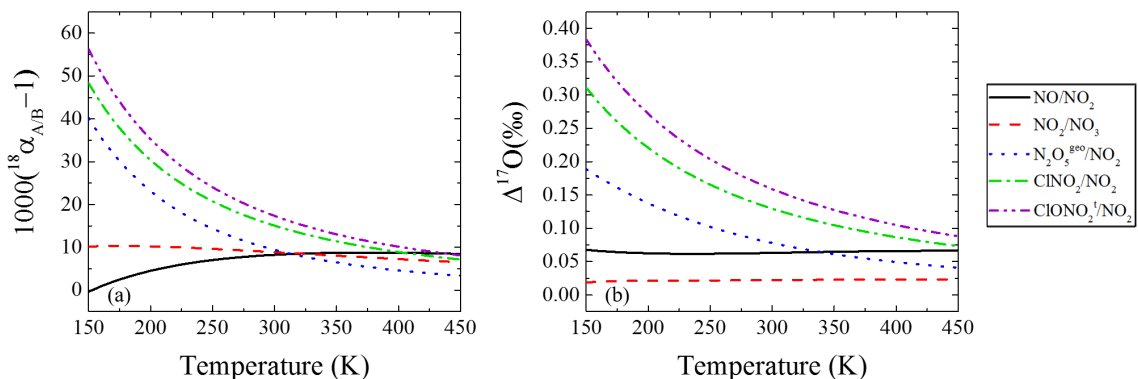


Fig. 6.3.: (a) Calculated O isotopic exchange enrichment factors ($1000(^{18}\alpha_{(A/B)} - 1)$) and (b) calculated O isotopic exchange induced mass-independence ($\Delta^{17}\text{O}(\text{‰}) = 1000\ln(^{17}\alpha_{(A/B)} - 1) - 0.52 \times 1000\ln(^{18}\alpha_{(A/B)} - 1)$) for the following exchange reactions: NO/NO₂, NO₂/NO₃, N₂O₅^{geo}/NO₂, ClNO₂/NO₂, and ClONO₂^t/NO₂.

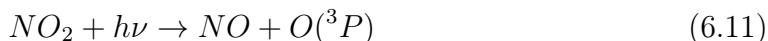
6.4 Discussion

Overall, our $^{18}\alpha_{A/B}$ calculations show that if isotopic equilibrium is achieved, it will influence the partitioning of ^{18}O between the considered molecules, without inducing a

significant $\Delta^{17}\text{O}$ signature, as expected for a MDFP (Fig. 6.3). Therefore, while $\Delta^{17}\text{O}$ of NO_y molecules should approximately represent the O mass-balance of precursor molecules (i.e. O_3 , H_2O , O_2), $\delta^{18}\text{O}$ may reflect both O mass-balance and possible influences from MDFP such as isotopic equilibrium exchange. Thus, $\delta^{18}\text{O}$ of NO_y molecules may provide additional information about NO_x oxidation pathways that is not observable in $\Delta^{17}\text{O}$ alone. Taking into account N and O isotopic mass-balance and assuming daytime isotopic equilibrium between NO and NO_2 [46,52,216,233] and nighttime isotopic equilibrium between NO_2 , NO_3 , and N_2O_5 [190,216,218], $\delta^{18}\text{O}$ - $\delta^{15}\text{N}$ compositions may be estimated for various HNO_3 formation pathways.

6.4.1 Predicted daytime HNO_3 $\delta^{18}\text{O}$ - $\delta^{15}\text{N}$ compositions

During the daytime, NO_x exists in a photochemical steady state in which NO is oxidized to NO_2 , which may photolyze back to NO leading to the production of O_3 [6].



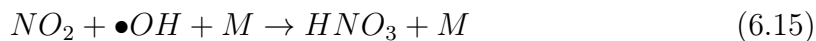
The photochemical cycling between NO- NO_2 - O_3 is rapid, and prior experimental investigations of this cycling has suggested that O isotopic equilibrium is achieved between O_3 and NO_x [55]. Based on a photochemical NO_x - O_3 isotope equilibrium model, $\delta^{18}\text{O}$ - NO_x has been estimated to have a value of $117 \pm 5\%$ relative to VSMOW [55]. While $\delta^{18}\text{O}$ - NO_x is assumed to reflect its photochemical equilibration with O_3 , $\delta^{15}\text{N}$ - NO_x should be related to local NO_x source emissions. Recently, a mass-balance $\delta^{15}\text{N}$ - NO_x model across the contiguous United States has been developed that suggests $\delta^{15}\text{N}$ - NO_x should typically range from -15 to 0‰ [208]. Exceptions include regions dominated by soil emissions (e.g. Great Plains during the summer) or coal-fired power plant emissions, in which $\delta^{15}\text{N}$ - NO_x is estimated to range from -31 to -21‰ and 5 to 9‰, respectively [208].

While the isotopic composition of NO_x is approximately known, the isotopic composition of its components, NO and NO_2 , may be altered relative to NO_x due to isotopic exchange. The rate of isotopic exchange between NO and NO_2 is rapid ($k = 8.14 \times 10^{-14} \text{ cm}^3 \text{ molecules}^{-1} \text{ s}^{-1}$ at 298 K; [192]) and may lead to the partitioning of ^{18}O between NO and NO_2 similar to exchange previously observed for ^{15}N [46,216]. The resulting $\delta^{18}\text{O}$ and $\delta^{15}\text{N}$ of the NO and NO_2 will depend on the fraction of NO and NO_2 relative to the total NO_x (i.e. $[\text{NO}]/[\text{NO}_x]$ and $[\text{NO}_2]/[\text{NO}_x]$) and the temperature dependent equilibrium exchange fractionation factors [46,216]. The impact of this exchange on $\delta^{15}\text{N}$ of NO and NO_2 has been previously derived [46,216], which we have adapted to also include $\delta^{18}\text{O}$, as the following (Eq. 6.13-6.14):

$$\delta^x N\text{-NO}_2(\text{‰}) = 1000 \times \left(\frac{({}^x\alpha_{\text{NO}_2/\text{NO}} - 1)(1 - f_{\text{NO}_2})}{(1 - f_{\text{NO}_2}) + ({}^x\alpha_{\text{NO}_2/\text{NO}} \times f_{\text{NO}_2})} \right) + \delta^x\text{-NO}_x \quad (6.13)$$

$$\delta^x\text{-NO}(\text{‰}) = \frac{(\delta^x\text{-NO}_x(\text{‰})) - (f_{\text{NO}_2} \times \delta^x\text{-NO}_2(\text{‰}))}{(1 - f_{\text{NO}_2})} \quad (6.14)$$

where x represents either ^{18}O or ^{15}N and f_{NO_2} is the fraction of NO_2 to the total NO_x . During the daytime, near equal concentrations of NO and NO_2 can occur [52,216] due to the emission of NO [204] and NO_2 photolysis [6]. Therefore, during the daytime, $\delta^{18}\text{O}$ and $\delta^{15}\text{N}$ of NO and NO_2 will likely reflect a complex function of the $\delta^{18}\text{O}$ and $\delta^{15}\text{N}$ of NO_x and the NO_x equilibrium isotopic fractionation factors. If the isotopic composition of daytime NO_2 is altered relative to NO_x , it would have important consequences for $\delta^{18}\text{O}$ and $\delta^{15}\text{N}$ of atmospheric nitrate produced during daylight hours, because it is primarily formed through the reaction between NO_2 and photochemically produced $\bullet\text{OH}$:



We will refer to HNO_3 produced through R4 as $\text{HNO}_3(1)$ in the following discussion. Assuming no kinetic isotope fractionation associated with 6.15 (this will be discussed in a forth coming paper), the δ^x of $\text{HNO}_3(1)$ can be calculated using mass-balance as the following (Eq. 6.16 - 6.17):

$$\delta^{15}\text{N-HNO}_3(1)(\text{‰}) = \delta^{15}\text{N-NO}_2(\text{‰}) \quad (6.16)$$

$$\delta^{18}O\text{-}HNO_3(1)(\text{‰}) = \frac{2}{3}(\delta^{18}O\text{-}NO_2(\text{‰})) + \frac{1}{3}(\delta^{18}O\text{-}\bullet OH(\text{‰})) \quad (6.17)$$

This model indicates that the N and O isotopic composition of $HNO_3(1)$ can be approximately calculated if $\delta^x\text{-}NO_2$ and $\delta^{18}O\text{-}\bullet OH$ are known. Using this proposed model, we calculated daytime $\delta^{15}N\text{-}NO_2$ according to Eq. 6.13 assuming local $\delta^{15}N\text{-}NO_x$ to range from -15 to 0‰ [208] and using N isotopic exchange fractionation factors for NO_2/NO from our previous study [101]. These NO_2/NO exchange fractionation factors were adapted to include corrections for ZPE anharmonicity (adapted β and α values can be found in the Appendix). Predicted daytime $\delta^{18}O\text{-}NO_2$ values, relative to VSMOW, were calculated from Eq. 6.13 assuming $\delta^{18}O\text{-}NO_x$ to range from 112 to 122‰ [55] and using O isotopic NO_2/NO exchange fractionation factors calculated in this study. The $\delta^{18}O$ of $\bullet OH$ should to a first order approximation reflect the $\delta^{18}O$ of local water vapor and the temperature dependent fractionation factor associated with equilibrium $\bullet OH/H_2O$ exchange, since the atmospheric concentration of $\bullet OH$ is orders of magnitude lower than H_2O . (Eq. 6.18):

$$\delta^{18}O\text{-}\bullet OH(\text{‰}) = \delta^{18}O\text{-}H_2O(\text{‰}) + 1000(\alpha_{\bullet OH/H_2O} - 1) \quad (6.18)$$

Therefore, $\delta^{18}O$ of $\bullet OH$ can be approximated using an estimated tropospheric water vapor $\delta^{18}O$ range of -25 to 0‰ (typical for mid-latitudes) [30] and O isotopic $\bullet OH/H_2O$ exchange fractionation factors calculated in this study.

The predicted $\delta^{18}O\text{-}\delta^{15}N$ ranges of NO , NO_2 , and $HNO_3(1)$ at 300 K with $f_{NO_2} = 0.70$ exhibit significant variation (Fig. 6.4). The $\delta^{15}N$ of $HNO_3(1)$ and NO_2 are calculated to range from -4.2 to 10.8‰, while $\delta^{15}N$ of NO is calculated to range from -40.2 to -25.2‰. The positive shift in $\delta^{15}N$ of $HNO_3(1)$ and NO_2 and the negative shift in $\delta^{15}N$ of NO relative to the assumed $\delta^{15}N\text{-}NO_x$ value (-15 to 0‰) is a direct result of the N isotopic exchange between NO and NO_2 that favors the partitioning of ^{15}N into NO_2 ($^{15}\alpha_{NO_2/NO} = 1.0370$ at 300 K). The $\delta^{18}O$ of NO , NO_2 , and $HNO_3(1)$ are estimated to range from 115.3 to 125.3‰, 109.5 to 119.5‰, and 52.8 to 67.8‰ at 300 K (Fig. 6.4). The positive shift in $\delta^{18}O$ of NO and negative shift in NO_2 relative to the assumed initial $\delta^{18}O\text{-}NO_x$ (112 to 122‰) is a result of their O isotopic

exchange that favors the formation of ^{18}O in NO ($^{18}\alpha_{\text{NO}_2/\text{NO}} = 0.992$ at 300 K). The estimated $\delta^{18}\text{O}$ - $\text{HNO}_3(1)$ shift of -56.7% relative to NO_2 is a result of the 1/3 O contribution from $\bullet\text{OH}$ that is predicted to have a $\delta^{18}\text{O}$ range of -60.5 to -35% due to its equilibration with H_2O at 300 K ($^{18}\alpha_{\bullet\text{OH}/\text{H}_2\text{O}} = 0.9645$ at 300 K).

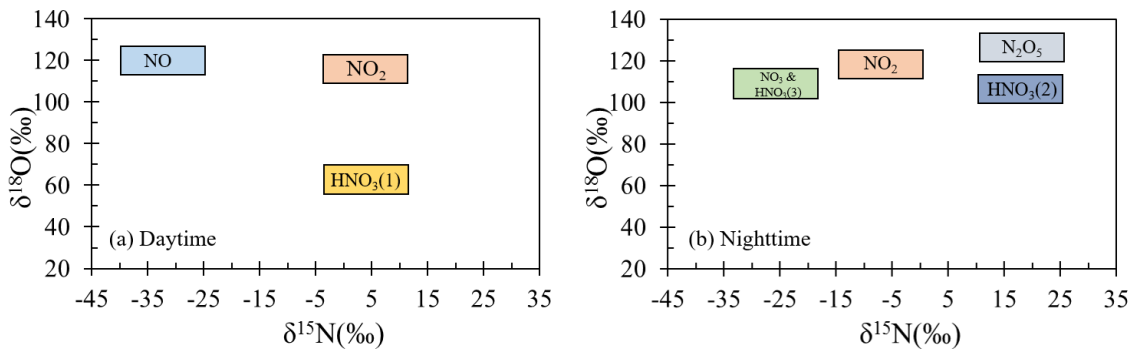


Fig. 6.4.: Estimated $\delta^{18}\text{O}$ - $\delta^{15}\text{N}$ compositions of several NO_y molecules assuming (a) daytime isotopic equilibrium between NO/NO_2 with $f_{\text{NO}_2} = 0.7$ and (b) nighttime isotopic equilibrium between NO_2 , NO_3 , and N_2O_5 . Where $\text{HNO}_3(1)$, $\text{HNO}_3(2)$, and $\text{HNO}_3(3)$ represent various HNO_3 production pathways that include $\text{NO}_2 + \bullet\text{OH} \rightarrow \text{HNO}_3(1)$, $\text{N}_2\text{O}_5 + \text{H}_2\text{O} + \text{surface} \rightarrow 2\text{HNO}_3(2)$, and $\text{NO}_3 + \text{R} \rightarrow \text{HNO}_3(3) + \text{R}\bullet$.

The impact of varying f_{NO_2} values on NO and NO_2 isotopic exchange and its influence on $\delta^{15}\text{N}$ and $\delta^{18}\text{O}$ of NO, NO_2 , and $\text{HNO}_3(1)$ are displayed in Table 6.4. Generally, it is observed that $\delta^{15}\text{N}$ is highly sensitive to f_{NO_2} , but $\delta^{18}\text{O}$ is not. For example, from $f_{\text{NO}_2} = 1$ to $f_{\text{NO}_2} = 0.55$, the shift in $\delta^{15}\text{N}$ of NO_2 and $\text{HNO}_3(1)$ is 16.3% , while the change in $\delta^{18}\text{O}$ of NO_2 and $\text{HNO}_3(2)$ is -3.8% and -2.5% , respectively (Table 6.4). The degree of sensitivity of $\delta^{15}\text{N}$ and $\delta^{18}\text{O}$ in $\text{HNO}_3(1)$ to f_{NO_2} is a result of the magnitude of the NO_2/NO equilibrium fractionation factors, in which N fractionation is fairly large ($^{15}\alpha_{\text{NO}_2/\text{NO}} = 1.0370$ at 300 K), while O fractionation is relatively minor ($^{18}\alpha_{\text{NO}_2/\text{NO}} = 0.992$ at 300 K). This isotope equilibrium mechanism predicts that $\delta^{15}\text{N}$ - $\text{HNO}_3(1)$ will be sensitive to diurnal fluctuations in f_{NO_2} , which is a phenomenon that has been previously observed [52]. Additionally, this mechanism

Table 6.4: Shift in $\delta^{15}\text{N}$ and $\delta^{18}\text{O}$ of NO , NO_2 , and $\text{HNO}_3(1)$ relative to NO_x as a function of f_{NO_2} .

f_{NO_2}	$\delta^{15}\text{N}$ - NO	$\delta^{18}\text{O}$ - NO	$\delta^{15}\text{N}$ - NO_2	$\delta^{18}\text{O}$ - NO_2	$\delta^{15}\text{N}$ - $\text{HNO}_3(1)$	$\delta^{18}\text{O}$ - $\text{HNO}_3(1)$
1	–	–	0	0	0	-57.5
0.85	-30.5	7.0	5.4	-1.2	5.4	-58.3
0.70	-25.3	5.8	10.8	-2.5	10.8	-59.2
0.55	-19.9	4.7	16.3	-3.8	16.3	-60.1

indicates that since O fractionation between NO and NO_2 is relatively minor, $\delta^{18}\text{O}$ - $\text{HNO}_3(1)$ is approximately equal to the O isotope mass-balance between NO_x - O_3 (in photochemical equilibrium) and $\bullet\text{OH}$.

In addition to f_{NO_2} dependence, the isotopic composition of $\text{HNO}_3(1)$ will also have a temperature dependence that is related to the temperature dependent $\alpha_{\text{NO}_2/\text{NO}}$ and $\alpha_{\bullet\text{OH}/\text{H}_2\text{O}}$ values. As temperature decreases, $^{15}\alpha_{\text{NO}_2/\text{NO}}$ increases [101, 216], and this will result in $\text{HNO}_3(1)$ having a higher $\delta^{15}\text{N}$ value relative to the $\delta^{15}\text{N}$ - NO_x for a fixed f_{NO_2} value. Additionally, while $^{18}\alpha_{\text{NO}_2/\text{NO}}$ is relatively insensitive to temperature (Fig. 6.2), $^{18}\alpha_{\bullet\text{OH}/\text{H}_2\text{O}}$ values change significantly with temperature (i.e. $^{18}\alpha_{\bullet\text{OH}/\text{H}_2\text{O}} = 0.9494$ and 0.9682 at 220 K and 330 K, respectively). Therefore, the $\delta^{18}\text{O}$ - $\text{HNO}_3(1)$ formed at lower temperatures will have a lower $\delta^{18}\text{O}$ that is primarily the result of the temperature dependence of isotopic exchange between $\bullet\text{OH}$ and H_2O for a fixed $\delta^{18}\text{O}$ - H_2O . Overall, while it is difficult to predict the exact range of $\delta^{18}\text{O}$ - $\delta^{15}\text{N}$ compositions of $\text{HNO}_3(1)$ due to its numerous dependences, the proposed mechanism predicts that $\delta^{15}\text{N}$ - $\text{HNO}_3(1)$ should reflect $\delta^{15}\text{N}$ - NO_2 , which should be slightly higher than $\delta^{15}\text{N}$ - NO_x ; however, $\delta^{18}\text{O}$ - $\text{HNO}_3(1)$ should be lower than $\delta^{18}\text{O}$ - NO_2 as a result of the O isotopic mass-balance between NO_2 and $\bullet\text{OH}$.

6.4.2 Predicted nighttime HNO_3 $\delta^{18}\text{O}$ - $\delta^{15}\text{N}$ space

During the nighttime, higher N oxides form and new pathways of HNO_3 production become important due to the absence of photochemically produced $\bullet\text{OH}$. Under these conditions, NO_2 is oxidized by O_3 forming the NO_3 radical (6.19), which exists at thermal equilibrium with NO_2 and N_2O_5 [234] (6.20). Subsequent hydrolysis of N_2O_5 on a wetted surface forms HNO_3 (6.21).



This HNO_3 formation pathway is typically most prevalent during the winter when N_2O_5 is thermally stable [10,235]. Nighttime HNO_3 may also form through hydrogen abstraction from organic compounds (R) by NO_3 :



Since photochemical cycling of NO_x shuts down during the night, nearly all NO_x exists as NO_2 . Thus, $\delta^x\text{-NO}_x$ is approximately equal to $\delta^x\text{-NO}_2$ as isotopic exchange between NO and NO_2 ceases [46,216]. However, isotopic equilibrium between NO_2 , NO_3 , and N_2O_5 is likely to be achieved mirroring its rapid chemical equilibrium rate (lifetime of 1 to 2 minutes; [190,218], which will have an impact on $\delta^{18}\text{O}$ and $\delta^{15}\text{N}$ of atmospheric nitrate produced during the night. Generally, the tropospheric concentrations of $[\text{NO}_2] \gg [\text{N}_2\text{O}_5] \geq [\text{NO}_3]$, as NO_2 is typically on the order of ppb while N_2O_5 and NO_3 are on the order of ppt (e.g. [235]). Therefore, in most cases the isotopic composition of N_2O_5 and NO_3 should reflect the exchange α 's with respect to NO_2 (i.e. $\alpha_{\text{N}_2\text{O}_5/\text{NO}_2}$ and $\alpha_{\text{NO}_3/\text{NO}_2}$) and can be determined from the following:

$$\delta^x\text{-N}_2\text{O}_5(\text{‰}) = \delta^x\text{-NO}_2(\text{‰}) + 1000 \times ({}^x\alpha_{\text{N}_2\text{O}_5/\text{NO}_2} - 1) \quad (6.23)$$

$$\delta^x\text{-NO}_3(\text{‰}) = \delta^x\text{-NO}_2(\text{‰}) + 1000 \times ({}^x\alpha_{\text{NO}_3/\text{NO}_2} - 1) \quad (6.24)$$

Assuming a negligible kinetic isotopic fractionation associated with 6.21, the isotopic composition of atmospheric nitrate produced through N_2O_5 hydrolysis, which we will refer to as $HNO_3(2)$, can be estimated from $\delta^x-N_2O_5$ and O isotopic mass-balance, our calculated exchange fractionation factors, and using an estimated $\delta^{18}O-H_2O$ range from -25 to 0‰.

$$\delta^{15}N-HNO_3(2)(\text{‰}) = \delta^{15}N-N_2O_5(\text{‰}) \quad (6.25)$$

$$\delta^{18}O-HNO_3(2)(\text{‰}) = \frac{5}{6}(\delta^{18}O-N_2O_5(\text{‰})) + \frac{1}{6}(\delta^{18}O-H_2O(\text{‰})) \quad (6.26)$$

Assuming this model, N_2O_5 and $HNO_3(2)$ have an estimated $\delta^{15}N$ range of 10.5 to 25.5‰ (Fig. 6.4), which is approximately 25.5‰ higher than NO_x as a result of the N_2O_5/NO_2 exchange ($^{15}\alpha_{N_2O_5/NO_2} = 1.0255$ at 300 K). $\delta^{18}O-N_2O_5$ is estimated to range from 121.4 to 131.4‰ (Fig. 6.4), as a result of the O isotopic exchange between N_2O_5/NO_2 ($^{18}\alpha_{N_2O_5/NO_2} = 1.0094$ at 300 K). Assuming O mass-balance between N_2O_5 and H_2O (Eq. 18), $\delta^{18}O-HNO_3(2)$ is predicted to range from 97.0 to 109.5 ‰ at 300 K. As temperatures decrease, the N and O fractionation from the N_2O_5/NO_2 isotopic exchange will increase, and this should result in higher $\delta^x-N_2O_5$ relative to the local NO_x .

Nitrate produced at night formed through the NO_3 hydrogen abstraction pathway, which we will refer to as $HNO_3(3)$, will have an O and N isotopic composition that is equal to the isotopic composition of NO_3 , assuming isotopic mass-balance and neglecting any kinetic isotopic fractionation associated with 6.22:

$$\delta^{15}N-HNO_3(3)(\text{‰}) = \delta^{15}N-NO_3(\text{‰}) \quad (6.27)$$

$$\delta^{18}O-HNO_3(3)(\text{‰}) = \delta^{18}O-NO_3(\text{‰}) \quad (6.28)$$

Assuming this isotopic mechanism, $\delta^{15}N$ of NO_3 and $HNO_3(3)$ are estimated to range from -33.1 to -18.1‰, which is approximately 18.4‰ lower than the $\delta^{15}N-NO_2$ (Fig. 6.4). Additionally, $\delta^{18}O$ of NO_3 and $HNO_3(3)$ is estimated to range from 102.9 to 112.9‰, which is approximately 9.7‰ lower than $\delta^{18}O-NO_2$ (Fig. 6.4). Both $\delta^{15}N$

and $\delta^{18}\text{O}$ are lower in $\text{HNO}_3(3)$ relative to NO_2 due to isotopic exchange between NO_3 and NO_2 that favors both ^{15}N and ^{18}O partitioning in NO_2 ($^{15}\alpha_{\text{NO}_3/\text{NO}_2} = 0.9819$ and $^{18}\alpha_{\text{NO}_3/\text{NO}_2} = 0.9901$ at 300 K). Our calculations indicate that as temperatures decrease, both the N and O fractionation resulting from the NO_3/NO_2 isotopic exchange will increase, which will result in higher $\delta^x\text{-HNO}_3(3)$ values.

It is important to note the uncertainty in the calculated $^x\beta$ of NO_3 that is related to the computational difficulties of NO_3 as previously discussed [172,173]. B3LYP/cc-pVTZ, EDF2/cc-pVTZ, and QCISD/cc-pVDZ models yielded $^{18}\beta$ within 3.8‰ at 300 K (Fig. 6.2) indicating general agreement. However, these methods found a wider range in $^{15}\beta$, from 1.0715 to 1.0864 at 300 K, indicating a disagreement as high as 14.9‰. Despite the uncertainty in $^{15}\beta$ of NO_3 , all of the considered computational methods indicate that the $^{15}\beta$ values of NO_3 are less than those of NO_2 (i.e. $^{15}\alpha_{\text{NO}_3/\text{NO}_2} < 1$). Therefore, while the actual $^{15}\beta$ values of NO_3 are somewhat uncertain, our calculations indicate that NO_3 should have lower $\delta^{15}\text{N}$ relative to NO_2 . In our calculations, we have used NO_3 $^{15}\beta$ and $^{18}\beta$ values calculated using EDF2/cc-pVTZ, because vibrational frequencies calculated with this method are in closer agreement with experimental data [229–231] (Table 6.1).

6.4.3 Implications of $\delta^{18}\text{O}$ - $\delta^{15}\text{N}$ compositions in HNO_3

Assuming the same range of starting N and O isotopic compositions of NO_x ($\delta^{15}\text{N-NO}_x$: -15 to 0‰, $\delta^{18}\text{O-NO}_x$: 112 to 122‰), our calculations suggest that different HNO_3 formation pathways yield relatively distinctive $\delta^{18}\text{O}$ - $\delta^{15}\text{N}$ compositions (Fig. 6.5). Our calculations indicate that $\text{HNO}_3(1)$ should result in the lowest $\delta^{18}\text{O}$ values and mid-ranged $\delta^{15}\text{N}$ values. Our model predicts that $\text{HNO}_3(2)$ and $\text{HNO}_3(3)$ should have high $\delta^{18}\text{O}$ values that are similar. However, $\text{HNO}_3(2)$ has the highest predicted $\delta^{15}\text{N}$ values, while $\text{HNO}_3(3)$ has the lowest $\delta^{15}\text{N}$ values. This suggests that $\delta^{18}\text{O}$ - $\delta^{15}\text{N}$ arrays for different HNO_3 production pathways can be used as isotopic end-

members in isotope mixing models that might explain ^{15}N and ^{18}O values observed in atmospheric nitrate.

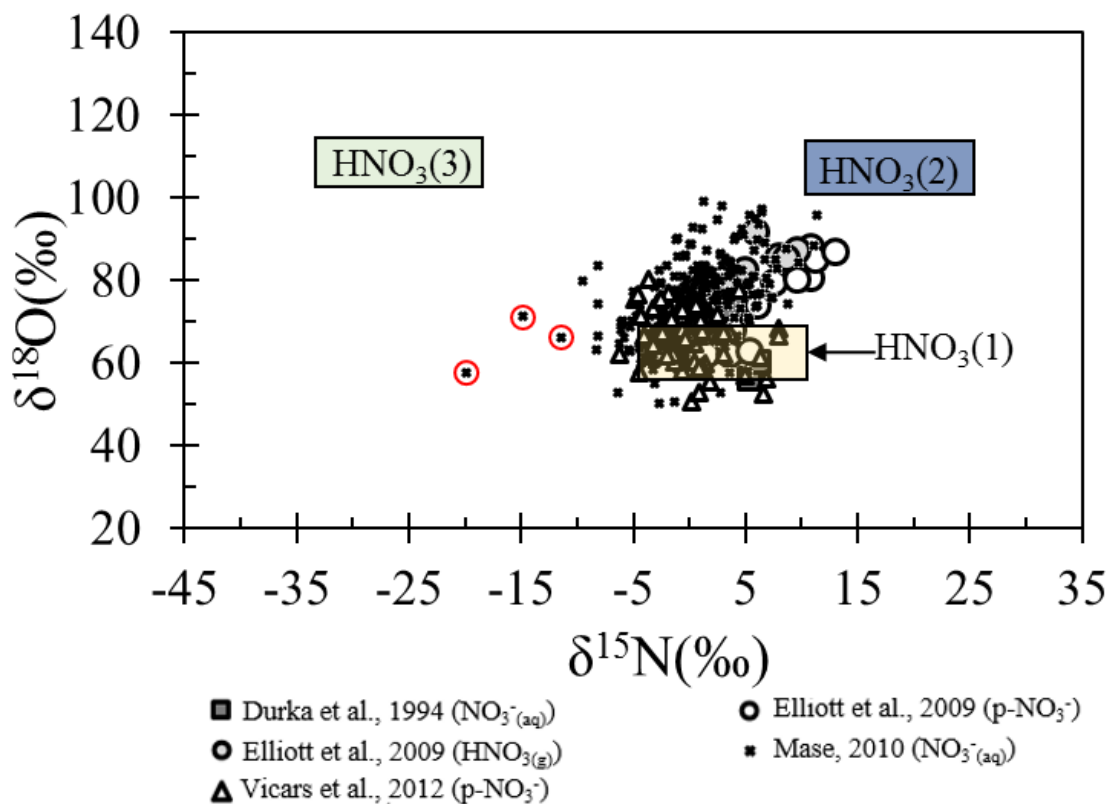


Fig. 6.5.: Predicted $\delta^{18}\text{O}$ - $\delta^{15}\text{N}$ compositions for three major HNO_3 production pathways that is compared with previous atmospheric nitrate measurements [28,49,51,52]. Where $\text{HNO}_3(1)$, $\text{HNO}_3(2)$, and $\text{HNO}_3(3)$ represent various HNO_3 production pathways that include $\text{NO}_2 + \bullet\text{OH} \rightarrow \text{HNO}_3(1)$, $\text{N}_2\text{O}_5 + \text{H}_2\text{O} + \text{surface} \rightarrow 2\text{HNO}_3(2)$, and $\text{NO}_3 + \text{R} \rightarrow \text{HNO}_3(3) + \text{R}\bullet$. The data points within the red circles are outside of the predicted equilibrium $\delta^{18}\text{O}$ - $\delta^{15}\text{N}$ space, which may indicate a NO_x source with an extremely low $\delta^{15}\text{N}$ value such as soil denitrification.

These predicted $\delta^{15}\text{N}$ and ^{18}O isotopic end-members were compared with measured $\delta^{18}\text{O}$ - $\delta^{15}\text{N}$ values of atmospheric nitrates (Fig. 6.5), including $\text{HNO}_3(\text{g})$ [28], p-NO_3^- [28,49,52] and $\text{NO}_3^-_{(\text{aq})}$ [51]. The measured $\delta^{18}\text{O}$ - $\delta^{15}\text{N}$ values in atmospheric

nitrate plot between the two major HNO_3 formation pathways $\text{HNO}_3(1)$ and $\text{HNO}_3(2)$ predicted by this equilibrium model (Fig. 6.5). However, some of the reported $\delta^{18}\text{O}$ - $\delta^{15}\text{N}$ values appear to represent a mixture of $\text{HNO}_3(1)$ and $\text{HNO}_3(3)$, which is most likely to occur for areas with high DMS/VOC concentrations such as marine and forest ecosystems [236]. Our predicted $\delta^{18}\text{O}$ - $\delta^{15}\text{N}$ compositions may explain both the $\delta^{18}\text{O}$ and $\delta^{15}\text{N}$ seasonal cycling typically observed in atmospheric nitrate, in which $\delta^{18}\text{O}$ and $\delta^{15}\text{N}$ values are highest in the winter and lowest during the summer [28,31,49,50,190]. During winter, the $\text{HNO}_3(2)$ pathway is generally most prominent [10,235], and our calculations suggest that this pathway results in high $\delta^{18}\text{O}$ and $\delta^{15}\text{N}$ values. During summer, the $\text{HNO}_3(1)$ pathway is generally most prominent due to the higher concentrations of photochemically produced $\bullet\text{OH}$ [10], and our calculations suggest this pathway will result in $\delta^{15}\text{N}$ and $\delta^{18}\text{O}$ values lower than those for the $\text{HNO}_3(2)$ pathway.

While $\delta^{18}\text{O}$ and $\Delta^{17}\text{O}$ of atmospheric nitrate has been previously linked to NO_x oxidation pathways [30,53,210], our calculations suggest that $\delta^{15}\text{N}$ may also be linked to oxidation chemistry. However, seasonal changes in $\delta^{15}\text{N}$ of atmospheric nitrate will also be impacted by changes in seasonal emissions of NO_x by a variety of processes, particularly NO emitted by nitrification and denitrification occurring in soils. In areas where NO_x emissions should not change seasonally, such as areas dominated by fossil-fuel combustion, any observed seasonal change in $\delta^{15}\text{N}$ of atmospheric nitrate suggests seasonal changes in NO_x oxidation chemistry. In areas in which NO_x emissions exhibit a large seasonal change, such as agricultural regions, the $\delta^{15}\text{N}$ of atmospheric nitrate will be a function of both the seasonal change in $\delta^{15}\text{N}$ - NO_x and in the NO_x oxidation equilibrium isotope effect. The equilibrium model indicates that it may be difficult to partition NO_x sources solely from $\delta^{15}\text{N}$ - HNO_3 values, since the $\delta^{15}\text{N}$ tends to be sensitive to equilibrium effects that may alter the original NO_x source $\delta^{15}\text{N}$ value as it is oxidized to HNO_3 (Fig. 6.4). However, evaluation of $\delta^{15}\text{N}$ - $\delta^{18}\text{O}$ space of atmospheric nitrate may help elucidate NO_x emission sources in some cases. Atmospheric nitrate outside of the calculated $\delta^{18}\text{O}$ - $\delta^{15}\text{N}$ compositional range might

indicate its NO_x precursor had a distinctive $\delta^{15}\text{N}$ outside of the typical range of -15 to 0‰. For example, soil denitrification events, which are estimated to have a low $\delta^{15}\text{N}$ - NO_x (approximately between -50 to -20‰; [39, 41, 42]) may be trackable with atmospheric nitrate $\delta^{18}\text{O}$ - $\delta^{15}\text{N}$ measurements. If emitted NO_x is oxidized through the $\text{HNO}_3(1)$ pathway, it should have low $\delta^{15}\text{N}$ and $\delta^{18}\text{O}$, which does not match the equilibrium predictions (Fig. 6.5). This sort of event may explain why a few of the atmospheric nitrate measurements from ref [49] is outside of the general predicted HNO_3 formation $\delta^{18}\text{O}$ - $\delta^{15}\text{N}$ range (Fig. 6.5). These rainwater nitrates were collected at N deposition sites after a storm saturated recently fertilized agricultural fields in the Midwestern U.S., suggesting NO produced by nitrification/denitrification.

While our predicted equilibrium $\delta^{18}\text{O}$ - $\delta^{15}\text{N}$ compositions generally agrees with atmospheric nitrate measurements [28, 49, 51, 52], it is important to point out the simplicity of our model. Primarily, we have ignored any kinetic isotope effects. If equilibrium between NO_2 , NO_3 , and N_2O_5 is achieved, kinetic isotope effects associated with the formation of NO_3 and N_2O_5 should be erased. However, kinetic isotopic effects will need to be considered for the photochemical cycling of NO_x , that includes NO_2 photolysis and NO oxidation, as these MDFPs are predicted to have an impact on the N and O isotopic composition of NO_2 [216], which may then be propagated into NO_y molecules. Additionally, we will need to determine kinetic isotope fractionation factors for the final step in forming atmospheric nitrate (i.e. 6.15, 6.21, 6.22), which may play an important role in its N and O isotopic composition. Our equilibrium model suggests that the isotopic composition of NO_2 drives the isotopic composition of atmospheric nitrate indicating the need for future *in situ* isotopic measurements of NO_2 . Determination of NO_x photochemical cycling fractionation factors, isotopic *in situ* measurements of NO_2 , and kinetic isotopic modeling of NO_x oxidation will be the subject for future research.

6.5 Conclusions

Hybrid density functional theory calculations indicate that oxygen equilibrium isotopic exchange involving NO_y molecules generally favors the formation ^{18}O in NO_y molecules other than NO and NO_2 at the most likely O exchange sites. Therefore, equilibrium isotope exchange may play a role in the $\delta^{18}\text{O}$ of atmospheric nitrate in addition to the O isotopic mass-balance of its precursor molecules and oxidants. A simple equilibrium and mass-balance model indicates that the three major HNO_3 formation pathways may have unique $\delta^{18}\text{O}$ - $\delta^{15}\text{N}$ compositions. This model generally predicts a range of $\delta^{18}\text{O}$ - $\delta^{15}\text{N}$ values consistent with HNO_3 measurements and suggests that $\delta^{18}\text{O}$ - $\delta^{15}\text{N}$ space of atmospheric nitrate may provide useful information about the conditions of NO_x oxidation pathways. This model may explain the seasonal changes typically observed in both $\delta^{18}\text{O}$ and $\delta^{15}\text{N}$ of atmospheric nitrate.

7. *AB INITIO* STUDY OF NITROGEN AND POSITION-SPECIFIC OXYGEN KINETIC ISOTOPE EFFECTS IN THE NO + O₃ REACTION

The following chapter is a reprint from an article currently in press (Walters, W. W.; Michalski, G. *Ab initio* study of nitrogen and position-specific oxygen kinetic isotope effects in the NO + O₃ reaction, *J. Chem. Phys.*).

7.1 Introduction

Nitrogen oxides (NO_x = NO + NO₂) are important trace gases that influence the concentrations of atmospheric oxidants that drive tropospheric and stratospheric chemistry [1–3,6]. During the daytime, NO_x exists in a closed photochemical cycle between NO-O₂-O₃-NO₂ in the atmosphere, known as the Leighton Cycle [6,7]. This cycle is initiated when NO₂ is photolyzed by UV-visible light in the blue region of the spectrum (< 400 nm) yielding O(³P) the ground state of the oxygen atom. This liberated oxygen atom can combine with O₂ to form O₃, which then oxidizes NO back to NO₂ [6,7] (7.1-7.4):



The analysis of the oxygen and nitrogen stable isotopes of NO_x and its oxidation product, atmospheric nitrate, may help in our understanding of this photochemical cycling [30,53–56] and sources of NO_x [33,45,208]. Variations in oxygen and nitrogen isotope compositions are reported using δ(‰) notation where δ^xO(‰) and δ¹⁵N(‰)

$= (R_{\text{sample}}/R_{\text{ref}} - 1) \times 1000$, where R_{sample} and R_{ref} denote the $^x\text{O}/^{16}\text{O}$ ($x = 17$ or 18) or $^{15}\text{N}/^{14}\text{N}$ in the sample or reference, respectively. The oxygen isotopic reference is Vienna Standard Mean Ocean Water (VSMOW) and the nitrogen isotopic reference is atmospheric air. However, $\delta^{18}\text{O}$ and $\delta^{15}\text{N}$ of NO_x may also be influenced by isotopic fractionation processes associated with the Leighton cycle, [46, 216], which may be propagated into atmospheric nitrate [216], yet few of these fractionation factors have been determined.

The photochemical cycling of NO_x is rapid, and prior experimental investigations of this cycling has suggested that isotopic equilibrium is achieved between O_3 and NO_x , erasing any original O isotopic NO_x signatures [55]. Several studies have shown that atmospheric O_3 has an elevated $\delta^{18}\text{O}$ and a strong mass-independent component that is quantified by $\Delta^{17}\text{O}$ notation [48, 57, 58, 212, 213, 237]:

$$\Delta^{17}\text{O}(\text{‰}) = 1000 \ln \left(1 + \frac{\delta^{17}\text{O}}{1000} \right) - 0.52 \times 1000 \ln \left(1 + \frac{\delta^{18}\text{O}}{1000} \right) \quad (7.5)$$

In Eq. 7.5 the λ is mass-dependent coefficient, which may be approximated as 0.52 [238]. During the photochemical cycling of NO_x , these elevated $\delta^{18}\text{O}$ and $\Delta^{17}\text{O}$ signatures of O_3 are transferred to NO_x as a result of 7.4 [55, 56, 209]. While $\Delta^{17}\text{O}$ of the transferred O atom from O_3 to NO_2 should be minimally impacted, $\delta^{18}\text{O}$ may be significantly altered as a result of the mass-dependent fractionation associated with the kinetic isotope effect of 7.4. Thus, the kinetic isotope effect associated with 7.4 may play an important role on the $\delta^{18}\text{O}$ of NO_x , which may be propagated into atmospheric nitrate, yet this fractionation factor is relatively unknown.

The kinetic isotope effect associated with R4 may also play an important role on the $\delta^{15}\text{N}$ of NO_2 . Previously, $\delta^{15}\text{N}$ of NO_x and atmospheric nitrate has been suggested to provide information about NO_x sources [27, 28, 32, 190]. Numerous studies have quantified $\delta^{15}\text{N}$ from various NO_x sources, and these results indicate that soil emission (denitrification), transportation related sectors, and coal-fired power plants have relatively distinctive $\delta^{15}\text{N}$ values [32, 33, 35, 39–43, 45, 100, 208]. These works have motivated several $\delta^{15}\text{N}$ studies of atmospheric nitrate as a way to partition NO_x

sources to evaluate local/regional changes in NO_x source budgets [27, 28, 112]. However, the isotopic fractionation processes associated with the photochemical cycling of NO_x such as 7.4, NO_2 photolysis, and NO_x isotopic exchange may alter the N isotopic composition of NO and NO_2 relative to total NO_x [216]; however, except for NO_x isotope exchange, these fractionation processes' impact on $\delta^{15}\text{N}$ is relatively unknown [216]. If these fractionation processes are significant, daytime $\delta^{15}\text{N}\text{-NO}_2$ may not equal $\delta^{15}\text{N}\text{-NO}_x$ [216, 217], which has important implications for atmospheric nitrate formed during the daytime, because it is primarily formed through the reaction between NO_2 and photochemically produced $\bullet\text{OH}$ [10]. Therefore, it is important to understand the kinetic isotope effect associated with 7.4 and its implications for $\delta^{15}\text{N}$ of daytime produced atmospheric nitrate.

Bigeleisen demonstrated kinetic isotope effects (KIEs) could be approximated for reactions such as 7.4 using transition state theory if the vibrational frequencies of the reactants and transition state are known [239]. Unfortunately, transition state frequencies for many isotopologues in NO_x related reactions, such as 7.4, are unknown. Previously, *ab initio* methods have been used to calculate the reaction mechanism, thermochemistry, and vibrational frequencies of [240], but only for the main isotopologues. The present study builds on Ref. [240] by employing *ab initio* methods to calculate nitrogen and position-specific oxygen KIEs associated with 7.4. This will allow for an understanding of the impact 7.4 has on the $\delta^{18}\text{O}$ value of the transferred O atom from O_3 to NO and on $\delta^{15}\text{N}$ as NO is oxidized to NO_2 .

7.2 Methods

The assumed reaction mechanism of 7.4 is shown in Fig. 7.1, which is based on the results from Ref. [240]. In this previous study, geometries and vibrational frequencies for all stationary points along the PES have been calculated by UHF, UMP2 and UMP4 methods with the 6-31G(d), 6-311G(d), and 6-311G(d,f) basis sets [240]. Unfortunately the UMP2 and UMP4 levels predicted anomalous vibra-

tional frequencies for the radicals NO and NO₂ due to spin contamination and for O₃ due to its multireference character [240]. These inaccurate vibrational frequencies will have a significant impact on the accuracy of the calculated KIEs. Therefore, we have recalculated the geometries for a portion of the potential energy surface (PES) that included the reactants, products, and rate-determining transition state, which has been previously determined to be the NO radical approach to O₃ (**TS1**, Fig. 7.1) [240], using the high-level quantum mechanical method CCSD(T) with the 6-31G(d) and 6-311G(d) basis sets. The reactants and products geometry optimizations were carried out using default convergence criteria, while TS1 was optimized from calculated force constants at the previously reported UMP2(full)/6-31G(d) geometry [240]. Vibrational frequency analysis was performed to confirm that the obtained structures are stationary points along the PES that correspond to either a local minimum (3n-6 or 3n-5 real normal modes of vibration) or a transition state (exactly one imaginary frequency). Systematic model errors in the calculated harmonic frequencies have been accounted for by applying a constant scale factor of 0.9899 and 0.9542 for CCSD(T)/6-31G(d) and CCSD(T)/6-311G(d), respectively. All calculations were performed with the Gaussian09 program package revision D.01 [226] on the Purdue Radon cluster.

Nitrogen and position-specific oxygen KIEs were calculated in accordance with the Born-Oppenheimer, rigid-rotor and harmonic approximations, using the complete Bigeleisen equations [239] as implemented in the ISOEFF program [241] at 220, 250, 273, 298, and 320 K. Both the Bigeleisen equations and the ISOEFF program define the calculated KIE as the ratio of reaction coefficients of the light to heavy isotope. However, since we are interested in the relative rate of the heavy to light isotope, we report all calculated KIEs as the ratio of the heavy to the light isotope (Eq. 7.6):

$$KIE = \alpha = \frac{k_H}{k_L} \quad (7.6)$$

where α is the calculated KIE, which is also referred to as the isotopic fractionation factor, and H and L refer to the heavy and light isotope of a particular isotopologue pair, respectively. Corrections for tunneling and anharmonicity were neglected as these isotope effects tend to be small [242] and tend to cancel each other out for

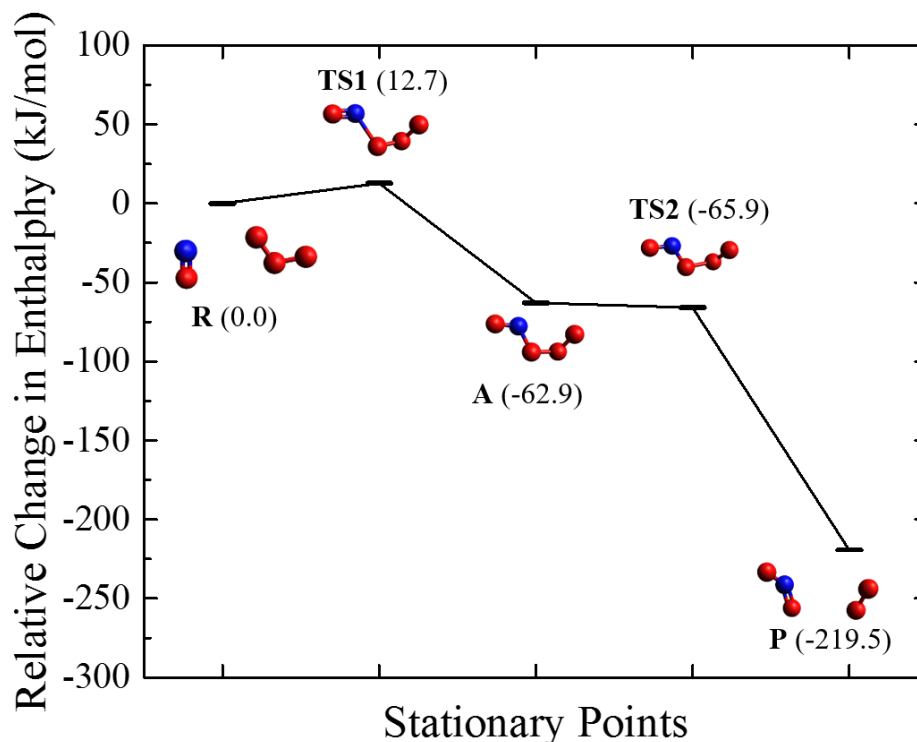


Fig. 7.1.: Schematic diagram of the assumed potential energy curve for the reaction $\text{NO} + \text{O}_3 \rightarrow \text{NO}_2 + \text{O}_2$ based on prior calculations using QCISD(T)/6-311G(2d)//UMP2(full)/6-31G(d) [240] where **R**, **TS1**, **A**, **TS2**, and **P** refer to the reactants, transition state 1, intermediate, transition state 2, and products, respectively. Relative energies with respect to the reactants $\text{NO} + \text{O}_3$ are given in kJ/mol and includes ZPE and thermal corrections (298 K).

heavy atoms [243]. Neglect of tunnel effects may be validated due to the involved heavy atoms and the observed low frequency modes along the reaction coordinate. Previously, errors in the frequencies and neglect of anharmonicity of the vibrational modes particularly the low-frequency modes associated with a floppy transition state

have been reported to cause little error in the calculated KIE using the complete Bigeleisen equations in the harmonic and rigid-rotor approximations (Beno et al., 1996). Thus, we expect these effects to minimally impact the calculated KIE.

7.3 Results and Discussion

7.3.1 Calculated geometries and vibrational frequencies

Table 7.1 compares the geometries and harmonic frequencies for the most abundant isotopologues of NO, O₃, NO₂, and O₂ calculated by CCSD(T)/6-31G(d) and CCSD(T)/6-311G(d) with experimental data [72, 79, 198, 199, 244–247]. Overall, the calculated geometries for the reactants and products are in excellent agreement with experimental data, as calculated bond lengths and bond angles are within 0.023 Å and 0.4 degrees of experimental data [72, 245, 247] (Table 7.1). Additionally, the calculated harmonic frequencies (scaled) are within a maximum difference of 92.2 cm⁻¹ and an average error of 29.9 cm⁻¹ and 43.9 cm⁻¹ relative to experimental data [79, 198, 199, 244] at CCSD(T)/6-31G(d) and CCSD(T)/6-311G(d), respectively. Cartesian coordinates of the optimized geometries and the scaled harmonic frequencies calculated for the major isotopologue of NO, O₃, NO₂, and O₂ from CCSD(T)-631G(d) and CCSD(T)/6-311G(d) computed force constants are available in the Appendix.

An important point in accurately calculating KIEs, is accounting for relative changes in vibrational energies due to substitution of a heavier isotope. Table 7.2 compares the differences in calculated vibrational zero point energies ($ZPE = \frac{1}{2}h\nu$) for various reactant and product ¹⁵N and ¹⁸O isotopologues relative to the major isotopologues for CCSD(T)/6-31G(d) and CCSD(T)/6-311G(d) with available experimental data [198, 202, 244, 246]. The difference in vibrational energies for each minor isotopologues relative to the most abundant are shown in parentheses in Table 7.2. Our calculated relative difference in ZPE due to substitution of a heavier isotope is within 1.2 cm⁻¹ of experimental data and an average relative difference of 0.34 and 0.61 cm⁻¹ for CCSD(T)/6-31G(d) and CCSD(T)/6-311G(d), respectively (Table 7.2).

Table 7.1: Calculated and experimental geometries and harmonic frequencies (cm⁻¹) of reactants and products calculated at CCSD(T)/6-31G(d) and CCSD(T)/6-311G(d). Bonds and angles are given in degrees and angstroms, respectively.

parameter	CCSD(T)/6-31G(d)	CCSD(T)/6-31G(d)	Exp
NO			
r(N-O)	1.169	1.154	1.154 ^a
ω_1	1947.7	1996.3	1904.1 ^b
O ₃			
r(O-O)	1.296	1.276	1.278 ^c
<(O-O-O)	116.5	116.9	116.8 ^c
ω_1	1106.8	1095.5	1103.2 ^d
ω_2	679.3	687.0	701.4 ^d
ω_3	984.3	988.2	1042.1 ^d
NO ₂			
r(N-O)	1.216	1.202	1.193 ^c
<(O-N-O)	133.7	134.0	134.1 ^c
ω_1	1333.4	1317.5	1355.9 ^e
ω_2	723.1	697.3	756.8 ^e
ω_3	1701.6	1697.7	1663.5 ^e
O ₂			
r(O-O)	1.229	1.210	1.208 ^f
ω_1	1562.7	1528.9	1580.4 ^g

^a ref. [247] ^b ref. [198] ^c ref. [245] ^d ref. [79] ^e ref. [199] ^f ref. [72] ^g ref. [244]

Table 7.2: Comparison of calculated ZPE (cm^{-1}) using fundamental frequencies derived from experimental data, and calculated using scaled CCSD(T)/6-31G(d), and CCSD(T)/6-311G(d) frequencies. The relative difference in the ZPE (ZPE) for the minor isotopologues relative to the most abundant is shown in parentheses (cm^{-1}).

	ZPE		
	Exp	CCSD(T)/6-31G(d)	CCSD(T)/6-311G(d)
$^{14}\text{N}^{16}\text{O}$	953.9 ^a	975.8	1000.1
$^{15}\text{N}^{16}\text{O}$	936.9 (17.1) ^a	958.4 (17.4)	982.3(17.9)
$^{14}\text{N}^{18}\text{O}$	928.8 (25.1) ^a	950.1 (25.7)	973.8 (26.3)
$^{16}\text{O}^{16}\text{O}^{16}\text{O}$	1425.9 ^b	1388	1388.2
$^{18}\text{O}^{16}\text{O}^{16}\text{O}$	1404.3 (21.6) ^b	1366.2 (21.7)	1366.5 (21.7)
$^{16}\text{O}^{18}\text{O}^{16}\text{O}$	1390.8 (35.1) ^b	1352.9 (35.1)	1352.9 (35.2)
$^{14}\text{N}^{16}\text{O}^{16}\text{O}$	1871.3 ^c	1882.8	1860
$^{15}\text{N}^{16}\text{O}^{16}\text{O}$	1841.3 (30.0) ^c	1852.2 (30.6)	1830.3 (29.7)
$^{14}\text{N}^{18}\text{O}^{16}\text{O}$	1844.0 (27.3) ^c	1855.3 (27.5)	1830.3 (29.7)
$^{16}\text{O}^{16}\text{O}$	791.8 ^d	782.9	766
$^{18}\text{O}^{16}\text{O}$	769.2 (22.5) ^d	760.8 (22.1)	744.4 (21.6)

^a ref. [198] ^b ref. [246] ^c ref. [202] ^d ref. [244]

This comparison shows the ability of our chosen level of theories to accurately reproduce changes in ZPE due to isotopic substitution. Therefore, CCSD(T)/6-31G(d) and CCSD(T)/6-311G(d) should be sufficient methods to calculate the relative changes in thermodynamic properties of the N and O isotopologues necessary to determine the KIEs of 7.4.

The calculated geometries of **TS1** and atom labeling scheme is displayed in Fig. 7.2. As expected for an exothermic reaction, **TS1** shows very small perturbations of geometrical parameters relative to the reactants [248]. Except for O_4 , the atoms of TS1 are nearly planar as evident from the dihedral angle $\angle(\text{O}_1\text{-N}_1\text{-O}_2\text{-O}_3)$ of -

169.6° and -171.3° at CCSD(T)/6-31G(d) and CCSD(T)/6-311G(d), respectively (Fig. 2), which is a similar finding to geometry of TS1 calculated at the UMP2/6-31(d) level of theory [240]. The imaginary frequency corresponding to the reaction coordinate is calculated to be 337.5i and 335.1i for CCSD(T)/6-31G(d) and CCSD(T)/6-311G(d), respectively, which is in close agreement with the previous calculated value of 352.9i at UMP2/6-31G(d) [240]. Cartesian coordinates of the optimized geometries and the scaled harmonic frequencies calculated for the major isotopologues of TS1 from CCSD(T)-631G(d) and CCSD(T)/6-311G(d) computed force constants are available in the Appendix.

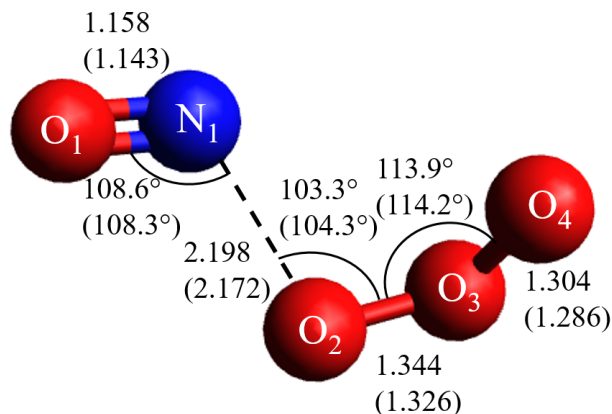


Fig. 7.2.: Optimized geometry of TS1 at CCSD(T)/6-31G(d) and CCSD(T)/6-311G(d) (given in parentheses). Bond lengths are in Angstroms and angles are in degrees. The dihedral angles of **TS1** $\angle(\text{O}_1\text{-N}_1\text{-O}_2\text{-O}_3)$ and $\angle(\text{N}_1\text{-O}_2\text{-O}_3\text{-O}_4)$ are -169.6°(-171.3°) and 77.8°(78.6°), respectively.

Table 7.3: Calculated isotopic enrichment factors (ϵ) at CCSD(T)/6-31G(d) and CCSD(T)/6-311G(d) expressed in units of per mil (‰) at 298 K.

Reaction	CCSD(T)/6-31G(d)	CCSD(T)/6-311G(d)
$\text{ON} + {}^{18}\text{OOO} \rightarrow \text{ON}^{18}\text{O} + \text{OO}$	-43.9	-44.7
$\text{ON} + {}^{17}\text{OOO} \rightarrow \text{ON}^{17}\text{O} + \text{OO}$	-23.3	-23.7
$\text{ON} + \text{O}^{18}\text{OO} \rightarrow \text{ONO} + {}^{18}\text{OO}$	-12.7	-14.1
$\text{O}^{15}\text{N} + \text{OOO} \rightarrow \text{O}^{15}\text{NO} + \text{OO}$	-7.7	-6.7
$\text{ON} + \text{O}^{17}\text{OO} \rightarrow \text{ONO} + {}^{17}\text{OO}$	-6.7	-7.4
${}^{17}\text{ON} + \text{OOO} \rightarrow {}^{17}\text{ONO} + \text{OO}$	0.2	-0.6
${}^{18}\text{ON} + \text{OOO} \rightarrow {}^{18}\text{ONO} + \text{OO}$	0.3	-1.3
$\text{ON} + \text{OO}^{17}\text{O} \rightarrow \text{ONO} + \text{O}^{17}\text{O}$	0.4	-0.2
$\text{ON} + \text{OO}^{18}\text{O} \rightarrow \text{ONO} + \text{O}^{18}\text{O}$	0.8	-0.3

7.3.2 Calculated kinetic isotope effects

Calculated nitrogen and position-specific oxygen α values at 298 K are reported in Table 7.3 as isotopic enrichment factors in units of per mil (‰) (7.7):

$$\epsilon(\text{‰}) = 1000(\alpha - 1) \quad (7.7)$$

Both the CCSD(T)/6-31G(d) and CCSD(T)/6-311G(d) methods calculate similar $\epsilon(\text{‰})$ values that differed by no more than 1.6‰ (Table 7.3). The largest KIE is observed to occur for the substitution of ${}^{18}\text{O}$ along the reaction coordinate (the $\text{ON} + {}^{18}\text{OOO} \rightarrow \text{ON}^{18}\text{O} + \text{OO}$) that is calculated to be -43.9 and -44.7‰ using CCSD(T)/6-31G(d) and CCSD(T)/6-311G(d) calculated frequencies, respectively (Table 7.3). The magnitude of the KIE is observed to decrease as the isotopic substitution position is further away for the reaction coordinate (i.e. secondary KIEs) as expected (Table 3). Isotopic enrichment factors have also been calculated at 220, 250, 273, and 320 K and are provided in the Appendix. These values will be useful for future isotopic modeling of NO_x chemistry.

Oxygen mass-dependent relationships ($\ln({}^{17}\alpha)/\ln({}^{18}\alpha)$) [238] for position-specific oxygen isotopic substitution are displayed in Table 4. Generally, ($\ln({}^{17}\alpha)/\ln({}^{18}\alpha)$) is

Table 7.4: Calculated oxygen mass-dependence relationships ($\ln(^{17}\alpha)/\ln(^{18}\alpha)$) and mass-independence values ($\Delta^{17}\text{O}$) at 298 K.

Reaction	$\ln(^{17}\alpha)/\ln(^{18}\alpha)$		$\Delta^{17}\text{O}(\text{‰})$	
	CCSD(T)/ 6-31G(d)	CCSD(T)/ 6-311G(d)	CCSD(T)/ 6-31G(d)	CCSD(T)/ 6-311G(d)
$^x\text{ON} + \text{OOO} \rightarrow ^x\text{ONO} + \text{OO}$	0.707	0.482	-0.05	-0.05
$\text{ON} + ^x\text{OOO} \rightarrow \text{ON}^x\text{O} + \text{OO}$	0.524	0.525	0.20	0.21
$\text{ON} + \text{O}^x\text{OO} \rightarrow \text{ONO} + ^x\text{OO}$	0.527	0.527	0.08	0.10
$\text{ON} + \text{OO}^x\text{O} \rightarrow \text{ONO} + \text{O}^x\text{O}$	0.527	0.526	-0.01	0.02

$\Delta^{17}\text{O}(\text{‰})$ calculated from Eq. 7.8.

found to range between 0.5244 to 0.5270, which is close to generally accepted value of 0.520 [238]. However, ($\ln(^{17}\alpha)/\ln(^{18}\alpha)$) is found to have an anonymously large deviation from 0.520 for the $^x\text{ON} + \text{OOO} \rightarrow ^x\text{ONO} + \text{O}_2$ reaction that is calculated to be 0.7072 and 0.4822 for CCSD(T)/6-31G(d) and CCSD(T)/6-311G(d), respectively (Table 7.5), which occurs due to both $^{18}\alpha$ and $^{17}\alpha$ being close to unity [141]. Despite this deviation, this reaction will have a minimal impact on $\Delta^{17}\alpha$ being close to unity, where $\Delta^{17}\text{O}$ is calculated as:

$$\Delta^{17}\text{O}(\text{‰}) = 1000 \ln\left(1 + (^{17}\alpha - 1)\right) - \lambda \times 1000 \ln\left(1 + (^{18}\alpha - 1)\right) \quad (7.8)$$

In Eq. 7.8, λ is assumed to be 0.52.

7.3.3 Comparison with experimental data

KIE in Unreacted O_3

Previously, Ref. [249] experimentally determined the kinetic isotopic fractionation associated with the $\text{NO} + \text{O}_3 \rightarrow \text{NO}_2 + \text{O}_2$ reaction by reacting NO with excess O_3 and measuring the O isotopic composition of the unreacted O_3 and reported an overall $\epsilon(\text{‰})$ of -30.5‰ for ^{18}O . This experimentally determined $\epsilon(\text{‰})$ value

does not correspond a singular KIE, rather it is roughly a statistical average for all the KIEs associated with the various ^{18}O isotopomers of O_3 and their reactions with NO . In order to quantitatively evaluate our calculated KIEs with respect to the results obtained by Ref. [249], we modeled the kinetics for reactions of the various O_3 isotopomers with NO using a subset of a previously published NO_x cycle chemical kinetics model [55], utilizing *Kintecus*, a chemical kinetics compiler [73].

The NO_x cycling kinetics model previously published by Ref. [55] contains numerous facets of the NO_x cycle including NO_2 dissociation, oxygen isotope exchange, ozone formation, ozone dissociation, NO oxidation by O_3 , NO oxidation by O -atom, NO_2 reaction with O -atom, NO_2 exchange with O -atom, NO exchange with O -atom, NO_2 exchange with NO , and NO oxidation by O_2 . Here, we are only interested in the KIE associated with the reaction of the various isotopomers of O_3 with NO , so only the reactions pertaining to this reaction was used in the present study, which are displayed in Table 7.5. In our model, we have only considered ^{18}O isotopic substitution due to this reaction being a mass-dependent fractionation process. Since we are interested in the relative change of the ^{18}O isotopic composition of O_3 , the starting composition is unimportant, so we specified a starting $\delta^{18}\text{O}(\text{O}_3)$ of 0‰ that was assumed to be uniformly distributed within O_3 . While there is experiment evidence that $\delta^{18}\text{O}$ is not uniformly distributed within O_3 [250], this should have a minor impact on the relative change of bulk isotopic composition of $\delta^{18}\text{O}$ in our model. The reaction of NO with the main isotopologue of O_3 ($^{16}\text{O}^{16}\text{O}^{16}\text{O}$) was set to $1.73 \times 10^{-14} \text{ cm}^3\text{molecules}^{-1}\text{s}^{-1}$ [206], and the reactions of NO with the ^{18}O substituted O_3 isotopologues/isotopomers were scaled by their position-specific oxygen α value. Additionally, the reactions involving the asymmetric isotopic substituted O_3 isotopologue ($^{18}\text{O}\text{OO}$) were scaled by 0.5 to account for reaction channel symmetry (Table 7.5). Our model was initiated with a $\text{NO}:\text{O}_3$ ratio of 0.95:1 so that O_3 was slightly in excess as in the experiment conducted by Ref. [249].

Table 7.5: Adapted rate constants (k) at 298 K (10^{-14} cm³molecules⁻¹s⁻¹) of NO reactions with various O₃ isotopologues using KIEs calculated at CCSD(T)/6-31G(d) and CCSD(T)/6-311G(d).

Reaction	CCSD(T)/6-31G(d)	CCSD(T)/6-311G(d)
$^{16}\text{O}^{14}\text{N} + ^{16}\text{O}^{16}\text{O}^{16}\text{O} \rightarrow ^{16}\text{O}^{14}\text{N}^{16}\text{O} + ^{16}\text{O}^{16}\text{O}$	1.730	1.730
$^{16}\text{O}^{14}\text{N} + ^{18}\text{O}^{16}\text{O}^{16}\text{O} \rightarrow ^{16}\text{O}^{14}\text{N}^{18}\text{O} + ^{16}\text{O}^{16}\text{O}$	0.827	0.826
$^{16}\text{O}^{14}\text{N} + ^{18}\text{O}^{16}\text{O}^{16}\text{O} \rightarrow ^{16}\text{O}^{14}\text{N}^{16}\text{O} + ^{18}\text{O}^{16}\text{O}$	0.866	0.864
$^{16}\text{O}^{14}\text{N} + ^{16}\text{O}^{18}\text{O}^{16}\text{O} \rightarrow ^{16}\text{O}^{14}\text{N}^{16}\text{O} + ^{18}\text{O}^{16}\text{O}$	1.708	1.706

From the model output, a Rayleigh-type distillation curve of the $\delta^{18}\text{O}$ of unreacted O_3 was constructed in the form of:

$$\ln(1 + 0.001 \times \delta_f) = \ln(1 + 0.001 \times \delta_0) + (\alpha - 1)\ln(f) \quad (7.9)$$

Where δ_f and δ_0 are the initial and final $\delta^{18}\text{O}$ of O_3 respectively and f is the fraction of unreacted O_3 . Fig. 7.3 displays our calculated Rayleigh type distillation curve for O_3 , where the slope of the line indicates an $\epsilon(\text{‰})$ value of -18.6‰ and -19.6‰ for CCSD(T)/6-31G(d) and CCSD(T)/6-311G(d), respectively, which differs from the experimentally determined value of -30.5‰ [249]. However, re-analysis of the experimental data from Ref. [249] indicates there might be a high-leverage, influential x data point at $\ln(f) = -3.047$. Fig. 7.4 compares two linear regression models of the experimental data from Ref. [249] that includes all of the data points (Model A) and the omission of the data point at $\ln(f) = -3.047$ (Model B). While the R^2 values from the two models does not vary by much ($R^2 = 0.966$ and 0.969), the slopes drastically change from -0.0305 ± 0.003 to -0.0209 ± 0.003 for Model A and Model B, respectively (Fig. 7.4). The calculated $\epsilon(\text{‰})$ from Model B is $-20.9 \pm 0.003\text{‰}$, which is in excellent agreement with our calculated and modeled value at both CCSD(T)/6-31G(d) and CCSD(T)/6-311G(d). This might suggest that the data point at $\ln(f) = -3.047$ might be influenced by other isotopic fractionation processes such as the formation of higher order nitrogen oxide species such as NO_3 and N_2O_5 that might have a different α . Also, it is also important to point out the limitations in our calculated α values from the Bigeleisen equations that are obtained within the conventional transition state theory with harmonic normal modes and rigid rotor approximations [239]. Additional uncertainties may be due to neglect of the α associated with the $\text{NO} + \text{O}_3$ reaction pathway proceeding through the O extraction from the apex O atom position of O_3 that recent experimental data shows may have a branching ratio of $8 \pm 5\%$ [251]. However, our calculated α values tends to agree quite well with a significant portion of the experimental data.

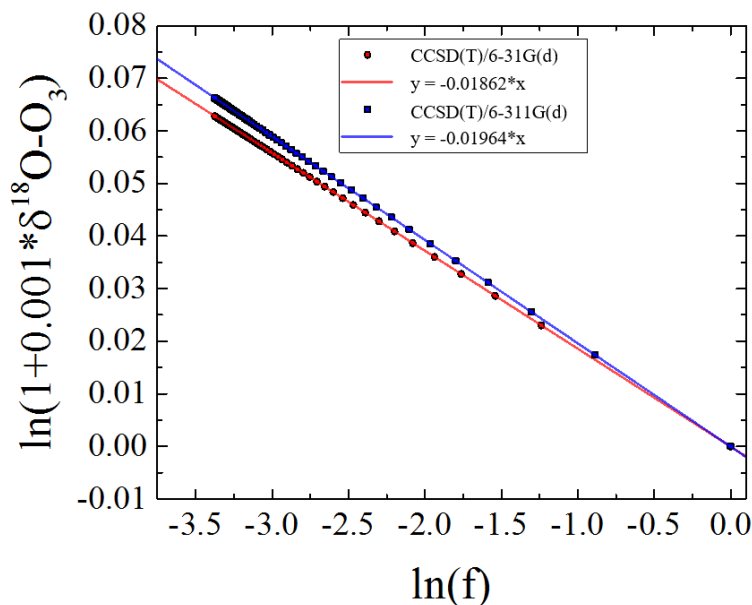


Fig. 7.3.: Rayleigh distillation model of unreacted O_3 in the $\text{NO} + \text{O}_3$ reaction calculated using KIEs at CCSD(T)/6-31G(d) and CCSD(T)/6-311G(d) within *Kintecus*. The slopes of the linear regression model indicate an overall $\epsilon(\text{‰})$ of -18.6‰ and -19.6‰ for unreacted O_3 at CCSD(T)/6-31G(d) and CCSD(T)/6-311G(d), respectively.

O Transfer KIE

Another important KIE to consider is the O transfer during the oxidation of NO by O_3 to NO_2 , which will be referred to as $^{18}\epsilon(\text{O-trans})$ (Eq. 7.10):

$$\epsilon_{\text{O-trans}}(\text{‰}) = \delta^{18}\text{O}(\text{NO}_2(\text{O-trans}))(\text{‰}) - \delta^{18}\text{O}(\text{aO}_3)(\text{‰}) \quad (7.10)$$

where $\delta^{18}\text{O}(\text{NO}_2(\text{O-trans}))$ and $\delta^{18}\text{O}(\text{aO}_3)$ are the $\delta^{18}\text{O}$ values of the transferred O atom in NO_2 and asymmetric O_3 , respectively. Previously, Ref. [56] reacted NO with O_3 at a 1:1 ratio at room temperature and measured the $\delta^{18}\text{O}$ of the transferred O atom in NO_2 . Using their experimental data, statistical models of previous studies of

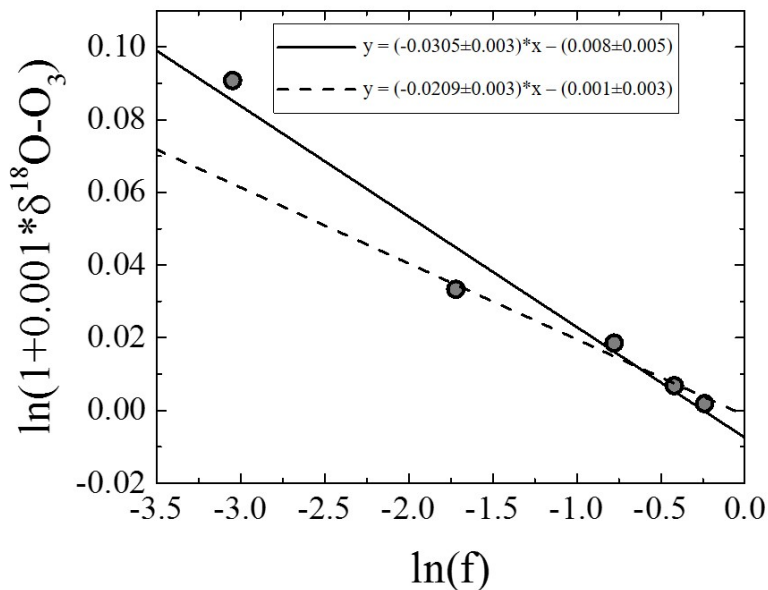


Fig. 7.4.: Rayleigh distillation model of unreacted O₃ in the NO + O₃ reaction calculated using prior experimental data [249]. Inclusion of all experimental data indicate a slope of -0.0305 ± 0.003 that corresponds to an $\epsilon(\text{‰})$ of $-30.5 \pm 0.003\text{‰}$ (solid line, $R^2 = 0.966$). Omission of the data point at $\ln(f) = -3.04$ indicates a slope of -0.0209 ± 0.003 that corresponds to an $\epsilon(\text{‰})$ of $-20.9 \pm 0.003\text{‰}$ (dashed line, $R^2 = 0.969$).

the intermolecular isotope distributions of O₃ [252], and the enrichment of asymmetric and symmetric O₃ isotopologues in the stratosphere as a function of altitude by [253], $^{18}\epsilon_{(\text{O-trans})}$ was estimated to be -23.9 and -20.8‰ [56]. Under the experimental conditions (i.e. 1:1 ratio of NO:O₃), the products, NO₂ and O₂, reflect the partitioning of ¹⁸O based on the position-specific α values for the ¹⁸O isotopomers of O₃, as there is a minimal isotopic fractionation impacting the residual O₃ since it nearly completely reacts.

Using our *Kintecus* model, we have estimated the $^{18}\epsilon_{(\text{O-trans})}$ using our O₃ isotopologue dependent KIEs and a NO:O₃ ratio of 1:1. The ¹⁸O isotopic composition of

O_3 was assumed to be uniformly distributed with a starting $\delta^{18}\text{O}(\text{O}_3) = \delta^{18}\text{O}_{(\text{aO}_3)} = 0\text{‰}$. From the output of our model, we estimate $\delta^{18}\text{O}(\text{NO}_2(\text{O-trans}))$ and thus $^{18}\epsilon_{(\text{O-trans})}$ (Eq. 7.9) to be -22.8‰ for both CCSD(T)/6-31G(d) and CCSD(T)/6-311G(d) calculated α values, respectively. These values are in excellent agreement with the experimental determined values that are estimated to range between -23.9 and -20.8‰ [56].

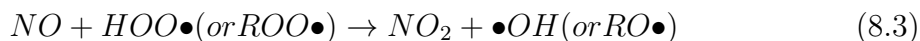
7.4 Conclusion

Ab initio calculations have been carried out to investigate the nitrogen and oxygen KIEs associated with NO reaction with O_3 . The calculated KIEs were generally close to unity except for primary KIEs, in which relatively large enrichment factors were calculated to be -44.7 and -6.7‰ for the $^{16}\text{O}^{14}\text{N} + ^{18}\text{O}^{16}\text{O}^{16}\text{O} \rightarrow ^{16}\text{O}^{14}\text{N}^{18}\text{O} + ^{16}\text{O}^{16}\text{O}$ and $^{16}\text{O}^{15}\text{N} + ^{16}\text{O}^{16}\text{O}^{16}\text{O} \rightarrow ^{16}\text{O}^{16}\text{N}^{16}\text{O} + ^{16}\text{O}^{16}\text{O}$ reactions, respectively at 298 K (CCSD(T)/6-311G(d)). Kinetic modeling of our calculated oxygen position-specific KIEs indicate excellent agreement between our values and prior experimental measurements. Our calculations indicate the O mass-dependent relationship ($\ln(^{17}\alpha)/\ln(^{18}\alpha)$) is generally near the expected value of 0.52. Cases in which ($\ln(^{17}\alpha)/\ln(^{18}\alpha)$) deviates from the expected value occurs for when the calculated KIEs are close to unity and thus have a minor impact on $\Delta^{17}\text{O}$, as expected for a mass-dependent fractionation process. This indicates that NO reaction with O_3 may play a significant role on the $\delta^{15}\text{N}$ and $\delta^{18}\text{O}$ values of NO and NO_2 , without altering $\Delta^{17}\text{O}$. This has important implications for utilizing $\delta^{15}\text{N}$ and $\delta^{18}\text{O}$ as tools for NO_x source partitioning and for understanding NO_x photochemical cycling. The calculated KIEs will be useful for future work aimed at modeling NO_x isotope chemistry and will help guide future ambient NO_x isotopic measurements.

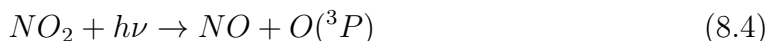
8. SUMMERTIME DIURNAL VARIATIONS IN THE ISOTOPIC COMPOSITION OF ATMOSPHERIC NITROGEN DIOXIDE AT A SMALL MIDWESTERN CITY

8.1 Introduction

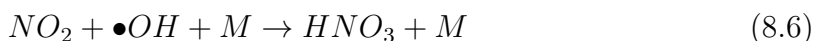
Nitrogen oxides ($\text{NO}_x = \text{nitric oxide (NO)} + \text{nitrogen dioxide (NO}_2\text{)}$) play a key role in controlling the concentrations of atmospheric oxidants that drive tropospheric chemistry [1, 3, 6]. During the daytime, NO_x exists in a photochemical steady state known as the Leighton Cycle [6, 7], in which emitted NO is converted to NO_2 via oxidation by either ozone (O_3) (R8.1) or peroxy radicals (R8.3). Peroxy radicals are produced when radical species such as the hydrogen radical ($\bullet\text{H}$), the methyl radical ($\bullet\text{CH}_3$), and organic radicals ($\bullet\text{R}$) combine with atmospheric O_2 (R8.2) [8]:



The formed NO_2 may subsequently photolyze back to NO (R8.4), which leads to the liberation of an O atom in the ground state that may react with O_2 to form O_3 (R8.5) [6, 7]:



Termination of this cycle occurs when NO_2 is further oxidized, which occurs primarily through its reaction with photochemically produced hydroxyl radicals ($\bullet\text{OH}$) during the daytime leading to the formation of atmospheric nitrates (R6) [10].



During the nighttime, NO_x photochemical cycling ceases, and NO is completely oxidized to NO_2 . Due to the absence of photochemically produced $\bullet\text{OH}$, NO_2 may further react with O_3 (R8.7), leading to the formation of the nitrate radical (NO_3), which exists at thermal equilibrium with NO_2 and dinitrogen pentoxide (N_2O_5) (R8.8) [234]. Subsequent hydrolysis of N_2O_5 on a wetted surface forms HNO_3 (R8.9).



Nighttime HNO_3 may also form from following hydrogen abstraction from organic compounds (R) by NO_3 (R8.10) [128]:



Once HNO_3 is formed, it is subsequently removed via wet and/or dry deposition leading to degradation of drinking water, soil acidification, eutrophication, and biodiversity change in terrestrial ecosystems [4]. Thus, due to the importance of NO_x on tropospheric chemistry and its implications for the environment and human health, it is important to understand the relative importance of NO_x emission sources and the oxidation processes (R8.1-R8.6) responsible for its removal.

Sources of NO_x are both of natural (lightning, soil nitrification/denitrification, and wildfires) and anthropogenic (fossil fuel combustion, industry, agricultural) origin [4, 12, 13], but there are uncertainties in the temporal and spatial contributions of various emission sources. The nitrogen (N) stable isotope composition ($\delta^{15}\text{N}$) of NO_x and atmospheric nitrate may provide a tool for partitioning local NO_x emission sources [27, 28, 34, 45, 216]. Typically, variations in terrestrial isotopic compositions are reported using delta notation where $\delta(\text{‰}) = (\text{R}_{\text{sample}}/\text{R}_{\text{ref}} - 1) \times 1000$, where R_{sample} and R_{ref} denote the atomic abundance ratio of a less abundant isotope to the most abundant isotope in a sample or reference, respectively. Atmospheric N_2 (for $^{15}\text{N}/^{14}\text{N}$)

and Vienna Standard Mean Ocean Water (VSMOW; (for $^{18}\text{O}/^{16}\text{O}$) are used as reference materials for reported δ (‰) values. Numerous studies have quantified the $\delta^{15}\text{N}$ signatures (“fingerprints”) of various NO_x emission sources, which indicate relatively distinctive $\delta^{15}\text{N}(\text{NO}_x)$ values for soil emissions (nitrification/denitrification), transportation sector, and coal-fired power plants [32, 33, 35, 36, 39–43, 45, 100, 208, 254]. While *in situ* $\delta^{15}\text{N}(\text{NO}_x)$ may be a useful indicator for local NO_x source partitioning [45, 47], it is challenging to collect *in situ* NO_x because it is highly reactive and typically has low mixing ratios (typically on the order of ppb_v). Rather the $\delta^{15}\text{N}(\text{NO}_x)$ values have been inferred from the ^{15}N of atmosphere nitrate, which is easier to collect and analyze for isotopic composition. However, NO_x source partitioning based on $\delta^{15}\text{N}$ values of atmospheric nitrate are complicated due to possible kinetic [190], equilibrium [101, 217], and photolytic isotope effects that occur during NO_x oxidation to atmospheric nitrate. For example, previous works have suggested isotopic exchange between NO and NO_2 [46, 216] occurring during the NO_x photochemical cycling might alter NO_2 $\delta^{15}\text{N}$ values, which may then be propagated into the ^{15}N value of atmospheric nitrate [188]. Previous $\delta^{15}\text{N}(\text{NO}_2)$ measurements have indicated that seasonal and diurnal $\delta^{15}\text{N}(\text{NO}_2)$ might be dictated by NO_x photolytic reactions [46]; however, this study was in an urban area dominated by a single NO_x emission source (vehicle emissions). Thus, the role of multiple significant NO_x emission sources with variable emission contributions to the total local NO_x emission budget may also play a significant role on $\delta^{15}\text{N}(\text{NO}_2)$. Therefore, it is still unclear at locations with multiple significant NO_x emission sources if $\delta^{15}\text{N}(\text{NO}_2)$ reflects NO_x emission sources, chemistry effects, or a combination of both. It is important to understand the influences on $\delta^{15}\text{N}$ of NO_2 since it is precursor to atmospheric nitrate.

The analysis of the oxygen (O) stable isotope composition ($\delta^{18}\text{O}$) of NO_x and atmospheric nitrate may allow for an understanding of NO_x photochemical cycling and an evaluation of changing daytime and nighttime oxidation chemistry [30, 53–55]. Prior experimental investigations suggest that O isotopic equilibrium is achieved between NO_x and O_3 , [55] erasing any original NO_x source O isotopic signature. Atmo-

spheric O_3 has a characteristic elevated $\delta^{18}O$ [48, 57, 58, 107, 212, 237]. The coupling between NO_x and O_3 in the Leighton Cycle is believed to be the driver of high $\delta^{18}O$ observed in atmospheric nitrates [53, 56, 255]. A recent $NO-O_2-O_3-NO_2$ cycle isotopic model under tropospheric conditions predicts $\delta^{18}O-NO_x$ of 117‰ relative to VSMOW [55]. However, previous O isotopic measurements that have been performed using Ogawa passive diffusion collectors indicate lower than expected $\delta^{18}O$ values for atmospheric NO_x [39, 47]. For example, $\delta^{18}O$ of NO_2 at an urban location was found to be $50.5 \pm 3.2\text{‰}$ during the summer and $47.4 \pm 1.2\text{‰}$ during the winter [47], significantly lower than the model predictions. The apparent disagreement between measured and expected $\delta^{18}O$ of *in situ* NO_2 has been suggested to be the result of the modification of the O isotopic composition of atmospheric NO_x during the capture and conversion to nitrite on the passive sampler [47]. Thus, accurate *in situ* measurements of the O isotopic composition of NO_x are currently unavailable. Additionally, it is important to note that NO_x will not achieve photochemical equilibrium with O_3 during the nighttime. Thus, nighttime NO_x may have a significantly different O isotopic composition that will represent a combination of source effects and oxidation chemistry. Therefore, in order to improve our understanding of the O isotopic composition of NO_x and atmospheric nitrate, daytime and nighttime O isotopic measurements of *in situ* NO_x are required. In this study, the diurnal variations in $\delta^{15}N$ and $\delta^{18}O$ values of *in situ* NO_2 was determined using an active sampling technique and the data was evaluated in the context of source and chemical isotope effects.

8.2 Methods

8.2.1 Sampling Location

NO_2 was collected from ambient air on the rooftop of a building (Hampton Hall of Civil Engineering) on the campus of Purdue University ($40.426^\circ N$, $86.908^\circ W$) (Fig 8.1) [256]. The surrounding land-use (radius of 1.5 km) is urban/sub-urban where the sister cities of Lafayette-West Lafayette, IN. combined have population of roughly

150,000. The sampling location was approximately 12 m above ground and was directly above a loading dock with light daytime diesel truck and gasoline vehicle traffic and approximately 50 m from a regularly traveled road during the daytime that experiences moderate weekday rush hour traffic at approximately 7-8 am and 5-6 pm. The 2011 U.S. EPA emission inventory estimates the following NO_x emission budget for the county of the sampling location (Tippecanoe): Mobile = 59.4%, Fuel Combustion = 35.3%, Biogenic = 4.2%, Industry = 0.7%, Waste = 0.3%, and Fire = 0.1%. However, the local NO_x emission budget should be dominated by anthropogenic NO_x emission particularly from vehicles. To the north and west of the sample location is mostly roads, a golf course, and agricultural fields (maize and soybean). Approximately 2 km south of the sampling site is an electrical-heat cogeneration plant that operates 3 natural gas boilers and one coal-fired boiler.

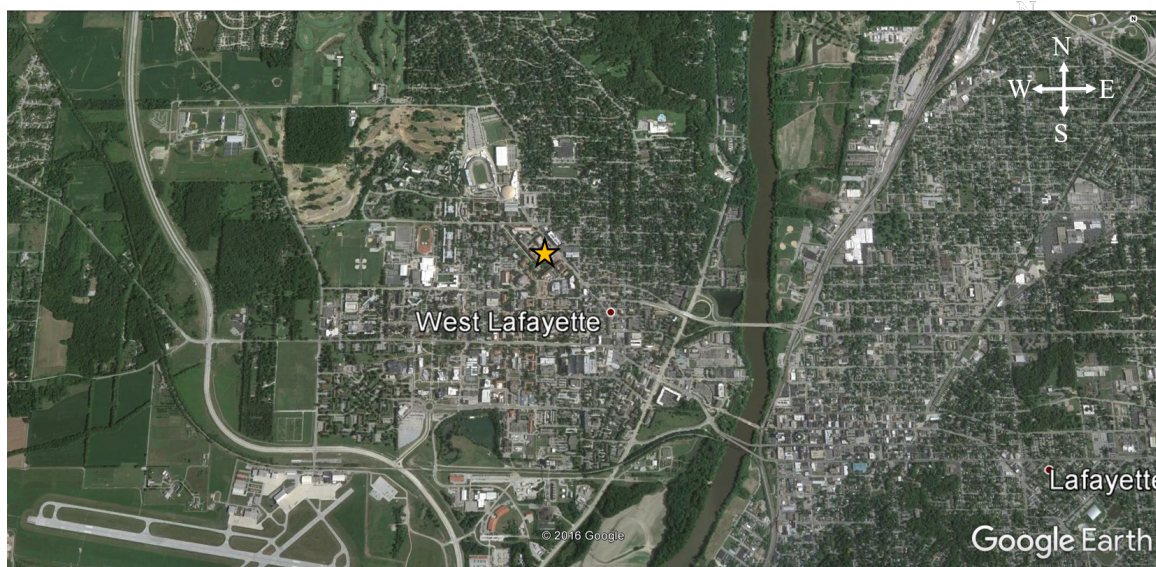


Fig. 8.1.: Location of sampling site (star) for *in situ* NO₂ collection. Image from Google Earth [256]

8.2.2 NO₂ Collection

NO₂ was collected using an active sampling apparatus depicted in Fig. 8.2. Briefly, ambient air was drawn through a denuder tube (I.D. = 3 mm and length = 1 m) using a diaphragm pump and flow controlled to 2 L/min. Prior to the denuder tube a Millipore Fluoropore membrane filter (9 mm diameter) removed particulate matter > 1 μm. The denuder tubes were coated with 0.5 mL of a 2.5 M potassium hydroxide, 25% by weight guaiacol (C₇H₈O₂), and methanol and air dried. This coating selectively reacts with NO₂ to form nitrite (NO₂⁻) [36, 41, 193]. A second denuder tube was connected in series with the first tube to check for NO₂ breakthrough. The denuder tubes were held vertically to prevent gravitational sedimentation of < 1 μm particulate matter to the tube wall and heavier oxidized forms of N (i.e. HNO_{3(g)} and N₂O₅) that generally have diffusion constants too small to allow diffusion to the sides of the denuder tube [194]. All connections between the various components of the sampling apparatus was made using 1/16" Teflon tubing and ultratorr fittings.

The sampling inlet (1/16" Teflon tubing) was mounted on the side of a building and sheltered from precipitation and direct sunlight. NO₂ was collected separately during the daytime and nighttime for a collection period of approximately 6 and 8 hours, respectively during the weekdays from July 7 to August 4, 2016. Daytime and nighttime collection typically occurred between 8:30 am to 4:00 pm and 9:30 pm to 5:30 am, respectively. NO-NO₂-NO_x concentration measurements of ambient air were simultaneously measured using a Thermo Scientific 42i NO_x analyzer. After collection, the denuder tubes were separately rinsed with 3 mL of 18.2 MΩ Millipore Water. NO₂⁻ test strips (Aquacheck) were used to check for NO₂⁻ breakthrough in the elutant of the second denuder tube, which did not occur occur. Thus, the elutant from the second denuder tube was discarded and the elutant from the first denuder tube was immediately placed in a freezer until isotopic analysis.

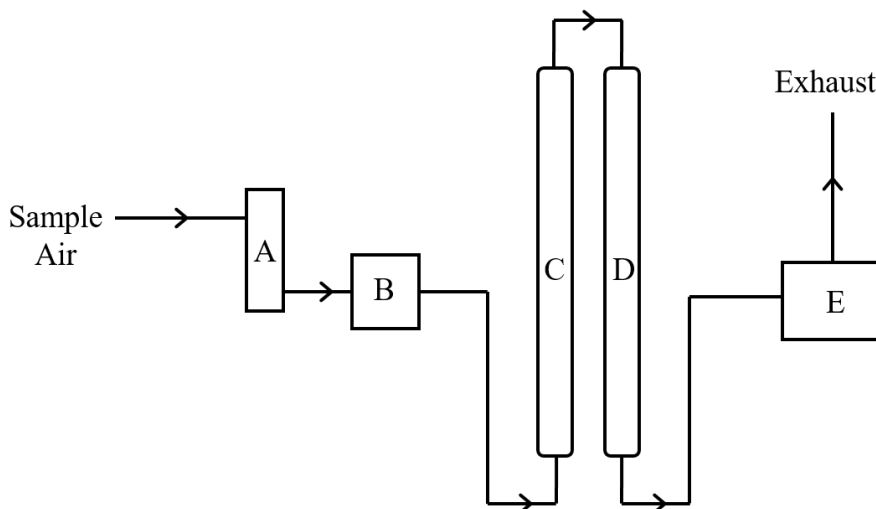


Fig. 8.2.: Sampling apparatus schematic for collection of atmospheric NO_2 , where A is the flow meter (2 L/min), B is aerosol filter, C is the NO_2 binding denuder tube, D is the NO_2 breakthrough denuder tube, and E is the peristaltic pump.

8.2.3 Isotopic Characterization

Isotopic analysis ($\delta^{18}\text{O}$ & $\delta^{15}\text{N}$) was performed on the product NO_2^- in the elutant from the first tube. Samples were left out at room temperature to thaw approximately 2 hours before the analysis. The entire elutant of approximately 3 mL from each sample was converted into nitrous oxide (N_2O) using sodium azide in an acetic acid buffer [195]. The product N_2O was extracted and purified using an automated headspace gas chromatography system and analyzed by a Thermo Delta V Continuous Flow Isotope Ratio Mass Spectrometer for m/z 44, 45, and 46 at the Purdue Stable Isotopes Lab. Measured $\delta^{15}\text{N}$ (relative to air N_2) and $\delta^{18}\text{O}$ (relative to VSMOW) was calibrated to KNO_2^- salts that included RSIL-N7373, RSIL-N23, RSIL-10219 with the following ($\delta^{15}\text{N}(\text{‰})$, $\delta^{18}\text{O}(\text{‰})$) values: (-79.6, 4.5), (3.7, 11.4), and (2.8, 88.5) [257]. Direct calibration of our NO_2^- samples to NO_2^- standards and the direct conversion of NO_2^- to N_2O using the sodium azide method [195], allows us

to ignore the uncertainty in correcting for isotopic fractionation of $\delta^{18}\text{O}$ using typical nitrate isotopic reference materials [258].

Our NO_2^- samples typically contained between 30 and 60 nmoles of NO_2^- based on the product N_2O yield. Linearity effects were corrected by using variable NO_2^- amounts of the standards that ranged between 20 and 250 nmoles. We found our isotopic precision to be highly dependent on the amount of NO_2^- analyzed. Near our sample sizes of 25-60 nmoles, the average standard deviation between the residual values of the calibrated standards for $\delta^{15}\text{N}$ and $\delta^{18}\text{O}$ was 1.1‰ and 0.6‰, respectively. This uncertainty is slightly higher than our usual isotopic precision for $\delta^{15}\text{N}$ and $\delta^{18}\text{O}$ of 0.6‰, and 0.4‰ that is found at NO_2^- amounts greater than 200 nmoles. Thus, we report $\delta^{15}\text{N}(\text{NO}_2)$ and $\delta^{18}\text{O}(\text{NO}_2)$ raw measurement errors of $\pm 1.1\%$ and $\pm 0.6\%$. Additionally, since our NO_2 samples are of atmospheric origin, $\delta^{15}\text{N}$ was also corrected for N_2O isobaric influences from $\Delta^{17}\text{O}$ [259]. We estimated a $\Delta^{17}\text{O}$ of $35 \pm 5\%$ during the daytime and a $\Delta^{17}\text{O}$ of $17.5 \pm 2.5\%$ during the nighttime. This typically resulted in a $\delta^{15}\text{N}$ correction of -2% during the daytime and -1% during the nighttime. Since the $\Delta^{17}\text{O}$ for these samples is somewhat unknown, we estimate an additional $\delta^{15}\text{N}$ uncertainty of $\pm 0.5\%$. Thus, our reported $\delta^{15}\text{N}(\text{NO}_2)$ measurements are reported with an error of $\pm 1.6\%$.

8.2.4 Control Tests

Previous control tests demonstrated the robustness for characterizing $\delta^{15}\text{N}(\text{NO}_2)$ [216] using the denuder tubes employed in this study. We have found this method results in an isotopic precision for $\delta^{15}\text{N}(\text{NO}_2)$ of approximately $\pm 0.7\%$, with excellent isotopic accuracy [216]. Additionally, it was found that NO does not bind on the denuder tube that is specifically designed to bind NO_2 [216]. Further control tests were conducted using an NO_2 bulb and indicate a $\delta^{18}\text{O}(\text{NO}_2)$ of $-1.8 \pm 1.2\%$ ($n = 7$), which indicates excellent precision; however, the $\delta^{18}\text{O}$ value of the NO_2 bulb is currently unknown. Since nearly 100% of NO_2 binds on the denuder tube, $\delta^{18}\text{O}$

fractionation due to incomplete NO_2 collection should not be of concern. Assuming that $\delta^{18}\text{O}(\text{NO}_2)$ is conserved as it is bound as NO_2^- , the only other $\delta^{18}\text{O}$ fractionation that needs to be addressed is the $\delta^{18}\text{O}$ exchange of NO_2^- with water once eluted from the denuder tube. The elutant is extremely basic ($\text{pH} > 12$), so that $\delta^{18}\text{O}$ exchange with water should be minimal [258]. This was tested by periodically injecting 20 to 50 nmoles of a standard KNO_2^- salt (RISL-N10219) salt into the eluted guaciaol/KOH mixture over a period of one month. The controls were immediately placed in a freezer until isotopic analysis. Our control tests indicate that O isotopic exchange between NO_2^- and H_2O does occur in our samples, reaching approximately 3.5% within the first three days, based on a laboratory water $\delta^{18}\text{O}$ of -8‰ (Fig. 8.3). After this initial exchange, no further exchange in $\delta^{18}\text{O}$ is observed, as all control samples that were kept in solution between 3 to 31 days prior to isotopic analysis indicated an average O exchange with water of $2.7 \pm 2\%$ (Fig. 8.3). This consistent fraction of O exchange between $\text{NO}_2^- \leftrightarrow \text{H}_2\text{O}$ water is hypothesized to be the result of the time it took for the samples to completely freeze and thereby slowing the exchange to a negligible rate. Our samples were analyzed between 3 and 20 days of collection and were corrected assuming an O isotopic exchange of $2.7 \pm 2\%$ with water. The degree of uncertainty in the amount of $\delta^{18}\text{O}$ exchange ($\pm 2\%$) adds an uncertainty in our reported $\delta^{18}\text{O}(\text{NO}_2)$ of about 1.5‰. Therefore, the uncertainty in our $\delta^{18}\text{O}(\text{NO}_2)$ measurements is reported as $\pm 2.1\%$, which is the error propagation of our raw $\delta^{18}\text{O}(\text{NO}_2^-)$ measurement at 25 nmoles of NO_2^- and the uncertainty in $\delta^{18}\text{O}$ resulting from NO_2^- exchange with water.

8.3 Results

8.3.1 Measured $[\text{NO}_x]$ and $f(\text{NO}_2)$

The average measured NO_x concentrations and average fraction of NO_2 relative to total NO_x ($f(\text{NO}_2) = \text{NO}_2/\text{NO}_x$) for each hour during our collection period of July 7 to August 4, 2016 varied at our sampling location (Fig. 8.4). Daytime $[\text{NO}_x]$

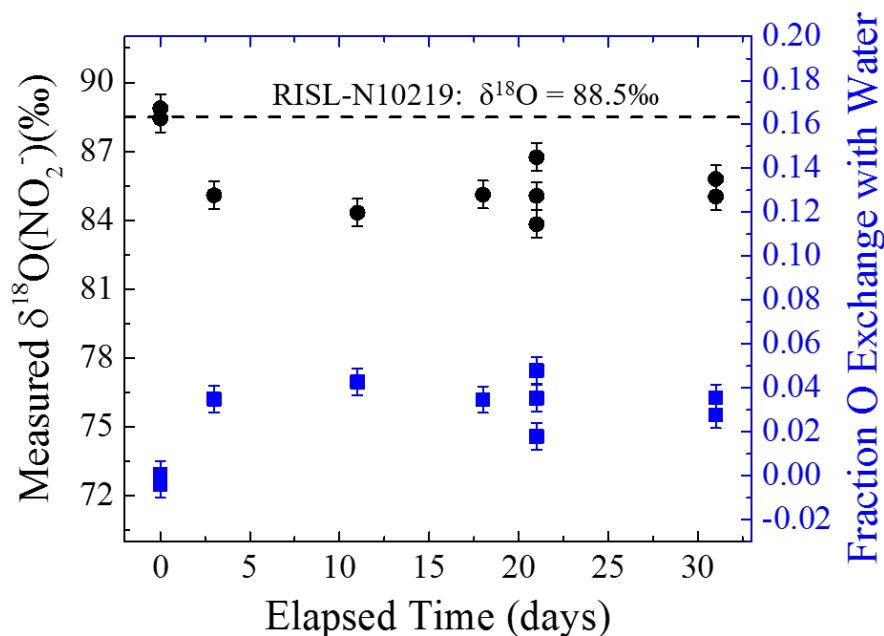


Fig. 8.3.: Impacts of $\delta^{18}\text{O}$ exchange between NO_2^- and water ($\delta^{18}\text{O} = -8\text{‰}$) contained within the KOH/guacoil elutant as a function of time contained within solution before isotopic analysis, where the black circles represent the measured $\delta^{18}\text{O}(\text{NO}_2^-)$ and the blue squares represent the estimated fraction of O exchange between NO_2^- and water. The NO_2^- standard (RISL-N10219) has a $\delta^{18}\text{O}$ of 88.5‰. Solutions immediately analyzed show no impacts of isotopic exchange with water. However, after about 3 days, a constant isotopic exchange is observed of about 2 to 5% with an average exchange of $2.7 \pm 2\%$, lowering the measured $\delta^{18}\text{O}$ of RISL-N10219 by about 2 to 4‰.

measurements indicate a large early morning peak in $[\text{NO}_x]$ between 6 and 10 am that reaches an average high of 7.1 ± 4.1 ppb_v at 8:00 am (Fig. 8.4). After this morning peak, $[\text{NO}_x]$ steadily decreases throughout the day (Fig. 8.4) to a baseline $[\text{NO}_x]$ of approximately 2.5 ± 0.4 ppb_v (Fig. 8.4). A smaller NO_x peak near 5 pm

is also observed on some of the collection days; however, this afternoon peak is not obvious in the 1 hour averaged $[\text{NO}_x]$ measurements that spans our entire collection period. These $[\text{NO}_x]$ profiles are typical of urban areas and result from the emission of NO from transportation sources during the early morning [204, 260, 261]. During our collection periods (daytime 8:30 am to 4:00 pm, nighttime 9:30 am to 5:30 am), average NO_x concentrations ranged from 1.5 to 7.9 ppb_v. The diurnal cycling of $[\text{NO}_x]$ was somewhat averaged out during our collection periods as daytime averages (4.3 ± 1.8 ppb_v ($\bar{x} \pm 1\sigma$)) were within 1 standard deviation of nighttime averages (3.6 ± 1.4 ppb_v).

A diurnal cycle in $f(\text{NO}_2)$ is also observed with daytime values averaging 0.82 ± 0.04 and nighttime values averaging 0.91 ± 0.004 . Additionally, $f(\text{NO}_2)$ values are observed to be lowest when $[\text{NO}_x]$ concentrations are highest (Fig. 8.4), which is related to the emission of transportation NO_x predominately as NO. During our collection periods, average $f(\text{NO}_2)$ values ranged from 0.751 to 0.95. Daytime collection periods had an average lower $f(\text{NO}_2)$ of 0.81 ± 0.03 than did nighttime of 0.92 ± 0.02 .

8.3.2 $\delta^{15}\text{N}(\text{NO}_2)$

The measured $\delta^{15}\text{N}(\text{NO}_2)$ values had large variations ranging from -29.7‰ to 8.1‰ (Fig. 8.4) and averaged $-7.0 \pm 7.9\text{‰}$ ($n = 33$). These $\delta^{15}\text{N}(\text{NO}_2)$ values are outside the range previously reported of -3.6‰ to -9.0‰ in an urban location [47], but near the previously reported range of -24.6‰ to 7.3‰ from a roadside transect [37]. Additionally, our average $\delta^{15}\text{N}(\text{NO}_2)$ value is close to the $\delta^{15}\text{N}(\text{NO}_x)$ value predicted by isotope mass-balance for our sampling region during July to August period of approximately -9‰ [208]. Generally, the $\delta^{15}\text{N}(\text{NO}_2)$ values tended to be negative as 27 out of the 33 collection periods including 13 of 18 daytime and 14 of 15 nighttime had $\delta^{15}\text{N}$ values less than 0‰ . Samples collected during the nighttime had $\delta^{15}\text{N}(\text{NO}_2)$ that ranged from -29.7‰ to 0.7‰ and averaged $-10.9 \pm 8.2\text{‰}$ ($n = 15$). Sample collected during the daytime had $\delta^{15}\text{N}(\text{NO}_2)$ values that ranged from

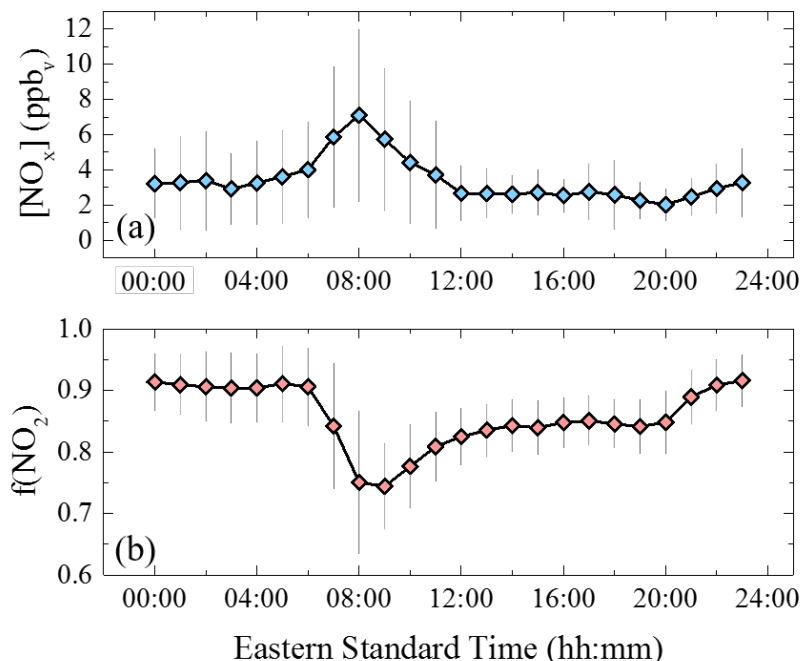


Fig. 8.4.: Averaged diurnal variations in $[\text{NO}_x]$ (a) and $f(\text{NO}_2)$ (b) at our sampling location during the collection period of July 7 to August 4, 2016. Diamonds represent averages for each hour taken from measurements at 30 second intervals each day and the gray lines represent $\pm 1\sigma$ for each hour.

-19.0 to 8.1‰ and averaged $-3.8 \pm 6.0\text{‰}$ ($n = 18$). On average, daytime $\delta^{15}\text{N}(\text{NO}_2)$ values were 7‰ higher than nighttime; however, the daytime and nighttime means are not statistical significantly different (two-sided t-test $p > 0.05$).

8.3.3 $\delta^{18}\text{O}(\text{NO}_2)$

There was large variation in $\delta^{18}\text{O}(\text{NO}_2)$ as values (Fig. 8.5), ranging from 41.5‰ to 117.0‰ that averaged $75.6 \pm 21.9\text{‰}$ ($n = 33$). The highest $\delta^{18}\text{O}(\text{NO}_2)$ measurement of 117.0‰ is in excellent agreement with a prior $\text{NO}-\text{O}_2-\text{O}_3-\text{NO}_2$ cycle experiment that found $\delta^{18}\text{O}(\text{NO}_x)$ value of $117.0 \pm 4\text{‰}$ relative to VSMOW [55] for photochemically equilibrated NO_x . The observed variation in $\delta^{18}\text{O}(\text{NO}_2)$ val-

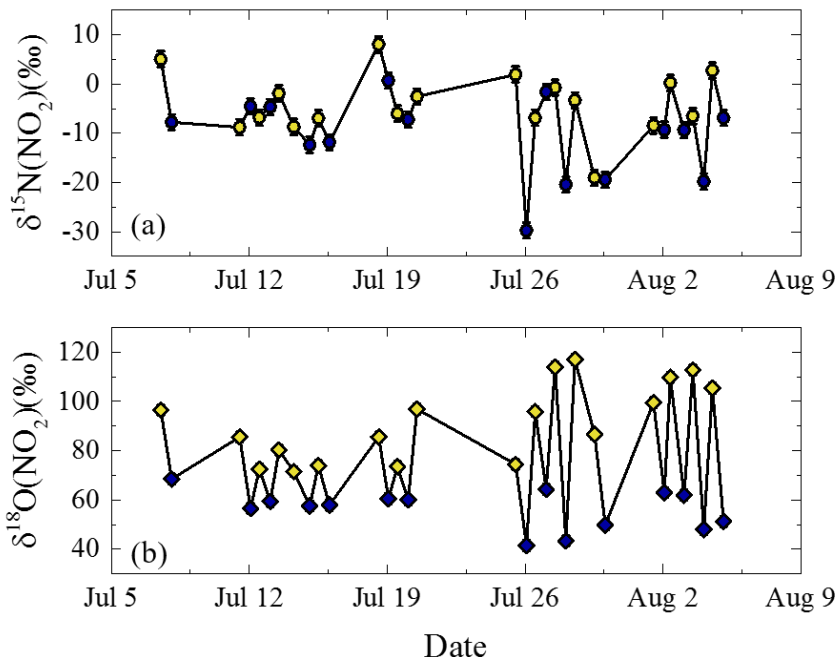


Fig. 8.5.: Measured (a) $\delta^{15}\text{N}(\text{NO}_2)$ and (b) $\delta^{18}\text{O}(\text{NO}_2)$ of *in situ* NO_x collected from July 7, 2016 to August 5, 2016 during the daytime (yellow) and nighttime (dark blue).

ues ($\pm 21.9\text{‰}$) is significantly reduced when comparing samples collected during the daytime and nighttime separately. During the daytime, $\delta^{18}\text{O}(\text{NO}_2)$ ranged from 71.5‰ to 117.0‰ and averaged $91.8 \pm 15.2\text{‰}$ ($n = 18$), while during the nighttime, $\delta^{18}\text{O}(\text{NO}_2)$ ranged from 41.5‰ to 68.5‰ and averaged $56.2 \pm 7.8\text{‰}$ ($n = 15$). The daytime and nighttime means are statistically significantly different (two-side t-test $p < 0.05$). Our measured $\delta^{18}\text{O}(\text{NO}_2)$ values are both more variable and larger than recently reported $\delta^{18}\text{O}(\text{NO}_2)$ values at an urban location of $50.5 \pm 3.2\text{‰}$ and $47.4 \pm 1.2\text{‰}$ collected during the summer and winter, respectively using Ogawa diffusion samplers [47]. Additionally, our $\delta^{18}\text{O}(\text{NO}_2)$ values are much larger than reported values of $-12.6 \pm 3.1\text{‰}$ and $-2.0 \pm 5.0\text{‰}$ inside and outside of a tunnel using Ogawa diffusion samplers [39].

8.4 Discussion

8.4.1 $\delta^{15}\text{N}(\text{NO}_2)$

Nighttime $\delta^{15}\text{N}(\text{NO}_2)$

As *a priori*, our nighttime $\delta^{15}\text{N}(\text{NO}_2)$ values are assumed to reflect $\delta^{15}\text{N}(\text{NO}_x)$ [46, 216] as nearly all NO_x exists as NO_2 (Fig. 8.4). During the nighttime NO_2 collection, $f(\text{NO}_2)$ averaged 0.918 ± 0.02 ; thus, $\delta^{15}\text{N}(\text{NO}_2)$ should be within 1 to 2‰ of $\delta^{15}\text{N}(\text{NO}_x)$ assuming that NO_x isotopic exchange may elevate $\delta^{15}\text{N}(\text{NO}_2)$ values relative to $\delta^{15}\text{N}(\text{NO}_x)$ [216]. Therefore, the large variability observed in nighttime $\delta^{15}\text{N}(\text{NO}_2)$ that was found to span 30.4‰ cannot be explained in terms of NO_x isotope effects alone and is likely the result of changing relative contributions of various NO_x emission sources at our sampling location.

At our sampling location, we would expect vehicle emissions to be the dominant NO_x emission source and this should be reflected in our measured $\delta^{15}\text{N}(\text{NO}_2)$. Previously, a mass-balance model of NO_x emitted from gasoline-powered vehicles estimates $\delta^{15}\text{N}(\text{NO}_x)$ to range between -5 to -1‰, which reflects the balance of high NO_x emission with lower $\delta^{15}\text{N}(\text{NO}_x)$ values and lower NO_x emission with higher $\delta^{15}\text{N}(\text{NO}_x)$ due to the catalytic reduction of NO_x through three-way catalytic converters [100]. Diesel engines tend to emit NO_x with a $\delta^{15}\text{N}$ lower than gasoline engines that is near -19‰ without selective catalytic NO_x reduction (SCR) [45, 208], but subsequently increase as SCR technology reduces NO_x [208]. For Tippecanoe county, the 2011 EPA estimates that on-road mobile sector to be comprised of 40.0% diesel and 60.0% gasoline. Applying mass-balance based on the U.S. EPA on-road NO_x emission estimate, we approximate the on-road $\delta^{15}\text{N}(\text{NO}_x)$ signature to range between -11 to -4‰. This estimated range of transportation related $\delta^{15}\text{N}(\text{NO}_x)$ values tends to match 9 out of 15 of the measured nighttime $\delta^{15}\text{N}(\text{NO}_2)$. Samples within this range had an average $\delta^{15}\text{N}(\text{NO}_2)$ of -8.2 ± 2.6 ‰ ($n = 9$). These values are in close agreement with $\delta^{15}\text{N}(\text{NO}_2)$ and $\delta^{15}\text{N}(\text{NO}_x)$ values of -8.3 ± 0.9 ‰ and -9.7 ± 0.7 ‰ from a recent

study at a sampling location dominated by vehicle emissions [47]. Assuming this on-road transportation $\delta^{15}\text{N}(\text{NO}_x)$ signature, our $\delta^{15}\text{N}(\text{NO}_2)$ measurements indicate that in general NO_x emitted from the transportation sector tends to compose most of the nighttime NO_x at our sampling site, as expected. Since the overall on-road transportation sector's $\delta^{15}\text{N}(\text{NO}_x)$ signature is still somewhat unknown, future studies should aim to further constrain this value from roadside $\delta^{15}\text{N}(\text{NO}_x)$ measurements.

From the measured nighttime $\delta^{15}\text{N}(\text{NO}_2)$, four of the collection periods have much lower $\delta^{15}\text{N}(\text{NO}_2)$ than the expected $\delta^{15}\text{N}(\text{NO}_x)$ range of the transportation sector (Fig. 8.5). These values correspond to collection periods on July 25 to July 26, July 27 to July 28, July 29 to Jul 30, and August 3 to August 4 that have $\delta^{15}\text{N}(\text{NO}_2)$ of -29.7‰ , -20.4‰ , -19.4‰ , and -19.8‰ , respectively and are statistically significantly different from the rest of the nighttime $\delta^{15}\text{N}(\text{NO}_2)$ measurements (two-side t-test, $p < 0.05$). Previous studies have indicated that biogenic NO_x emissions have a low $\delta^{15}\text{N}(\text{NO}_x)$ with values ranging between -48.6 to -19.9‰ [41, 42], which is within our range of estimated $\delta^{15}\text{N}(\text{NO}_2)$ from the observed “anomalous” NO_x . Thus, these collection periods' $\delta^{15}\text{N}(\text{NO}_2)$ may reflect possible influences from biogenic NO_x . Agricultural fields can be a significant source of NO_x due to biogenic soil NO_x emissions (nitrification and denitrification) [262–264]; thus, our lower $\delta^{15}\text{N}(\text{NO}_2)$ during some nights might be reflective of nearby agricultural $\delta^{15}\text{N}(\text{NO}_x)$ transported to our sampling location. However, this is probably unlikely because maize and soybean fertilization typically does not occur during the summer months, and the typical stagnant conditions during the night would limit the possibility of NO_x transport from agricultural regions that are more than 5 km from our sampling site. Therefore, the lower $\delta^{15}\text{N}(\text{NO}_2)$ values observed may be representative of an urban biogenic NO_x signature. We hypothesis that this urban biogenic NO_x may have been the result of N fertilization of local landscapes and from the nearby golf course (less than 1.5 km from sampling site).

One of the collection periods (July 18 to July 19) had a $\delta^{15}\text{N}(\text{NO}_2)$ values that was positive (0.7‰) and slightly larger than the on-road transportation sector's

$\delta^{15}\text{N}(\text{NO}_x)$ signature. It is interesting to note that this collection period was characterized by stagnant conditions and the formation of early morning fog, which was reported to occur between July 19 3:30 am to July 19 5:30 am. The onset of fog formation coincides with an increase in $[\text{NO}_x]$, reaching as high as 10 ppb_v (Fig. 8.6) relative to its baseline $[\text{NO}_x]$ of 2.5 ppb_v. The increase in $[\text{NO}_x]$ during fog events has been previously observed and is suggested to occur due to the stagnant conditions during periods of fog formation [265]. We hypothesize that the increase in $\delta^{15}\text{N}(\text{NO}_x)$ may be related to NO_2 reaction with wetted aerosols during the fog event that occurs faster for the lighter $^{14}\text{NO}_2$ than for $^{15}\text{NO}_2$. This will result in an increase in $\delta^{15}\text{N}(\text{NO}_2)$ and may explain the slightly higher $\delta^{15}\text{N}(\text{NO}_2)$ values observed during this time period. However, this explanation is somewhat complicated by an increase in $[\text{NO}_x]$ and a decrease in $f(\text{NO}_2)$, which may have made the NO_x isotopic exchange more influential on the partitioning of ^{15}N between NO and NO_2 and may have resulted in a higher $\delta^{15}\text{N}(\text{NO}_2)$ [216]. Additionally, coal-fired emissions from the local utility and chiller plant may have contributed to the NO_x at our sampling location, which would have increased the $\delta^{15}\text{N}(\text{NO}_2)$ as previous studies indicate an elevated $\delta^{15}\text{N}(\text{NO}_x)$ coal-fired power plant signature that ranges from 6.0 to 19.8‰ [35, 40]. Additionally, coal-fired power plant emissions might explain the somewhat higher $\delta^{15}\text{N}(\text{NO}_2)$ value relative to the other nighttime measurements observed on July 26 to July 27 of -1.7‰.

Daytime $\delta^{15}\text{N}(\text{NO}_2)$

The majority of daytime $\delta^{15}\text{N}(\text{NO}_2)$ values appears to be within the range estimated for the transportation sector (9 out of 18 measurements; $\delta^{15}\text{N}(\text{NO}_2) = -6.5 \pm 2.1\text{‰}$), indicating that at our sampling location daytime $\delta^{15}\text{N}(\text{NO}_2)$ is approximately representative of local (on-road transportation) NO_x sources. There is also evidence for the emission of biogenic NO_x during the collection period on July 29 that had a much lower $\delta^{15}\text{N}(\text{NO}_2)$ of -19.0‰ (statistically a daytime $\delta^{15}\text{N}(\text{NO}_2)$ outlier; $p <$

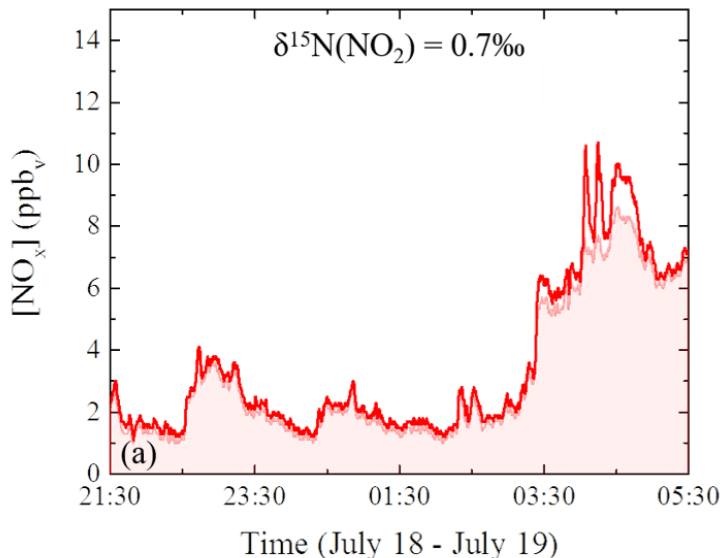


Fig. 8.6.: Measured $[\text{NO}_x]$ (red line) and $[\text{NO}_2]$ (shaded) concentrations for the July 18 to July 19 nighttime sampling periods that had a high $\delta^{15}\text{N}(\text{NO}_2)$. Fog formation was indicated to occur between July 19 3:30 am and July 19 5:30 am that coincides with an increase in $[\text{NO}_x]$.

0.05). In addition to source contributions, $\delta^{15}\text{N}(\text{NO}_2)$ may have also been impacted by meteorological events during two of the collection periods (July 7 and July 18) that may have increased $\delta^{15}\text{N}(\text{NO}_2)$. On July 7, 2016, the formation of an early morning fog that persisted until approximately 10 am was reported. No other fog formation was reported during our daytime collection of NO_2 . This fog event may have led to an increase in $\delta^{15}\text{N}(\text{NO}_2)$ due to the reaction of NO_x on wetted aerosols, as we have previously suggested, and this may explain the relatively high $\delta^{15}\text{N}(\text{NO}_2)$ for this day of 5.0‰. On July 18, early morning rain and thunderstorms were reported to occur between 2 am and 7 am. This may have had an impact on $\delta^{15}\text{N}(\text{NO}_2)$ for this collection period due to possible NO generation from lightning that has an estimated $\delta^{15}\text{N}(\text{NO}_x)$ of -0.5 to 1.4‰ based on simulated laboratory sparks [43], as well as the

precipitation scavenging of NO_2 [266] that might favor the loss of $^{14}\text{NO}_2$ of *in situ* NO_x . Both of these possibilities might explain the relatively high $\delta^{15}\text{N}(\text{NO}_2)$ of 8.1‰ for this day. NO_x contributions from coal-fired power plants may explain the daytime $\delta^{15}\text{N}(\text{NO}_2)$ measurements between -1.9 to 2.8‰ that are higher than the estimated on-road transportation's $\delta^{15}\text{N}(\text{NO}_x)$ range, but occurred on days with a significant reported meteorological event.

8.4.2 $\delta^{18}\text{O}(\text{NO}_2)$

Daytime $\delta^{18}\text{O}(\text{NO}_2)$

The measured $\delta^{18}\text{O}(\text{NO}_2)$ was found to be the largest during the daytime with an average value of $91.8 \pm 15.2\text{‰}$ (Fig. 8.5). During the daytime, the $\delta^{18}\text{O}(\text{NO}_2)$ is expected to reflect the oxidants responsible for the conversion of NO to NO_2 , as the photochemical cycling of NO_x is rapid and erases any original $\delta^{18}\text{O}(\text{NO}_x)$ signature. For an urban area, we would expect O_3 to dominate the conversion of NO to NO_2 and $\delta^{18}\text{O}(\text{NO}_2)$ to reflect its photochemical equilibrium with $\delta^{18}\text{O}(\text{O}_3)$ [48,53,211]. Previously, tropospheric O_3 has been reported to have elevated $\delta^{18}\text{O}(\text{O}_3)$ values ranging from 95 to 130‰ [48,57,58], and a prior experimental investigation found that the photochemical cycling of $\text{NO}-\text{O}_2-\text{O}_3-\text{NO}_2$ to result in $\delta^{15}\text{N}(\text{NO}_2)$ of 117‰ [55]. This experimental value is in excellent agreement with our highest measured daytime $\delta^{18}\text{O}(\text{NO}_2)$ values (Fig. 8.7), which might suggest that photochemical cycling of NO with O_3 as the primary oxidant results in $\delta^{18}\text{O}$ of *in situ* NO_x near 117‰. However, there is large variability in daytime $\delta^{18}\text{O}(\text{NO}_2)$ that spans 45.5‰ with collection periods that had $\delta^{18}\text{O}(\text{NO}_2)$ values as low as 71.5‰, much lower than the experimental value and the previously measured $\delta^{18}\text{O}$ of tropospheric O_3 .

NO may also be oxidized by peroxy radicals and this may be reflected in the $\delta^{18}\text{O}(\text{NO}_2)$. Peroxy radicals are estimated to have an oxygen isotopic composition that reflects tropospheric O_2 [30] that is approximately 23‰ [60]. Thus, the lower observed daytime $\delta^{18}\text{O}(\text{NO}_2)$ may be the result of NO oxidation by peroxy radicals.

Using an isotope mass-balance between the measured $\delta^{18}\text{O}(\text{NO}_2)$ and estimated $\delta^{18}\text{O}$ of NO_2 resulting from NO oxidation with O_3 and peroxy radicals of 117‰ and 23‰, respectively, the NO oxidation branching ratio can be estimated:

$$\delta^{18}\text{O}(\text{NO}_2) = x \times (\delta^{18}\text{O}(\text{O}_3)) + (1 - x) \times (\delta^{18}\text{O}(\text{ROO}\bullet\text{orHOO}\bullet)) \quad (8.11)$$

Overall, we estimate the branching ratio of NO oxidation by O_3 to be 0.732 ± 0.161 , signifying that O_3 was generally the dominate daytime oxidant at our sampling location as expected. However, NO oxidation through peroxy radicals seems to have played a significant role and reached a branching ratio as high as 0.484 during our sampling period (Fig. 8.7). This is important since NO oxidation through peroxy radicals occurs without the loss of an O_3 providing a pathway for the buildup of tropospheric O_3 . Thus, the isotopic composition of daytime NO_2 may provide a useful way to assess $\text{VOC-NO}_x\text{-O}_3$ chemistry which will can incorporated into tropospheric chemical models for estimating the amount of tropospheric O_3 generated.

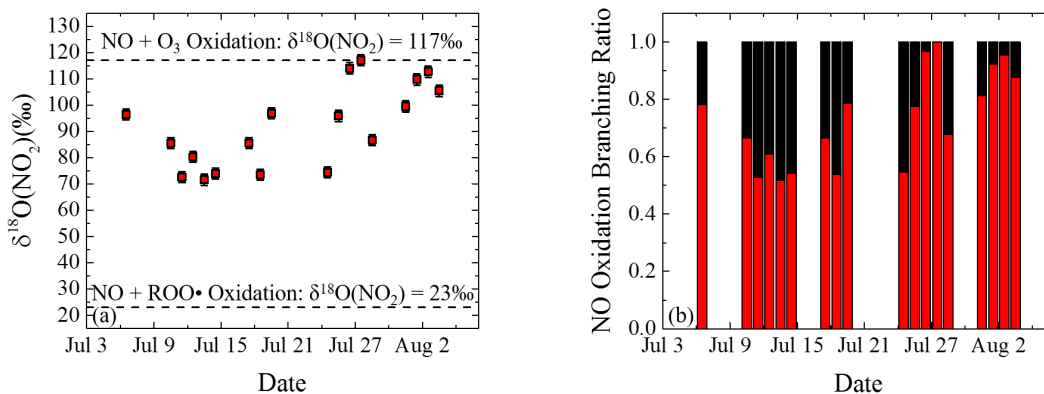


Fig. 8.7.: (a) Daytime $\delta^{18}\text{O}(\text{NO}_2)$ (‰) shown between previous $\delta^{18}\text{O}(\text{NO}_x)$ estimation of 117‰ resulting from $\text{NO-O}_3\text{-NO}_2\text{-O}_2$ photochemical cycling [55] and the estimated $\delta^{18}\text{O}(\text{ROO}\bullet)$ of 23‰ [30] and (b) estimated NO oxidation branching ratio between O_3 (red) and $\text{ROO}\bullet$ (black).

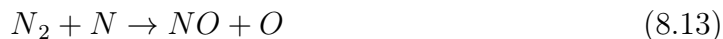
Nighttime $\delta^{18}\text{O}(\text{NO}_2)$

The measured nighttime $\delta^{18}\text{O}(\text{NO}_2)$ was much lower than the daytime averaging $56.2 \pm 7.8\%$. During the nighttime, the photochemical cycling of NO_x ceases, and nighttime $\delta^{18}\text{O}(\text{NO}_2)$ should reflect the mass-balance between $\delta^{18}\text{O}$ of the emitted NO and the $\delta^{18}\text{O}$ of the O atom transferred from the responsible oxidant:

$$\delta^{18}\text{O}(\text{NO}_{2\text{night}}) = \frac{1}{2}(\delta^{18}\text{O}(\text{NO}_{\text{source}})) + \frac{1}{2}(\delta^{18}\text{O}(\text{O}_{\text{oxidant}})) \quad (8.12)$$

Where $\delta^{18}\text{O}_{(\text{oxidant})}$ can be approximated to be the daytime $\delta^{18}\text{O}(\text{NO}_2)$ average of $91.8 \pm 15.2\%$. Thus, nighttime $\delta^{18}\text{O}(\text{NO}_2)$ should have a source component, and this is supported in a plot of nighttime $\delta^{18}\text{O}(\text{NO}_2)$ vs $\delta^{15}\text{N}(\text{NO}_2)$ that indicates a correlation ($R^2 = 0.617$) (Fig. 8.8). Nighttime NO_x sources were shown to be a mixture of soil, vehicle NO_x and influenced by fog formation based on their $\delta^{15}\text{N}(\text{NO}_2)$. For the collection samples that indicated the collected NO_2 originated mainly from the transportation sector ($\delta^{15}\text{N}(\text{NO}_2)$ within the range of -11% to -3%), we estimate the $\delta^{18}\text{O}(\text{NO}_{\text{source}})$ from the transportation sector to be $7.1 \pm 2.7\%$ based on Eq. 8.12.

NO emitted from vehicles is produced “thermally” originating by the reaction between nitrogen and oxygen in the intake air known as the Zeldovich Mechanism [70]:



These reactions indicate that the O atom in thermally produced NO originates from air O_2 . In order to form NO, air O_2 must break apart which will likely induce an isotope effect as observe for $\delta^{15}\text{N}(\text{NO})$ for thermally produced NO_x [100]. We can estimate this isotope effect of the breaking of a diatomic bond using the Arrhenius equation as the following:

$$\alpha_{\text{H/L}} = \frac{k_{\text{H}}}{k_{\text{L}}} = \exp\left(\frac{h(\nu_{\text{H}} - \nu_{\text{L}})}{2k_{\text{B}}T}\right) \quad (8.16)$$

where α is the isotopic fractionation factors, H and L refer to the heavy ($^{18}\text{O}^{16}\text{O}$) and light ($^{16}\text{O}^{16}\text{O}$) O_2 isotopologue respectively, h is Planck's constant, ν is vibrational frequency, k_b is Boltzmann's constant, and T is temperature (K). Using ν of 1580.36 cm^{-1} and 1535.73 cm^{-1} for $^{16}\text{O}^{16}\text{O}$ and $^{18}\text{O}^{16}\text{O}$, respectively [244], and assuming a combustion temperature of 2200 K , we estimate $\alpha_{\text{H/L}}$ to be 0.986 . Assuming no other isotope effects during the formation of thermal NO, Eq. 8.16 approximates that $\delta^{18}\text{O}$ of thermally produced NO should be roughly -14.4‰ (calculated from $1000 \cdot (\alpha_{\text{H/L}} - 1)$) relative to air O_2 . Using an air O_2 $\delta^{18}\text{O}$ value of 23‰ [60], this suggests a thermal $\delta^{18}\text{O}(\text{NO})$ signature of 8.6‰ . This estimated value is within the error of our derived value of $7.1 \pm 2.7\text{‰}$. No other $\delta^{18}\text{O}_{(\text{NO}_{\text{source}})}$ such as soil can be predicted from our dataset due to the mix of NO sources present during periods soil NO was important. However, collection periods in which soil emissions were expected to contribute to the NO_x budget ($\delta^{15}\text{N} < -11\text{‰}$), indicate that $\delta^{18}\text{O}(\text{NO})$ is lower than our estimated value for vehicle $\delta^{18}\text{O}(\text{NO})$ (Fig. 8.8).

8.5 Conclusion

NO_2 has been collected during the daytime and nighttime separately at a small Midwestern city (West Lafayette, IN, USA) from ambient air during the summertime and measured for $\delta^{15}\text{N}$ and $\delta^{18}\text{O}$. A wide range of $\delta^{15}\text{N}(\text{NO}_2)$ values are found ranging from -29.7‰ to 8.1‰ and averaging $-7.0 \pm 7.9\text{‰}$ ($n = 33$). On average, $\delta^{15}\text{N}(\text{NO}_2)$ tends to be higher during the daytime ($-3.8 \pm 6.0\text{‰}$) than during the nighttime ($-10.9 \pm 8.2\text{‰}$). The large variations observed in $\delta^{15}\text{N}(\text{NO}_2)$ is suspected to be largely the result of changing influences of NO_x emissions. Generally, we find that our collection site, $\delta^{15}\text{N}(\text{NO}_2)$ appears to be largely reflective of vehicle emissions. We also find evidence for influences from biogenic soil emissions from nearby agricultural fields, and possibly from lightning and coal-fired power plants. Meteorological events such as fog and rain are also hypothesized to alter the measured $\delta^{15}\text{N}(\text{NO}_2)$. Overall, this study provides evidence that $\delta^{15}\text{N}(\text{NO}_2)$ tends to reflect NO_x sources when $f(\text{NO}_2)$

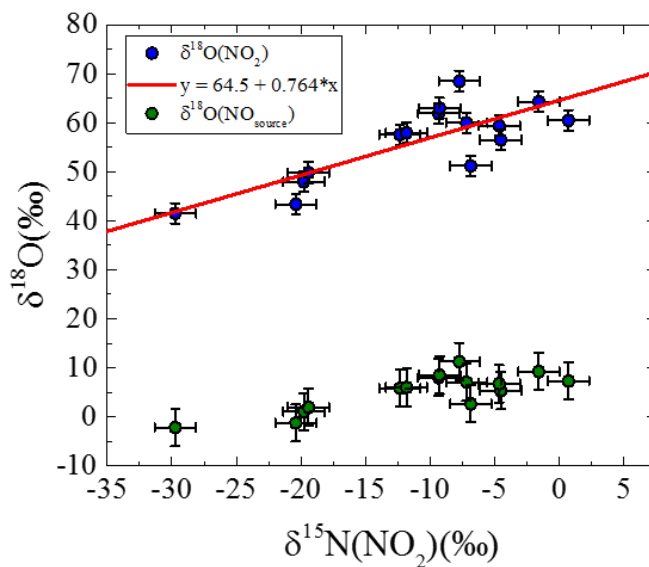


Fig. 8.8.: Linear least squares regression model between $\delta^{18}\text{O}(\text{NO}_2)$ (blue) and $\delta^{15}\text{N}(\text{NO}_2)$ during the nighttime indicates a correlation ($R^2 = 0.617$) which indicates that nighttime $\delta^{18}\text{O}(\text{NO}_2)$ is influenced by $\delta^{18}\text{O}(\text{NO})$ emission signatures. Applying a mass-balance model, the $\delta^{18}\text{O}(\text{NO})$ source has been estimated (green).

values are high and may possibly be used as a proxy for NO_x source partitioning. Future $\delta^{15}\text{N}(\text{NO}_x)$ studies need to better constrain $\delta^{15}\text{N}(\text{NO}_x)$ signatures and its time evolution for soil emissions as well as explore the possible meteorological effects on $\delta^{15}\text{N}(\text{NO}_2)$.

Measured $\delta^{18}\text{O}(\text{NO}_2)$ values were found to range from 41.5‰ to 117.0‰ and averaged $75.6 \pm 21.9\text{‰}$ ($n = 33$). During the daytime, $\delta^{18}\text{O}(\text{NO}_2)$ ranged from 71.5 to 117.0‰ and averaged $91.8 \pm 15.2\text{‰}$ ($n = 18$), while during the nighttime, $\delta^{18}\text{O}(\text{NO}_2)$ ranged from 41.5 to 68.5‰ and averaged $56.2 \pm 7.8\text{‰}$ ($n = 15$). The diurnal variation in $\delta^{18}\text{O}(\text{NO}_2)$ is a direct result of the photochemical cycling of NO_x . We estimate that NO oxidation by O_3 results in a $\delta^{18}\text{O}(\text{NO}_2)$ of 117‰, while NO oxidation by peroxy radicals results in $\delta^{18}\text{O}(\text{NO}_2)$ of 23‰. From a mass-balance model, we estimate the branching ratio of daytime NO oxidation by O_3 to be 0.732

± 0.161 . During the nighttime, $\delta^{18}\text{O}(\text{NO}_2)$ is impacted by the $\delta^{18}\text{O}(\text{NO})$ signature of NO emission sources resulting in a lowering of $\delta^{18}\text{O}(\text{NO}_2)$ during the nighttime. We estimate vehicles to emit $\delta^{18}\text{O}(\text{NO})$ of approximately 8.6‰ based on a simple model, which tends to agree with our estimated value of $7.1 \pm 2.7\text{‰}$ based on back calculation from our nighttime $\delta^{18}\text{O}(\text{NO}_2)$. Our sampling method provides some of the first elevated $\delta^{18}\text{O}(\text{NO}_2)$ measurements and has the potential to be used to characterize NO_x cycling and track tropospheric O_3 production. Future work should aim toward fine-tuning our method to develop collection techniques that can be used to characterize $\delta^{15}\text{N}$, $\delta^{18}\text{O}$, and $\Delta^{17}\text{O}$ at much finer time intervals. This will be the subject for future research. Additionally, new techniques need to be developed to understand the $\delta^{18}\text{O}(\text{NO})$ signature from NO_x sources to aid in our interpretation of nighttime $\delta^{18}\text{O}(\text{NO}_2)$ measurements.

9. CONCLUSION

9.1 $\delta^{15}\text{N}(\text{NO}_x)$ Characterization Studies

The $\delta^{15}\text{N}$ signatures of NO_x from fossil-fuel combustion have been analyzed for vehicles, buses, trucks, lawn equipment, air planes, and natural gas-fired power plants. In each of the sources, NO_x is produced thermally via high temperature reactions between N_2 and O_2 in the combustion chamber. The $\delta^{15}\text{N}(\text{NO}_x)$ emitted from vehicles was observed to have a large range from -19.1 to 9.8‰. This large range of values is a combination of thermally produced NO_x that tends to be depleted in ^{15}N and subsequent reduction of NO_x in the 3-way catalytic converter that kinetically favors the reduction of $^{14}\text{NO}_x$. This results in the emission of NO_x with a higher $\delta^{15}\text{N}$ as a function of catalytic reduction efficiency. Using an isotope mass-balance model that utilized average commute times, $\delta^{15}\text{N}(\text{NO}_x)$ from gasoline vehicles across the United States was estimated and it indicated that vehicle NO_x should have negative $\delta^{15}\text{N}$ values (-2.5 ± 1.5 ‰). Diesel vehicles tended to have a lower $\delta^{15}\text{N}(\text{NO}_x)$ than gasoline vehicles resulting in lower $\delta^{15}\text{N}(\text{NO}_x)$ for the overall transportation sector. The results in these two studies have helped determine the isotopic mechanism responsible for the $\delta^{15}\text{N}(\text{NO}_x)$ signature in vehicle exhaust. However, the overall isotopic signature from vehicles is somewhat uncertain due to the large range of $\delta^{15}\text{N}$ values observed. This indicates the need for future $\delta^{15}\text{N}(\text{NO}_x)$ measurements from roadsides to help improve upon our constraint on the transportation sector's $\delta^{15}\text{N}(\text{NO}_x)$ signature. Thermally produced NO_x tended to have $\delta^{15}\text{N}(\text{NO}_x)$ values that are negative explains why natural gas burners and diesel engines tend to produce NO_x with a lower $\delta^{15}\text{N}(\text{NO}_x)$ of approximately -19 to -15‰ since they lack catalytic reduction. These $\delta^{15}\text{N}(\text{NO}_x)$ measurements, along with other literature values indicate that $\delta^{15}\text{N}(\text{NO}_x)$ has been characterized for approximately 80% of the NO_x emission budget in the

United States. While the number of studies is limited, they do indicate that there are distinctive values for soil NO_x emission (denitrification/nitrification), thermal NO_x from fossil-fuel combustion, and fuel source NO_x from fossil-fuel combustion (such as coal combustion). Using the 2011 US-EPA NO_x emission inventory, a mass-balance $\delta^{15}\text{N}(\text{NO}_x)$ model was created to predicted bi-monthly $\delta^{15}\text{N}(\text{NO}_x)$ values across the continental United States (isoscape). This model predicts spatial and temporal variations in $\delta^{15}\text{N}(\text{NO}_x)$ assuming the NO_x emission and NO_x ^{15}N assumptions are correct. In most urban areas, $\delta^{15}\text{N}(\text{NO}_x)$ is predicted to range between -13 to -4‰, reflecting the larger contribution from transportation NO_x . In regions dominated by soil emissions, such as the Great Plains, $\delta^{15}\text{N}(\text{NO}_x)$ is predicted to range from -31 to -15‰, while regions dominated by coal-fired power plant NO_x emissions have predicted $\delta^{15}\text{N}(\text{NO}_x)$ values ranging between 1-9‰. Future studies should aim to measure $\delta^{15}\text{N}(\text{NO}_x)$ in some of these distinctive $\delta^{15}\text{N}(\text{NO}_x)$ regions to test the validity of the model. Additionally, future studies should aim to quantify $\delta^{15}\text{N}(\text{NO}_x)$ from industrial processes, marine vessels, oil, and biomass-burning fossil-fuel combustion, which represents 8.5%, 2.9%, 1.9%, and 0.8% of NO_x emissions in the United States, but can be regionally even more important.

9.2 $\delta^{15}\text{N}$ and $\delta^{18}\text{O}$ Isotope Effects

The role equilibrium isotope effects has on $\delta^{15}\text{N}$ and $\delta^{18}\text{O}$ values of NO_x and its oxidation products (e.g. HNO_3 , HONO) has been evaluated using a combination of theoretical computational chemistry calculations and experimental investigations. Overall, it was determined that equilibrium isotope effects tend be large for ^{15}N and relatively small for ^{18}O . For molecules at isotopic equilibrium generally it is observed that ^{15}N prefers to partition into the more oxidized molecule, while ^{18}O prefers to partitioning into O atom positions that are bonded to more electronegative atoms. Isotopic equilibrium fractionation factors are calculated in the harmonic and rigid-rotor approximations. However, in my experimental investigation of the ^{15}N isotopic

exchange between NO and NO₂ found that inclusion of anharmonicity was essential for accurate calculation of equilibrium fractionation factors. Previously, N isotopic equilibrium between NO and NO₂ has been suggested to control the $\delta^{15}\text{N}$ of atmospheric NO and NO₂. Using my experimentally determined isotopic equilibrium fractionation factor for this exchange reaction, $\delta^{15}\text{N}$ of NO₂ was modeled as a function of time. During the daytime, isotopic exchange between NO and NO₂ is most significant due to the co-existence of both NO and NO₂ that results from the photochemical cycling of NO_x. The highest $\delta^{15}\text{N}(\text{NO}_2)$ are thus predicted to occur during the daytime. During the nighttime, the photochemical cycling of NO_x ceases, and nearly all NO_x exists as NO₂. Under these conditions, the isotopic exchange between NO and NO₂ nearly ceases and $\delta^{15}\text{N}(\text{NO}_2)$ approximately equals the $\delta^{15}\text{N}(\text{NO}_x)$. The simple case in which isotopic equilibrium between NO and NO₂ controls the ¹⁵N partitioning between these two molecules may not always be correct. The photochemical cycling of NO_x may also be influenced by other isotope effects such as NO oxidation and NO₂ photolysis. I have used *ab initio* methods to calculate the kinetic isotope effect of NO oxidation by O₃, which indicates that ¹⁴NO reacts faster than ¹⁵NO by approximately -7.2‰ at 298 K. This isotope fractionation factor is in the opposite direction as the isotopic exchange between NO and NO₂. If both of these factors are important on the ¹⁵N partitioning between NO and NO₂ in the atmosphere, then the actual $\delta^{15}\text{N}$ value of NO₂ may reflect a mixture of these two fractionation factors. Future studies need to also determine the photolytic isotope effect associated with NO₂ photolysis and conduct isotopic modeling of the photochemical cycling of NO_x to help elucidate the isotope effect controls on $\delta^{15}\text{N}$ of NO and NO₂.

Using the calculated isotope effects, a simple model was constructed that predicts $\delta^{18}\text{O}$ - $\delta^{15}\text{N}$ relationships between the major atmospheric nitrate formation pathways. During the daytime, atmospheric nitrate is primarily produced through the reaction between NO₂ and •OH. Assuming isotopic equilibrium between NO and NO₂ as well as assuming O isotopic mass-balance, $\delta^{15}\text{N}$ and $\delta^{18}\text{O}$ was predicted for this pathway of -4.2 to 10.8‰ and 52.8 to 67.8‰, respectively. During the nighttime,

atmospheric nitrate may be produced through either the hydrolysis of N_2O_5 or the hydrogen abstraction by NO_3 . Under nighttime conditions, isotopic equilibrium may be achieved between NO_2 , NO_3 and N_2O_5 . Using equilibrium isotope effects and mass-balance, $\delta^{15}\text{N}$ and $\delta^{18}\text{O}$ was predicted for N_2O_5 hydrolysis of 10.5 to 25.5‰ and 97.0 to 109.5‰, respectively and for NO_3 hydrogen abstraction of -33.1 to -18.1‰ and 102.9 to 112.9‰, respectively. Thus, the three major pathways for atmospheric nitrate formation may have distinctive $\delta^{18}\text{O}$ - $\delta^{15}\text{N}$ arrays. In general, the predicted values tend to agree with the range of reported $\delta^{18}\text{O}$ - $\delta^{15}\text{N}$ values of atmospheric nitrate and may help explain the seasonal trend observed in both $\delta^{15}\text{N}$ and $\delta^{18}\text{O}$ in which lower values are observed during the summer (reflecting greater contribution of $\text{NO}_2 + \bullet\text{OH}$ reaction) and higher values are observed during the winter (reflecting greater contribution of N_2O_5 hydrolysis). The key driver in our isotope model is NO_2 as this molecule is assumed to be in equilibrium with NO during the daytime and NO_3 and N_2O_5 during the nighttime. Thus, future studies need to accurately determine the diurnal isotopic composition of NO_2 .

9.3 *in situ* NO_x Isotopic Measurements

In order to evaluate the influences of NO_x emission sources and isotope effects on the influences of NO_2 , which serves as precursor molecule to atmospheric nitrate, ambient NO_2 was collected and analyzed for its isotopic composition. NO_2 was collected from ambient air at a small Midwestern city (West Lafayette, IN, USA) during the daytime and nighttime separately between July 7 to August 5, 2016. A strong diurnal profile is observed in $\delta^{18}\text{O}(\text{NO}_2)$ in which large values are observed during the daytime and low values are observed during the nighttime. This is the result from the photochemical cycling of NO_x that erases any initial $\delta^{18}\text{O}(\text{NO}_x)$ signature from various emission sources. Our daytime $\delta^{18}\text{O}(\text{NO}_2)$ values suggest that NO oxidation primarily occurred through O_3 but on some days NO oxidation by $\text{ROO}\bullet$ may have been important. Thus, $\delta^{18}\text{O}(\text{NO}_2)$ may serve as a useful proxy for assessing

the NO oxidation branching ratios. This could be an important way to track ROO• oxidation which has important implications since this reaction provides a pathway the formation of tropospheric O₃. Nighttime $\delta^{18}\text{O}(\text{NO}_2)$ was hypothesized to have a source component; however, $\delta^{18}\text{O}(\text{NO}_x)$ source values are relatively unknown due to the difficulty in preserving $\delta^{18}\text{O}$ in NO_x collection devices from emission sources that primarily emit NO_x as NO. Future work should aim to develop techniques for identifying characterizing $\delta^{18}\text{O}(\text{NO})$ of NO_x sources.

Nighttime $\delta^{15}\text{N}(\text{NO}_2)$ is assumed to reflect NO_x emission sources as isotope effects that may partition ¹⁵N between NO and NO_x such be relatively unimportant since during the night NO_x primarily exists as NO₂. In general, it is found that nighttime $\delta^{15}\text{N}(\text{NO}_2)$ tends to be negative and close to the range of estimated $\delta^{15}\text{N}(\text{NO}_x)$ from the transportation sector. However, there are a few occasions in which nighttime $\delta^{15}\text{N}(\text{NO}_2)$ is much lower than expected from the transportation sector. This indicates that soil emissions may have been an important source of NO_x on some occasions at the sampling location. Thus, $\delta^{15}\text{N}(\text{NO}_2)$ may serve as a useful tracer for changing relative importance of NO_x emission sources and an evaluation of the long-range transport of NO_x from agricultural fields into cities. Daytime $\delta^{15}\text{N}(\text{NO}_2)$ tended to be on average larger than nighttime $\delta^{15}\text{N}(\text{NO}_2)$. Daytime $\delta^{15}\text{N}(\text{NO}_2)$ is suspected to be a complex function of $\delta^{15}\text{N}(\text{NO}_x)$ sources and isotope effects that may partition ¹⁵N between NO and NO₂. Thus, the slightly larger daytime $\delta^{15}\text{N}(\text{NO}_2)$ may reflect either greater contributions from NO_x sources with a higher $\delta^{15}\text{N}(\text{NO}_x)$ signature or possible isotope effects. Using a previously derived daytime ¹⁵N fractionation factor between NO and NO_x I estimate daytime $\delta^{15}\text{N}(\text{NO}_2)$ to be approximately 2 to 4‰ higher relative to total NO_x. Accounting for these possible isotope effects suggests that $\delta^{15}\text{N}(\text{NO}_2)$ primarily derives from vehicles as expected at this sampling location. The large variations in diurnal $\delta^{15}\text{N}(\text{NO}_2)$ was not observed as previously predicted in an ¹⁵N isotopic equilibrium model between NO and NO₂. This may have been the result of the NO₂ sampling set-up in which NO₂ was sampled over a course of 8 hours and these large variations in $\delta^{15}\text{N}(\text{NO}_2)$ thus may have been averaged out. Future

studies should aim to sample ambient NO_2 at fine intervals (1 to 2 hours) as well as characterize $\Delta^{17}\text{O}$.

9.4 Future Outlook

This research suggests the potential to use the stable isotopes of NO_x to partition NO_x emission sources and evaluate NO_x oxidation pathways. Future research can build off this work by improving and further characterizing NO_x from various emission sources with a focus on soil emissions. As NO_x emissions from fossil-fuel combustion continues to decrease due to advent of NO_x reduction technology, soil emitted NO_x may increase in the future as the demand for food increases with increasing population. Soil NO_x may become an extremely important source of NO_x and better estimates of its contribution to the NO_x emission budget need to be accurately known. The $\delta^{15}\text{N}$ of ambient NO_x may be a useful tracer for $\delta^{15}\text{N}(\text{NO}_x)$ under conditions in which NO_x primarily exists as NO_x . Since NO_2 is generally easier to collect than NO , the isotope effects associated with the photochemical cycling of NO_x needs to be better addressed. I have presented research related to the equilibrium isotope effect between NO and NO_2 as well as NO oxidation by O_3 , but the photolysis of NO_2 needs to be determined. Once these factors are known, they can be included in the next generation of atmospheric chemistry models to help predict the isotope effects of the photochemical cycle of NO_x under varying conditions. My results also suggest that $\delta^{18}\text{O}(\text{NO}_x)$ signatures may play an important role on $\delta^{18}\text{O}(\text{NO}_2)$ during the nighttime. Thus, $\delta^{18}\text{O}(\text{NO}_x)$ signatures need to be determined in the future. Due to the difficulties in preserving $\delta^{18}\text{O}(\text{NO})$ using typical NO_x collection devices, this may require the development of an optical based system. This system could be extremely useful if it could measure $\delta^{15}\text{N}$ and $\delta^{18}\text{O}$ of both NO and NO_2 . Additionally, there may be additional useful information in the clumped isotope signatures of NO ($^{15}\text{N}^{18}\text{O}$) and NO_2 ($^{15}\text{N}^{18}\text{O}^{16}\text{O}$) that may provide an additional dimension for partition NO_x sources and understanding atmospheric processes.

This research also suggests the potential to use $\delta^{18}\text{O}(\text{NO}_x)$ to evaluate the oxidation pathways of NO. However, there are still several limitations in this approach. The $\delta^{18}\text{O}$ values of ROO• needs to be determined via experimental and/or theoretical approaches, and the isotope effect associated with the reaction between ROO• and NO needs to be addressed as well. Modeling of these effects in the next generation of atmospheric chemistry models and comparing to field $\delta^{18}\text{O}(\text{NO}_2)$ measurement will enable an evaluation of our chemistry models. Additionally, it will enable an estimate of the spatial and temporal variations in the generation of tropospheric O_3 through NO reactions with ROO•.

NO_x represents a major Nr compound and future work should apply the same techniques used this research to ammonia (NH_3). Combining isotopic fingerprint measurements of NO_x and NH_3 may enable the creation of “unmixing” isotope models that may help better constrain emission sources and will help guide future regulations. Once NH_3 emission sources have accurately been characterized for $\delta^{15}\text{N}$ signatures, trace gas collectors for isotopic analysis that can be readily deployed into the field need to be developed and implemented across the United States.

LIST OF REFERENCES

LIST OF REFERENCES

- [1] P. J. Crutzen, *Gas-phase nitrogen and methane chemistry in the atmosphere*. Dordrecht, Holland: D. Reidel Publishing Company, 1973.
- [2] P. J. Crutzen, "The role of NO and NO₂ in the chemistry of the troposphere and stratosphere," *Annual review of earth and planetary sciences*, vol. 7, pp. 443–472, 1979.
- [3] J. A. Logan, "Nitrogen oxides in the troposphere: Global and regional budgets," *Journal of Geophysical Research: Oceans*, vol. 88, pp. 10785–10807, Dec. 1983.
- [4] J. N. Galloway, F. J. Dentener, D. G. Capone, E. W. Boyer, R. W. Howarth, S. P. Seitzinger, G. P. Asner, C. Cleveland, P. Green, and E. Holland, "Nitrogen cycles: past, present, and future," *Biogeochemistry*, vol. 70, no. 2, pp. 153–226, 2004.
- [5] M. G. Lawrence and P. J. Crutzen, "Influence of NO_x emissions from ships on tropospheric photochemistry and climate," *Nature*, vol. 402, no. 6758, pp. 167–170, 1999.
- [6] P. Leighton, *Photochemistry of air pollution*. New York: Academic, 1961.
- [7] B. J. Finlayson-Pitts and J. N. Pitts Jr, *Chemistry of the upper and lower atmosphere: theory, experiments, and applications*. Academic press, 1999.
- [8] K. U. Ingold, "Peroxy radicals," *Accounts of Chemical Research*, vol. 2, no. 1, pp. 1–9, 1969.
- [9] S. Solomon, D. Qin, M. Manning, Z. Chen, M. Marquis, K. B. Averyt, M. Tignor, and H. L. Miller, *IPCC, 2007: Climate change 2007: The physical science basis*. New York: Cambridge University Press, 2007.
- [10] J. G. Calvert, A. Lazrus, G. L. Kok, B. G. Heikes, J. G. Walega, J. Lind, and C. A. Cantrell, "Chemical mechanisms of acid generation in the troposphere," *Nature*, vol. 317, no. 6032, pp. 27–35, 1985.
- [11] J. M. Melillo and E. B. Cowling, "Reactive nitrogen and public policies for environmental protection," *AMBIO: A Journal of the Human Environment*, vol. 31, no. 2, pp. 150–158, 2002.
- [12] S. Reis, R. W. Pinder, M. Zhang, G. Lijie, and M. A. Sutton, "Reactive nitrogen in atmospheric emission inventories a review," *Atmos. Chem. Phys. Discuss*, vol. 9, pp. 12–413, 2009.

- [13] L. Jaegle, L. Steinberger, R. V. Martin, and K. Chance, "Global partitioning of NO_x sources using satellite observations: Relative roles of fossil fuel combustion, biomass burning and soil emissions," *Faraday Discussions*, vol. 130, pp. 407–423, 2005.
- [14] "EPA - TTN EMC Method 7 - Nitrogen Oxide (NO_x)."
- [15] C. A. M. Brenninkmeijer, "Applications of stable isotope analysis to atmospheric trace gas budgets," in *EPJ Web of Conferences*, vol. 1, pp. 137–148, EDP Sciences, 2009.
- [16] C. A. M. Brenninkmeijer, C. Janssen, J. Kaiser, T. Rockmann, T. S. Rhee, and S. S. Assonov, "Isotope Effects in the Chemistry of Atmospheric Trace Compounds," *Chemical Reviews*, vol. 103, pp. 5125–5162, Dec. 2003.
- [17] M. J. Whiticar, "Carbon and hydrogen isotope systematics of bacterial formation and oxidation of methane," *Chemical Geology*, vol. 161, no. 1, pp. 291–314, 1999.
- [18] C. M. Stevens and A. Engelkemeir, "Stable carbon isotopic composition of methane from some natural and anthropogenic sources," *Journal of Geophysical Research: Atmospheres*, vol. 93, no. D1, pp. 725–733, 1988.
- [19] C. D. Keeling, "The concentration and isotopic abundances of carbon dioxide in the atmosphere," *Tellus*, vol. 12, no. 2, pp. 200–203, 1960.
- [20] C. D. Keeling, T. P. Whorf, M. Wahlen, and J. v. d. Plicht, "Interannual extremes in the rate of rise of atmospheric carbon dioxide since 1980," *Nature*, vol. 375, no. 6533, pp. 666–670, 1995.
- [21] C. A. M. Brenninkmeijer, T. Rockmann, M. Braunlich, P. Jockel, and P. Bergamaschi, "Review of progress in isotope studies of atmospheric carbon monoxide," *Chemosphere - Global Change Science*, vol. 1, pp. 33–52, Aug. 1999.
- [22] C. M. Stevens, L. Krout, D. Walling, A. Venters, A. Engelkemeir, and L. E. Ross, "The isotopic composition of atmospheric carbon monoxide," *Earth and Planetary Science Letters*, vol. 16, pp. 147–165, Oct. 1972.
- [23] K.-R. Kim and H. Craig, "Nitrogen-15 and oxygen-18 characteristics of nitrous oxide: A global perspective," *Science*, vol. 262, no. 5141, pp. 1855–1857, 1993.
- [24] T. Rahn and M. Wahlen, "Stable isotope enrichment in stratospheric nitrous oxide," *Science*, vol. 278, no. 5344, pp. 1776–1778, 1997.
- [25] H. Craig, C. C. Chou, J. A. Welhan, C. M. Stevens, and A. Engelkemeir, "The Isotopic Composition of Methane in Polar Ice Cores," *Science*, vol. 242, p. 1535, Dec. 1988.
- [26] H. Friedli, H. Lotscher, H. Oeschger, U. Siegenthaler, and B. Stauffer, "Ice core record of the $^{13}\text{C}/^{12}\text{C}$ ratio of atmospheric CO_2 in the past two centuries," *Nature*, vol. 324, no. 6094, pp. 237–238, 1986.

- [27] E. M. Elliott, C. Kendall, S. D. Wankel, D. A. Burns, E. W. Boyer, K. Harlin, D. J. Bain, and T. J. Butler, "Nitrogen isotopes as indicators of NO_x source contributions to atmospheric nitrate deposition across the midwestern and northeastern United States," *Environmental Science & Technology*, vol. 41, no. 22, pp. 7661–7667, 2007.
- [28] E. M. Elliott, C. Kendall, E. W. Boyer, D. A. Burns, G. G. Lear, H. E. Golden, K. Harlin, A. Bytnerowicz, T. J. Butler, and R. Glatz, "Dual nitrate isotopes in dry deposition: Utility for partitioning NO_x source contributions to landscape nitrogen deposition," *Journal of Geophysical Research. Biogeosciences*, vol. 114, no. 4, 2009.
- [29] G. Michalski, *Isotopic studies of nitrate and nitrogen dioxide: atmospheric and biosphere N cycling*. PhD thesis, University of California, San Diego, 2003.
- [30] G. Michalski, S. K. Bhattacharya, and D. F. Mase, "Oxygen isotope dynamics of atmospheric nitrate and its precursor molecules," in *Handbook of environmental isotope geochemistry*, pp. 613–635, Springer, 2012.
- [31] H. D. Freyer, "Seasonal trends of NH_4^+ and NO_3^- nitrogen isotope composition in rain collected at Julich, Germany," *Tellus*, vol. 30, no. 1, pp. 83–92, 1978.
- [32] T. H. E. Heaton, " $^{15}\text{N}/^{14}\text{N}$ ratios of nitrate and ammonium in rain at Pretoria, South Africa," *Atmospheric Environment (1967)*, vol. 21, no. 4, pp. 843–852, 1987.
- [33] H. Moore, "The isotopic composition of ammonia, nitrogen dioxide and nitrate in the atmosphere," *Atmospheric Environment (1967)*, vol. 11, no. 12, pp. 1239–1243, 1977.
- [34] C. Kendall, "Tracing nitrogen sources and cycling in catchments," *Isotope tracers in catchment hydrology*, vol. 1, pp. 519–576, 1998.
- [35] T. H. E. Heaton, " $^{15}\text{N}/^{14}\text{N}$ ratios of NO_x from vehicle engines and coal-fired power stations," *Tellus B*, vol. 42, no. 3, pp. 304–307, 1990.
- [36] M. Ammann, R. Siegwolf, F. Pichlmayer, M. Suter, M. Saurer, and C. Brunold, "Estimating the uptake of traffic-derived NO_2 from ^{15}N abundance in Norway spruce needles," *Oecologia*, vol. 118, pp. 124–131, Feb. 1999.
- [37] K. Redling, E. Elliott, D. Bain, and J. Sherwell, "Highway contributions to reactive nitrogen deposition: tracing the fate of vehicular NO_x using stable isotopes and plant biomonitors," *Biogeochemistry*, vol. 116, pp. 261–274, May 2013.
- [38] M. M. Savard, C. Begin, A. Smirnoff, J. Marion, and E. Rioux-Paquette, "Tree-ring nitrogen isotopes reflect anthropogenic NO_x emissions and climatic effects," *Environmental science & technology*, vol. 43, no. 3, pp. 604–609, 2009.
- [39] J. D. Felix and E. M. Elliott, "Isotopic composition of passively collected nitrogen dioxide emissions: Vehicle, soil and livestock source signatures," *Atmospheric Environment*, vol. 92, pp. 359–366, Aug. 2014.

- [40] J. D. Felix, E. M. Elliott, and S. L. Shaw, "Nitrogen Isotopic Composition of Coal-Fired Power Plant NO_x : Influence of Emission Controls and Implications for Global Emission Inventories," *Environmental Science & Technology*, vol. 46, pp. 3528–3535, Mar. 2012.
- [41] D. Li and X. Wang, "Nitrogen isotopic signature of soil-released nitric oxide (NO) after fertilizer application," *Atmospheric Environment*, vol. 42, pp. 4747–4754, June 2008.
- [42] J. D. Felix and E. M. Elliott, "The agricultural history of human-nitrogen interactions as recorded in ice core $\delta^{15}\text{N-NO}_3^-$," *Geophysical Research Letters*, vol. 40, no. 8, pp. 1642–1646, 2013.
- [43] T. Hoering, "The isotopic composition of the ammonia and the nitrate ion in rain," *Geochimica et Cosmochimica Acta*, vol. 12, no. 1, pp. 97–102, 1957.
- [44] M. G. Hastings, J. C. Jarvis, and E. J. Steig, "Anthropogenic Impacts on Nitrogen Isotopes of Ice-Core Nitrate," *Science*, vol. 324, pp. 1288–1288, June 2009.
- [45] D. L. Fibiger, M. G. Hastings, A. F. Lew, and R. E. Peltier, "Collection of NO and NO_2 for Isotopic Analysis of NO_x Emissions," *Analytical Chemistry*, vol. 86, pp. 12115–12121, Dec. 2014.
- [46] H. D. Freyer, D. Kley, A. Volz-Thomas, and K. Kobel, "On the interaction of isotopic exchange processes with photochemical reactions in atmospheric oxides of nitrogen," *Journal of Geophysical Research*, vol. 98, no. D8, pp. 14791–14796, 1993.
- [47] B. Dahal and M. G. Hastings, "Technical considerations for the use of passive samplers to quantify the isotopic composition of NO_x and NO_2 using the denitrifier method," *Atmospheric Environment*, vol. 143, pp. 60–66, Oct. 2016.
- [48] W. C. Vicars and J. Savarino, "Quantitative constraints on the ^{17}O excess signature of surface ozone: Ambient measurements from 50 N to 50 S using the nitrite-coated filter technique," *Geochimica et Cosmochimica Acta*, vol. 135, pp. 270–287, 2014.
- [49] D. F. Mase, "A coupled modeling and observational approach to understanding oxygen-18 in atmospheric nitrate," 2010.
- [50] F. Beyn, V. Matthias, and K. Dahnke, "Changes in atmospheric nitrate deposition in Germany An isotopic perspective," *Environmental Pollution*, vol. 194, pp. 1–10, Nov. 2014.
- [51] W. Durka, E.-D. Schulze, G. Gebauer, and S. Voerkeliust, "Effects of forest decline on uptake and leaching of deposited nitrate determined from ^{15}N and ^{18}O measurements," *Nature*, vol. 372, pp. 765–767, Dec. 1994.
- [52] W. C. Vicars, S. Morin, J. Savarino, N. L. Wagner, J. Erbland, E. Vince, J. M. F. Martins, B. M. Lerner, P. K. Quinn, D. J. Coffman, and others, "Spatial and diurnal variability in reactive nitrogen oxide chemistry as reflected in the isotopic composition of atmospheric nitrate: Results from the CalNex 2010 field study," *Journal of Geophysical Research: Atmospheres*, vol. 118, no. 18, 2013.

- [53] G. Michalski, Z. Scott, M. Kabling, and M. H. Thiemens, "First measurements and modeling of $\Delta^{17}\text{O}$ in atmospheric nitrate," *Geophysical Research Letters*, vol. 30, p. 1870, Aug. 2003.
- [54] S. Morin, J. Savarino, M. M. Frey, N. Yan, S. Bekki, J. W. Bottenheim, and J. M. Martins, "Tracing the origin and fate of NO_x in the Arctic atmosphere using stable isotopes in nitrate," *Science*, vol. 322, no. 5902, pp. 730–732, 2008.
- [55] G. Michalski, S. K. Bhattacharya, and G. Girsch, " NO_x cycle and the tropospheric ozone isotope anomaly: an experimental investigation," *Atmospheric Chemistry and Physics*, vol. 14, no. 10, pp. 4935–4953, 2014.
- [56] J. Savarino, S. K. Bhattacharya, S. Morin, M. Baroni, and J.-F. Doussin, "The $\text{NO} + \text{O}_3$ reaction: A triple oxygen isotope perspective on the reaction dynamics and atmospheric implications for the transfer of the ozone isotope anomaly," *The Journal of chemical physics*, vol. 128, no. 19, p. 194303, 2008.
- [57] D. Krankowsky, F. Bartecki, G. G. Klees, K. Mauersberger, K. Schellenbach, and J. Stehr, "Measurement of heavy isotope enrichment in tropospheric ozone," *Geophysical Research Letters*, vol. 22, pp. 1713–1716, July 1995.
- [58] J. C. Johnston and M. H. Thiemens, "The isotopic composition of tropospheric ozone in three environments," *Journal of Geophysical Research: Atmospheres*, vol. 102, no. D21, pp. 25395–25404, 1997.
- [59] M. K. Dubey, R. Mohrschladt, N. M. Donahue, and J. G. Anderson, "Isotope specific kinetics of hydroxyl radical (OH) with water (H_2O): Testing models of reactivity and atmospheric fractionation," *The Journal of Physical Chemistry A*, vol. 101, no. 8, pp. 1494–1500, 1997.
- [60] P. Kroopnick and H. Craig, "Atmospheric oxygen: isotopic composition and solubility fractionation," *Science*, vol. 175, no. 4017, pp. 54–55, 1972.
- [61] A. Smirnoff, M. M. Savard, R. Vet, and M.-C. Simard, "Nitrogen and triple oxygen isotopes in near-road air samples using chemical conversion and thermal decomposition," *Rapid Communications in Mass Spectrometry*, vol. 26, pp. 2791–2804, Dec. 2012.
- [62] S. Morin, J. Savarino, S. Bekki, S. Gong, and J. W. Bottenheim, "Signature of Arctic surface ozone depletion events in the isotope anomaly ($\Delta^{17}\text{O}$) of atmospheric nitrate," *Atmospheric Chemistry and Physics*, vol. 7, no. 5, pp. 1451–1469, 2007.
- [63] D. H. Campbell, C. Kendall, C. C. Chang, S. R. Silva, and K. A. Tonnessen, "Pathways for nitrate release from an alpine watershed: determination using $\delta^{15}\text{N}$ and $\delta^{18}\text{O}$," *Water Resources Research*, vol. 38, no. 5, pp. 101–109, 2002.
- [64] R. Atkinson, "Atmospheric chemistry of VOCs and NO_x ," *Atmospheric environment*, vol. 34, no. 12, pp. 2063–2101, 2000.
- [65] J. Pearson, D. M. Wells, K. J. Sellar, A. Bennett, A. Soares, J. Woodall, and M. J. Ingrouille, "Traffic exposure increases natural ^{15}N and heavy metal concentrations in mosses," *New Phytologist*, vol. 147, pp. 317–326, Aug. 2000.

- [66] S. G. Jennings, "The mean free path in air," *Journal of Aerosol Science*, vol. 19, no. 2, pp. 159–166, 1988.
- [67] W. J. Massman, "A review of the molecular diffusivities of H₂O, CO₂, CH₄, CO, O₃, SO₂, NH₃, N₂ O, NO, and NO₂ in air, O₂ and N₂ near STP," *Atmospheric Environment*, vol. 32, no. 6, pp. 1111–1127, 1998.
- [68] N. V. Heeb, C. J. Saxer, A.-M. Forss, and S. BrÄijhlmann, "Trends of NO, NO₂, and NH₃ emissions from gasoline-fueled Euro3 to Euro 4 passenger cars," *Atmospheric Environment*, vol. 42, no. 10, pp. 2543–2554, 2008.
- [69] D. M. Sigman, K. L. Casciotti, M. Andreani, C. Barford, M. Galanter, and J. K. Bohlke, "A bacterial method for the nitrogen isotopic analysis of nitrate in seawater and freshwater," *Analytical chemistry*, vol. 73, no. 17, pp. 4145–4153, 2001.
- [70] Y. B. Zeldovich, "The oxidation of nitrogen in combustion and explosions," *Acta Physicochim. URSS*, vol. 21, no. 4, pp. 577–628, 1946.
- [71] P. Richet, Y. Bottinga, and M. Janoy, "A review of hydrogen, carbon, nitrogen, oxygen, sulphur, and chlorine stable isotope enrichment among gaseous molecules," *Annual Review of Earth and Planetary Sciences*, vol. 5, pp. 65–110, 1977.
- [72] K. P. Huber and G. Herzberg, "Constants of diatomic molecules," in *Molecular Spectra and Molecular Structure. IV. Constants of Diatomic Molecules*, pp. 8–689, Van Nostrand Reinhold Co., 1979.
- [73] J. C. Ianni, "Kintecus," 2014.
- [74] R. Atkinson, D. L. Baulch, R. A. Cox, R. F. Hampson Jr, J. A. Kerr, and J. Troe, "Evaluated kinetic and photochemical data for atmospheric chemistry: supplement III. IUPAC subcommittee on gas kinetic data evaluation for atmospheric chemistry," *Journal of Physical and Chemical Reference Data*, vol. 18, no. 2, pp. 881–1097, 1989.
- [75] D. L. Baulch, C. J. Cobos, R. A. Cox, P. Frank, G. Hayman, T. Just, J. A. Kerr, T. Murrells, M. J. Pilling, J. Troe, and others, "Evaluated kinetic data for combustion modeling. Supplement I," *Journal of Physical and Chemical Reference Data*, vol. 23, no. 6, pp. 847–848, 1994.
- [76] K. Thielen and P. Roth, "N atom measurements in high-temperature N₂ dissociation kinetics," *AIAA journal*, vol. 24, no. 7, pp. 1102–1105, 1986.
- [77] W. Tsang and R. F. Hampson, "Chemical kinetic data base for combustion chemistry. Part I. Methane and related compounds," *Journal of Physical and Chemical Reference Data*, vol. 15, no. 3, pp. 1087–1279, 1986.
- [78] J. A. Manion, R. E. Huie, R. D. Levin, D. R. Burgess Jr, V. L. Orkin, W. Tsang, W. S. McGivern, J. W. Hudgens, V. D. Knyazev, D. B. Atkinson, and others, "NIST chemical kinetics database, NIST standard reference database 17, version 7.0 (web version), release 1.4. 3, data version 2008.12, National Institute of Standards and Technology, Gaithersburg, Maryland, 20899-8320," *Web address: <http://kinetics.nist.gov>*, 2008.

- [79] T. Shimanouchi, "Tables of molecular vibrational frequencies. Consolidated volume II," *Journal of Physical and Chemical Reference Data*, vol. 6, no. 3, pp. 993–1102, 1977.
- [80] R. Isermann, *Engine modeling and control : modelling and electronic management of internal combustion engines*. Heidelberg: Springer, 2014.
- [81] K. C. Taylor, "Nitric oxide catalysis in automotive exhaust systems," *Catalysis Reviews Science and Engineering*, vol. 35, no. 4, pp. 457–481, 1993.
- [82] H. Arai and H. Tominaga, "An infrared study of nitric oxide adsorbed on rhodium-alumina catalyst," *Journal of Catalysis*, vol. 43, no. 1, pp. 131–142, 1976.
- [83] W. C. Hecker and A. T. Bell, "Reduction of NO by CO over silica-supported rhodium: infrared and kinetic studies," *Journal of Catalysis*, vol. 84, no. 1, pp. 200–215, 1983.
- [84] F. Solymosi and J. Sarkany, "An infrared study of the surface interaction between NO and CO on Rh/Al₂O₃ catalyst," *Applications of Surface Science*, vol. 3, no. 1, pp. 68–82, 1979.
- [85] R. J. Baird, R. C. Ku, and P. Wynblatt, "The chemisorption of CO and NO on Rh (110)," *Surface Science*, vol. 97, no. 2-3, pp. 346–362, 1980.
- [86] C. T. Campbell and J. M. White, "Chemisorption and reactions of nitric oxide on rhodium," *Applications of Surface Science*, vol. 1, no. 3, pp. 347–359, 1978.
- [87] A. A. Chin and A. T. Bell, "Kinetics of nitric oxide decomposition on silica-supported rhodium," *The Journal of Physical Chemistry*, vol. 87, no. 19, pp. 3700–3706, 1983.
- [88] T. W. Root, L. D. Schmidt, and G. B. Fisher, "Adsorption and reaction of nitric oxide and oxygen on Rh (111)," *Surface science*, vol. 134, no. 1, pp. 30–45, 1983.
- [89] R. E. Hayes, L. S. Mukadi, M. Votsmeier, and J. Gieshoff, "Three-way catalytic converter modelling with detailed kinetics and washcoat diffusion," *Topics in catalysis*, vol. 30, no. 1-4, pp. 411–415, 2004.
- [90] L. S. Mukadi and R. E. Hayes, "Modelling the three-way catalytic converter with mechanistic kinetics using the NewtonKrylov method on a parallel computer," *Computers & chemical engineering*, vol. 26, no. 3, pp. 439–455, 2002.
- [91] G. C. Koltsakis and A. M. Stamatelos, "Catalytic automotive exhaust aftertreatment," *Progress in Energy and Combustion Science*, vol. 23, no. 1, pp. 1–39, 1997.
- [92] U. C. Bureau, "American Community Survey, 2011 American Community Survey 5-Year Estimate, travel time to work by zip code, table B08303."
- [93] C. T. Garten, "Nitrogen Isotope Composition of Ammonium and Nitrate in Bulk Precipitation and Forest Throughfall," *International Journal of Environmental Analytical Chemistry*, vol. 47, pp. 33–45, Apr. 1992.

- [94] L. Geng, B. Alexander, J. Cole-Dai, E. J. Steig, J. Savarino, E. D. Sofen, and A. J. Schauer, "Nitrogen isotopes in ice core nitrate linked to anthropogenic atmospheric acidity change," *Proceedings of the National Academy of Sciences*, vol. 111, pp. 5808–5812, Apr. 2014.
- [95] S. D. Burch, M. A. Keyser, C. P. Colucci, T. F. Potter, D. K. Benson, and J. P. Biel, "Applications and benefits of catalytic converter thermal management," tech. rep., SAE Technical Paper, 1996.
- [96] P. M. Laing, "Development of an alternator-powered electrically-heated catalyst system," tech. rep., SAE Technical Paper, 1994.
- [97] P. L. Burk, J. K. Hochmuth, D. R. Anderson, S. Sung, S. J. Tauster, C. O. Tolentino, J. Rogalo, G. Miles, M. Niejako, A. Punke, and others, "Cold start hydrocarbon emissions control," tech. rep., SAE Technical Paper, 1995.
- [98] H. Levy, "Normal Atmosphere: Large Radical and Formaldehyde Concentrations Predicted," *Science*, vol. 173, pp. 141–143, July 1971.
- [99] S.-W. Kim, A. Heckel, G. J. Frost, A. Richter, J. Gleason, J. P. Burrows, S. McKeen, E.-Y. Hsie, C. Granier, and M. Trainer, "NO₂ columns in the western United States observed from space and simulated by a regional chemistry model and their implications for NO_x emissions," *Journal of Geophysical Research: Atmospheres*, vol. 114, p. D11301, June 2009.
- [100] W. W. Walters, B. D. Tharp, H. Fang, B. J. Kozak, and G. Michalski, "Nitrogen isotope composition of thermally produced NO_x from various fossil-fuel combustion sources," *Environmental science & technology*, 2015.
- [101] W. W. Walters and G. Michalski, "Theoretical calculation of nitrogen isotope equilibrium exchange fractionation factors for various NO_y molecules," *Geochimica et Cosmochimica Acta*, vol. 164, pp. 284–297, Sept. 2015.
- [102] C. T. Bowman, "Kinetics of pollutant formation and destruction in combustion," *Progress in Energy and Combustion Science*, vol. 1, no. 1, pp. 33–45, 1975.
- [103] A. N. Hayhurst and I. M. Vince, "Nitric oxide formation from N₂ in flames: The importance of prompt NO," *Progress in Energy and Combustion Science*, vol. 6, no. 1, pp. 35–51, 1980.
- [104] J. L. Toof, "A Model for the Prediction of Thermal, Prompt, and Fuel NO_x Emissions From Combustion Turbines," *Journal of Engineering for Gas Turbines and Power*, vol. 108, pp. 340–347, Apr. 1986.
- [105] J. B. Heywood, "Pollutant formation and control in spark-ignition engines," *Progress in Energy and Combustion Science*, vol. 1, no. 4, pp. 135–164, 1976.
- [106] S. M. Correa, "A review of NO_x formation under gas-turbine combustion conditions," *Combustion science and technology*, vol. 87, no. 1-6, pp. 329–362, 1993.
- [107] L. Q. Maurice, H. Lander, T. Edwards, and W. E. Harrison III, "Advanced aviation fuels: a look ahead via a historical perspective," *Fuel*, vol. 80, pp. 747–756, Apr. 2001.

- [108] L. Tsague, J. Tsogo, and T. T. Tatietsse, "Prediction of the production of nitrogen oxide in turbojet engines," *Atmospheric Environment*, vol. 40, pp. 5727–5733, Sept. 2006.
- [109] J. A. Miller and C. T. Bowman, "Mechanism and modeling of nitrogen chemistry in combustion," *Progress in Energy and Combustion Science*, vol. 15, no. 4, pp. 287–338, 1989.
- [110] J. W. Bozzelli and A. M. Dean, "O + NNH: A possible new route for NO_x formation in flames," *International Journal of Chemical Kinetics*, vol. 27, pp. 1097–1109, Nov. 1995.
- [111] H. C. Urey, "The thermodynamic properties of isotopic substances," *J. chem. Soc.*, vol. 7, pp. 562–581, 1947.
- [112] F. Beyn, V. Matthias, A. Aulinger, and K. Dahnke, "Do N-isotopes in atmospheric nitrate deposition reflect air pollution levels?," *Atmospheric Environment*, vol. 107, pp. 281–288, Apr. 2015.
- [113] U. E. Office of Air Quality Planning and Standards, "2011 National Emissions Inventory Data & Documentation."
- [114] M. Flamme, "Low NO_x combustion technologies for high temperature applications," *Energy Conversion and Management*, vol. 42, pp. 1919–1935, Oct. 2001.
- [115] J. B. Heywood, *Internal combustion engine fundamentals*, vol. 930. Mcgraw-hill New York, 1988.
- [116] L. Guzzella and C. Onder, *Introduction to modeling and control of internal combustion engine systems*. Springer Science & Business Media, 2009.
- [117] R. C. Flagan and J. H. Seinfeld, *Fundamentals of Air Pollution Engineering 1988*. Englewood Cliffs, NJ: Prentice-Hall.
- [118] G. Loffler, R. Sieber, M. Harasek, H. Hofbauer, R. Hauss, and J. Landauf, "NO_x formation in natural gas combustion a new simplified reaction scheme for CFD calculations," *Fuel*, vol. 85, pp. 513–523, Mar. 2006.
- [119] Nicholas A. Smith, *Flame Temperature Imaging of a Low NO_x Burner via Laser Rayleigh Scattering*. PhD thesis, Marquette University, 2009.
- [120] P. Bielaczyc, J. Merkisz, and J. Pielecha, "Investigation of Exhaust Emissions from DI Diesel Engine During Cold and Warm Start," SAE Technical Paper 2001-01-1260, SAE International, Warrendale, PA, Mar. 2001.
- [121] M. Weilenmann, P. Soltic, C. Saxer, A.-M. Forss, and N. Heeb, "Regulated and nonregulated diesel and gasoline cold start emissions at different temperatures," *Atmospheric Environment*, vol. 39, pp. 2433–2441, Apr. 2005.
- [122] S. Brandenberger, O. Krocher, A. Tissler, and R. Althoff, "The State of the Art in Selective Catalytic Reduction of NO_x by Ammonia Using Metal Exchanged Zeolite Catalysts," *Catalysis Reviews*, vol. 50, pp. 492–531, Dec. 2008.

- [123] Y. Hu, S. Naito, N. Kobayashi, and M. Hasatani, "CO₂, NO_x and SO₂ emissions from the combustion of coal with high oxygen concentration gases," *Fuel*, vol. 79, no. 15, pp. 1925–1932, 2000.
- [124] T. Le Bris, F. Cadavid, S. Caillat, S. Pietrzyk, J. Blondin, and B. Baudoin, "Coal combustion modelling of large power plant, for NO_x abatement," *Fuel*, vol. 86, pp. 2213–2220, Sept. 2007.
- [125] D. Gerard and L. B. Lave, "Implementing technology-forcing policies: The 1970 Clean Air Act Amendments and the introduction of advanced automotive emissions controls in the United States," *Technological Forecasting and Social Change*, vol. 72, pp. 761–778, Sept. 2005.
- [126] X. Yan, T. Ohara, and H. Akimoto, "Statistical modeling of global soil NO_x emissions," *Global Biogeochemical Cycles*, vol. 19, no. 3, 2005.
- [127] U. E. I. Administration, "Total consumption for United States, monthly."
- [128] R. P. Wayne, I. Barnes, P. Biggs, J. P. Burrows, C. E. Canosa-Mas, J. Hjorth, G. Le Bras, G. K. Moortgat, D. Perner, G. Poulet, G. Restelli, and H. Sidebottom, "The nitrate radical: Physics, chemistry, and the atmosphere," *Atmospheric Environment. Part A. General Topics*, vol. 25, no. 1, pp. 1–203, 1991.
- [129] T. Nielsen, U. Samuelsson, P. Grennfelt, and E. L. Thomsen, "Peroxyacetyl nitrate in long-range transported polluted air," *Nature*, vol. 293, pp. 553–555, Oct. 1981.
- [130] C. Voigt, J. Schreiner, A. Kohlmann, P. Zink, K. Mauersberger, N. Larsen, T. Deshler, C. Kroger, J. Rosen, A. Adriani, and others, "Nitric acid trihydrate (NAT) in polar stratospheric clouds," *Science*, vol. 290, no. 5497, pp. 1756–1758, 2000.
- [131] J. H. Seinfeld and S. N. Pandis, *Atmospheric chemistry and physics: from air pollution to climate change*. New York: John Wiley & Sons, 2006.
- [132] G. M. Begun and W. H. Fletcher, "Partition function ratios for molecules containing nitrogen isotopes," *The Journal of Chemical Physics*, vol. 33, no. 4, pp. 1083–1085, 1960.
- [133] E. U. Monse, W. Spindel, and M. J. Stern, "Analysis of isotope-effect calculations illustrated with exchange equilibria among oxynitrogen compounds," *ACS Advance Chemistry*, vol. 89, pp. 148–184, 1969.
- [134] T. Driesner, T. K. Ha, and T. M. Seward, "Oxygen and hydrogen isotope fractionation by hydration complexes of Li⁺, Na⁺, K⁺, Mg²⁺, F, Cl, and Br: a theoretical study," *Geochimica et Cosmochimica Acta*, vol. 64, pp. 3007–3033, Sept. 2000.
- [135] K. Yamaji, Y. Makita, H. Watanabe, A. Sonoda, H. Kanoh, T. Hirotsu, and K. Ooi, "Theoretical estimation of lithium isotopic reduced partition function ratio for lithium ions in aqueous solution," *The Journal of Physical Chemistry A*, vol. 105, no. 3, pp. 602–613, 2001.

- [136] T. Oi, "Calculations of reduced partition function ratios of monomeric and dimeric boric acids and borates by the ab initio molecular orbital theory," *Journal of nuclear science and technology*, vol. 37, no. 2, pp. 166–172, 2000.
- [137] E. Schauble, G. R. Rossman, and H. P. Taylor, "Theoretical estimates of equilibrium chromium-isotope fractionations," *Chemical Geology*, vol. 205, no. 1, pp. 99–114, 2004.
- [138] A. D. Anbar, A. A. Jarzecki, and T. G. Spiro, "Theoretical investigation of iron isotope fractionation between $\text{Fe}(\text{H}_2\text{O}_6^{3+})$ and $\text{Fe}(\text{H}_2\text{O}_6^{2+})$: Implications for iron stable isotope geochemistry," *Geochimica et Cosmochimica Acta*, vol. 69, pp. 825–837, Feb. 2005.
- [139] J. H. Seo, S. K. Lee, and I. Lee, "Quantum chemical calculations of equilibrium copper (I) isotope fractionations in ore-forming fluids," *Chemical Geology*, vol. 243, no. 3, pp. 225–237, 2007.
- [140] J. A. Tossell, "Calculating the partitioning of the isotopes of Mo between oxidic and sulfidic species in aqueous solution," *Geochimica et Cosmochimica Acta*, vol. 69, no. 12, pp. 2981–2993, 2005.
- [141] T. Otake, A. C. Lasaga, and H. Ohmoto, "Ab initio calculations for equilibrium fractionations in multiple sulfur isotope systems," *Chemical Geology*, vol. 249, pp. 357–376, Apr. 2008.
- [142] J. Bigeleisen and M. G. Mayer, "Calculation of Equilibrium Constants for Isotopic Exchange Reactions," *The Journal of Chemical Physics*, vol. 15, pp. 261–267, May 1947.
- [143] G. Michalski and S. K. Bhattacharya, "The role of symmetry in the mass independent isotope effect in ozone," *Proceedings of the National Academy of Sciences*, vol. 106, pp. 5493–5496, Apr. 2009.
- [144] Q. Liu, J. A. Tossell, and Y. Liu, "On the proper use of the Bigeleisen Mayer equation and corrections to it in the calculation of isotopic fractionation equilibrium constants," *Geochimica et Cosmochimica Acta*, vol. 74, no. 24, pp. 6965–6983, 2010.
- [145] Y. Shao, Z. Gan, E. Epifanovsky, A. T. Gilbert, M. Wormit, J. Kussmann, A. W. Lange, A. Behn, J. Deng, X. Feng, D. Ghosh, M. Goldey, P. R. Horn, L. D. Jacobson, I. Kaliman, R. Z. Khaliullin, T. KuÅ, A. Landau, J. Liu, E. I. Proynov, Y. M. Rhee, R. M. Richard, M. A. Rohrdanz, R. P. Steele, E. J. Sundstrom, H. L. Woodcock, P. M. Zimmerman, D. Zuev, B. Albrecht, E. Alguire, B. Austin, G. J. O. Beran, Y. A. Bernard, E. Berquist, K. Brandhorst, K. B. Bravaya, S. T. Brown, D. Casanova, C.-M. Chang, Y. Chen, S. H. Chien, K. D. Closser, D. L. Crittenden, M. Diedenhofen, R. A. DiStasio, H. Do, A. D. Dutoi, R. G. Edgar, S. Fatehi, L. Fusti-Molnar, A. Ghysels, A. Golubeva-Zadorozhnaya, J. Gomes, M. W. Hanson-Heine, P. H. Harbach, A. W. Hauser, E. G. Hohenstein, Z. C. Holden, T.-C. Jagau, H. Ji, B. Kaduk, K. Khistyayev, J. Kim, J. Kim, R. A. King, P. Klunzinger, D. Kosenkov, T. Kowalczyk, C. M. Krauter, K. U. Lao, A. D. Laurent, K. V. Lawler, S. V. Levchenko, C. Y. Lin, F. Liu, E. Livshits, R. C. Lochan, A. Luenser, P. Manohar, S. F. Manzer, S.-P. Mao, N. Mardirossian, A. V. Marenich, S. A. Maurer, N. J. Mayhall, E. Neuscammann, C. M. Oana, R. Olivares-Amaya, D. P. OÅNeill, J. A.

- Parkhill, T. M. Perrine, R. Peverati, A. Prociuk, D. R. Rehn, E. Rosta, N. J. Russ, S. M. Sharada, S. Sharma, D. W. Small, A. Sodt, T. Stein, D. StÅijck, Y.-C. Su, A. J. Thom, T. Tsuchimochi, V. Vanovschi, L. Vogt, O. Vydrov, T. Wang, M. A. Watson, J. Wenzel, A. White, C. F. Williams, J. Yang, S. Yeganeh, S. R. Yost, Z.-Q. You, I. Y. Zhang, X. Zhang, Y. Zhao, B. R. Brooks, G. K. Chan, D. M. Chipman, C. J. Cramer, W. A. Goddard, M. S. Gordon, W. J. Hehre, A. Klamt, H. F. Schaefer, M. W. Schmidt, C. D. Sherrill, D. G. Truhlar, A. Warshel, X. Xu, A. Aspuru-Guzik, R. Baer, A. T. Bell, N. A. Besley, J.-D. Chai, A. Dreuw, B. D. Dunietz, T. R. Furlani, S. R. Gwaltney, C.-P. Hsu, Y. Jung, J. Kong, D. S. Lambrecht, W. Liang, C. Ochsenfeld, V. A. Rassolov, L. V. Slipchenko, J. E. Subotnik, T. Van Voorhis, J. M. Herbert, A. I. Krylov, P. M. Gill, and M. Head-Gordon, "Advances in molecular quantum chemistry contained in the Q-Chem 4 program package," *Molecular Physics*, vol. 113, pp. 184–215, Jan. 2015.
- [146] C. Lee, W. Yang, and R. G. Parr, "Development of the Colle-Salvetti correlation-energy formula into a functional of the electron density," *Physical review B*, vol. 37, no. 2, p. 785, 1988.
- [147] A. D. Becke, "Density functional thermochemistry. III. The role of exact exchange," *The Journal of Chemical Physics*, vol. 98, pp. 5648–5652, Apr. 1993.
- [148] C. Y. Lin, M. W. George, and P. M. Gill, "EDF2: A density functional for predicting molecular vibrational frequencies," *Australian journal of chemistry*, vol. 57, no. 4, pp. 365–370, 2004.
- [149] F. Jensen, *Introduction to Computational Chemistry*. New York: Wiley, 1999.
- [150] T. H. Dunning, "Gaussian basis sets for use in correlated molecular calculations. I. The atoms boron through neon and hydrogen," *The Journal of Chemical Physics*, vol. 90, pp. 1007–1023, Jan. 1989.
- [151] J. Foresman and A. B. Frisch, *Exploring Chemistry with Electronic Structure Methods*, vol. 302. Pittsburg, PA: Gaussian, Inc., 1996.
- [152] J. Bigeleisen and L. Friedman, "The Infra-Red Spectra of N₁₅N₁₄O₁₆ and N₁₄N₁₅O₁₆. Some Thermodynamic Properties of the Isotopic N₂O Molecules," *The Journal of Chemical Physics*, vol. 18, pp. 1656–1659, Dec. 1950.
- [153] A. Chedin, C. Amiot, and Z. Cihla, "The potential energy function of the nitrous oxide molecule using pure vibrational data," *Journal of Molecular Spectroscopy*, vol. 63, no. 3, pp. 348–369, 1976.
- [154] E. Leifer, "The Exchange of Oxygen Between NO and NO₂," *The Journal of Chemical Physics*, vol. 8, pp. 301–303, Apr. 1940.
- [155] G. M. Begun and C. E. Melton, "Nitrogen Isotopic Fractionation between NO and NO₂ and Mass Discrimination in Mass Analysis of NO₂," *The Journal of Chemical Physics*, vol. 25, pp. 1292–1293, Dec. 1956.
- [156] L. B. Yeatts, "Fractionation of Nitrogen and Oxygen Isotopes between Gaseous NO and Liquid NOCl," *The Journal of Chemical Physics*, vol. 28, pp. 1255–1255, June 1958.

- [157] L. L. Brown and J. S. Drury, "Exchange and Fractionation of Nitrogen Isotopes between NO and NO₂," *The Journal of Chemical Physics*, vol. 48, pp. 1400–1400, Feb. 1968.
- [158] L. N. Kauder, T. I. Taylor, and W. Spindel, "Isotope Enrichment Factors for Nitrogen-15 in the Nitric Oxide–Nitric Acid Exchange System," *The Journal of Chemical Physics*, vol. 31, pp. 232–235, July 1959.
- [159] A. C. Lasaga, "Atomic treatment of mineral-water surface reactions," *Reviews in Mineralogy and Geochemistry*, vol. 23, no. 1, pp. 17–85, 1990.
- [160] A. C. Lasaga, *Kinetic theory in the earth sciences*. Princeton, NJ: Princeton University Press, 1998.
- [161] J. Tomasi and M. Persico, "Molecular Interactions in Solution: An Overview of Methods Based on Continuous Distributions of the Solvent," *Chemical Reviews*, vol. 94, pp. 2027–2094, Nov. 1994.
- [162] R. A. Robinson and R. H. Stokes, *Electrolyte solutions*. New York: Academic Press, 1959.
- [163] A. Klamt and G. Schuurmann, "COSMO: a new approach to dielectric screening in solvents with explicit expressions for the screening energy and its gradient," *Journal of the Chemical Society, Perkin Transactions 2*, pp. 799–805, Jan. 1993.
- [164] T. N. Truong and E. V. Stefanovich, "A new method for incorporating solvent effect into the classical, ab initio molecular orbital and density functional theory frameworks for arbitrary shape cavity," *Chemical Physics Letters*, vol. 240, pp. 253–260, June 1995.
- [165] V. Barone and M. Cossi, "Quantum Calculation of Molecular Energies and Energy Gradients in Solution by a Conductor Solvent Model," *The Journal of Physical Chemistry A*, vol. 102, pp. 1995–2001, Mar. 1998.
- [166] M. Cossi, N. Rega, G. Scalmani, and V. Barone, "Energies, structures, and electronic properties of molecules in solution with the C-PCM solvation model," *Journal of Computational Chemistry*, vol. 24, pp. 669–681, Apr. 2003.
- [167] D. M. Chipman, "Reaction field treatment of charge penetration," *The Journal of Chemical Physics*, vol. 112, pp. 5558–5565, Apr. 2000.
- [168] E. Cancès, B. Mennucci, and J. Tomasi, "A new integral equation formalism for the polarizable continuum model: Theoretical background and applications to isotropic and anisotropic dielectrics," *The Journal of Chemical Physics*, vol. 107, pp. 3032–3041, Aug. 1997.
- [169] Y. Liu and J. A. Tossell, "Ab initio molecular orbital calculations for boron isotope fractionations on boric acids and borates," *Geochimica et Cosmochimica Acta*, vol. 69, pp. 3995–4006, Aug. 2005.
- [170] C. G. Malmberg and A. A. Maryott, "Dielectric Constant of Water from 0 to 100 C," *Journal of research of the National Bureau of Standards*, vol. 56, pp. 1–8, 1956.

- [171] K. K. Irikura, "Experimental vibrational zero-point energies: Diatomic molecules," *Journal of physical and chemical reference data*, vol. 36, no. 2, pp. 389–397, 2007.
- [172] V. R. Morris, S. C. Bhatia, and J. H. Hall, "Ab initio self-consistent field study of the vibrational spectra for nitrate radical geometric isomers," *Journal of Physical Chemistry*, vol. 94, no. 19, pp. 7414–7418, 1990.
- [173] A. K. Dutta, N. Vaval, and S. Pal, "Performance of the EOMIP-CCSD(2) Method for Determining the Structure and Properties of Doublet Radicals: A Benchmark Investigation," *Journal of Chemical Theory and Computation*, vol. 9, pp. 4313–4331, Oct. 2013.
- [174] W. J. Hehre, "Ab initio molecular orbital theory," *Acc. Chem. Res.*, vol. 9, pp. 399–406, 1976.
- [175] J. S. Andrews, D. Jayatilaka, R. G. Bone, N. C. Handy, and R. D. Amos, "Spin contamination in single-determinant wavefunctions," *Chemical physics letters*, vol. 183, no. 5, pp. 423–431, 1991.
- [176] E. R. Davidson and W. T. Borden, "Symmetry breaking in polyatomic molecules: real and artifactual," *The Journal of Physical Chemistry*, vol. 87, no. 24, pp. 4783–4790, 1983.
- [177] D. J. Thouless, *The quantum mechanics of many-body systems*. New York: Academic Press, 1961.
- [178] J. Cizek and J. Paldus, "Stability Conditions for the Solutions of the Hartree Fock Equations for Atomic and Molecular Systems. Application to the Pi-Electron Model of Cyclic Polyenes," *The Journal of Chemical Physics*, vol. 47, no. 10, pp. 3976–3985, 1967.
- [179] R. G. Pearson, *Symmetry rules for chemical reactions*, vol. 1. New York: Wiley, 1976.
- [180] J. C. Saeh and J. F. Stanton, "Application of an equation-of-motion coupled cluster method including higher-order corrections to potential energy surfaces of radicals," *The Journal of Chemical Physics*, vol. 111, pp. 8275–8285, Nov. 1999.
- [181] J. F. Stanton, "On the vibronic level structure in the NO₃ radical. I. The ground electronic state," *The Journal of Chemical Physics*, vol. 126, p. 134309, Apr. 2007.
- [182] K. B. Bravaya, E. Epifanovsky, and A. I. Krylov, "Four Bases Score a Run: Ab Initio Calculations Quantify a Cooperative Effect of H Bonding and π Stacking on the Ionization Energy of Adenine in the AATT Tetramer," *The Journal of Physical Chemistry Letters*, vol. 3, pp. 2726–2732, Sept. 2012.
- [183] E. Epifanovsky, M. Wormit, T. KuÅŽ, A. Landau, D. Zuev, K. Khistyayev, P. Manohar, I. Kaliman, A. Dreuw, and A. I. Krylov, "New implementation of high-level correlated methods using a general block tensor library for high-performance electronic structure calculations," *Journal of Computational Chemistry*, vol. 34, pp. 2293–2309, Oct. 2013.

- [184] G. M. Begun, "Nitrogen Isotope Effect in the Distillation of N_2O_4 ," *The Journal of Chemical Physics*, vol. 25, pp. 1279–1280, Dec. 1956.
- [185] L. L. Brown and G. M. Begun, "Nitrogen Isotopic Fractionation between Nitric Acid and the Oxides of Nitrogen," *The Journal of Chemical Physics*, vol. 30, pp. 1206–1209, May 1959.
- [186] D. Hurtmans, M. Herman, and J. Vander Auwera, "Integrated band intensities in N_2O_4 in the infrared range," *Journal of Quantitative Spectroscopy and Radiative Transfer*, vol. 50, pp. 595–602, Dec. 1993.
- [187] W. Spindel, M. J. Stern, and E. U. Monse, "Further studies on temperature dependences of isotope effects," *The Journal of Chemical Physics*, vol. 52, no. 4, pp. 2022–2035, 1970.
- [188] J. Savarino, S. Morin, J. Erbland, F. Granec, M. D. Patey, W. Vicars, B. Alexander, and E. P. Achterberg, "Isotopic composition of atmospheric nitrate in a tropical marine boundary layer," *Proceedings of the National Academy of Sciences of the United States of America*, vol. 110, pp. 17668–17673, Oct. 2013.
- [189] C. P. Rinsland, R. E. Boughner, J. C. Larsen, G. M. Stokes, and J. W. Brault, "Diurnal variations of atmospheric nitric oxide: Ground-based infrared spectroscopic measurements and their interpretation with time-dependent photochemical model calculations," *Journal of Geophysical Research: Atmospheres*, vol. 89, pp. 9613–9622, Oct. 1984.
- [190] H. D. Freyer, "Seasonal variation of $^{15}N/^{14}N$ ratios in atmospheric nitrate species," *Tellus B*, vol. 43, no. 1, pp. 30–44, 1991.
- [191] F. H. Verhoek and F. Daniels, "The dissociation constants of nitrogen tetroxide and of nitrogen trioxide," *Journal of the American Chemical Society*, vol. 53, pp. 1250–1263, Apr. 1931.
- [192] H. D. Sharma, R. E. Jarvis, and K. Y. Wong, "Isotopic exchange reactions in nitrogen oxides," *The Journal of Physical Chemistry*, vol. 74, pp. 923–933, Feb. 1970.
- [193] E. L. Williams and D. Grosjean, "Removal of atmospheric oxidants with annular denuders," *Environmental Science & Technology*, vol. 24, pp. 811–814, June 1990.
- [194] Z. Ali, C. L. P. Thomas, and J. F. Alder, "Denuder tubes for sampling of gaseous species. A review," *Analyst*, vol. 114, pp. 759–769, Jan. 1989.
- [195] M. R. McIlvin and M. A. Altabet, "Chemical Conversion of Nitrate and Nitrite to Nitrous Oxide for Nitrogen and Oxygen Isotopic Analysis in Freshwater and Seawater," *Analytical Chemistry*, vol. 77, pp. 5589–5595, Sept. 2005.
- [196] E. Ryabenko, M. A. Altabet, and D. W. Wallace, "Effect of chloride on the chemical conversion of nitrate to nitrous oxide for $\delta^{15}N$ analysis," *Limnology and Oceanography: Methods*, vol. 7, pp. 545–552, July 2009.
- [197] E. B. Wilson, J. C. Decius, and P. C. Cross, *Molecular Vibrations*. McGraw-Hill, New York, 1955.

- [198] “Molecular constants of nitric oxide from the near infrared spectrum,”
- [199] R. E. Blank and C. D. Hause, “Molecular constants for the (3, 0, 1) band of NO_2 ,” *Journal of Molecular Spectroscopy*, vol. 34, pp. 478–486, June 1970.
- [200] A. Henry, M. F. Le Moal, P. Cardinet, and A. Valentin, “Overtone bands of $^{14}\text{N}^{16}\text{O}$ and determination of molecular constants,” *Journal of Molecular Spectroscopy*, vol. 70, pp. 18–26, Apr. 1978.
- [201] J. L. Teffo, A. Henry, P. Cardinet, and A. Valentin, “Determination of molecular constants of nitric oxide from (1-0), (2-0), (3-0) bands of the $^{15}\text{N}^{16}\text{O}$ and $^{15}\text{N}^{18}\text{O}$ isotopic species,” *Journal of Molecular Spectroscopy*, vol. 82, pp. 348–363, Aug. 1980.
- [202] G. Michalski, R. Jost, D. Sugny, M. Joyeux, and M. Thiemens, “Dissociation energies of six NO_2 isotopologues by laser induced fluorescence spectroscopy and zero point energy of some triatomic molecules,” *The Journal of Chemical Physics*, vol. 121, pp. 7153–7161, Oct. 2004.
- [203] I. D. of Environmental Management, “Indpls-Washington Park Data by Site by Date.”
- [204] H. O. Gao, “Day of week effects on diurnal ozone/ NO_x cycles and transportation emissions in Southern California,” *Transportation Research Part D: Transport and Environment*, vol. 12, no. 4, pp. 292–305, 2007.
- [205] C. E. P. Agency, “Air Quality Data (PST) Query Tool.”
- [206] R. Atkinson, D. L. Baulch, R. A. Cox, J. N. Crowley, R. F. Hampson, R. G. Hynes, M. E. Jenkin, M. J. Rossi, and J. Troe, “Evaluated kinetic and photochemical data for atmospheric chemistry: Volume I-gas phase reactions of O_x , HO_x , NO_x and SO_x species,” *Atmospheric chemistry and physics*, vol. 4, no. 6, pp. 1461–1738, 2004.
- [207] D. D. Parrish, P. C. Murphy, D. L. Albritton, and F. C. Fehsenfeld, “The measurement of the photodissociation rate of NO_2 in the atmosphere,” *Atmospheric Environment (1967)*, vol. 17, no. 7, pp. 1365–1379, 1983.
- [208] W. W. Walters, S. R. Goodwin, and G. Michalski, “Nitrogen Stable Isotope Composition ($\delta^{15}\text{N}$) of Vehicle-Emitted NO_x ,” *Environmental Science & Technology*, vol. 49, pp. 2278–2285, Feb. 2015.
- [209] M. H. Thiemens, “History and applications of mass-independent isotope effects,” *Annu. Rev. Earth Planet. Sci.*, vol. 34, pp. 217–262, 2006.
- [210] J. Savarino, J. Kaiser, S. Morin, D. M. Sigman, and M. H. Thiemens, “Nitrogen and oxygen isotopic constraints on the origin of atmospheric nitrate in coastal Antarctica,” *Atmospheric Chemistry and Physics*, vol. 7, no. 8, pp. 1925–1945, 2007.
- [211] B. Alexander, M. G. Hastings, D. J. Allman, J. Dachs, J. A. Thornton, and S. A. Kunasek, “Quantifying atmospheric nitrate formation pathways based on a global model of the oxygen isotopic composition ($\Delta^{17}\text{O}$) of atmospheric nitrate,” *Atmos. Chem. Phys.*, vol. 9, pp. 5043–5056, July 2009.

- [212] M. H. Thiemens and J. E. Heidenreich, "The Mass-Independent Fractionation of Oxygen: A Novel Isotope Effect and Its Possible Cosmochemical Implications," *Science*, vol. 219, pp. 1073–1075, Mar. 1983.
- [213] K. Mauersberger, P. Lammerzahl, and D. Krankowsky, "Stratospheric ozone isotope enrichments revisited," *Geophysical Research Letters*, vol. 28, no. 16, pp. 3155–3158, 2001.
- [214] T. A. Berhanu, J. Savarino, S. K. Bhattacharya, and W. C. Vicars, " ^{17}O excess transfer during the $\text{NO}_2 + \text{O}_3 \rightarrow \text{NO}_3 + \text{O}_2$ reaction," *The Journal of Chemical Physics*, vol. 136, p. 044311, Jan. 2012.
- [215] B. Alexander and L. J. Mickley, "Paleo-Perspectives on Potential Future Changes in the Oxidative Capacity of the Atmosphere Due to Climate Change and Anthropogenic Emissions," *Current Pollution Reports*, pp. 1–13, May 2015.
- [216] W. W. Walters, D. S. Simonini, and G. Michalski, "Nitrogen isotope exchange between NO and NO_2 and its implications for $\delta^{15}\text{N}$ variations in tropospheric NO_x and atmospheric nitrate," *Geophysical Research Letters*, vol. 43, p. 2015GL066438, Jan. 2016.
- [217] W. W. Walters and G. Michalski, "Theoretical calculation of oxygen equilibrium isotope fractionation factors involving various NO_y molecules, OH , and H_2O and its implications for isotope variations in atmospheric nitrate," *Geochimica et Cosmochimica Acta*, vol. 191, pp. 89–101, Oct. 2016.
- [218] A. R. Amell and F. Daniels, "Kinetics of the Exchange of N^{15} between N^{15}O_2 and N_2O ," *Journal of the American Chemical Society*, vol. 74, pp. 6209–6212, Dec. 1952.
- [219] M. J. Stern, W. Spindel, and E. U. Monse, "Temperature dependences of isotope effects," *The Journal of Chemical Physics*, vol. 48, no. 7, pp. 2908–2919, 1968.
- [220] J. R. Lyons, "Transfer of mass-independent fractionation in ozone to other oxygen-containing radicals in the atmosphere," *Geophysical Research Letters*, vol. 28, no. 17, pp. 3231–3234, 2001.
- [221] O. Redlich, "Eine allgemeine Beziehung zwischen den Schwingungsfrequenzen isotoper Molekeln," *Z. Physikal. Chem. B*, vol. 28, pp. 371–382, 1935.
- [222] D. R. Coulson, "Statistical factors in reaction rate theories," *Journal of the American Chemical Society*, vol. 100, no. 10, pp. 2992–2996, 1978.
- [223] E. L. I. Pollak and P. Pechukas, "Symmetry numbers, not statistical factors, should be used in absolute rate theory and in Broensted relations," *Journal of the American Chemical Society*, vol. 100, no. 10, pp. 2984–2991, 1978.
- [224] R. E. Pennington and K. A. Kobe, "Contributions of Vibrational Anharmonicity and Rotation-Vibration Interaction to Thermodynamic Functions," *The Journal of Chemical Physics*, vol. 22, pp. 1442–1447, Aug. 1954.
- [225] E. A. Schauble, P. Ghosh, and J. M. Eiler, "Preferential formation of ^{13}C - ^{18}O bonds in carbonate minerals, estimated using first-principles lattice dynamics," *Geochimica et Cosmochimica Acta*, vol. 70, no. 10, pp. 2510–2529, 2006.

- [226] M. J. Frisch, G. W. Trucks, H. B. Schlegel, G. E. Scuseria, M. A. Robb, J. R. Cheeseman, G. Scalmani, V. Barone, B. Mennucci, G. A. Petersson, H. Nakatsuji, M. Caricato, X. Li, H. P. Hratchian, A. F. Izmaylov, J. Bloino, G. Zheng, J. L. Sonnenberg, M. Hada, M. Ehara, K. Toyota, R. Fukuda, J. Hasegawa, M. Ishida, T. Nakajima, Y. Honda, O. Kitao, H. Nakai, T. Vreven, J. A. Montgomery Jr, J. E. Peralta, F. Ogliaro, M. Bearpark, J. J. Heyd, E. Brothers, K. N. Kudin, V. N. Staroverov, R. Kobayashi, J. Normand, K. Raghavachari, A. Rendell, J. C. Burant, S. S. Iyengar, J. Tomasi, M. Cossi, N. Rega, J. M. Milliam, M. Klene, J. E. Knox, J. B. Cross, V. Bakken, C. Adamo, J. Jaramillo, R. Gomperts, R. E. Stratmann, O. Yazyev, A. J. Austin, R. Cammi, C. Pomelli, J. W. Ochterski, R. L. Martin, K. Morokuma, V. G. Zakrzewski, G. A. Voth, P. Salvador, J. J. Dannenberg, S. Dapprich, A. D. Daniels, A. Farkas, J. B. Foresman, J. V. Ortiz, J. Cioslowski, and D. J. Fox, "Gaussian 09, Revision D.01.," 2009.
- [227] P. Sinha, S. E. Boesch, C. Gu, R. A. Wheeler, and A. K. Wilson, "Harmonic vibrational frequencies: scaling factors for HF, B3lyp, and MP2 methods in combination with correlation consistent basis sets," *The Journal of Physical Chemistry A*, vol. 108, no. 42, pp. 9213–9217, 2004.
- [228] A. P. Scott and L. Radom, "Harmonic vibrational frequencies: an evaluation of Hartree-Fock, Moller-Plesset, quadratic configuration interaction, density functional theory, and semiempirical scale factors," *The Journal of Physical Chemistry*, vol. 100, no. 41, pp. 16502–16513, 1996.
- [229] B. Kim, P. L. Hunter, and H. S. Johnston, "NO₃ radical studied by laser induced fluorescence," *The Journal of Chemical Physics*, vol. 96, pp. 4057–4067, Mar. 1992.
- [230] M. E. Jacox and W. E. Thompson, "The infrared spectroscopy and photochemistry of NO₃ trapped in solid neon," *The Journal of Chemical Physics*, vol. 129, p. 204306, Nov. 2008.
- [231] H. Beckers, H. Willner, and M. E. Jacox, "Conflicting Observations Resolved by a Far IR and UV/Vis Study of the NO₃ Radical," *ChemPhysChem*, vol. 10, no. 4, pp. 706–710, 2009.
- [232] J. K. B  hlke, S. J. Mroczkowski, and T. B. Coplen, "Oxygen isotopes in nitrate: New reference materials for ¹⁸O: ¹⁷O: ¹⁶O measurements and observations on nitrate-water equilibration," *Rapid Communications in Mass Spectrometry*, vol. 17, no. 16, pp. 1835–1846, 2003.
- [233] J. Savarino, S. Morin, J. Erbland, F. Grannec, M. D. Patey, W. Vicars, B. Alexander, and E. P. Achterberg, "Isotopic composition of atmospheric nitrate in a tropical marine boundary layer," *Proceedings of the National Academy of Sciences*, vol. 110, pp. 17668–17673, Oct. 2013.
- [234] A. G. Russell, G. J. McRae, and G. R. Cass, "The dynamics of nitric acid production and the fate of nitrogen oxides," *Atmospheric Environment (1967)*, vol. 19, no. 6, pp. 893–903, 1985.
- [235] W. L. Chang, P. V. Bhave, S. S. Brown, N. Riemer, J. Stutz, and D. Dabdub, "Heterogeneous atmospheric chemistry, ambient measurements, and model calculations of N₂O₅: A review," *Aerosol Science and Technology*, vol. 45, no. 6, 2011.

- [236] A. Geyer and U. Platt, "Temperature dependence of the NO_3 loss frequency: A new indicator for the contribution of NO_3 to the oxidation of monoterpenes and NO_x removal in the atmosphere," *Journal of Geophysical Research: Atmospheres*, vol. 107, no. D20, 2002.
- [237] W. C. Vicars, S. K. Bhattacharya, J. Erbland, and J. Savarino, "Measurement of the ^{17}O excess ($\Delta^{17}\text{O}$) of tropospheric ozone using a nitrite-coated filter," *Rapid Communications in Mass Spectrometry*, vol. 26, no. 10, pp. 1219–1231, 2012.
- [238] M. F. Miller, "Isotopic fractionation and the quantification of ^{17}O anomalies in the oxygen three-isotope system: an appraisal and geochemical significance," *Geochimica et Cosmochimica Acta*, vol. 66, no. 11, pp. 1881–1889, 2002.
- [239] J. Bigeleisen, "The Relative Reaction Velocities of Isotopic Molecules," *The Journal of Chemical Physics*, vol. 17, pp. 675–678, Aug. 1949.
- [240] J. Peiras-Garca and I. Nebot-Gil, "Ab Initio Study of the Mechanism and Thermochemistry of the Atmospheric Reaction $\text{NO} + \text{O}_3 \rightarrow \text{NO}_2 + \text{O}_2$," *The Journal of Physical Chemistry A*, vol. 106, pp. 10302–10310, Oct. 2002.
- [241] V. Anisimov and P. Paneth, "ISOEFF98. A program for studies of isotope effects using Hessian modifications," *Journal of Mathematical Chemistry*, vol. 26, no. 1-3, pp. 75–86, 1999.
- [242] R. E. Weston, "Anomalous or Mass-Independent Isotope Effects," *Chemical Reviews*, vol. 99, pp. 2115–2136, Aug. 1999.
- [243] P. Adamczyk, A. Dybala-Defratyka, and P. Paneth, "DFT study of trichloroethene reaction with permanganate in aqueous solution," *Environmental science & technology*, vol. 45, no. 7, pp. 3006–3011, 2011.
- [244] H. D. Babcock and L. Herzberg, "Fine Structure of the Red System of Atmospheric Oxygen Bands.," *The Astrophysical Journal*, vol. 108, p. 167, 1948.
- [245] G. Herzberg, *Electronic Spectra and Electronic Structure of Polyatomic Molecules*. New York: Van Nostrand, 1966.
- [246] J. I. Steinfeld, S. M. Adler Golden, and J. W. Gallagher, "Critical Survey of Data on the Spectroscopy and Kinetics of Ozone in the Mesosphere and Thermosphere," *Journal of Physical and Chemical Reference Data*, vol. 16, pp. 911–951, Oct. 1987.
- [247] F. J. Lovas, E. Tiemann, J. S. Coursey, S. A. Kotochigova, J. Chang, K. Olsen, and R. A. Dragoset, "NIST: Diatomic Spectral Database," Dec. 2014.
- [248] G. S. Hammond, "A Correlation of Reaction Rates," *Journal of the American Chemical Society*, vol. 77, pp. 334–338, Jan. 1955.
- [249] S. Chakraborty and S. Chakraborty, "Isotopic fractionation of the O_3 nitric oxide reaction," *Current Science-bangalore*, vol. 85, no. 8, pp. 1210–1211, 2003.
- [250] C. Janssen, "Intramolecular isotope distribution in heavy ozone ($^{16}\text{O}^{18}\text{O}^{16}\text{O}$ and $^{16}\text{O}^{16}\text{O}^{18}\text{O}$)," *Journal of Geophysical Research: Atmospheres (1984–2012)*, vol. 110, no. D8, 2005.

- [251] J. Savarino, S. K. Bhattacharya, S. Morin, M. Baroni, and J.-F. Doussin, "The $\text{NO}^+ + \text{O}_3$ reaction: A triple oxygen isotope perspective on the reaction dynamics and atmospheric implications for the transfer of the ozone isotope anomaly," *The Journal of chemical physics*, vol. 128, no. 19, p. 194303, 2008.
- [252] S. K. Bhattacharya, A. Pandey, and J. Savarino, "Determination of intramolecular isotope distribution of ozone by oxidation reaction with silver metal," *Journal of Geophysical Research: Atmospheres*, vol. 113, no. D3, 2008.
- [253] M.-C. Liang, F. W. Irion, J. D. Weibel, C. E. Miller, G. A. Blake, and Y. L. Yung, "Isotopic composition of stratospheric ozone," *Journal of Geophysical Research: Atmospheres*, vol. 111, no. D2, 2006.
- [254] C. E. Snape, C. G. Sun, A. E. Fallick, R. Irons, and J. Haskell, "Potential of stable nitrogen isotope ratio measurements to resolve fuel and thermal NO_x in coal combustion," *Papers of the American Chemical Society*, vol. 225, pp. U843–U843, 2003.
- [255] S. Morin, J. Savarino, M. M. Frey, N. Yan, S. Bekki, J. W. Bottenheim, and J. M. Martins, "Tracing the origin and fate of NO_x in the Arctic atmosphere using stable isotopes in nitrate," *Science*, vol. 322, no. 5902, pp. 730–732, 2008.
- [256] "Google Earth."
- [257] J. K. BÅhlke, R. L. Smith, and J. E. Hannon, "Isotopic analysis of N and O in nitrite and nitrate by sequential selective bacterial reduction to N_2O ," *Analytical chemistry*, vol. 79, no. 15, pp. 5888–5895, 2007.
- [258] K. L. Casciotti, J. K. Bohlke, M. R. McIlvin, S. J. Mroczkowski, and J. E. Hannon, "Oxygen isotopes in nitrite: analysis, calibration, and equilibration," *Analytical Chemistry*, vol. 79, no. 6, pp. 2427–2436, 2007.
- [259] M. G. Hastings, D. M. Sigman, and F. Lipschultz, "Isotopic evidence for source changes of nitrate in rain at Bermuda," *Journal of Geophysical Research: Atmospheres*, vol. 108, no. D24, 2003.
- [260] J. G. Murphy, D. A. Day, P. A. Cleary, P. J. Wooldridge, and R. C. Cohen, "Observations of the diurnal and seasonal trends in nitrogen oxides in the western Sierra Nevada," *Atmospheric Chemistry and Physics*, vol. 6, no. 12, pp. 5321–5338, 2006.
- [261] K. F. Boersma, D. J. Jacob, M. Trainic, Y. Rudich, I. DeSmedt, R. Dirksen, and H. J. Eskes, "Validation of urban NO_2 concentrations and their diurnal and seasonal variations observed from the SCIAMACHY and OMI sensors using in situ surface measurements in Israeli cities," *Atmospheric Chemistry and Physics*, vol. 9, no. 12, pp. 3867–3879, 2009.
- [262] J. Ludwig, F. X. Meixner, B. Vogel, and J. FÅrstner, "Soil-air exchange of nitric oxide: An overview of processes, environmental factors, and modeling studies," *Biogeochemistry*, vol. 52, no. 3, pp. 225–257, 2001.
- [263] S. M. Van Dijk, A. Gut, G. A. Kirkman, B. M. Gomes, F. X. Meixner, and M. O. Andreae, "Biogenic NO emissions from forest and pasture soils: Relating laboratory studies to field measurements," *Journal of Geophysical Research: Atmospheres*, vol. 107, no. D20, 2002.

- [264] G. C. M. Vinken, K. F. Boersma, J. D. Maasakkers, M. Adon, and R. V. Martin, "Worldwide biogenic soil NO_x emissions inferred from OMI NO₂ observations," *Atmospheric Chemistry and Physics*, vol. 14, no. 18, pp. 10363–10381, 2014.
- [265] J. Notholt, J. Hjorth, and F. Raes, "Formation of HNO₂ on aerosol surfaces during foggy periods in the presence of NO and NO₂," *Atmospheric Environment. Part A. General Topics*, vol. 26, pp. 211–217, Jan. 1992.
- [266] J.-M. Yoo, Y.-R. Lee, D. Kim, M.-J. Jeong, W. R. Stockwell, P. K. Kundu, S.-M. Oh, D.-B. Shin, and S.-J. Lee, "New indices for wet scavenging of air pollutants (O₃, CO, NO₂, SO₂, and PM₁₀) by summertime rain," *Atmospheric Environment*, vol. 82, pp. 226–237, 2014.

APPENDICES

A. SUPPLEMENTARY DATA CHAPTER 6

Table A.1: Adapted $^{15}\beta$ regression coefficients as a function of temperature (150 to 450 K) for NO, NO₂, NO₃, and N₂O₅ that include corrections for zero point energy anharmonicity.

Molecule	A	B	C	D	$^{15}\beta(298\text{K})$
NO	5.4801	-9.8232	6.7075	0.66049	1.0669
NO ₂	9.1062	-16.973	12.850	0.45663	1.1064
NO ₃ *	6.0862	-12.640	11.394	-0.03768	1.0870
N ₂ O ₅	9.4789	-18.048	15.232	0.61362	1.1359

$^{15}\beta$ values adapted from [101]. All $^{15}\beta$ values were calculated using B3LYP/cc-pVTZ, except for NO₃, which was calculated from EDF2/cc-pVTZ. Regression fit: $1000(\beta - 1) = \frac{A}{T^4} \times 10^{10} + \frac{B}{T^3} \times 10^8 + \frac{C}{T^2} \times 10^6 + \frac{D}{T} \times 10^4$ (typical misfit of the regression is 0.1‰). Typical misfit in the regression is < 0.01‰.

Table A.2: Adapted $^{15}\alpha_{A/B}$ regression coefficients as a function of temperature (150 to 450 K) for N isotopic exchange reactions between NO, NO₂, NO₃, and N₂O₅ that include corrections for zero point energy anharmonicity.

Exchange	A	B	C	D	$^{15}\alpha(300\text{K})$
NO ₃ /NO ₂	-2.7193	3.6759	-0.92418	-0.54189	0.9819
N ₂ O ₅ /NO ₂	0.69398	-1.9859	2.3876	0.16308	1.0255
NO ₂ /NO	3.8834	-7.7299	6.0101	-0.17928	1.0370

Regression fit: $1000(\beta - 1) = \frac{A}{T^4} \times 10^{10} + \frac{B}{T^3} \times 10^8 + \frac{C}{T^2} \times 10^6 + \frac{D}{T} \times 10^4$ (typical misfit of the regression is 0.1‰). Typical misfit in the regression is < 0.01‰.

B. SUPPLEMENTARY DATA CHAPTER 7

Table B.1: Cartesian coordinates of the optimized geometries of reactants and products calculated at CCSD(T)/6-31G(d) and CCSD(T)/6-311G(d).

	CCSD(T)/6-31G(d)			CCSD(T)/6-311G(d)		
	x	y	z	x	y	z
NO						
N	0.00000	0.00000	-0.62332	0.00000	0.00000	-0.61560
O	0.00000	0.00000	0.54541	0.00000	0.00000	0.53865
O3						
O	0.00000	-0.45458	0.00000	0.00000	0.44535	0.00000
O	1.10218	0.22727	0.00000	1.08739	-0.22288	0.00000
O	-1.10218	0.22730	0.00000	-1.08739	-0.22247	0.00000
NO2						
N	0.00000	-0.33239	0.00000	0.00000	0.32694	0.00000
O	1.11788	0.14525	0.00000	1.10624	-0.14302	0.00000
O	-1.11788	0.14559	0.00000	-1.10624	-0.14305	0.00000
O2						
O	0.00000	0.00000	0.61463	0.00000	0.00000	0.60512
O	0.00000	0.00000	-0.61463	0.00000	0.00000	-0.60512

Table B.2: Scaled harmonic frequencies for the major ^{15}N , ^{17}O , and ^{18}O isotopologues of the reactants and products calculated using the ISOEFF program from force constants computed at CCSD(T)/6-31G(d) and CCSD(T)/6-311G(d).

	ω_1	ω_2	ω_3		ω_1	ω_2	ω_3
$^{15}\text{N}^{16}\text{O}$				$^{16}\text{O}^{15}\text{N}^{16}\text{O}$			
A	1912.9			A	713.7	1319.4	1663.9
B	1960.6			B	689.3	1303.8	1660.3
$^{14}\text{N}^{17}\text{O}$				$^{17}\text{O}^{14}\text{N}^{16}\text{O}$			
A	1920.7			A	723.1	1333.4	1701.6
B	1968.5			B	692.1	1303.6	1689.5
$^{14}\text{N}^{18}\text{O}$				$^{18}\text{O}^{14}\text{N}^{16}\text{O}$			
A	1896.4			A	710.1	1306.9	1686.2
B	1943.7			B	686.5	1290.6	1682.7
$^{17}\text{O}^{16}\text{O}^{16}\text{O}$				$^{17}\text{O}^{16}\text{O}$			
A	671.1	977.9	1098.5	A	1539.4		
B	678.6	981.7	1087.6	B	1506.2		
$^{18}\text{O}^{16}\text{O}^{16}\text{O}$				$^{18}\text{O}^{16}\text{O}$			
A	663.5	971.6	1091.9	A	1518.6		
B	670.8	975.3	1081.4	B	1485.8		
$^{16}\text{O}^{17}\text{O}^{16}\text{O}$							
A	675.2	966.9	1091.4				
B	683.1	970.8	1080.0				

where A and B refer to CCSD(T)/6-31G(d) and CCSD(T)/6-311G(d), respectively.

Table B.3: Cartesian coordinates of the optimized geometries of **TS1** calculated at CCSD(T)/6-31G(d) and CCSD(T)/6-311G(d).

	CCSD(T)/6-31G(d)			CCSD(T)/6-311G(d)		
	x	y	z	x	y	z
TS1						
N	-1.36421	-0.39236	0.38925	-1.36021	-0.40322	0.37377
O	-2.3008	-0.08826	-0.22076	-2.28425	-0.0766	-0.21452
O	0.31541	0.88806	-0.21946	0.30507	0.86292	-0.21217
O	1.37721	0.30378	0.36163	1.36118	0.30038	0.35934
O	1.80187	-0.76026	-0.26201	1.80818	-0.73388	-0.2597

Table B.4: Calculated isotope enrichment factors ($\epsilon(\text{‰})$) for the major heavy NO and O₃ isotopologues as a function of temperature using CCSD(T)/6-31G(d) frequencies.

Temp (K)	¹⁶ O ¹⁵ N	¹⁸ O ¹⁴ N	¹⁸ O ¹⁶ O ¹⁶ O	¹⁶ O ¹⁸ O ¹⁶ O	¹⁶ O ¹⁶ O ¹⁸ O
220	-4.2	3.2	-50.7	-16.4	1.3
250	-5.9	1.8	-47.7	-14.9	1.0
273	-6.8	1.0	-45.7	-13.8	0.9
298	-7.7	0.3	-43.9	-12.7	0.8
320	-8.3	-0.2	-42.5	-11.8	0.7

Table B.5: Calculated isotope enrichment factors ($\epsilon(\text{‰})$) for the major heavy NO and O₃ isotopologues as a function of temperature using CCSD(T)/6-31G(d) frequencies.

Temp (K)	¹⁶ O ¹⁵ N	¹⁸ O ¹⁴ N	¹⁸ O ¹⁶ O ¹⁶ O	¹⁶ O ¹⁸ O ¹⁶ O	¹⁶ O ¹⁶ O ¹⁸ O
220	-2.7	2.7	-51.8	-18.4	-0.3
250	-4.6	0.7	-48.6	-16.6	-0.3
273	-5.8	-0.4	-46.6	-15.3	-0.3
298	-6.7	-1.3	-44.7	-14.1	-0.3
320	-7.4	-1.9	-43.2	-13.0	-0.3

VITA

VITA

Wendell Walters

Purdue University

Department of Earth, Atmospheric, and Planetary Sciences

550 Stadium Mall Drive

West Lafayette, IN 47907

Email: waltersw@purdue.edu

EDUCATION AND RESEARCH

Purdue University, West Lafayette, IN

Department of Earth, Atmospheric, and Planetary Sciences & Purdue Climate Change
Research Center

- Graduate research with Dr. Greg Michalski, Aug. 2012 - Present
- Bilsland Dissertation Fellowship Summer 2016 - Fall 2016
- NSF Graduate Research Fellow (NSF-GRFP), Fall 2013 - Summer 2016
- Purdue Climate Change Research Center Fellow, Fall 2012 - Summer 2013

University of Maryland, College Park, MD

Department of Chemistry and Biogeochemistry

- B. S., Chemistry (Scholars), May 2012
- Undergraduate research with Dr. Amy Mullin, Aug. 2010 - July, 2012
- Project: " Construction of an OPO-based transient IR absorption spectrometer to study isotope effects in molecular collisions"

PUBLICATIONS

- **Walters, W. W.**; Michalski, G. Theoretical calculation of oxygen equilibrium isotope fractionation factors involving various NO_y molecules, .OH, and H₂O and its implications for isotope variations in atmospheric nitrate. *Geochim. Cosmochim. Acta* **2016**, *191*, 89-101.
- Lyons, W. B.; Deuerling, K.; Welch, K. A.; Welch, S. A.; Michalski, G.; **Walters, W. W.**; Nielsen, U.; Wall, D. H.; Hogg, I.; Adams, B. J. The soil geochemistry in the Beardmore Glacier Region, Antarctica: implications for terrestrial ecosystem history. *Sci. Rep.* **2016**, *6*, 26189.
- **Walters, W. W.**; Simonini, D. S.; Michalski, G. Nitrogen isotope exchange between NO and NO₂ and its implications for ¹⁵N variations in tropospheric NO_x and atmospheric nitrate. *Geophys. Res. Lett.* **2016**, *43*(1), 440-448.
- **Walters, W. W.**; Tharp, B. D.; Fang, H.; Kozak, B. J.; Michalski, G. Nitrogen isotope composition of thermally produced NO_x from various fossil-fuel combustion sources. *Environ. Sci. Technol.* **2015**, *49*(19), 11363-11371.
- **Walters, W. W.**; Michalski, G. Theoretical calculation of nitrogen equilibrium isotope exchange fractionation factors for various NO_y molecules. *Geochim. Cosmochim. Acta* **2015**, *164*, 284-297.
- **Walters, W. W.**; Goodwin, S. R.; Michalski, G. Nitrogen stable isotope composition (¹⁵N) of vehicle-emitted NO_x. *Environ. Sci. Technol.* **2015**, *49*(4), 2278-2285.
- Echebiri, G. O.; Smarte, M. D.; **Walters, W. W.**; Mullin, A. S. Performance of a high-resolution mid-IR optical-parametric-oscillator transient absorption spectrometer. *Optics Express* **2014**, *22*(12), 14885-14895.

Manuscripts in press:

- **Walters, W. W.**; Michalski, G. Ab initio study of nitrogen and position-specific oxygen kinetic isotope effects in the NO + O₃ reaction, *J. Chem. Phys.*

Manuscripts in prep:

- **Walters, W. W.**; Fang, H.; Michalski, G. Summertime diurnal variations in the isotopic composition of atmospheric nitrogen dioxide at a small Midwestern city.
- **Walters, W. W.**; Michalski, G. Isotope compositions of Antarctic nitrate and sulfate aerosols.
- Fang, H.; Michalski, G.; **Walters, W. W.** Incorporating nitrogen isotopes in the Regional Atmospheric Chemistry Mechanism Model (RCAM).

HONORS

Awards

- Purdue Earth, Atmospheric, and Planetary Sciences Outstanding Graduate Student of the Year, 2016
- Henry Silver Environmental Science Graduate Student of the Year, 2015
- American Institute of Chemists Award, 2012
- Bruce Jarvis Scholarship Endowment, 2011
- Isidore and Annie Adler Chemistry Scholarship, 2010

Fellowships and Grants

- NSF Atmospheric Geological Sciences Postdoctoral Research Fellowship (NSF AGS-PRF, \$172,000), 2016
- P. F. Low Travel Grant (\$1,000), 2015
- Purdue Climate Change Research Center Travel Grant (\$600), 2015
- Geological Society of American Graduate Research Grant (\$900), 2014
- NSF Graduate Research Fellow Program Recipient (NSF GRFP, \$96,000), 2013
- Purdue Climate Change Research Center Travel Grant (\$2,000), 2013
- P. F. Low Travel Grant (\$1,500), 2013

- Purdue Climate Change Research Center Graduate Fellowship (\$21,000), 2012

SOCIETIES AND ACTIVITIES

- Purdue Climate Change Research Center Graduate Committee, (2015-Present)
- Purdue Graduate Student Government Senator, (2013-2014)
- Purdue Graduate Student Grant Committee, (2013-2014)
- American Geophysical Union, (2013-Present)
- Geological Society of America, (2013- Present)
- Earth, Atmospheric, and Planetary Sciences Graduate Student Association, (2012-Present)
- American Chemical Society, (2011-Present)

TEACHING

Purdue University, West Lafayette, IN

- Teaching Assistant: EAPS521/CHM581, Atmospheric Chemistry, Fall 2015
- Guest Laboratory Instructor: EAPS591, Stable Isotope Instrumentation, Spring 2014

University of Maryland, College Park, MD

- Teaching Assistant, CHM132, General Chemistry 1 Lab, Fall 2009, Spring 2010, and Fall 2011
- Tutor, CHM131, General Chemistry 1, Fall 2011
- Tutor, CHM271, General Chemistry 2, Summer 2010

PRESENTATIONS

- Purdue University, Department of Earth, Atmospheric, and Planetary Sciences Expo, Feb. 2016 (Talk)

- American Geophysical Union, Dec. 2015 (Poster)
- Purdue University, Department of Earth, Atmospheric, and Planetary Sciences Expo, Feb. 2015 (Talk)
- American Geophysical Union, Dec. 2014 (Poster)
- Indiana University, Crossroads Geology Conference, March 2014 (Talk)
- Purdue University, Department of Earth, Atmospheric, and Planetary Sciences Expo, Feb. 2014 (Talk)
 - Prize: outstanding student presentation
- American Geophysical Union, Dec. 2013 (Talk)